Overcoming Barriers in Structural Biology

Through Method Development of Serial

Crystallography

by

Chelsie E. Conrad

A Dissertation Presented in Partial Fulfillment
of the Requirements for the Degree
Doctor of Philosophy

Approved November 2016 by the
Graduate Supervisory Committee:

Petra Fromme, Chair
Alexandra Ros
James Allen

ARIZONA STATE UNIVERSITY

December 2016

ABSTRACT

Serial crystallography (SX) is a relatively new structural biology technique that collects X-ray diffraction data from microcrystals via femtosecond pulses produced by an X-ray free electron laser (X-FEL) or by synchrotron radiation, allowing for challenging protein structures to be solved from microcrystals at room temperature. Because of the youth of this technique, method development is necessary for it to achieve its full potential.

Most serial crystallography experiments have relied on delivering sample in the mother liquor focused into a stream by compressed gas. This liquid stream moves at a fast rate, meaning that most of the valuable sample is wasted. For this reason, the liquid jet can require 10-100 milligrams of sample for a complete data set. Agarose has been developed as a slow moving microcrystal carrier to decrease sample consumption and waste. The agarose jet provides low background, no Debye-Sherrer rings, is compatible for sample delivery in vacuum environments, and is compatible with a wide variety of crystal systems. Additionally, poly(ethylene oxide) which is amenable for data collection in atmosphere has been developed for synchrotron experiments. Thus this work allows sample limited proteins of difficult to crystallize systems to be investigated by serial crystallography.

Time-resolved serial X-ray crystallography (TR-SX) studies have only been employed to study light-triggered reactions in photoactive systems. While these systems are very important, most proteins in Nature are not light-driven. However, fast mixing of two liquids, such as those containing enzyme protein crystals and substrates, immediately before being exposed to an X-ray beam would allow conformational changes and /or intermediates to be seen by diffraction. As a model, 3-deoxy-D-manno-2-octulosonate-8-phosphate synthase (KDO8PS), has been developed for TR-SX. This enzyme initializes the first step of lipopolysaccharide synthesis by a net aldol condensation between arabinose-5-phosphate, phosphoenol pyruvate, and water. During this reaction, a short lived intermediate is formed and has been observed on a millisecond timescale using other methods. Thus KDO8PS is an ideal model protein for studying diffusion times into a crystal and short mixing times (<10 ms). For

these experiments, microcrystals diffracting to high resolution have been developed and characterized.

.

DEDICATION

This thesis is dedicated to my grandfather, Max Leroy Sweat PhD, who sparked my curiosity with a basement full of treasures and believed I could become anything I wanted to be. Thank you Guddy, for   looking down on me as I follow in your footsteps, I hope that I can leave the legacy of science and character that you have.

ACKNOWLEDGMENTS

TABLE OF CONTENTS

LIST OF TABLES

LIST OF FIGURES

CHAPTER 1

INTRODUCTION

1.1 STRUCTURE DETERMINATION

Solving the three-dimensional structure of proteins, viruses, and nucleic acids increases our understanding of the function of the macromolecule, aids in finding similar systems in nature, aids in designing new pharmaceutical targets, and provides insight to dynamic process of these macromolecules. However, the small size of these macromolecules can make their physical structure or folding in nature difficult to solve as the average carbon-carbon bond is only 1.54 Å but the wavelength of visible light limits our ability to see object below 2 µm. Thus researchers have used a wide variety of methods, X-ray crystallography, transmission electron microscopy, and nuclear magnetic resonance to probe the physical attributes of these macromolecules at high special resolution. A brief overview of X-ray crystallography is described below, for an in depth review of the subject the reader is referred to (Woolfson, 1997; Drenth, 2007; Rupp, 2010) .

1.1.1. X-RAY DIFFRACTION

X-ray crystallography has been the primary method for structure determination of biological macromolecules. As a result, this technique has been used to solve over 90% of the structures in the protein data base (Mizianty, Fan et al. 2014). The field of X-ray diffraction for the study of the structure of molecules was first proposed Max von Laue in 1899. The first X-ray diffraction experiment was carried out in 1912 by Max von Laue, which was followed by the realization that X-ray diffraction could be used for atomic structure determination of matter by the Braggs (Friedrich, Knipping et al. 1912, Bragg, Bragg 1913) and the first diffraction of a protein was obtained in 1934 on pepsin (W. T. Astbury 1934) but it wasn't until 1958 that the first structure of a protein, myoglobin, was solved (Kendrew, Bodo et al. 1958). These early X-ray diffraction experiments were carried out using X-ray tubes as X-ray sources. Where the electrons

are generated by applying a high voltage to a cathode, the electrons are then accelerated by a large potential difference towards an anode (typically composed of tungsten, copper, or molybdenum) within a vacuum tube. The sudden electron deceleration upon collision with the anode results in Bremsstahlung radiation (Zink 1997). The majority of this energy is dissipated as heat which can erode the anode or damage the tube, resulting in a loss of vacuum. By rotating the anode at (3000 to 9000 rpms/minute) heat is evenly dispersed across the surface of the anode, allowing for greater exposure times and a higher electrical load (Zink 1997). The X-ray radiation produced by X-ray tubes made a significant impact in the field of structural biology, including the structure of DNA in 1953 solved by Rosalind Franklin (Watson and Crick 1953). However the X-rays produced by these tubes cannot be focused and the X-ray light is limited to discrete wavelengths determined by the metal composition of the anode.

In the 1960s it was realized that X-ray light from synchrotron particle accelerators (used for particle physics since the 1930s) could be harnessed to overcome the restrictions of rotating anodes. Additionally synchrotron light sources produce over 100,000 times the flux of rotating anodes (Williams 1982). But it wasn't until the 1981 that a particle accelerator was dedicated to synchrotron radiation (Helliwell 1984). In a synchrotron (Figure 1.1) electrons are generated by heating the cathode to nearly 1000°C, usually composed of tungsten. The electrons are then intersected with a low energy microwave signal, producing bunches. The bunched electrons are then accelerated in a linear accelerator where they are sped up to nearly the speed of light. Then, the electrons enter the booster ring where they are accelerated further by resonating radio frequency cavities and are boosted from mega electron volts to giga electron volts (Helliwell 1984). The electrons are then injected into a storage ring where they are forced to move through bending magnets, undulators, or wigglers. As the electrons move through these magnets, they are forced to change direction which results in a loss of momentum which is accounted for by the production of photons, which is called synchrotron radiation. The energy in the storage ring is then maintained by radio frequency cavities with attracting voltages plates (Williams 1982) allowing radiation to be produced for hours or even days.
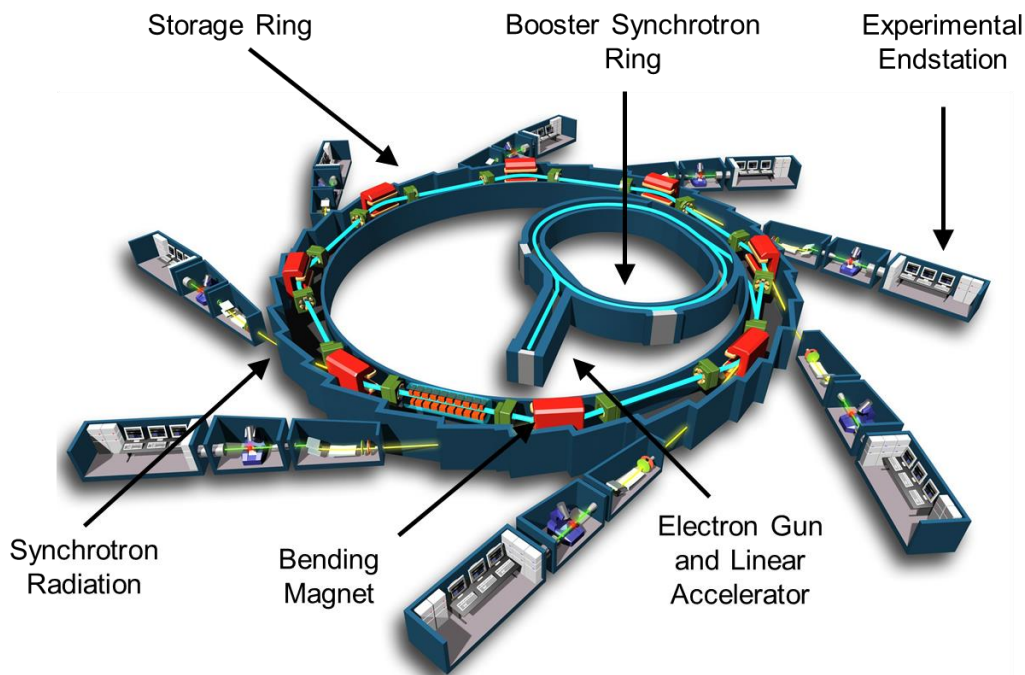
Figure 1.1 Illustration of a synchrotron light source. Electrons, generated from an electron gun, are accelerated in a linear accelerator and then enter into a storage ring where their speed and energy are further increased. Then, the electrons are then injected into the storage ring. As the electrons are forced to change direction in the bending magnets, they produce synchrotron radiation. The electrons remain in the storage ring, constantly producing more radiation. Thus, each endstation can operate simultaneously. At each endstation, a single wavelength is then selected by using a monochromator, which separates the light into its constituent wavelengths. The monochromatic beam is then focused using mirrors. Figure adapted and used with permission from schéma de principe Copyright © Chaix & Morel et associés,

In X-ray crystallography, the position of each atom in the macromolecule(s) is probed by illuminating crystals of the macromolecule with X-rays (0.01-10 nanometer wavelength). When X-rays interact with the electrons of an atom, the X-rays are refracted from their original angle (Figure 1.2). However with current X-ray sources, the signal from one macromolecule is not intense enough to be detected, so the protein must be crystallized. In a crystal, the molecules are packed in repeating blocks, termed unit cells where the asymmetric units in the unit cell relate to each other by crystallography symmetry operations. The diffracted waves from planes in the

3
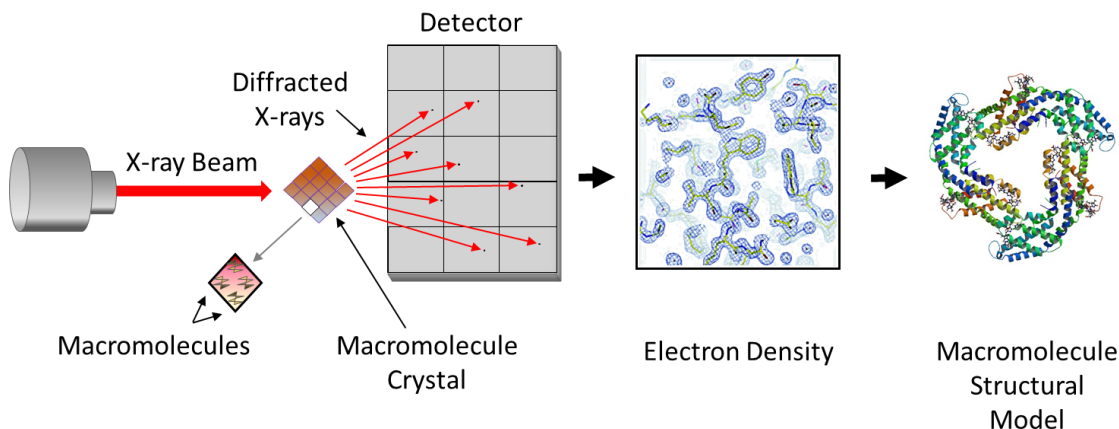
Figure 1.2 Overview of an X-ray crystallography experiment. A crystal, composed of many ordered macromolecules in a crystalline lattice is illuminated by X-rays. The diffracted X-rays produce reflections on a detector. The crystal is then rotated through the beam until the planes met the Bragg conditions to obtain all reflections that originate from planes within a crystal. The reflections contain information about the amplitude of the diffracted X-rays, however the phase must be solved via additional methods. Once the phase has been solved, an electron density map of the macromolecule can be generated which is used to make a model of the three-dimensional structure of the macromolecule.

crystal result in both constructive and deconstructive interference, providing an amplified signal when certain conditions are met. The conditions in which diffraction occurs from planes within a crystal was originally described by William Lawrence Bragg and his father William Henry Bragg in 1913 (Bragg and Bragg 1913). This is now referred to as Bragg's law (equation 1).

Equation 1: $$n\lambda = 2dSin(\theta)$$

Where d is the spacing between planes in the crystal, 2θ is the angle between a normal vector perpendicular to the planes and the propagating beam, and $n\lambda$ is an integer number multiple of the wavelength of the X-rays. The Bragg spots or 'reflections', signals that arise from meeting these conditions, are enhanced by constructive interference due to the translational symmetry

4
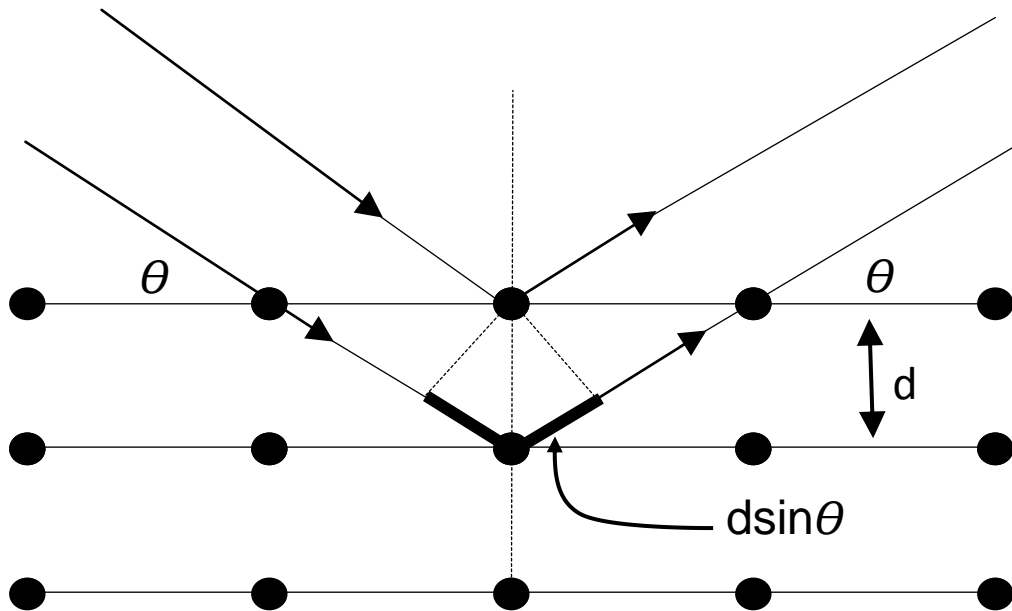
Figure 1.3 Depiction of Bragg's Law. The conditions of Bragg's law are met when diffraction by X-ray scattering from lattice planes results in constructive interference.

inherent in a crystal and were originally detected by a film, now photon detector or charge-coupled devices are used as detectors. Each reflection is the product of scattering functions of electrons in a discrete plane within the crystal and corresponds to a point in reciprocal space (K-space). To obtain a three-dimensional rendering, the crystal is rotated on a goniometer in the X-ray beam. The relationship between the scattered waves and the crystal planes (hkl) is termed the crystallographic structure factor. These structure factors are a sum of all molecular and subsequently atomic scattering factors in the unit cell and are described by an amplitude and phase. Equation 2 describes a structure factor as a Fourier term.

Equation 2: $$f_{hkl} = f_j e^{2\pi(hxj + kyj + lzj)}$$

Where Fhkl (see equation 3) is the structure factor at a particular h,k,l, fj is the scattering factor of atom j (of N atoms), h, k, I are the miller indices that satisfy Bragg's law for of a specific reflection in the reciprocal lattice, xj , yj , zj are the coordinates of atom j in the unit cell (real space). As can be noted, this takes the form of a Fourier transform between the electron density (scatterer positions in space) and structure factors (elastic scattering functions). Since electrons in a molecule can be thought of as a 'cloud', the spatial electron density, ρ(x,y,z), is essentially equivalent to the summed scattering factors from the previous equation where the discrete sum becomes continuous. By integrating ρ(x,y,z), the average values will be equal to the actual values (equation 3).

Equation 3: $$F_{hkl} = \int_h \int_k \int_l \rho(x,y,z)e^{2\pi(hxj + kyj + lzj)} \, dxdydz$$

By taking an inverse Fourier transform, an equation to obtain electron density from structure factors is generated (equation 4).

Equation 4: $$\rho(x,y,z) = \frac{1}{V}\sum_h \sum_k \sum_l F_{hkl} \, e^{2\pi(hxj + kyj + lzj)}$$

Because we only measure the scalar structure factor amplitude from the intensities of the reflections, we lose the phases this is called "the phase problem". Briefly, to recover the phases, several different methods can be employed. Molecular replacement uses prior information from a similar molecule (approximately >25% sequence identity but varies with each system) (Scapin 2013) with use of an iterative process, searching for orientation and position. This method requires no additional data collection to determine the phases (Rossmann and Blow 1962). Multiple isomorphous replacement, where marker atoms, typically a heavy atoms are soaked into the crystal. Difference data from the intensity differences between the native crystal and the

heavy atom derivative crystal allows for the sub structure of heavy atom to be determined using Patterson search methods or direct methods (Perutz 1956, Kendrew, Bodo et al. 1958). The placement of the heavy atoms allows for the starting phases of the macromolecule to be determined. Multiple data sets with different heavy atoms or difference in occupancy must be collected for multiple isomorphous replacement. In anomalous scattering from heavy atoms for structure phasing, data are collected at two different wavelengths, one being the absorption edge of the heavy atom. At the absorption edge, the phase and amplitude of the structure factor change, leading to a breakdown of Friedel's law. The Friedel pairs (hkl and –h-k-l) have the same amplitude and phase when scattering is fully elastic. When data are collected at the absorption edge, a phase shift occurs changing both the intensities and phases.

X-ray crystallography faces several limitations. The largest limitation is growing well diffracting crystals of the macromolecular molecule. To grow crystals, conditions must be found to slowly approach the supersaturation phase where the macromolecule precipitates or crystallizes from the solution. Creating a super saturated solution is usually achieved by change of the physical and chemical parameters. Examples include the addition or removal of salt, addition of a "precipitant", change in pH, and/or change in temperature. Finding conditions that form large crystals (>0.1 mm) can require a significant amount of time and most screening for crystallization is still done by trial and error. For some crystals this can take years and even then some molecules resist crystallization especially if they contain flexible domains. Crystallization is extremely difficult for macromolecules with flexible regions and in some cases these regions must be removed for crystallization to be possible. Lastly, crystals of macromolecules are prone to radiation damage. This can be reduced by cryogenically freezing of the crystals, however this can affect diffraction quality or the molecule structure and cryo preservation conditions must be found by trial and error. Both limitations are described in further detail in chapter two in regards to how new techniques can help to overcome these challenges.

CHAPTER 2

SERIAL FEMTOSECOND CRYSTALLOGRAPHY: A REVOLUTION INSTRUCTURAL BIOLOGY

Jose M. Martin-Garcia [a, b], Chelsie E. Conrad [a, b], Jesse Coe [a, b], Petra Fromme [a, b]

[a] School of Molecular Sciences, Arizona State University, Tempe, AZ 85287-1604, USA
[b] Center for Applied Structural Discovery, The Biodesign Institute, Arizona State University, Tempe, AZ 85287-7401, USA

This chapter is a published review on serial femtosecond crystallography. I wrote the sample characterization and sample delivery portions of this publication. I also made figures and edited the manuscript. *Three additional figures have been added as marked.

Macromolecular crystallography at synchrotron sources has proven to be the most influential method within structural biology, producing thousands of structures since its inception. While its utility has been instrumental in progressing our knowledge of structures of molecules, it suffers from limitations such as the need for large, well-diffracting crystals, and radiation damage that can hamper native structural determination. The recent advent of X-ray free electron lasers (XFELs) and their implementation in the emerging field of serial femtosecond crystallography (SFX) has given rise to a remarkable expansion upon existing crystallographic constraints, allowing structural biologists access to previously restricted scientific territory. SFX relies on exceptionally brilliant, micro-focused X-ray pulses, which are femtoseconds in duration, to probe Nano/micrometer sized crystals in a serial fashion. This results in data sets comprised of individual snapshots, each capturing Bragg diffraction of single crystals in random orientations prior to their subsequent destruction. Thus structural elucidation while avoiding radiation damage, even at room temperature, can now be achieved. This emerging field has cultivated new methods for nanocrystallogenesis, sample delivery, and data processing. Opportunities and challenges within SFX are reviewed herein.

2.1. INTRODUCTION

Macromolecular crystallography at synchrotron sources has proven to be the most influential method within structural biology, producing thousands of structures since its inception. While its utility has been instrumental in progressing our knowledge of structures of molecules, it suffers from limitations such as the need for large, well-diffracting crystals, and radiation damage that can hamper native structural determination. The recent advent of X-ray free electron lasers

(XFELs) and their implementation in the emerging field of serial femtosecond crystallography (SFX) has given rise to a remarkable expansion upon existing crystallographic constraints, allowing structural biologists access to previously restricted scientific territory. SFX relies on exceptionally brilliant, micro-focused X-ray pulses, which are femtoseconds in duration, to probe nano/micrometer sized crystals in a serial fashion. This results in data sets comprised of individual snapshots, each capturing Bragg diffraction of single crystals in random orientations prior to their subsequent destruction. Thus structural elucidation while avoiding radiation damage, even at room temperature, can now be achieved. This emerging field has cultivated new methods for nanocrystallogenesis, sample delivery, and data processing. Opportunities and challenges within SFX are reviewed herein.

Since the invention of the first light bulb by Thomas Alva Edison in 1879, light sources have been the primary tools for the investigation of matter. But it was the discovery of X-rays in 1895 by Wilhelm Conrad Roentgen which catalyzed a revolutionary change in our understanding of the physical world. The ability of X-rays to reveal the invisible has made them one of the most important research and diagnostic tools in medicine, chemistry, and physics in the last century. One of the most powerful sources of X-rays in modern research are synchrotrons, in which electrons are accelerated by radiofrequency cavities to extremely high energies (typically ≥ 3 GeV) and transferred to a storage ring in which they can be maintained at high current in stable 'bunches' for hours. The electrons are then subsequently perturbed in an undulating electromagnetic field to induce X-ray emission. The first synchrotron facility was built in the early 1970's and due to the increasing demand from both the scientific community and private research sector; the number of synchrotron facilities has grown quickly since. In the last three decades, synchrotrons have been built or are in the construction phase in 24 countries. APS at the Argonne National Laboratory (Chicago, USA), the ESRF (Grenoble, France), PETRA III (Hamburg, Germany), Spring-8 (Harima Science Park City, Japan), and DIAMOND (Oxfordshire, England) are currently the largest and most powerful synchrotron light sources. X-ray methods have also played an increasingly more important role in the life sciences as evidenced by medical

9

X-ray imaging, X-ray scattering, and highlighted here, X-ray crystallography. The latter typically makes use of X-rays from 3.5 keV to 20 keV (3.5 Å to 0.6 Å) to enable the determination of the atomic structure of matter. The most difficult and challenging biomolecules, such as large complexes and membrane proteins, are almost exclusively solved with synchrotron radiation. However, in spite of the usefulness and power of these facilities, there are two important areas in which synchrotron facilities are limited in addressing the full range of current scientific challenges. The main limitations are primary and secondary X-ray damage which cannot be outrun by pulse durations currently available at synchrotron sources (tens of ps). Secondary damage can be minimized by freezing but primary damage is unavoidable.

To overcome these limitations a new light source has emerged in the form of the X-ray free electron laser (XFEL) which has improved upon many of the properties of synchrotron radiation sources, in some cases by orders of magnitude. Free electron lasers (FELs) have been used over many years since their conception by John Madey in the early 70's (Madey 1971), initially operating at infrared wavelengths. More recently, visible and near ultraviolet wavelengths were achieved (2012). Since its discovery, the idea of extending FELs to shorter wavelengths, in particular to the X-ray regime, have been considered and explored by many scientists (see (Pellegrini 2012) for a review on the development of FELs). After many years of theoretical and experimental work along with new technological advances, three XFELs are currently operational. Namely, they are the Deutsches Elektronen-Synchrotron's (DESY) Free-electron LASer in Hamburg (FLASH), SLAC's Linac Coherent Light Source (LCLS), and RIKEN's Spring-8 Angstrom Compact free electron LAser (SACLA). At its core, an XFEL consists of an electron source, a linear accelerator, and undulator magnets spaced to produce X-ray wavelengths (typically ranging from 0.01 to 10 nm) (Madey 1971, Dattoli 1984, Saldin 2000). Briefly, a relativistic electron beam is accelerated to almost the speed of light in a linear accelerator prior to interaction with the undulator. Upon interaction with the undulator, the electrons move in curved paths via the magnets. The long length of an XFEL undulator allows the relativistic electrons to interact with their emitted radiation which causes bunching of the electrons with spacing equal to

the wavelength of the emitted X-rays. As the electrons bunch, their emission becomes more coherent and allows for a stronger interaction between the two. This results in beam with highly coherent pulses with femtosecond duration. The coherence causes radiative emission proportional to the number of electrons squared in contrast to a synchrotron (incoherent) in which the radiative emission scales proportional to the number of electrons due to cancelation effects from the out of phase generated electromagnetic fields (C. Pellegrini 2003). Because the number of electrons in a bunch is on the order of a billion, this causes a massive increase in flux compared to synchrotron sources. Furthermore, the high longitudinal coherence (and thus, ultrashort duration) of the pulses pushes the peak brilliance orders of magnitude higher than that achievable at a synchrotron. The output wavelength can by tuned by modulating the electron energy and magnetic field strength. Figure 2.1 illustrates this principle. XFELs generate high gain, ultrashort pulsed X-rays with only a single undulator pass (Claudio Pellegrini 2004), accomplished by the interaction between oscillating electrons, moving at relativistic speeds, with their emitted
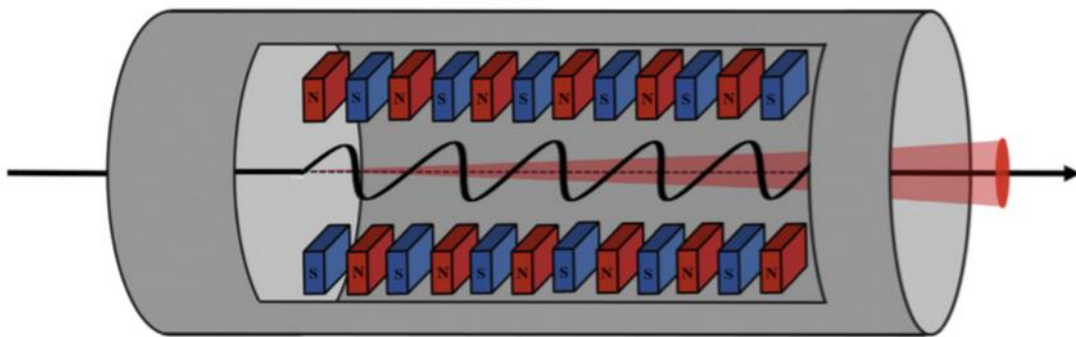
Figure 2.1 Schematic representation of an undulator segment at an XFEL instrument. A relativistic electron beam (solid line) is brought to high energy in a linear accelerator (not pictured) prior to interaction with the undulator. The electrons then travel on a sinusoidal path, induced by a special arrangement of magnets called an undulator, a periodic array of magnetic dipoles shown as red and blue boxes. Because the electrons move in curved paths via the magnets, the change in momentum causes the emission of monochromatic radiation the same way a synchrotron does (depicted as a red cone).

electromagnetic waves (for a more detailed overview of XFEL physics please refer to Ackermann et al. (Ackermann, Asova et al. 2007) and McNeil et al. (McNeil and Thompson 2010)).The

interaction between the electrons and their radiation causes spatial redistribution of the electrons into compact bunches perpendicular to their direction of motion. This generates coherent X-ray pulses with durations of tens of femtoseconds. The first hard XFEL, LCLS, was built at the SLAC National Accelerator Laboratory in California and has been in operation since April 2009(Emma 2010). It produces X-ray pulses of approximately 3 mJ energy at 120 Hz. Each pulse has a duration that ranges from around 300 fs down to a few femtoseconds with up to 1013 coherent photons per pulse. Thus, the LCLS instrument has set a new standard, with a peak X-ray brilliance over ten orders of magnitude higher than that of the most powerful synchrotron radiation
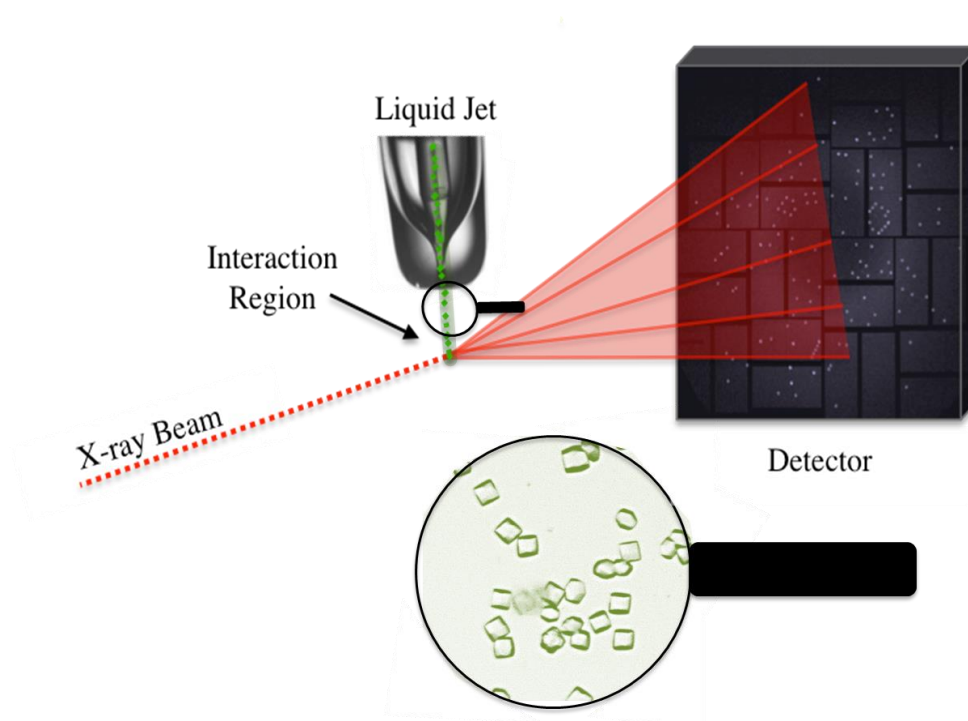
Figure 2.2 Schematic representation of the experimental setup of a typical SFX experiment at LCLS. Randomly oriented nanocrystals (Banerjee, Bartesaghi et al.) in their mother liquor are delivered into the focus of X-ray beam by a gas-focused liquid injector. The X-ray beam, which is transverse to the jet, hits the crystals in the interaction region. Diffraction snapshots of single crystals are recorded using a Cornell-SLAC pixel array detector (CSPAD) located in the forward-scattering region.

sources (Altarelli 2010). XFELs are unique light sources that can be used to explore matter at atomic length and femtosecond time scales. The increase in brightness along with ultra- short pulses has facilitated the appearance of a new application of XFEL technology in the field of

structural biology via serial femtosecond crystallography (SFX)(Chapman, Fromme et al. 2011, Spence, Weierstall et al. 2012). A typical setup for SFX data collection is illustrated in Figure 2.2.

The technique of macromolecular X-ray crystallography and its historical success in determining the structure of biological macromolecules has always suffered from a major bottleneck, namely the production of well diffracting crystals. This problem is especially prevalent in the structure determination of membrane proteins, which are notorious for their difficulty in forming high diffraction quality crystals. In some cases, years have been devoted to determining crystallization conditions for a membrane protein and it is not uncommon that only showers of nanocrystals (crystals between 200 nm and 10 μm) are observed while attempts to grow larger crystals remain unsuccessful. These nanocrystals were once seen as only a possible intermediate towards achieving useable crystals (Cusack, Belrhali et al. 1998). Modern microfocus beamlines have expanded the usefulness of these nanocrystals but even they experience constraints on what is achievable mainly due to severe X-ray damage by long exposure times, often requiring cryo-cooling and necessitating crystals larger than 10 μm, which must be even larger in the case of large unit cells (common in membrane proteins and large complexes)(Smith, Fischetti et al. 2012). With the advent of XFELs, crystals which would have previously been too small for use have been shown to be suitable for structure determination (Chapman, Fromme et al. 2011). Generally, these small crystals are easier to produce and possess significantly less long range disorder. Furthermore, nanocrystals are ideal for time resolved studies as a greater percentage of molecules in the crystal can be activated homogeneously by light or rapid mixing. For light activated reactions, time domains ranging from the femtosecond to microsecond regimes can be probed and temporal resolution of reactions induced by mixing can range from seconds down to microseconds (Holton 2009, Schmidt, Srajer et al. 2013, Kupitz, Basu et al. 2014, Tenboer, Basu et al. 2014, Wang, Weierstall et al. 2014, Barends, Foucar et al. 2015).

In addition to the challenges of sample preparation, the problem of X-ray induced radiation damage has hindered progress in structure determination even in well-diffracting

crystals. Traditionally, cryogenic cooling of crystals has been the most successful way to minimize damage, increasing the radiation dose tolerance by a factor between 30 and 50 (Owen, Rudino-Pinera et al. 2006, Holton 2009, Howells, Beetz et al. 2009). Cryo-cooling works by slowing the dispersion of radiation-induced reactive products that occur during the X-ray exposure. Upon exposure to X-rays, photoionization and processes related to Auger decay take place, leading to heat as well as the production of radicals and photo-ions. These diffuse within the crystal at rates dependent on available kinetic energy. This can lead to subsequent chemical reactions that result in the breaking of chemical bonds and thus a reduction in the diffraction quality of the crystal, eventually the destruction of the crystal can even occur (Figure 2.3). While cryo-cooling does not influence the primary X-ray damage (i.e. photoionization and Auger decay), it slows down diffusion of the secondary processes of X-ray induced damage, radicals and heat progression. This method thus allows crystals to tolerate longer exposure times, improving the signal to noise ratio. Nonetheless, even at cryogenic temperatures site-specific radiation damage remains a problem, in which rapid photo-damage by the X-ray beam in areas with high X-ray cross sections can occur, decreasing diffraction until it ultimately terminates. In such cases, partial data sets from many crystals must be merged in order to obtain a structural model. Furthermore, these models can exhibit significant artifacts from damage which can be substantially different from the native structure (Carugo and Carugo 2005). Examples of radiation damage include the breakage of disulfide bonds and salt bridges, tyrosine residues becoming hydrolyzed, decarboxylation of glutamate and aspartate residues, B-factor increase, and loss of diffraction progressing from high to low resolution (Burmeister 2000, Ravelli and McSweeney 2000, Garman and Owen 2006, Liu, Wacker et al. 2013). Radiation damage is particularly troublesome in limiting resolution of high-Z catalytic centers, causing metalloproteins to be the most prone to local radiation damage. For example, spectroscopy has shown that X-ray radiation exposure to cryo-cooled, photosystem II (PSII) crystals leads to the metal center becoming photo-reduced below the native oxidation state. This effect was still seen at 4% of average doses used for crystallography (Yano, Kern et al. 2005).

In 2000 Neutze et al. (Neutze, Wouts et al. 2000) conducted molecular dynamic simulations on the time course of the Coulomb explosion of T4 lysozyme at a total flux of 3.8 x 10^6 12 keV photons per $Å^2$ over pulse durations of 2, 10, and 50 fs (the presumed theoretical flux achievable by an XFEL) in vacuum (Figure 2.4). At this time, XFELs were still in the planning phases. They predicted that the onset of the Coulomb explosion would occur at 5-10 fs and predicted that if the pulses are short, diffraction of the molecule could be collected before it
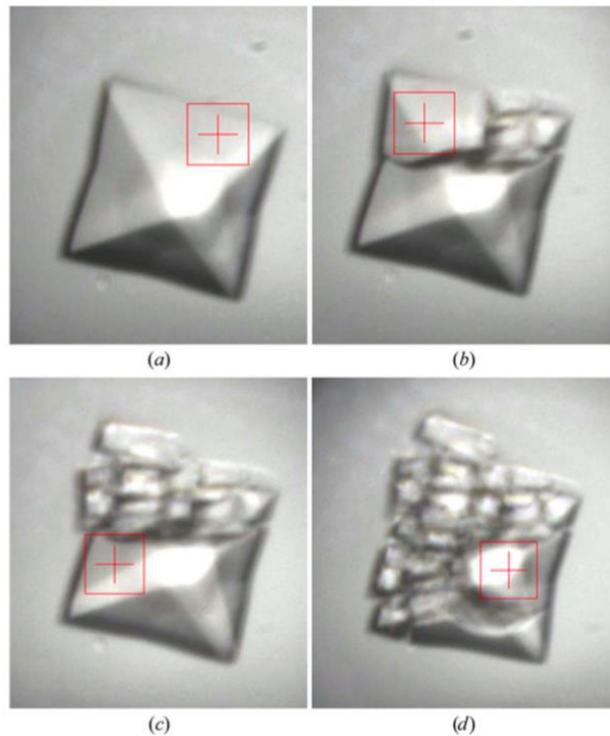
Figure 2.3 Example of X-ray radiation damage to a protein crystal at room temperature. Four images of a bovine enterovirus 2 crystal during data collection. (a) Prior to any exposure. (b) After a 0.5 s exposure. (c) After a second 0.5 s exposure. (d) After a third 0.5 s exposure. The beam cross-section of 20 x20 mm is shown. Figure and adapted imaged used with permission from (Axford, Owen et al. 2012).
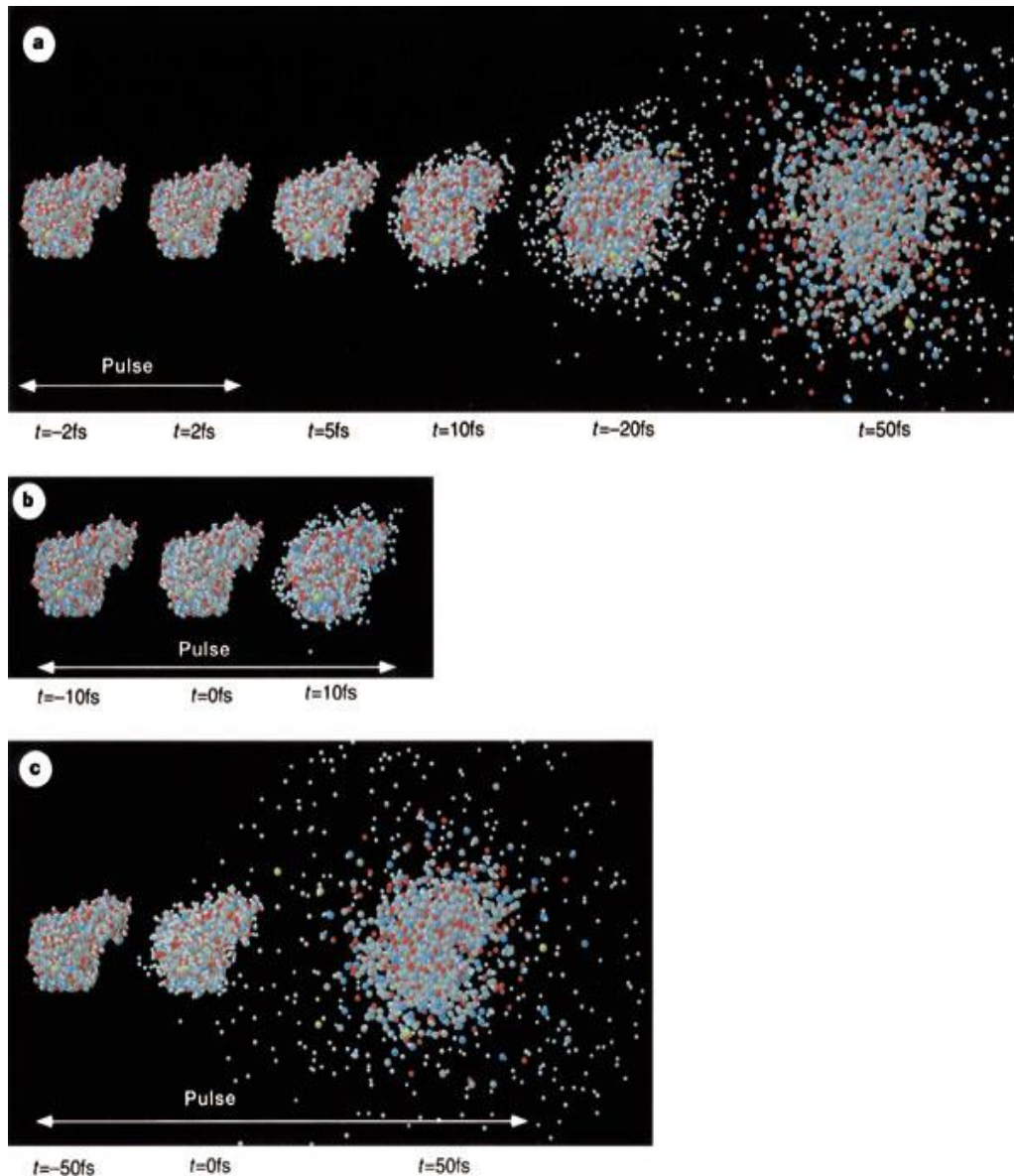
Figure 2.4 Simulation of a coulomb explosion of a T4 lysozyme molecule induced by radiation damage from an X-ray free electron laser pulse. The integrated X-ray intensity was 3×10^{12} (12 keV) photons per 100-nm diameter spot (3.8×10^6 photons per $Å^2$) in all cases. a, A protein exposed to an X-ray pulse with an FWHM of 2 fs, and disintegration followed in time. Atomic positions in the first two structures (before and after the pulse) are practically identical at this pulse length because of an inertial delay in the explosion. $R_{nucl} = 3\%$, $R_{elec} = 11\%$ b, Lysozyme exposed to the same number of photons as in a, but the FWHM of the pulse was 10 fs. Images show the structure at the beginning, in the middle and near the end of the X-ray pulse. $R_{nucl} = 7\%$, $R_{elec} = 12\%$ c, Behavior of the protein during an X-ray pulse with an FWHM of 50 fs. $R_{nucl} = 26\%$, $R_{elec} = 30\%$. Image reprinted and caption modified with permission from ((Neutze, Wouts et al. 2000).

16

destroyed referred to as "diffraction before destruction". This principle relies on an XFELs ability to deliver a sufficient number of photons (~10^{13} photons/pulse, orders of magnitude greater than that required to form a plasma) for structure determination on time scales competing with primary radiation damage events. The first experimental demonstration of this principle was carried out using the soft XFEL, FLASH, located at DESY (Ayvazyan 2006). In this experiment an intense 25 fs, 4×10^3 W/cm^2 pulse, containing 10^{12} photons, produced a coherent diffraction pattern from a non-periodic object before destruction occurred (Chapman, Barty et al. 2006). Thus, XFELs have the potential to minimize the effects of radiation damage and reduce the size restrictions on crystals suitable for X-ray structure determination. SFX requires new data processing and handling as the determination of crystallographic structures is based on thousands of snapshot diffraction patterns at room temperature by continuous delivery of orientationally unrelated nanocrystals in their mother liquor (Chapman, Fromme et al. 2011, Boutet, Lomb et al. 2012, Sierra, Laksmono et al. 2012, Weierstall, Spence et al. 2012, Weierstall 2014).

In December 2009 the first SFX experiment was carried out at LCLS, using nanocrystals of photosystem I (PSI) as the first sample. PSI mediates the conversion of light energy from the sun to chemical energy in plants, green algae, and cyanobacteria, is one of the most complex membrane proteins crystalized so far, the entire complex consisting of 36 proteins and 381 cofactors(Jordan, Fromme et al. 2001). Tens of thousands of diffraction patterns were collected, which allowed for the determination of the PSI structure, providing a proof of concept for SFX (Chapman, Fromme et al. 2011). Furthermore, this study resolved interference fringes between the Bragg peaks which were originally suggested by Sayre in 1952 (Sayre 1952). He proposed that diffraction from crystals with a countable number of unit cells, would show the Fourier transforms of the crystals in the diffraction pattern leading to fringes between the Bragg peaks directly related to the number of unit cells (n-1)(Sayre 1952). This theory came to fruition in the first SFX experiments when these fringes were detected in the diffraction patterns. In the future, with higher spatial resolution detectors, these shape transforms can be used for direct phasing (Spence, Kirian et al. 2011).

Six years after the first SFX experiments were carried out (Chapman, Fromme et al. 2011), evidence has continued to mount that XFELs make overcoming radiation damage in protein crystallography an attainable realization (Lomb, Barends et al. 2011, Aquila, Hunter et al. 2012, Barty, Caleman et al. 2012, Boutet, Lomb et al. 2012, Johansson, Arnlund et al. 2012, Koopmann, Cupelli et al. 2012, Sierra, Laksmono et al. 2012, Johansson, Arnlund et al. 2013, Liu, Wacker et al. 2013, Redecke, Nass et al. 2013, Barends, Foucar et al. 2014, Hunter, Segelke et al. 2014, Sawaya, Cascio et al. 2014, Fenalti, Zatsepin et al. 2015, Kang, Zhou et al. 2015). In addition, SFX not only mitigates radiation damage but is suitable for crystals with as little as a few hundred unit cells. Thereby, data can be collected from nanocrystals eliminating the need to grow large crystals. Experimental evidence is emerging that nanocrystals may show significantly less long-range disorder than their larger counterparts, making them ideal candidates for the structure determination of challenging proteins (Weierstall, James et al. 2014).

2.2. NANOCRYSTALLIZATION AND CHARACTERIZATION

Because nanocrystals were previously seen as merely a stepping stone for the desired growth of large crystals, nanocrystal growth methods have remained largely unexplored. Due to the serial nature of SFX, a few unique characteristics must be considered for the development of nanocrystallization techniques. First, a different crystal in a random orientation is used for each diffraction pattern, with patterns being captured in a serial fashion (Chapman, Fromme et al. 2011). Thus, to constantly replenish the sample between X-ray pulses, crystals are delivered to the X-ray interaction region by a liquid jet (in a typical SFX experiment) composed of crystals in their mother liquor at room temperature (Chapman, Fromme et al. 2011). The delivery of the crystals to the X-ray region is much more rapid than the X-ray repetition rate. Consequently, most crystals do not interact with the X-rays (Weierstall, James et al. 2014). Additionally, since diffraction patterns represent "still frame" slices through the Ewald sphere, only partial reflections can be recorded (i.e. there is no goniometer and therefore no rotation to record full profiles of reflections). In order to measure accurate structure factors of the Miller indices (h, k, l), high

redundancy of the data sets (>50) are required via Monte Carlo data analysis methods (Kirian, Wang et al. 2010). Due to approximately one in every ten thousand crystals resulting in a diffraction pattern and the necessity for high multiplicity of the data, tens to hundreds of milligrams of sample may be needed for successful SFX data sets, where samples are delivered in a liquid jet. The hit rate (percentage of pulses that result in crystal diffraction) is largely a function of crystal density and as such, must be considered in growth methods and characterization of the crystals.

Since data from many crystals must be merged in analysis of SFX data, it is also important to consider crystal homogeneity. For example, if there is a large size distribution in the sample, then the data set will be composed of diffraction patterns with varying relative Bragg peak intensities (directly related to the number of unit cells and hence, the size). This can lead to scaling issues which become problematic in subsequent analysis. Furthermore, the presence of some outlying (e.g. larger) crystals may necessitate attenuation of the beam to prevent damage to the detector. This in turn would limit resolution on images obtained from the more plentiful smaller crystals. Size inhomogeneity can also lead to instabilities or clogging in the liquid jet(Kupitz, Grotjohann et al. 2014). Therefore, it is imperative to consider and monitor crystal size distribution while screening conditions for nanocrystallization. These considerations become even more pronounced in time-resolved experiments where the crystal size is the primary parameter in reaction initiation homogeneity (Tenboer, Basu et al. 2014, Ibrahim, Chatterjee et al. 2015). To meet the need for large sample volumes, optimized crystal density and crystal size homogeneity, in addition to the traditional optimization of crystal diffraction quality, nanocrystallization techniques are rapidly emerging to address the unique challenges present in SFX.

2.2.1. NANOCRYSTALLOGENESIS

As is the case in the growth of macroscopic crystals, knowledge of a proteins phase space is highly beneficial for the optimization of crystallization conditions. Driven by thermodynamics, the formation of protein crystals requires a controlled decrease in solubility of

the protein that ideally avoids the formation of non-ordered precipitation. Traditionally, the supersaturated area of phase space is typically reached by gradually increasing the precipitant concentration, allowing for few nucleation sites to form that grow by addition of the free protein to the nuclei over time, resulting in a few large crystals (McPherson 1999). In contrast to this approach, nanocrystallization is best achieved by inducing a high number of nucleation sites, whereby the free protein concentration is rapidly decreased by the formation of a plethora of nuclei followed by their growth into a multitude of small crystals (Kupitz, Grotjohann et al. 2014, McPherson and Cudney 2014). Typically this is achieved by increase of the concentration of protein, precipitating agents, or both as compared to optimized conditions for large crystal growth for the same protein (Kupitz, Grotjohann et al. 2014). While the approaches for each size regime differ, they both rely fundamentally on the knowledge of the proteins phase space and may be even more important for growth of well-ordered nanocrystals as formation of amorphous precipitate is best avoided.

Many of the existing methods for macro-crystallogenesis are also applicable for nanocrystallization with modification necessary to occupy a different area of phase space (Hunter, Segelke et al. 2014, Kupitz, Grotjohann et al. 2014, Bublitz, Nass et al. 2015, Sugahara, Mizohata et al. 2015, Wu, Nogly et al. 2015, Yamashita, Pan et al. 2015). Batch methods, in which the protein and precipitating conditions are mixed to homogeneity initially, provide a good example of well established methodology that needs little modification for suitability in SFX (outside of parameter values). This is illustrated in Figure 2.5 where a batch approach for macro- and nanocrystals differs only by starting point within the phase space (Schlichting 2015). It has been reported in some cases that large crystals grown by traditional methods can also be mechanically crushed to obtain the smaller crystals needed for SFX (Redecke, Nass et al. 2013, Stevenson, Makhov et al. 2014). This is, however, not generally applicable and may lead to loss of quality or destruction of fragile crystals, such as those common amongst membrane proteins. Nanocrystalline showers with traditional methods such as vapor diffusion have been obtained,
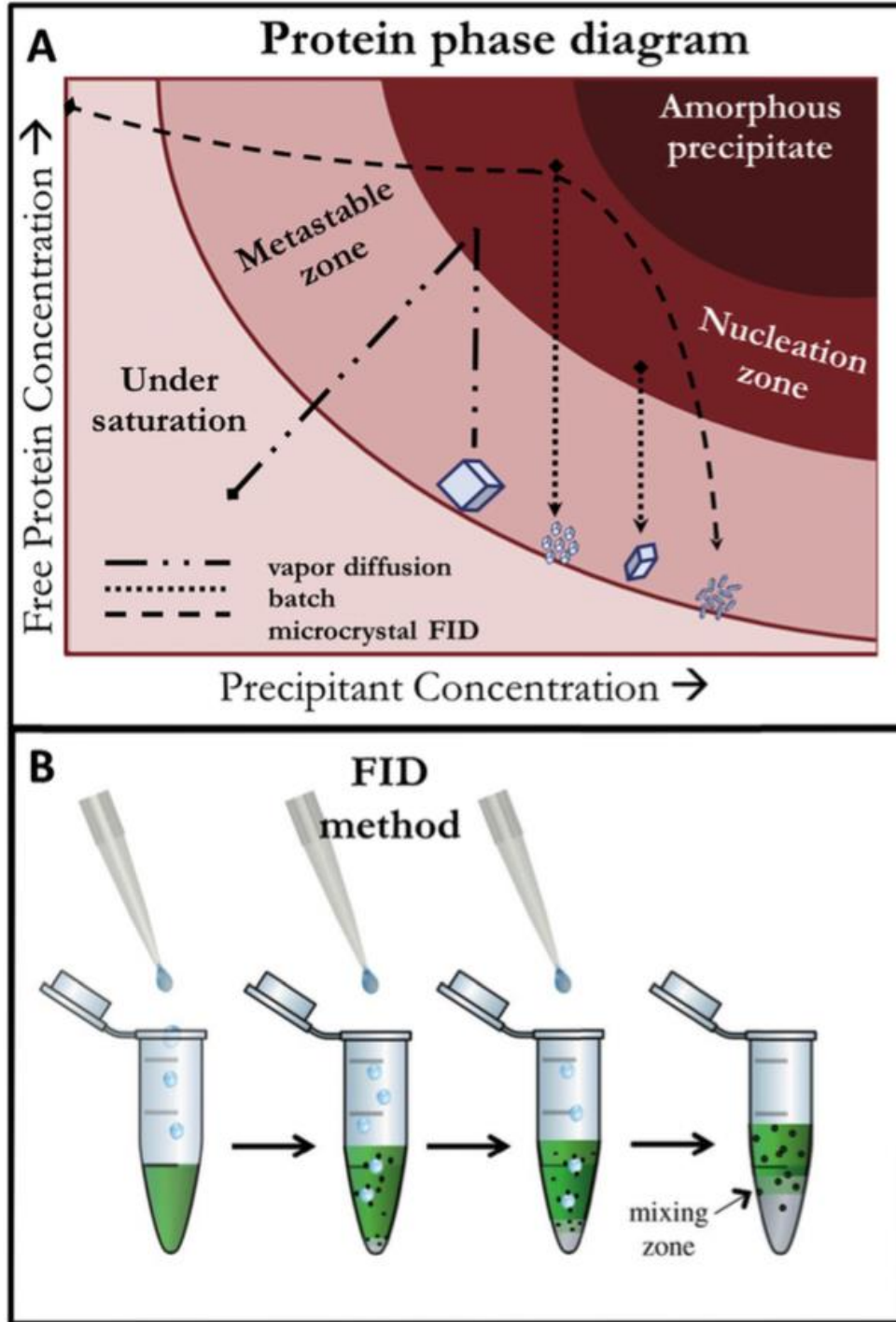
Figure 2.5 A) 2-dimensional slice of a typical free protein phase diagram with selected crystallogenesis methods exemplifying the general relationship between phase space occupation and resultant crystalline protein. B) Depiction of the microcrystalline FID method in the case of a denser precipitant being dropped through a protein solution and the subsequent interface resulting in microcrystal pelleting.

using a brute force approach with many individual setups to scale for SFX experiments (Lawrence, Conrad et al. 2015). While this poses no theoretical issue, the concern for this type of nanocrystal preparation is due to the tedious nature of sample preparation involved to obtain enough material for full data set collection. While this can in part be alleviated with sample conserving delivery systems (Conrad, Basu et al. 2015, Fromme, Ishchenko et al. 2015, Sugahara, Mizohata et al. 2015) (assuming they are compatible), sample density and homogeneity remain challenging and necessitate specific consideration.

The nanocrystalline free interface diffusion (FID) method is an example of a technique that has been developed from an existing method for SFX applications (Kupitz, Grotjohann et al. 2014). In this method, one solution (either the protein or precipitant solution) is added drop wise to the other. The less dense of the two (typically the protein/buffer solution) is first placed in a vessel, typically a microcentrifuge tube. The denser solution (typically precipitants such as high concentration salts, polyethylene glycol, etc.) is then added drop wise, thereby allowing for a high nucleation rate at the protein/precipitant interface of the two solutions but still inducing some mixing immediately. Nanocrystals will form at the interface, owing to the access of areas of phase space that typically results in high nucleation rates (i.e. high concentrations of both protein and precipitants). Additional benefits arise in the common scenario where the denser solution is the precipitant since this allows crystals that form at the interface to settle due to gravity into the precipitant rich layer. This provides a way to effectively quench crystal growth as well as accumulate a high density of nanocrystals, allowing practical optimization of crystal density by resuspension to a desired concentration. Gentle centrifugation of the setup has also been shown to expedite crystal formation (e.g. PSII forming nanocrystals in as little as 30 min with centrifugation in contrast to 1 day without centrifugation (Kupitz, Grotjohann et al. 2014)) and has led to improvement of crystal size and homogeneity due to the tendency for crystals to spend less time in relatively high concentrations of free protein after nuclei formation, resulting in more uniform growth throughout the sample. It is important to note that over time, full mixing of the two layers will occur (rate proportional to miscibility). This could lead to the dissolution of the crystals

22

if the mixture represents an under saturated portion of phase space. Oswald ripening and decreased size homogeneity can also occur if there is high mobility or an appreciable amount of free protein left over after complete mixing has occurred. This can be avoided by harvesting the crystal pellet or removal of the free protein layer before considerable mixing occurs.

2.2.2. IN-VIVO CRYSTALLIZATION

Crystallization in vivo using insect and mammalian cells is a highly innovative approach towards nanocrystallography that has been recently discovered (Koopmann, Cupelli et al. 2012, Redecke, Nass et al. 2013, Gallat, Matsugaki et al. 2014, Ginn, Messerschmidt et al. 2015). This technique was first applied in SFX in 2012 after nanocrystals were identified by electron microscopy inside insect cells when cathepsin B from *Trypanosoma brucei* was overexpressed using the recombinant baculovirus system (Koopmann, Cupelli et al. 2012). Redecke and co-workers observed needle shaped nanocrystals protruding out of the cell after 70 h but were still surrounded by the cell membrane (Redecke, Nass et al. 2013). The crystals were 10-15 μm in length and about 0.5-1 μm in width. These crystals were isolated and used for SFX analysis (Redecke, Nass et al. 2013). It has been proposed that this spontaneous crystallization may occur due to accumulation of the protein in a specific organelle such as the endoplasmic reticulum, peroxisomes, or secretory granules (Doye and Poon 2006, Koopmann, Cupelli et al. 2012). In vivo crystallization is not limited to the Sf9 insect cells and has been demonstrated for multiple proteins in cockroaches, seeds, and bacterial cells (Doye and Poon 2006, Gallat, Matsugaki et al. 2014, Sawaya, Cascio et al. 2014). However, little is understood about the mechanism of in-vivo crystallization as it was initially hypothesized to be a rare occurrence. Additionally, the crystals were not probed when they were first found as they were too small for macrocrystallography (Doye and Poon 2006, Koopmann, Cupelli et al. 2012) . With the advent of XFELs, in vivo crystallization could potentially become a major method for crystallization, thus removing the bottleneck of determining crystallization conditions for applicable proteins. Before in

vivo crystallization comes to fruition as a more general method, further research needs to be done towards understanding the necessary mechanistic components involved.

2.2.3. GROWING CRYSTALS USING LCP

Lipidic cubic phase (LCP), a bicontinuous mesophase that acts as a membrane-mimetic, has been used to crystallize a variety of membrane proteins, notably G coupled-protein receptors, ion channels, and transporters (Liao, Li et al. 2012, Caffrey 2015). Unlike membrane protein crystals grown *in surfo* (in partial or full detergent micelles), which usually exhibit type II micelle crystal packing and often have a high solvent content, crystals grown in LCP feature type I crystal packing, see Figure. 2.6 (Katona, Andréasson et al. 2003). This packing allows for hydrophilic protein-protein and hydrophobic protein-lipid-protein interactions and thus, often leads to tighter and more rigid packing, in turn possibly leading to a lower solvent content and better diffraction (Liu, Ishchenko et al. 2014). To crystallize membrane proteins in LCP, purified protein at high concentration (usually > 20 mg/mL) is mixed with molten monoolein in Hamilton gas-tight syringes using a syringe-mixer(Cheng, Hummel et al. 1998). For standard crystallography, special robots (e.g. Flexus Crystal IMP, Gryphon LCP, NT8-LCP, Mosquito LCP, ProCrys Meso) can be used to dispense the LCP and precipitant and crystals are often grown in micro-batch assays of <1 nL-100 nL. Cherezov and colleagues have had notable success in adapting the LCP crystallization method for SFX (Liu, Wacker et al. 2013, Liu, Ishchenko et al. 2014, Liu, Wacker et al. 2014, Fenalti, Zatsepin et al. 2015, Zhang, Unal et al. 2015). In this method, protein laden LCP is injected in another syringe containing precipitate solution and incubated for 24 h to two weeks to permit crystallization (Liu, Wacker et al. 2013, Liu, Wacker et al. 2014). Excess precipitate solution is removed and the crystals embedded in the LCP are delivered using a high-viscosity-injector.
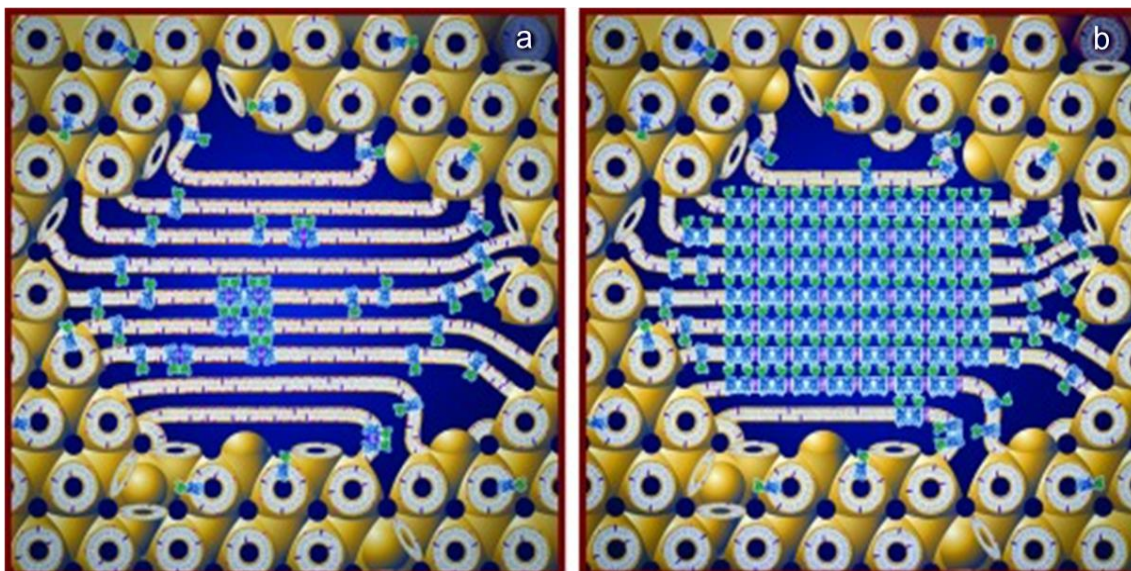
Figure 2.6 Diagram of crystallization within lipidic cubic phase. First the protein is reconstituted into the "biscontinious" cubic phase (yellow). (a) Once precipitant is added, the cubic phase is less stable and the protein migrates into the lamellar phase, sheet like arrangement in the center. (b) as local protein concentration increases, nucleation and crystallization begin. Image reprinted with permission from (Caffrey 2015).

2.2.4. CRYSTAL DETECTION AND CHARACTERIZATION

Some SFX experiments have been carried out with crystals that are of 5 μm and can therefore be identified by established methods such as polarized light microscopy in combination with UV- fluorescence microscopy. Nanocrystals are very difficult to identify and differentiate from amorphous precipitate, particularly if the crystal size is on the order or smaller than 1 μm, nearing the limit of resolution for optical microscopy methods. Techniques such as tryptophan fluorescence and birefringence may also be limited since the signal for each is proportional to crystal size. Alternative methods for detecting small crystals have proven to overcome the aforementioned difficulties. One of the most useful methods for rapid feedback during initial and optimization stages of crystallogenesis is the use of second-order harmonic generation (Prince and Kheshgi) spectroscopy, in particular the SONICC (second order non-linear imaging of chiral crystals) instrument invented by G. Simpson (Wampler, Kissick et al. 2008). SONICC can identify nanocrystals of chiral molecules as small as 100 nm (Wampler, Kissick et al. 2008). When a

chiral crystal is exposed to two 1024 nm photons in a strong field, frequency doubling occurs due to inherent polarization anisotropy, allowing a detector to measure the 512 nm photon output. Constructive interference arising from crystalline translational symmetry increases the probability of this occurring, allowing for practical measurements to be taken. It should be cautioned that the signal strength depends on the space group (with higher symmetry leading to decreased signal in general) and also the specific molecular polarization susceptibility (higher SHG is typical in molecules with a chromophore) (Newman, Scarborough et al. 2015). While truly centrosymmetric space groups are impossible in natural protein crystals, many of the high symmetry space groups can still lead to attenuation of signal below detection, resulting in false negatives. Furthermore, some precipitants are chiral (e.g. sugars, chiral salts) and can crystallize in space groups that can be active in SHG (i.e. false positives) so care must be taken when interpreting results.

The most trustworthy method to verify the existence of diffracting crystals is X-ray powder diffraction, which can be carried out at either cryogenic or ambient temperatures. For room temperature powder diffraction measurements, a high density pellet of crystals is transferred to an X-ray transparent capillary (Steitz, Richmond et al. 1974, Balbirnie, Grothe et al. 2001, Von 2007). In contrast with cryogenic powder diffraction, room temperature powder diffraction measurements are ideal for optimizing relative resolution for an XFEL since this ensures that there are not artifacts arising from the freezing process. It is also important to include buffer in the capillary to avoid drying out of the small crystals which can affect diffraction quality. While powder diffraction data can be collected from nanocrystals at low flux X-ray home sources, it requires several microliters of dense crystal sample which is more than is produced from commercial screens (Stevenson, Makhov et al. 2014). It also depends highly on the sample quality and density so establishing conditions for powder diffraction typically requires synchrotron radiation to produce measurable diffraction for un-optimized samples (Stevenson, DePonte et al. 2014).

Transmission electron microscopy (TEM) is another reliable method to monitor nanocrystal quality and requires low sample volumes. Strong correlations exist between crystals that have highly ordered lattices visible through TEM and crystals that feature better X-ray

diffraction quality (Stevenson, DePonte et al. 2014). While this technique can provide insightful characterization, it requires elaborate sample preparation and often involves negative staining which can affect electron diffraction and is only suitable for very thin nanocrystals (<200 nm) (Stevenson, DePonte et al. 2014, Wen 2014). Large crystals can be mechanically crushed in order to achieve dimensions suitable for TEM (Stevenson, Makhov et al. 2014).

In protein crystallography, dynamic light scattering (DLS) is commonly used to analyze protein homogeneity since a monodisperse (i.e. homogenous and non-aggregated) sample is ideal for crystallization (Proteau, Shi et al. 2010). In addition, DLS is also used in SFX experiments to determine nanocrystal size distribution and homogeneity across multiple conditions (Schubert, Meyer et al. 2015). DLS measures the light scattered by particles in solution. As molecules in solution undergo Brownian motion, the change in intermolecular distance leads to constructive and destructive interference of the scattered light. Fluctuations in intensity over time are indicative of the particle size and can be derived from the Stokes-Einstein relation. DLS only requires a few microliters of sample for analysis at broad range of concentrations (about 10^8-10^{12} crystals/mL)(Filipe, Hawe et al. 2010) . However, large particles such as dust or aggregates can affect the accuracy of size determination (Berne and Pecora 2000). Another important parameter to take into account in SFX experiments is the crystal density. Crystal density can be optimized by using nanoparticle tracking analysis (NTA), which, like DLS, infers the Brownian motion of particles in solution and relates this movement to an equivalent hydrodynamic radius. Unlike DLS, NTA uses video to track the Brownian motion and thus, captures the light scattering signal from individual particles (Carr and Malloy 2006). This not only allows for particle size to be determined on a particle-by-particle basis but also allows for particle concentration to be estimated which is extremely helpful for optimizing crystal density for SFX experiments (Filipe, Hawe et al. 2010). However only particles <1 μm can be detected and 1 mL of particle concentrations of 10^7-10^9 crystals/mL (Filipe, Hawe et al. 2010) is required. Therefore, DLS and NTA provide a means to monitor nanocrystal size. Furthermore, microfluidic

27

devices using dielectrophoresis have been invented that can sort nanocrystals according to size (Abdallah, Roy-Chowdhury et al. 2015).

2.3. SAMPLE DELIVERY METHODS

The majority of SFX data has been collected from a jet of small crystals (typically 200 nm-10 µm) in their mother liquor. This scheme allows the sample to be constantly replenished for each XFEL pulse as the crystals are destroyed with each shot. While this has shown great success and breadth, limitations of this method have trigged multiple strategies to deliver crystals to the X-ray interaction region to be born over the last 6 years. In this section the current crystal delivery methods used at XFELs are reviewed and summarized in Table 2.1.

2.3.1. GAS-FOCUSED LIQUID INJECTORS

In preparation for the first SFX experiments, the gas dynamic virtual nozzle (GDVN) was invented to continuously deliver crystals to the X-ray pulses (DePonte, Weierstall et al. 2008, Weierstall, Spence et al. 2012). Based on the principle that flowing gas encompassing a liquid can focus the liquid jet to a smaller diameter (1/10 the original capillary size) the GDVN produces a liquid jet that is only a few microns in diameter (DePonte, Weierstall et al. 2008, Weierstall, Spence et al. 2012). This is achieved by mounting a smaller capillary inside a larger capillary. Crystals in their mother liquor are delivered through the smaller, inner capillary and high-pressured gas flows through the interstitial space between the larger, outer capillary and the inner capillary (see Figure 2.7). The GDVN has been used successfully for many SFX experiments (see Table 2.1) including time-resolved studies (Aquila, Hunter et al. 2012, Redecke, Nass et al. 2013, Kupitz, Basu et al. 2014) and has thus far been the workhorse for the majority of SFX experiments. While the GDVN has experienced much success, several limitations exist. Namely, clogging of the smaller, inner capillary can occur due to blockage from aggregating crystals, the shear forces experienced during jetting have been suspected to damage some fragile crystals (Demirci, Sierra et al. 2013, Stevenson, DePonte et al. 2014), and ice can form on the nozzle by

28

"back spraying" of debris from the explosion at the X-ray interaction region (DePonte, Weierstall et al. 2008, Demirci, Sierra et al. 2013). Clogging events can be decreased by filtering the sample prior to sample loading and using in-line filters upstream from the nozzle. However, filtering could result in loss of sample and damage to crystals, thus highlighting the need for knowledge and control over the size distribution (Demirci, Sierra et al. 2013). One challenge when using the GDVN is that the X-ray pulse repetition rates currently available (≤120 Hz) are low compared to the minimal flow rate of the GDVN at 10 µL/min, thus the majority of crystals never interact with the X-ray beam since they flow through the interaction region between pulses (Weierstall 2014). Therefore, large sample volumes are needed to produce a complete SFX dataset using this
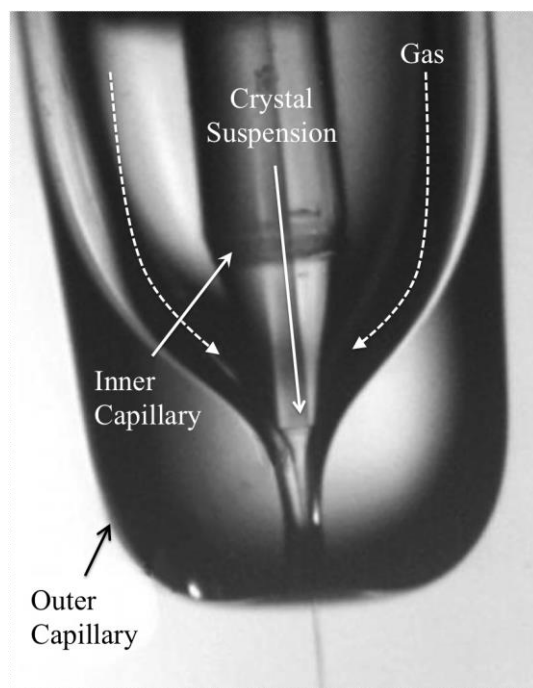
Figure 2.7 Schematic of GDVN. The GDVN is assembled by placing a smaller, hollow-core fused silica optical fiber (inner capillary) inside a larger, borosilicate glass capillary (outer capillary). Crystals are passed through the inner capillary while a focusing gas is passed through the outer capillary and thus occupies the space in between the two capillaries. A thin, micrometer jet is produced when the co-flowing gas meets the crystals as they exit the inner capillary.

method. Data sets using the GDVN can require 10 mL of crystal suspensions, typically containing on the order of 10^9-10^{11} crystals/mL (Chapman, Fromme et al. 2011, Schlichting and Miao 2012, Kupitz, Grotjohann et al. 2014, Galli, Son et al. 2015).

Several strategies have been proposed to reduce the flow rate of the GDVN. First, the GDVN can be operated in a pulsed mode whereby the jet is switched on and off, using a high performance liquid chromatography (HPLC) valve, as to minimize sample loss between pulses. It has been reported that flow times of 300 µs separated by times of 2 ms without flow could reduce the GDVN sample consumption by a factor of four (Weierstall 2014). Similar to a pulsed method, droplets can be used to deliver crystals to the X-ray beam. In acoustic droplet ejection, droplets can be produced by a piezoelectric transducer (Chen and Basaran 2002). To optimally synchronize the crystal filled drops, the droplets would be trigged by the XFEL. However, droplet speeds produced tend to be unstable on the necessary timescales, making synchronization difficult. Additional challenges faced by this method include large droplet size and thus high background (Soares, Engel et al. 2011, Roessler, Kuczewski et al. 2013), crystal settling without the addition of a viscous solution (Weierstall 2014), and compatibility with high vacuum (Weierstall 2014). To date, neither the pulsed liquid jet nor acoustic droplet ejection has been employed at an XFEL successfully.

2.3.2. ELECTROSPINNING INJECTORS

In one method of counteracting the fast consumption of sample by the GDVN, an electrospun liquid microjet, which uses high electric fields instead of gas to focus the liquid, has been implemented (Sierra, Laksmono et al. 2012). Electrospinning allows for a slower moving jet and thus, fewer sample flows between XFEL pulses and the amount of sample needed for a dataset can be reduced (Weierstall, James et al. 2014). The slow speed is also suitable for experiments with long pump-probe delay times as it allows for longer incubation times compared to those achievable with the GDVN (Sierra, Laksmono et al. 2012). However, to form a

continuous jet and prevent crystal settling, the crystals must be suspended in a suitable viscous media (e.g. glycerol, PEG, or sucrose); otherwise the electrospun jet breaks up into highly charged droplets once surface tension is overcome. The embedding media also serves as a cryo-protectant, necessary to prevent jet dehydration due to the length of time spent in vacuum, making this method not universally suitable. Caution of the impact of the electric field and the high charge of the jet and droplets on the sample must also be considered as they are unknown at present (Sierra, Laksmono et al. 2012).

2.3.3. *HIGH-VISCOSITY MEDIA INJECTORS*

LCP has a viscosity similar to vacuum grease, which makes harvesting tens of thousands of small crystals from their sticky, viscous environment impractical. Thus, an alternative method was devised so that the crystal laden LCP could be delivered directly to an X-ray beam. To extrude such a viscous material, the high viscosity injector (commonly referred to as the "LCP injector") amplifies the pressure of an HPLC using a hydraulic stage to extrude the viscous media out of a capillary (Figure 2.8). A co-flowing gas stream ensures that the highly viscous fluid does not curl back onto the nozzle and forms a stable jet (Weierstall, James et al. 2014). Unlike the GDVN, the jet is not focused to a smaller size and maintains the inner diameter of the capillary it is extruded from (10-100 µm). In addition, the high viscosity injector has been shown to work both in vacuum and in air (Nogly P 2015). To decrease sample consumption for soluble nanocrystals, crystals have been successfully manually mixed post-crystallization with LCP and grease (Fromme, Ishchenko et al. 2015, Sugahara, Mizohata et al. 2015). Recently, agarose-based gels have been shown to be compatible for the sample delivery of both soluble and membrane proteins which are embedded into pre-gelled agarose using a coupled syringe setup as described in Conrad et al.(Conrad, Basu et al. 2015). The agarose jet also offers an improved background over grease (Sugahara, Mizohata et al. 2015) or LCP, leading to higher quality data (Conrad, Basu et al. 2015).

31
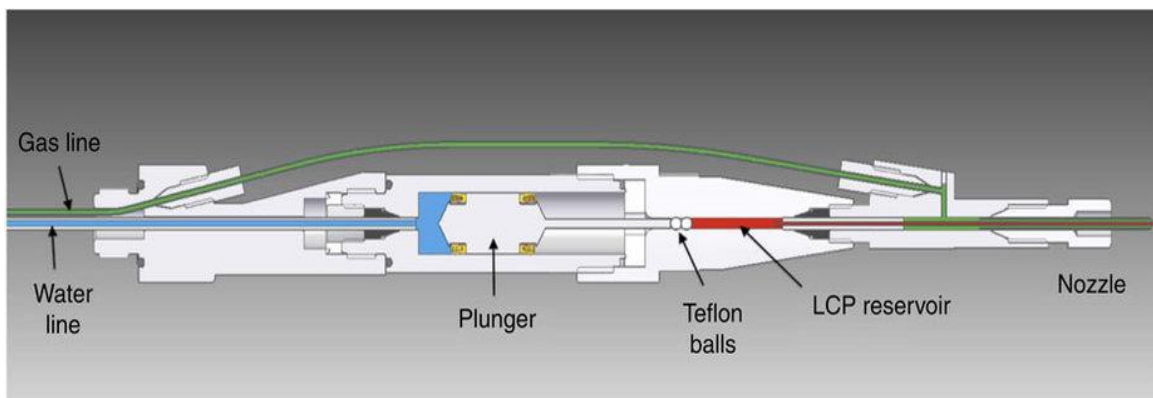
Figure 2.8 High Viscosity Injector. LCP (or high viscosity medium) depicted in red is extruded from the nozzle on the right. Water, at a pressure of up to 300 psi, drives the hydraulic plunger, which amplifies the pressure 34 times to drive medium through a capillary with an inner diameter of 10–50 μm. Two spherical Teflon beads are used to provide a tight seal against a pressure of up to 10,000 psi. The co-flowing gas is necessary for reliable extrusion and to maintain co-axial flow. Image and caption modified and used with permission from (Weierstall, James et al. 2014).

2.3.4. FIXED TARGETS

For most experiments that use a flowing jet, either liquid, viscous, or electrospun, the optimal crystal hit rate is usually around 10-30%, as higher crystals densities tend to lead to clogging. Flowing jets remain the ideal method for sample delivery for most SFX experiments as they do not require freezing and are the most practical technique for conducting time-resolved experiments. But for a small subset of experiments, fixed targets may be beneficial since this approach has the potential to decrease the sample quantities necessary for a data set to be collected. Fixed targets vary from traditional goniometers, to windowed sample support wafers/grids (analogous to electron microscopy holders), and to microfluidic chips(Hunter, Segelke et al. 2014, Feld, Heymann et al. 2015, Mueller, Marx et al. 2015). The main advantage of sample support wafers is their compatibility with 2D nanocrystals, which require scaffolding and

Table 2.1: Summary of sample delivery methods currently being deployed for SFX.

Sample Delivery Method	Average Flow Rate	Advantages	Limitations	Vacuum or Atmosphere	Examples of systems/ proteins studied
Gas Dynamic Virtual Nozzle (DePonte, Weierstall et al. 2008)	10-25 µL/min (Schlichting 2015)	Amenable for TR-SFX(Aquila, Hunter et al. 2012, Kupitz, Basu et al. 2014), compatible with most systems	High sample consumption (Weierstall 2014, Weierstall, James et al. 2014, Sugahara, Mizohata et al. 2015), clogging (Demirci, Sierra et al. 2013), freezing around nozzle tip (Weierstall 2014), fragile crystals might be damaged during jetting (Demirci, Sierra et al. 2013, Stevenson, DePonte et al. 2014), requires crystals to be filtered (Cohen, Soltis et al. 2014)	Vacuum	Photosystem I & II (Kern, Alonso-Mori et al. 2013, Kupitz, Basu et al. 2014), photosystem I-ferredoxin (Aquila, Hunter et al. 2012), lysozyme (Boutet, Lomb et al. 2012), cathepsin B (Redecke, Nass et al. 2013), photosynthetic reaction center (Johansson, Arnlund et al. 2013),Cry3A (Sawaya, Cascio et al. 2014), photoactive yellow protein (Tenboer, Basu et al. 2014), P-type ATPase (Bublitz, Nass et al. 2015), myoglobin (Barends, Foucar et al. 2015), phycocyanin (Fromme, Ishchenko et al. 2015), B subunit of cholera toxin-membrane-proximal region of gp41(Lee, Cherni et al. 2014), CPV17 polyhedrin (Ginn, Messerschmidt et al. 2015), trans-acting acyl transferase (Stevenson, Makhov et al. 2014), RNA polymerase B II (Stevenson, Makhov et al. 2014), parathyroid hormone receptor 1 (Stevenson, DePonte et al. 2014)
Electrospinning (Sierra, Laksmono et al. 2012)	140-3100 nL/min (Sierra, Laksmono et al. 2012)	consumption (Sierra, Laksmono et al. 2012), compatible with membrane proteins (Kern, Alonso-Mori	Requires cryoprotectant to prevent the jet from freezing (Sierra, Laksmono et al. 2012), unknown if high electric fields affect crystals (Conrad, Basu et al. 2015)	Vacuum	Photosystem II (Kern, Alonso-Mori et al. 2012), 30S ribosomal subunit (Demirci, Sierra et al. 2013), thermolysin (Hattne, Echols et al. 2014)

Table 2.1 Continued Summary of sample delivery methods currently being deployed for SFX.

Sample Delivery Method	Average Flow Rate	Advantages	Limitations	Vacuum or Atmosphere	Examples of system/proteins studied
Agarose (Conrad, Basu et al. 2015)	100-200 nL/min (Conrad, Basu et al. 2015)	Low sample consumption (Conrad, Basu et al. 2015), compatible with membrane proteins (Conrad, Basu et al. 2015), low background (Conrad, Basu et al. 2015)	Requires cryoprotectant to prevent the jet from freezing (Conrad, Basu et al. 2015)	Both	Phycocyanin (Conrad, Basu et al. 2015), photosystem I & II (Conrad, Basu et al. 2015), sindbis virus (Lawrence, Conrad et al. 2015)
Fixed Target: Goniometer (Cohen, Soltis et al. 2014) (Grids/Mesh/Loops)	NA	Semi-automated data collection (grid only) (Cohen, Soltis et al. 2014), amenable to micro- and to macro-crystals (Cohen, Soltis et al. 2014), compatible with standard goniometers (Cohen, Soltis et al. 2014)	Requires cryopreservation and freezing (Cohen, Soltis et al. 2014), requires hitting the crystal in a different position each shot to avoid damage, not amenable for TR-SFX	Atmosphere	RNA polymerase II (Cohen, Soltis et al. 2014), general transcription factor IIB (Cohen, Soltis et al. 2014), large nucleic acid scaffold (Cohen, Soltis et al. 2014), monomeric iron-containing hydrogenase (Cohen, Soltis et al. 2014), sperm whale myoglobin (Cohen, Soltis et al. 2014), cytochrome c oxidase (Hirata, Shinzawa-Itoh et al. 2014), synaptotagmin-1 SNARE complex (Zhou, Lai et al. 2015), β2-adrenoreceptor/nanobody complex (Cohen, Soltis et al. 2014), cyclophilin A (Keedy, Kenner et al. 2015)

Table 2.1 Continued Summary of sample delivery methods currently being deployed for SFX.

Sample Delivery Method	Average Flow Rate	Advantages	Limitations	Vacuum or Atmosphere	Examples of systems/ proteins studied
Lipidic Cubic Phase (Weierstall, James et al. 2014)	50-200 nL/min (Liu, Wacker et al. 2013)	Low sample consumption (Liu, Wacker et al. 2013), crystals grown in LCP do not need to be harvested (Liu, Wacker et al. 2013), some soluble crystals post-crystallization can be mixed to conserve sample (Fromme, Ishchenko et al. 2015)	Debye Sherrer rings (Conrad, Basu et al. 2015), not shown to be compatible with membrane proteins (Conrad, Basu et al. 2015)	Both	5-HT2B receptor (Liu, Wacker et al. 2013), smoothened receptor (Weierstall, James et al. 2014), human delta opioid receptor (Fenalti, Zatsepin et al. 2015), human angiotensin receptor (Zhang, Unal et al. 2015), rhodopsin arrestin complex (Kang, Zhou et al. 2015), diacylglycerol kinase (Li, Stansfeld et al. 2015), lysozyme (Fromme, Ishchenko et al. 2015), phycocyanin (Fromme, Ishchenko et al. 2015)
Grease (Sugahara, Mizohata et al. 2015)	460-480 nL/min (Sugahara, Mizohata et al. 2015)	Low sample consumption (Sugahara, Mizohata et al. 2015)	Debye-Sherrer rings (Conrad, Basu et al. 2015), not shown to be compatible with membrane proteins (Conrad, Basu et al. 2015)	Atmosphere	Lysozyme (Sugahara, Mizohata et al. 2015), glucose isomerase (Sugahara, Mizohata et al. 2015), thaumatin (Sugahara, Mizohata et al. 2015), fatty acid–binding protein type 3 (Sugahara, Mizohata et al. 2015), luciferin-regenerating enzyme (Yamashita, Pan et al. 2015)

Table 2.1 Continued Summary of sample delivery methods currently being deployed for SFX.

Sample Delivery Method	Average Flow Rate	Advantages	Limitations	Vacuum or Atmosphere	Examples of system/proteins studied
Fixed target: sample supports (wafers (Hunter, Segelke et al. 2014) (Pedrini, Tsai et al. 2014, Feld, Heymann et al. 2015) and chips (Lyubimov, Murray et al. 2015, Mueller, Marx et al. 2015))	NA	Low sample consumption (Lyubimov, Murray et al. 2015), compatible with 2D crystals (Pedrini, Tsai et al. 2014), target can be rotated about a fixed angle (Lyubimov, Murray et al. 2015)	Commercial wafer/chip material is not X-ray transparent (Feld, Heymann et al. 2015, Lyubimov, Murray et al. 2015), low data collection rates (<10 Hz, limited by velocity of sample holder) (Hunter, Segelke et al. 2014), crystal traps can produce crystal orientation biases (Lyubimov, Murray et al. 2015) and fill rate is limited to ~50% to prevent crystal stacking (Mueller, Marx et al. 2015), in vacuum experiments requires emerging crystals in oil (Hunter, Segelke et al. 2014, Feld, Heymann et al. 2015), unless crystals are grown on a chip they must be transferred (Lyubimov, Murray et al. 2015, Mueller, Marx et al. 2015)	Both	Rapid encystment protein 24 kDa (Hunter, Segelke et al. 2014), bacteriorhodopsin (Pedrini, Tsai et al. 2014), anthrax toxin protective antigen (Feld, Heymann et al. 2015), lysozyme(Lyubimov, Murray et al. 2015), sperm whale myoglobin (Mueller, Marx et al. 2015)

thus, cannot be delivered in a flowing jet (Li, Stansfeld et al. 2015). In order to prevent dehydration, crystals must be immersed in oil before being painted onto the support grid. Microfluidic devices have also been used for fixed target experiments at XFELs and have been designed to trap single crystals (Feld, Heymann et al. 2015). These traps can theoretically ensure that the X-ray beam interacts with only one crystal at a time but with current designs, crystalstacking will occur before all the traps are filled. Fixed targets can result in crystal orientation bias (Lyubimov, Murray et al. 2015, Mueller, Marx et al. 2015). Currently, fixed target approaches are severely limited by slow data acquisition. Data acquisition rates are primarily limited by the velocity of the fixed target stage and the time it takes to replace the sample grid or chip. For example, if the stage motor could operate at 120 Hz and automated scripts aligned the X-rays to each window/trap, a fixed target containing 800 window/traps, the sample holder would need to be replaced every 6.67 min. In addition, some fixed targets produce high background due to the support material (Pedrini, Tsai et al. 2014, Li, Stansfeld et al. 2015, Lyubimov, Murray et al. 2015).

Recently, data has also been collected at XFELs with a conventional goniometer approach on very large crystals (up to millimeters in size) under cryogenic conditions. This method has been used to determine a dark structure of PSII with minimal X-ray damage at 1.95 Å resolution (Suga, Akita et al. 2015). However, this approach is low throughput and tedious as it can require days or even weeks of very precious data collection time at FELs on hundreds of individually mounted crystals (Suga, Akita et al. 2015). The experiment required freezing, attenuation, and translation of the beam focus by 50 µm at an X-ray spot size of 1 µm to avoid X-ray damage. Furthermore, freezing and the large crystal size prohibits time-resolved experiments from being feasible. Except for cases like PSII, where X-ray damage significantly alters the structure of the catalytic metal complex, it is questionable if this is advantageous compared to standard macromolecular crystallography at synchrotron sources.

2.4. STRUCTURAL DYNAMICS AND MOLECULAR MOVIES: CHALLENGES AND OPPORTUNITIES

In addition to broadening the array of macromolecules available to crystallography, SFX also expands upon the information that can be obtained regarding functional dynamics. Macromolecular crystals typically exhibit extremely high solvent content and weak electrostatic contacts in comparison to their smaller molecular counterparts. While this has always presented a challenge to crystallogenesis of well-diffracting crystals, the porous nature of macromolecular crystals lend them to intact catalytic or functional activity in the crystalline phase Table 2 (Hofbauer, Zouni et al. 2001, Moffat 2001, Fromme, Bottin et al. 2002). This is because large solvent channels that are present in the crystals can allow for conformational movement of the proteins or even the diffusion of a substrate to active sites in crystals. This property indicates an exciting opportunity to see intermediate structures over the course of a functional reaction. By achieving time-resolved structure determination (i.e. multiple structures along a reaction pathway), one can begin to directly understand the relationship between structure and function of macromolecules. This has numerous applications such as rational drug design and renewable energy by unraveling the mechanism of biochemical processes. However, some important considerations must be taken into account in order to realize reliable time-resolved structures.

Time-resolved crystallography has historically been performed on large single crystals by Laue multi-wavelength crystallography (for a review see (Hajdu and Johnson 1990)) and has exhibited considerable gains over the past twenty years, moving from the millisecond (Genick, Borgstahl et al. 1997) to the picosecond (Schotte, Cho et al. 2012) temporal resolution regimes. This has opened the door to viewing conformationally dynamic proteins in action on an atomic scale. While this technique continues to improve, both within its experimental parameters and subsequent data analysis, it faces some hard limitations due to the nature of large crystals and current synchrotron sources, namely: 1) temporal resolution is limited by pulse length achievable using a synchrotron, 2) irreversible reactions cannot be studied as the induction of a reaction would cause a permanent modification of the molecules in the crystal, 3) only light activated,

pump-probe type experiments are generally feasible at present, with limited light penetration being one of the major obstacles, and 4) homogeneity of reaction initiation must be considered and presents a challenge. SFX presents an opportunity to complement the Laue method by providing access to experiments previously impossible by overcoming the above challenges via its unique experimental characteristics. XFELs have pulse durations on the order of tens of femtoseconds, which, within the framework of time-resolved crystallography, allow access to detect and resolve fast time points in catalytic reaction processes. Thereby, more temporally constrained intermediates can be detected along a reaction pathway. Recent work has pushed temporal resolution to the sub picosecond regime (Barends, Foucar et al. 2015, Pande, Hutchinson et al. 2015), which is utterly out of reach at existing synchrotron sources. This allows insight into ultrafast intermediates and therefore, the promise of a much finer understanding of catalytic mechanisms.

With irreversible reactions one must consider the way in which data is collected. In traditional crystallography a crystal is rotated during data collection and each diffraction pattern corresponds to a rotational increment of the reciprocal space. If an irreversible reaction is to be probed fully, data collection would require thousands of large crystals for each time point as the crystal would be permanently altered after the induction of the reaction. This would require an oppressively large number of crystals to collect a complete data set from individual crystals. The serial "diffraction before destruction" nature of SFX experiments completely bypasses this constraint, as only one diffraction pattern is collected from each crystal. Since the sample is constantly replenished, there is no constraint on the reversibility of a reaction. The utilization of Monte Carlo merging of an immense number of individual crystals in random orientations leads to accurate structure factors for time-resolved experiments due to implications from the central limit theorem.

Considerations of structural homogeneity and the constraint of Laue to predominantly pump-probe style experiments are highly intertwined due to one parameter: diffusion. Thus far, Laue crystallography has been predominantly limited to photo-activated reactions since

chemically activated reactions would necessitate diffusion of a substrate throughout the crystal, limiting reaction timescales available. While the large solvent channels in crystalline macromolecules often allow for diffusion to take place via soaking with a diffusing substrate (Bolduc, Dyer et al. 1995, Stoddard and Farber 1995, Helliwell, Nieh et al. 2003) (assuming the active site is unobstructed and the substrate is sufficiently small relative to the solvent channels), the size of the crystal limits diffusion times, thereby constraining the time regime of reaction intermediates accessible in an experiment. There have been chemically activated time-resolved experiments performed successfully by incorporating photo-activated caged substrates into the crystal (Schlichting, Rapp et al. 1989, Stoddard, Cohen et al. 1998, Ursby, Weik et al. 2002), thus reducing diffusion times to that of the photo-penetration of the pump laser. However, the incorporation of caged substrates requires extensive knowledge about a given system and is not generally compatible (Schmidt 2013). The small size of the crystals used in SFX theoretically allow for diffusion times on microsecond time scales, allowing access to many reactions on the short millisecond and even microsecond regimes in the absence of caged substrates. For example, a crystal with dimensions of 0.5 x 0.5 x 0.5 μm^3 has been modeled to exhibit a diffusion time of 17 μs, while a 3 x 4 x 5 μm^3 crystal is estimated to take 1 ms, and a large 300 x 400 x 500 μm^3 crystal would take 9.5 s (Schmidt 2013). Many biological reactions occur with intermediates observed in the time range of ms and faster but significantly less occur in the longer regime of seconds. One must also consider reaction homogeneity since Bragg diffraction relies upon translational symmetry of the molecules in the crystal. This means that in order to observe an intermediate structure, a sufficient proportion of the molecules must be in a single conformation during probing in order for a structure to be elucidated.

Photoactivated reactions have one major advantage over substrate or other diffusion based reactions as initiation is homogeneous and rapid. However, the degree of reaction initiation by photoinduction is also limited by the size of the crystal since molecules absorb the light as it travels through the crystal causing a decrease in transmission with increasing path length. When considering faster time points, the reaction homogeneity of the molecules in the crystal is

sensitive to the lifetime of the intermediate state as compared to the time difference of reaction initiation from the front and back surfaces of the crystal relative to the pump beam. The distance traveled with respect to the front and back of photo-activated crystals is not the main cause of this temporal offset (though this is on the order of picoseconds for large crystals); instead, it is the attenuation of the pump intensity as it proceeds through the crystal, undergoing absorption and scattering. Depending on the particular robustness of the sample, one can attempt to address this by increasing the power of the laser but this approach is constrained by photo-damage and heating effects that can occur. Thus, the size of nanocrystals provides an advantage, allowing a much smaller difference of reaction initiation throughout the crystal and requiring decreased pump intensities for maximal reaction initiation. Furthermore, the volume of the crystal itself is so small that in practice, the whole crystal can be illuminated by the pump, minimizing considerations of the intensity profile of the pump laser. Because of these attributes, SFX provides the basis for a much higher reaction initiation yield, a point which as has already been shown in practice (Tenboer, Basu et al. 2014).

2.4.1. TIME-RESOLVED SERIAL FEMTOSECOND CRYSTALLOGRAPHY

The structure-mechanistic relationship found in biological reactions is rarely explained through resolution of a single, static structure. Instead, the dynamics between initial and final states embody the mechanism. TR-SFX permits access to transient intermediates that occur as a reaction is proceeding, providing still snapshots of these states. Snapshots of the initial, intermediate, and final state(s) can be viewed in a quick succession from start to finish to reveal motion of the enzyme and thus a "molecular movie" can be obtained to unravel how these biological molecules proceed in nature.

The first time-resolved SFX (TR-SFX) experiment was carried out on PSI-ferredoxin co-crystals which undergo electron transfer reactions that lead to the subsequent undocking of ferredoxin and dissolution of the crystals upon light excitation, leading to a rapid loss of diffracting quality upon pumping. Large differences have been obtained in the diffraction patterns between

the excited and uninitiated reactions as revealed by the Wilson plot. The timing of these differences agrees with the time range previously found by spectroscopic methods for electron transfer (Setif and Bottin 1995, Diaz-Quintana, Leibl et al. 1998). These experiments provided the proof of concept for TR-SFX, (though an electron density map was not obtained due to data limitations) (Aquila, Hunter et al. 2012).

The first successful TR-SFX experiment was performed using PSII, the membrane protein responsible for splitting water into its constituent protons, electrons and oxygen (Kupitz, Basu et al. 2014). This process provides the electrons for the photosynthetic electron transfer chain in oxygenic photosynthesis. The catalytic oxygen evolving cluster, structurally the most interesting domain in PSII, is particularly susceptible to radiation damage due to the presence of 5 Mn atoms. The X-ray photo-damage processes are virtually eliminated by the "diffraction before destruction" (Neutze, Wouts et al. 2000) nature of SFX. A further concern of time-resolved studies with X-rays is that local photo-damage can be induced by repeated illumination of the crystal by the pump laser in Laue time-resolved experiments. Again, this problem is mitigated by TR-SFX since relatively low pump energy and flux can be applied per crystal due to smaller, more permeable crystals. Indeed, TR-SFX has succeeded in 'shining the first light' on the undamaged ground state of PSII using single and multiple laser excitations prior to diffraction, allowing multiple states to be studied along the multiple-excitation reaction pathway. This revealed large conformational changes occurring in the photoexcited "double flash state" of PSII, which includes movement of the protein via its coordination of the oxygen evolving cluster (Kupitz, Basu et al. 2014). Though higher resolution is needed to provide a deeper understanding of the water splitting process, TR-SFX in general provides the most feasible path forward toward obtaining a series of initial, final and intermediate structures during a reaction, i.e. molecular movies of biomolecules at work.

More recently, atomic resolution has been achieved for TR-SFX using PYP (Tenboer, Basu et al. 2014). This experiment also pushed the limits on the time-resolution available at an XFEL, capturing reaction time points down to the sub-picosecond regime (Pande, Hutchinson et

al. 2015). These studies improve upon the temporal resolution that has been achieved in Laue crystallography (Schotte, Cho et al. 2012) by orders of magnitude and is only significantly limited by beam characteristics (i.e. time-jitter) (Pande, Hutchinson et al. 2015). As developments continue with future generation sources, temporal resolution will be pushed even further. In addition to ultrafast time resolution, it is notable that the TR-SFX studies on PYP have also shown huge improvement on reaction initiation (40% at XFELs with nanocrystals compared to 10-15% achieved at a synchrotron with larger crystals (Schmidt, Srajer et al. 2013, Tenboer, Basu et al. 2014)), allowing for stronger signal from transient intermediates to be detected, leading to data that can be easily interpretable. Even more recently, research in this time domain has led to novel observations of global structural changes in myoglobin upon lysis of an Fe-CO bond that occur within a few picoseconds (Barends, Foucar et al. 2015).

Though no mixing TR-SFX work has been published to date, the stage is set for 'on the fly' mixing experiments that take advantage of the nature of SFX. Many enzymes have biologically interesting intermediates that occur on time scales faster than those accessible to soaking experiments of large crystals. Although one could scale down the size of the crystals and thereby, narrow the reaction initiation temporal profile, the tradeoff with decreased diffraction severely limits the range of this method. In theory, the sizes of crystals available for SFX alleviates this concern, decreasing necessary mixing times such that a new regime of reactions is accessible. Delivery methods based on the GDVN have already been developed for time-resolved mixing experiments e.g. a double focused mixing jet (Wang, Weierstall et al. 2014) where a jet containing crystals is mixed within a stream containing the desired substrate prior to discharging from the nozzle. For a more in depth look at substrate mixing techniques, the reader is referred to (Schmidt 2013).

Indeed, the most promising areas for XFELs to push the boundaries within structural biology is the ability to study temporal dynamics with femtosecond pulses, allowing access to ultrafast timescales and thereby, short lived intermediates. Without sacrificing resolution, TR-SFX paves the way for dynamic structural elucidation of biological processes that feature fast (<100

ps) conformational changes, irreversible reactions, non-photoactivated inductions, and to those which are limited by crystal size. TR-SFX can also avoid the local radiation damage often experienced in the active sites of macromolecules and generate a higher fraction of intermediate states (Tenboer, Basu et al. 2014). This has far reaching implications for many fields, notably alternative energy and drug design, which both rely heavily on understanding the relationship between structure and mechanism. The reactions accessible to TR-SFX studies will continue to broaden as 'mix and inject' methods for chemo-activated reactions continue development. With TR-SFX and other time-resolved XFEL methods (such as time-resolved wide angle X-ray scattering, e.g. (Arnlund, Johansson et al. 2014)), it is evident that XFELs provide new ways to explore a novel regime of time-resolved structural biology, leading towards true movies of dynamic macromolecules in action.

2.4.2. DATA ACQUISITION AND DATA PROCESSING IN SFX

The short duration pulses delivered by XFELs have necessitated the development of new detector technologies capable of integrating all of the photons that arrive within the time duration of a few femtoseconds, while sustaining full-frame readout at the XFEL pulse repetition rate. Although X-ray charge coupled device (CCD) detectors are very common at synchrotrons, few CCD detectors have readout speeds that match the LCLS repetition rate. Two CCD's were used at LCLS for the first experiments (at 2 keV), the pnCCD and the fCCD (Strüder 2010, Doering, Chuang et al. 2011) . Due to their very low noise and high quantum efficiency over a large range of energies, they have been used for imaging and spectroscopy experiments. However, a larger dynamic range then the CCDs can currently cover (a few hundred thousands of photons) is necessary for SFX experiments at atomic resolution (energies >6 keV). The first detector specifically designed for higher energies presently used for SFX experiments at LCLS was the Cornell-SLAC pixel array detector (CSPAD) (Koerner 2009, Philipp 2010, Philipp H. T. 2011, Hart P. 2012). Today the CSPAD is the principal detector used for SFX experiments at LCLS. It consists of 64 separate modules (194 x 185 pixels each), allowing cost-effective replacement and experimental flexibility. The CSPAD is tiled to produce a 2.3 megapixel detector, with readout

speeds matching the repetition rate of 120 Hz (Hart P. 2012). The panel distribution leaves an adjustable sized hole in the middle to allow for adjustable incident beam focuses, preventing the beam from damaging the detector (the beam is powerful enough to melt through a conventional beam stop)(White, Barty et al. 2013).

The use of detectors composed of multiple modules introduces unique concerns, namely the exact location of each module must be known in order to correctly assess the data. While the experimental geometry may be known to low precision prior to an experiment, it can be subsequently refined using the collected data. In this case, assembling a physically correct image during initial processing is futile and a known calibration sample is used to refine the experimental geometry. The detector geometry is specified in a pixel location map containing the coordinates of each detector pixel in a suitably defined coordinate system. All constraints for an experimental geometry description are saved in a single text file which can be implemented within any of the available SFX software (White, Barty et al. 2013, Barty, Kirian et al. 2014, Hattne, Echols et al. 2014). The success of indexing, predicting spot locations using a crystal orientation matrix and integrating reflection intensities depends upon the precise knowledge of the location of these sensors in three-dimensional space. This means that an accurate calibration and refinement of the tile metrology is critical.

Data analysis in SFX has unique challenges with respect to data sets collected at synchrotrons. This is due to the serial nature from snapshot diffraction patterns of randomly oriented crystals with unknown partiality and shot to shot variation in the beam characteristics. Furthermore, the images collected during an experiment consist not only of single crystal hits (one crystal in the beam) but also blank patterns (no crystal in the beam) and multi-hits (multiple crystals in the beam). The XFELs at LCLS and SACLA operate up to 120 Hz and 60 Hz, respectively, resulting in hundreds of thousands of patterns collected per hour, thus creating terabytes of data. Due to these challenges, conventional crystallographic data processing methods cannot be efficiently used for SFX data collection. Thus, new data analysis tools for SFX have been developed. In order to optimize efficiency during data collection it is important to have

rapid feedback during data collection. First, data is reduced by eliminating blank and multi-hit patterns which is implemented within the programs Cheetah (Barty, Kirian et al. 2014) and CASS (Foucar 2012). They perform the data pre-processing steps, evaluate the quality of each data frame, and reject all those frames that are not suitable for further analysis. Once the data size is reduced, detector artifacts are removed and background subtraction is performed. Each frame is then subjected to Bragg peak location analysis (so called 'peak finding') in which Bragg peaks are identified by searching for clusters of connected pixels based on a series of parameters including minimum numbers of pixels per peak, the number of peaks in a frame, intensity thresholds, and signal to noise ratio. A minimum number of Bragg peaks must be identified in the diffraction pattern as a further constraint, so that patterns with too few peaks (i.e. impossible to index) are rejected.

The background corrected and sorted diffraction patterns identified during the hit finding process are subjected to indexing and integration by programs such as CrysFEL (White, Barty et al. 2013), cctbx.xfel (Hattne, Echols et al. 2014), and nXDS (Kabsch 2010). The purpose of these programs is to identify Bragg peaks in the hits and then to perform indexing. Determining the unit cell parameters and the orientation of a crystal is carried out by the widely used algorithms such as MOSFLM (Powell 1999, Rossmann and van Beek 1999, Powell, Johnson et al. 2013), DIRAX (Diusenberg 1992), LABELIT (Sauter, Grosse-Kunstleve et al. 2004), and XDS (Kabsch 2010), based on the Bragg peak locations in a diffraction pattern. Once each pattern has been successfully indexed, the intensities are merged and integrated using the Monte Carlo method (Kirian, Wang et al. 2010, Kirian, White et al. 2011). One of the largest problems in SFX data analysis is the indexing ambiguity which occurs when the Bravais symmetry is higher than the space group symmetry. An indexing ambiguity arises in some polar space groups (like *P63*) where each pattern has multiple ways it can be indexed. In standard crystallography this indexing ambiguity is solved by exploration of the data set with both indexing options, where only one option leads to a correct X-ray structure. However, since many individual patterns are merged in SFX, the ambiguity must be solved before any additional processing to avoid artificial twinning. In

order to overcome the indexing ambiguity problem, CrystFEL has implemented an algorithm based on the expectation maximization approach (Liu, Poon et al. 2013) which has been successfully applied and validated using both simulated and experimental diffraction (Liu, Poon et al. 2013).

As with conventional crystallography, the "phase problem" has to be solved in order to reconstruct a real-space electron density map from the measured SFX intensities. Indeed, this presents itself as a primary challenge in serial crystallography data analysis. Until recently, all crystallographic structures so far determined by XFEL have been phased by molecular replacement, using phases from known or related structures (Chapman, Fromme et al. 2011, Boutet, Lomb et al. 2012, Johansson, Arnlund et al. 2012, Sierra, Laksmono et al. 2012, Redecke, Nass et al. 2013). This method limits the target protein molecules to be investigated by SFX since the protein of interest must have a known homologous structure. Even if it does, there is risk that phase bias can be introduced. However, some conventional phasing methods have also been suggested to be applied to SFX data such as multiple isomorphous replacement or multi/single-wavelength anomalous dispersion (MIR, MAD, SAD)(Son, Chapman et al. 2011, Sang-Kil Son 2013, Barends, Foucar et al. 2014, Barends, Foucar et al. 2015). Barends (Barends, Foucar et al. 2014) and co-workers have demonstrated for the first time that the conventional phasing method of SAD can also be successfully used for SFX experiments (Barends, Foucar et al. 2014). In this experiment they collected and solved the structure to 2.1 Å resolution of a lysozyme heavy atom derivative that gives a strong anomalous signal from two gadolinium atoms per asymmetric unit. The MAD phasing method has also been recently adapted to SFX by using modified Karle-Hendrickson equations (Son, Chapman et al. 2011, Sang-Kil Son 2013). This proposed generalized version of MAD phasing method offers another potential for experimental phasing for structural determination in SFX.

In addition to the classical methods, new phasing techniques have been proposed for SFX data analysis. Methods such as ab initio phasing by the evaluation of the shape transforms (or the oversampling method)(Chapman, Fromme et al. 2011, Spence, Kirian et al. 2011, Liu,

Poon et al. 2013, Kirian, Bean et al. 2014) and the "high-intensity radiation induced phasing" (HI-RIP)(Galli, Son et al. 2015) have been proposed. The phase transform method exploits the intensity scattered between neighboring Bragg peaks (or fringes) from crystals that contain less than 20 unit cells in each crystal direction. This phenomenon has historically been obscured by noise in large crystals due to inverse scaling of inter-Bragg intensity with the number of unit cells. Each recorded Bragg peak represents a particular portion of the Ewald sphere and phasing is achieved by oversampling between the Bragg peaks. The HI-RIP method takes advantage of the ionization process of the atoms that occur within the femtosecond timescale of the pulse in SFX experiments (Hau-Riege, London et al. 2004). The change in the electronic configuration of atoms leads to the modification of the atomic scattering factors during diffraction (Son, Chapman et al. 2011). In the case of SFX this would introduce the possibility of determining phases by varying the scattering factors of the heavy atoms. This new approach, which has been already tested with *Trypanosoma brucei* cathepsin B protein, would represent a powerful method of experimental phasing without the need to modify the protein crystals assuming sulfur atoms are present in the native structure (Galli, Son et al. 2015).

2.4.3. CHALLENGES AND OUTLOOK

Nearly six years after the first SFX data were collected using an XFEL at LCLS and four years after the proof of principle of SFX was published (Chapman, Fromme et al. 2011), a new era in structural biology has emerged. Figure. 2.9 shows a gallery illustrating the breadth of protein structures successfully solved with XFELs to date. The unique properties of XFELs (ultrashort, extremely intense pulses with high frequency and coherence) have attracted considerable attention of a wide community of scientists in fields ranging from material science, to chemistry, to structural biology, and to high energy physics. This has led to ground breaking discoveries but new science brings new challenges and access to experimental time at XFELs is

48
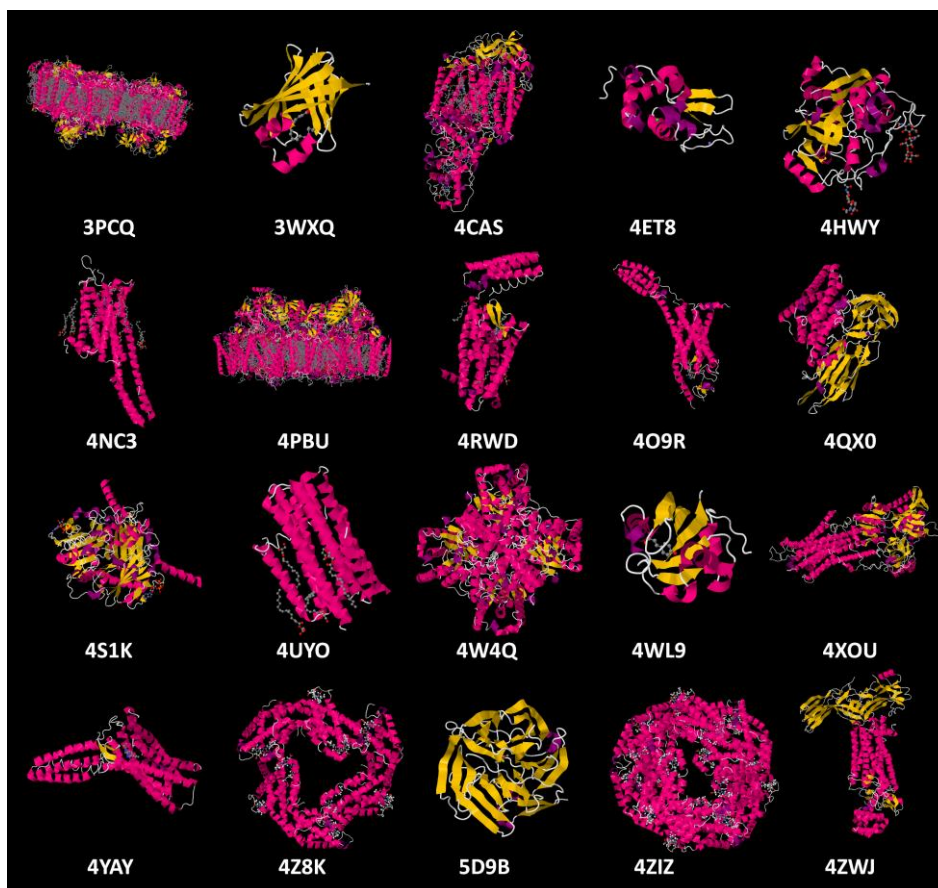
Figure 2.9 Select structures solved using XFELs by PDB code. From top left: photosystem I 3PCQ (Chapman, Fromme et al. 2011), FABP3 3WXQ (Sugahara, Mizohata et al. 2015), purple bacterial reaction center 4CAS (Johansson, Arnlund et al. 2013), lysozyme 4ET8 (Boutet, Lomb et al. 2012), cathepsin B 4HWY (Redecke, Nass et al. 2013), 5-HT2B 4NC3 (Liu, Wacker et al. 2013), photosystem II 4PBU   (Kupitz, Basu et al. 2014), d-opioid receptor 4RWD (Fenalti, Zatsepin et al. 2015), smoothened receptor (Weierstall, James et al. 2014), Cry3A 4QX0 (Sawaya, Cascio et al. 2014) , CPV17 polyhedron 4S1K (Ginn, Messerschmidt et al. 2015), diacylglycerol kinase 4UYO (Li, Stansfeld et al. 2015), xylose isomerase 4W4Q (Sugahara, Mizohata et al. 2015), photoactive yellow protein 4WL9 (Tenboer, Basu et al. 2014), SR Ca2þ-ATPase 4XOU (Bublitz, Nass et al. 2015), angiotensin II receptor 4YAY (Zhang, Unal et al. 2015), phycocyanin 4Z8K (Conrad, Basu et al. 2015), luciferin-regenerating enzyme 5D9B (Yamashita, Pan et al. 2015), C-phycocyanin   4ZIZ (Fromme, Ishchenko et al. 2015), rhodopsin-arrestin complex 4ZWJ (Kang, Zhou et al. 2015).

presently one of the major limitations. Currently, there are only two high energy XFELs in

operation in the world (i.e. only two experiments can take place in the world at the same time). It

is exceedingly unfortunate that due to this, beamtime is so scarce, thus becoming a major limiting

factor as the field progresses out of its initial stages. Fortunately, three new XFELs are currently

under construction, in South Korea (Kang, Zhou et al.), in Switzerland (SwissFEL), and in

Germany (European XFEL), which are expected to enter the commissioning phase in 2016 (Kang, Zhou et al.) and 2017 (European XFEL and SwissFEL). Furthermore, XFEL facilities are planned or are under initial stages of construction in Italy and China.

Along with the unprecedented new scientific opportunities, the successes of LCLS and SACLA have opened the eyes of the community for the need for further novel instrumentation developments in the field of XFELs. One challenge is the production of coherent photons of higher energies (50 keV or more). Another is the production of single spike pulses that are shorter than 1 fs. In addition, optics, diagnostics, detectors, sample delivery, and data acquisition must continue to be developed to keep up with the new development in data acquisition speed and X-ray pulse duration and intensity. Lower noise and higher dynamic range detectors are needed to take full advantage of these scientific opportunities. In this sense, a second generation of XFEL-capable detectors, the ePix family, is being developed at SLAC for this purpose. In parallel with the development of second generation XFELs, a new generation of detectors are being developed to meet the technical specifications required (such as the AGIPD (Allahgholi, Becker et al. 2015) at European XFEL or the Jungfrou at SwissFEL) (Denes and Schmitt 2014).

Research in the field of structural biology can now collect nearly damage-free X-ray data on biomacromolecular nanocrystals and continues to greatly impact the field by addressing many limitations faced by traditional crystallography. Going beyond SFX, computational simulations using rubisco have shown that a serial femtosecond imaging technique on individual molecules, in combination with the oversampling phasing method, could open a new horizon of structural elucidation of macromolecules without the need to first crystallize them (Miao, Chapman et al. 2004). However, with the photon flux of current XFELs, the ultimate goal of collecting atomic resolution data on a solution of individual, non-crystallized molecules remains currently out of reach. As the technique progresses, single particle imaging to atomic resolution may become feasible with future development of XFELs and data processing. In order to obtain high resolution

3D structural information of single large protein complexes, there are several challenges that need to be overcome. First, the pulse fluence of XFELs is not yet high enough to allow the

Table 2.2 Details of select structures solved using XFELs

Protein name	Organism	PDB code	Protein classification	Resolution	Space group	Unit cell	R_{work}, R_{free}	Year	Reference
Photosystem I	Thermosynechococcus elongatus	3PCQ	Membrane	8.98 Å	P6$_3$	281.0, 281.0, 165.2 90, 90, 120	0.25, 0.23	2010[a]	(Chapman et al., 2011)
FABP3	Homo sapiens	3WXQ	Soluble	1.6 Å	P2$_1$2$_1$2$_1$	133.25, 226.26, 307.09 90, 90, 90	0.178, 0.222	2014[b]	(Sugahara et al., 2015)
Purple bacterial reaction center	Blastochloris viridis	4CAS	Membrane	3.5 Å	P2$_1$2$_1$2$_1$	104.8, 104.8, 104.8 90, 90, 90	0.295, 0.329	2013[a]	(Johansson et al., 2013)
Lysozyme	Gallus gallus	4ET8	Soluble	1.9 Å	P4$_3$2$_1$2	33.71, 54.85, 70,66 90, 90, 90	0.196, 0.229	2012[a]	(Boutet et al., 2012)
Cathepsin B	Trypanosoma brucei	4HWY	Soluble	2.1 Å	P4$_2$2$_1$2	57.90, 84.80, 384.30 90, 90, 90	0.182, 0.213	2012[a]	(Redecke et al., 2013)
Serotonin receptor 5-HT2B	Homo sapiens	4NC3	Membrane	2.8 Å	C222$_1$	79.0, 79.0, 38.0 90, 90, 90	0.227, 0.270	2013[a]	(Liu et al., 2013)
Photosystem II	Thermosynechococcus elongatus	4PBU	Membrane	5.0 Å	P2$_1$2$_1$2$_1$	125.40, 125.40, 54.56 90, 90, 90	0.262, 0.261	2014[a]	(Kupitz et al., 2014)
ä-opioid receptor	Homo sapiens	4RWD	Membrane	2.7 Å	C121	61.50, 122.20, 168.50 90, 90, 90	0.208, 0.238	2014[a]	(Fenalti et al., 2015)
smoothened receptor	Homo sapiens	4O9R	Membrane	3.2 Å	P12$_1$1	40.50, 157.30, 52.40 90, 97, 90	0.232, 0.278	2014[a]	(Weierstall et al., 2014)
Cry3A	Bacillus thuringiensis	4QX0	Soluble	2.8 Å	C222$_1$	116.88, 134.81, 105.15 90, 90, 90	0.165, 0.192	2014[a]	(Sawaya et al., 2014)
CPV17 polyhedrin	Uranotaenia sapphirina cypovirus	4S1K	Soluble	2.2 Å	I23	156.23, 89.29, 96.42 90, 92.30, 90	0.14, 0.19	2015[a]	(Ginn et al., 2015)
Diacylglycerol kinase	Escherichia coli	4UYO	Membrane	2.18 Å	P2$_1$2$_1$2$_1$	75.30, 91.80, 141.70 90, 90, 90	0.208, 0.236	2014[a]	(Li et al., 2015)
Xylose isomerase	Streptomyces rubiginosus	4W4Q	Soluble	2.0 Å	I222	94.00, 100.00, 103.00 90, 90, 90	0.159, 0.196	2014[b]	(Sugahara et al., 2015)
Photoactive yellow protein	Halorhodospira halophila	4WL9	Soluble	1.6 Å	P6$_3$	66.90, 66.90, 40.80 90, 90, 90	0.198, 0.231	2014[a]	(Tenboer et al., 2014)
SR Ca^{2+}-ATPase	Oryctolagus cuniculus	4XOU	Membrane	2.8 Å	C121	162.00, 76.30, 151.10 90, 109, 90	0.304, 0.343	2015[a]	(Bublitz et al., 2015)
Angiotensin II receptor	Homo sapiens	4YAY	Membrane	2.9 Å	C121	72.80, 41.00, 167.70 90, 99.40, 90	0.228, 0.274	2015[a]	(Zhang et al., 2015)
Phycocyanin	Thermosynechococcus elongatus	4Z8K	Soluble	2.5 Å	P6$_3$	153.40, 153.40, 39.64 90, 90, 120	0.187, 0.255	2015[a]	(Conrad et al., 2015)
Luciferin regenerating enzyme	Photinus pyralis	5D9B	Soluble	1.5 Å	P2$_1$2$_1$2$_1$	186.38, 186.38, 60.34 90, 90, 120	0.184, 0.232	2015[b]	(Yamashita et al., 2015)
C-phycocyanin	Thermosynechococcus elongatus	4ZIZ	Soluble	1.75 Å	H32	109.24, 109.24, 452.64 90, 90, 90	0.204, 0.254	2015[a]	(Fromme et al., 2015)
Rhodopsin-arrestin complex	Homo sapiens	4ZWJ	Membrane, soluble	3.3 Å	P2$_1$2$_1$2$_1$	48.21, 77.59, 84.76 90, 90, 90	0.252, 0.293	2015[a]	(Kang et al., 2015)

[a] Denotes experiments done at LCLS.
[b] Denotes experiments done at SACLA.

measurement of high resolution diffraction signal from a single large protein complex. This can, in principle, be overcome by improving the XFEL peak intensity and using better focusing optics. Second, the dynamic range of the detectors presently used for single-particle imaging with XFELs is ~10^3. This has to be increased by at least 1-2 orders of magnitude. Finally, background free sample delivery is critical for single particle imaging with XFELs.

New future XFEL facilities such as the European XFEL will increase the repetition rate from 120 Hz to 27 kHz due to its superconducting linear accelerator (Altarelli M 2014). This will represent a significant increase of the pulse repetition rate available today. However, the pulses will not be evenly distributed over the time of 1 s but are delivered in form of ten 600 ms pulse trains (Allahgholi, Becker et al. 2015). This poses further challenges for sample injection as jets have to run very fast during the duration of the pulse train, whereas sample would run without interception with the X-rays in the time between the arrivals of the pulse trains. Sample delivery systems that could match these increased repetition rates are challenging. Neither current fixed target options nor viscous jets can match the increased data collection rates. At SLAC a new XFEL, LCLS II, is under development, which will operate in the low to medium energy regime (current planning includes a maximum energy of 5 keV), which will allow for data to be collected at repetition rates up to 1 MHz. Faster sample delivery injectors are presently under development to meet the needs of second-generation XFEL sources. Additionally, efficient diffraction-pattern screening algorithms and parallelized execution will be necessary to reduce the raw data stream into a more manageable set of data frames containing only diffraction patterns which have a high likelihood of being usable for indexing and intensity integration. This means that saving each and every frame for post analysis will no longer be practical and data reduction will have to be performed in real time. Developing programs further like Cheetah (Barty, Kirian et al. 2014) and CASS (Foucar 2012) to do both faster on-the-fly analysis would allow researchers to pass this information directly to indexing programs for auto-indexing on-the-fly without the need to save any intermediate data. Due to their effectiveness and high speed, Cheetah (Barty, Kirian et al. 2014) and CASS (Foucar 2012), have been demonstrated to be essential in the first stages of SFX data treatment.

To support next generation XFEL facilities, new features are continually under development to meet the constantly evolving needs of new experiments. In fact, while originally designed for implementation at LCLS, Cheetah has undergone several updates in the last year and a half and has now been implemented in serial millisecond crystallography experiments at

synchrotron sources (https://github.com/antonbarty/cheetah(Nogly P 2015)) and for SFX data collected at SACLA (https://github.com/biochem-fan/cheetah/ commits/online). In addition to Cheetah and CASS software, a new software system called Karabo is currently under development at the European XFEL. European users will have access to CrystFEL through Karabo to enable fast data analysis required by the immense data acquisition challenge.

With proof of principle experiments already displaying the breadth of the technique, it is clear that the future is not just bright but brilliant. As SFX emerges from its infancy, it is apparent that molecular movies will provide a bedrock for new advances and discoveries from structural biology, to medicine, to energy conversion.

2.4.4. ACKNOWLEDGEMENTS

2.5. MOTIVATION OF THIS DISSERTATION

This dissertation is focused on method development for serial crystallography (SX). In particular, it is focused on decreasing sample consumption for serial crystallography experiments as well as development of a model protein to further the technique of time-resolved diffusion based mixing experiments. SX represents a new technique where diffraction is collected from a new crystal with every X-ray pulse. Experiments specifically focusing on XFELs will be referred to as serial femtosecond crystallography (SFX) throughout while experiments specifically focusing on synchrotron data collection will be referred to as serial millisecond crystallography (SMX). The technique of SX is based upon delivering microcrystals to an X-ray beam. From this point forward in this dissertation, microcrystals will refer to crystals between 1-50 μms while nanocrystals will refer to crystals below 1 μm.

2.5.1. VISCOUS SAMPLE DELIVERY FOR MEMBRANE PROTEINS

Serial crystallography has proven to make a dramatic impact in the field of structural biology, however the large sample quantity currently required for this technique limits the macromolecules which can be probed and is a road-block for protein that can be produced only in small quantities. Viscous sample delivery with lipidic cubic phase (see section 2.2.3) has shown to drastically reduce sample consumption from milligrams (sometimes even grams) to micrograms of protein. The aim of this work was to develop a viscous, crystal delivery medium that would allow for crystals grown via vapor diffusion, dialysis, etc. to be mixed with the agarose post-crystallization. The requirements for this medium were that it must compatible with both soluble and membrane proteins, has low background, is compatible with in atmosphere or in vacuum experiments, and would decrease sample consumption by at least ten fold. Chapter 3 discusses the development of agarose as a carrier medium for serial femtosecond crystallography experiments in vacuum. Chapter 4 discusses a poly ethylene oxide as a carrier medium for serial crystallography experiments in atmosphere, in particular for experiments performed at synchrotrons.

2.5.2. TIME-RESOLVED DIFFUSION MIXING

Although useful, the static structure of an enzyme in many cases does not explain its mechanism of action. A movie of an enzyme in motion however, would provide significantly more insights. By initiating a reaction and taking "snapshots" of the enzyme in motion, the snapshots can be assembled in sequence to a "molecular movie" of the enzyme dynamics in the reaction cycle. These "molecular movies" can help structural biologists to understand the enzymes function, for example trying to unravel how photosystem II splits water.

Before the birth of serial crystallography, time-resolved diffusion mixing experiments were limited to extremely slow enzymes in which enzyme turnover time exceeded minutes or alterations to the enzyme kinetics were required. Although snapshots could be captured, only one

state could be resolved at a time. Now with the advent of serial crystallography, several states can be captured making these molecular movies by substrate diffusion possible (as described in section 2.4.1.)

SFX allows for much smaller crystals, crystals >10 μm, to be suitable for X-ray structure determination. Due to their small size, the diffusion time of substrate into these microcrystals allows for time-resolved mixing experiments of the wild-type enzyme to be possible on a millisecond time scale opposed to minutes or even hours which are required for macrocrystals (discussed further in chapter 2). Achieving these short time points would be a large advancement in the field of structure determination and enzymology as it would allow for these molecular movies to be made in high resolution.

As a model system, 3-deoxy-D-manno-2-octulosonate-8-phosphate synthase (KDO8PS) was chosen to study time-resolved diffusion mixing as time-resolved electrospray ionization mass spectrometry experiments has already been studied for *E. coli* KDO8PS. Thus, this enzyme allows for comparison of time-resolved results across multiple techniques. Chapter 5 discusses purification, macro- and micro- crystallization of KDO8PS, and proposed time-resolved mixing experiments.
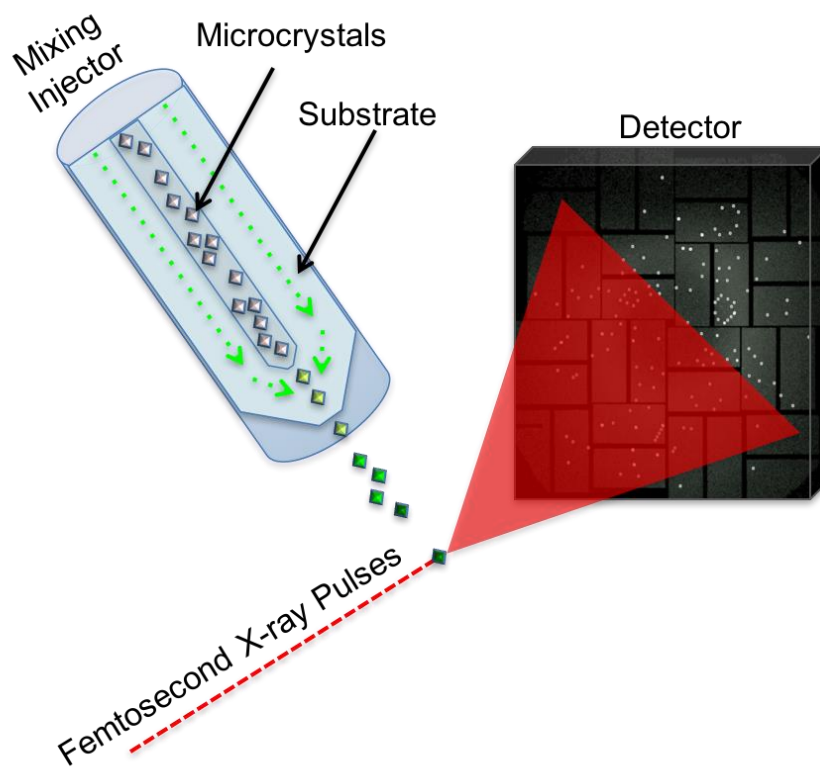
Figure 2.10 Diagram of time resolved diffusion triggered crystallography. Microcrystals are mixed with their substrate(s) at varying time points prior to diffraction.

CHAPTER 3

A NOVEL INERT CRYSTAL DELIVERY MEDIUM FOR SERIAL FEMTOSECOND CRYSTALLOGRAPHY

Chelsie E. Conrad,[a,b] Shibom Basu,[a,b] Daniel James,[b,c] Dingjie Wang,[c] Alexander Schaffer,[a,b] Shatabdi Roy-Chowdhury,[a,b] Nadia A. Zatsepin,[b,c] Andrew Aquila,[d] Jesse Coe,[a,b] Cornelius Gati,[e] Mark S. Hunter,[d] Jason E. Koglin,[d] Christopher Kupitz,[b,f] Garrett Nelson,[b,c] Ganesh Subramanian,[b,c] Thomas A. White,[e] Yun Zhao,[b,c] James Zook,[a,b] Sébastien Boutet,[d] Vadim Cherezov,[g] John C. H. Spence,[b,c] Raimund Fromme,[a,b] Uwe Weierstall[b,c], and Petra Fromme[a,b]*

a Department of Chemistry and Biochemistry, Arizona State University, PO Box 871604, Tempe, AZ 85287-1604, USA, b Center for Applied Structural Discovery, The Biodesign Institute, PO Box 875001, Tempe, AZ 85287-5001, USA, c Department of Physics, Arizona State University, PO Box 871604, Tempe, AZ 85287-1504, USA, d SLAC National Accelerator Laboratory, 2575 Sand Hill Road, Menlo Park, CA 94025, USA, e Center for Free-Electron Laser Science, Deutsches Elektronen-Synchrotron DESY, Notkestrasse 85, 22607 Hamburg, Germany, f Department of Physics, University of Wisconsin-Milwaukee, 1900 East Kenwood Boulevard, Milwaukee, WI 53211, USA, and g Bridge Institute, Department of Chemistry, University of Southern California, 3430 S. Vermont Avenue, Los Angeles, CA 90089, USA

This paper was published in IUCRJ under the same title in 2015. I developed the agarose technique and was awarded a 6 hour protein crystal screening beamtime at LCLS which allowed for the data collection of phycocyanin and photosystem II. During a collaborators beamtime, photosystem I was tested in atmosphere for a short period of time. The figures and texts have not been altered but the supplemental figures have been incorporated into the main body. Additionally, section 3.5 provides an update of improvements to the agarose delivery method.

Serial femtosecond crystallography (SFX) has opened a new era in crystallography by permitting nearly damage-free, room-temperature structure

determination of challenging proteins such as membrane proteins. In SFX, femtosecond X-ray free-electron laser pulses produce diffraction snapshots from nanocrystals and microcrystals delivered in a liquid jet, which leads to high protein consumption. A slow-moving stream of agarose has been developed as a new crystal delivery medium for SFX. It has low background scattering, is compatible with both soluble and membrane proteins, and can deliver the protein crystals at a wide range of temperatures down to 4ºC. Using this crystal laden agarose stream, the structure of a multi-subunit complex, phycocyanin, was solved to 2.5 Å resolution using 300 µg of microcrystals embedded into the agarose medium post-crystallization. The agarose delivery method reduces protein consumption by at least 100-fold and has the potential to be used for a diverse population of proteins, including membrane protein complexes.

3.1. INTRODUCTION

Serial femtosecond crystallography (SFX) is a novel structural biology technique that allows challenging protein structures to be solved from submicrometer/micrometer crystals at room temperature (Chapman, Fromme et al. 2011). In SFX, nanocrystals and/ or microcrystals are delivered in a liquid (DePonte, Weierstall et al. 2008) or a viscous stream (Weierstall, James et al. 2014) into the beam path of a hard X-ray free-electron laser (XFEL). XFEL radiation is composed of femtosecond pulses typically delivered at a rate of 1–120 Hz, and diffraction patterns are obtained before the crystals are destroyed (Neutze, Wouts et al. 2000, Barty, Caleman et al. 2012). SFX currently requires large data sets because the diffraction patterns are acquired from individual randomly oriented protein crystals. Most SFX experiments thus far have been based on protein crystals delivered using a gas dynamic virtual nozzle (GDVN), where the crystals are delivered to the X-ray beam in their mother liquor (DePonte, Weierstall et al. 2008). The gas focused GDVN liquid jet moves at a velocity of 10–20 m s^{-1}, which delivers crystals much faster than required to replenish the protein crystals between X-ray pulses at a pulse repetition rate of 120 Hz. Therefore, approximately only one out of every 10,000 crystals is probed by the X-ray pulses (Weierstall, James et al. 2014). This type of liquid jet can consume 10–100 mg of protein for the collection of a complete data set, which is particularly problematic for membrane proteins and other proteins that can only be produced in small amounts.

Membrane proteins are an important class of proteins that are of very high relevance in biology, compromising 60% of all current drug targets (Hopkins and Groom

2002). However, structure determination of membrane proteins lags far behind soluble protein structure determination, with less than 550 unique membrane protein structures determined so far out of over 100,000 structures currently deposited in the PDB. Membrane proteins are insoluble in water and therefore have to be extracted from the membrane in the form of protein–detergent micelles. Most membrane protein structures are obtained by either crystallization in solution in the form of protein–detergent micelles or crystallization in the lipidic environment of the lipidic cubic phase (LCP), a method for membrane protein crystallization pioneered by Landau & Rosenbusch (Landau and Rosenbusch 1996). LCP is a liquid crystalline phase that is spontaneously formed upon mixing monoacylglycerols (MAGs) and water, producing a continuous three-dimensional network of curved bilayers arranged into a cubic lattice with two networks of interconnecting continuous aqueous channels (Caffrey 2015). The architecture of the lipid formation encourages type 1 crystal packing and has similar properties to the native cell membrane (Caffrey 2015). Crystallization in LCP has been successful for structure determination of a wide range of membrane proteins, including microbial rhodopsins, photosynthetic complexes, β-barrels, enzymes, transporters, ion channels and especially G-protein-coupled receptors (GPCRs), a class of membrane proteins with high medicinal impact (Cherezov 2011). A new crystal delivery system has been developed for SFX which allows the delivery of crystals grown in LCP to the XFEL beam (Weierstall, James et al. 2014). The high viscosity of LCP results in a much slower flow rate of the stream, thus drastically decreasing the net mass of protein needed for structure determination by SFX. LCP as a delivery medium has been successfully used to determine GPCR structures using an XFEL (Liu, Wacker et al. 2013, Weierstall, James et al. 2014, Fenalti, Zatsepin et al. 2015, Zhang, Unal et al. 2015). Crystallization of membrane proteins in LCP has been highly optimized, contributing to the structures of over 60 unique membrane proteins to date (Caffrey and Cherezov 2009). However, it has been challenging to crystallize large multi-domain membrane complexes in LCP owing to the curvature associated with the lipid bilayer and the low diffusion constants of large membrane protein complexes in LCP. To date, the majority of membrane protein

structures solved by X-ray crystallography have been determined from crystals of protein–detergent micelles grown in solution, which have also been successfully used for SFX experiments (Chapman, Fromme et al. 2011, Aquila, Hunter et al. 2012, Johansson, Arnlund et al. 2012, Johansson, Arnlund et al. 2013, Kupitz, Basu et al. 2014). These membrane protein crystals were delivered either with the GDVN liquid injector (DePonte, Weierstall et al. 2008), requiring large amounts of protein, the gel injector (Weierstall, James et al. 2014) or an electrospinning injector (Sierra, Laksmono et al. 2012), which uses less protein but uses high electric fields which could be problematic for crystal stability.

To date, all membrane protein structures delivered in LCP for SFX (Liu, Wacker et al. 2013, Weierstall, James et al. 2014, Fenalti, Zatsepin et al. 2015, Zhang, Unal et al. 2015) have been based on crystals that were grown in LCP. Mixing of membrane protein crystals grown in the form of a protein–detergent micelle with LCP typically leads to dissolution of the crystals, very likely caused by partitioning of the detergent, which forms the protein–detergent micelle, into the lipidic phase. This leads to depletion of the detergent in the protein–detergent micelles in the crystals, resulting in denaturation of the protein. Recently, two other viscous media, a mineral oil-based grease and petroleum jelly, have been described as alternative crystal delivery carriers (Botha, Nass et al. 2015, Sugahara, Mizohata et al. 2015). The grease mixture (Sugahara, Mizohata et al. 2015) has been used to deliver crystals to the XFEL beam for SFX data collection of soluble model proteins at the SPring-8 Compact Free Electron Laser (SACLA XFEL), while petroleum jelly (Botha, Nass et al. 2015) has been used to deliver lysozyme at the Swiss Light Source (SLS). Both of these delivery methods have so far only been demonstrated at ambient pressure and they produce significant and undesirable Debye–Scherrer rings in the region of 3.77–5 Å. No results have been presented to date that show either medium to be suitable for the delivery of multi-protein complexes or membrane proteins. Thus, it is highly

desirable to develop an inert medium for the delivery of both soluble and membrane proteins to the XFEL beam at slow flow rates.

Here, we have explored and developed a new delivery medium for SFX based on agarose. Agarose is a versatile polysaccharide polymer. Extracted from seaweed, agarose dissolves in water at high temperatures (above 85°C) and forms a network of helical strands upon cooling, resulting in the formation of a gel material (Arnott, Fulmer et al. 1974). We show here that crystals grown via traditional crystallization methods (i.e. vapor diffusion and dialysis) can be embedded into agarose post-crystallization and prior to injection. Crystal delivery in agarose can be accomplished in an expansive temperature range from 4 to 30°C, allowing crystallization conditions over a wide range of temperatures to be compatible with crystal delivery. In contrast, Mebiol, a medium recently suggested as a viscous carrier by Botha et al. (Botha, Nass et al. 2015), is only viscous at temperatures above 25°C. We show here that crystals of complex membrane proteins such as the photosynthetic protein complexes photosystem I (PSI) and photosystem II (PSII) can be delivered in an agarose stream. Thus, agarose has the potential to be a general crystal delivery medium for SFX for both soluble and membrane proteins.

To test whether agarose could be used to deliver crystals of large, multi-protein complexes, phycocyanin (PC) was chosen as a model system. PC is a cyanobacterial antennae protein, part of the light-harvesting complex, which channels excitation energy to PSII, subsequently driving charge separation across the thylakoid membrane, the membrane that contains PSI and PSII. The PC complex forms a disc-like trimer in which each monomer is composed of two subunits, α and β (Schirmer, Bode et al. 1985).

3.2. MATERIALS AND METHODS

3.2.1. PROTEIN PURIFICATION AND CRYSTALLIZATION

PC was isolated from *Thermosynechococcus elongatus*. Briefly, the protein was obtained by disrupting a concentrated suspension of cells using a microfluidizer at 124

MPa. The resulting suspension was further purified by ultracentrifugation at 50,000xg for 1 h, in which large particles and aggregates were separated from the supernatant. The supernatant was then concentrated using Amicon Ultra-15 spin filters (Millipore, 100 kDa cutoff), in which most small cytosolic proteins are separated as they flow through the filters. PC was crystallized by free interface diffusion as described by Kupitz et al. (Kupitz, Grotjohann et al. 2014) for PSII (Saridakis and Chayen 2003). The precipitant solution consisting of 1.0 M ammonium sulfate, 40 mM 2-(Nmorpholino)ethanesulfonic acid (MES) pH 6.4 was added dropwise at 1 µL/s to an equal volume of protein solution (15 mg/mL). Crystals of 1–5 µm in size formed after 1 d and were confirmed via second-order nonlinear imaging of chiral crystals (Wampler, Kissick et al. 2008). Prior to embedding the crystals in the agarose medium, the crystals were filtered through a 10 µm stainless-steel filter.

PSI was isolated and purified in principle as described by Fromme & Witt (Fromme and Witt 1998) and Hunter & Fromme (Hunter and Fromme 2011) using crystallization at low ionic strength as the last purification step. The crystals were stabilized in a low ionic strength buffer that consisted of 5 mM MES pH 6.4, 0.02% β-dodecylmaltoside (β-DDM). PSII was isolated and purified as described by Kupitz et al. (Kupitz, Grotjohann et al. 2014). The concentrated protein was subjected to a series of batch crystallization steps with decreasing concentrations of precipitant, as described in Kupitz et al. (Kupitz, Grotjohann et al. 2014). The crystals were permitted to grow for 24 h and crystal growth was then terminated by the removal of the supernatant and the addition of buffer containing low salt (100 mM 1,4-piperazinediethanesulfonic acid pH 7.0, 5 mM $CaCl_2$, 10 mM tocopherol, 20% PEG 2000).

3.2.2 PREPARATION OF THE AGAROSE AND EMBEDDING OF CRYSTALS INTO THE VISCOUS MEDIUM

After a broad screening and optimization process, a solution of 5.6% (w/v) agarose and 30% glycerol was determined to form the most stable extrusion stream. In order to

obtain these conditions after mixing, 7% (w/v) ultralow-gelling temperature agarose (Sigma–Aldrich, catalog No. A5030) was dissolved in a solution of 30% glycerol and the crystallization buffer in a 15 mL centrifuge tube and submerged in a water bath filled with boiling water for 30 min. To draw up the agarose into a 100 µL syringe (Hamilton, Model 1710), the syringe was warmed by drawing up and quickly ejecting boiling water 10–15 times (to ensure the integrity of the syringe, we avoided dipping more than the needle in solutions at temperatures higher than 80°C). The agarose was then drawn up from a 15 mL centrifugation tube that remained submerged in the water bath. For PC, the agarose was dissolved in 600 mL glycerol and 1.4 mL of a solution consisting of 15% PEG 2000, 30 mM MgCl2, 75 mM HEPES pH 7.0. For PSII, the agarose was dissolved in 600 mL glycerol and 1.4 mL 100 mM PIPES pH 7.0, 5 mM CaCl2, 16% (w/w) PEG 2000. For PSI, the agarose was dissolved in 1.4 mL 5 mM MES pH 6.4, 0.02% -DDM, 600 mL 2.0 M sucrose. In the case of data collected at helium ambient pressure, 2 mL 5 mM MES pH 6.4, 0.02% -DDM was used. 20 µL of the boiling hot agarose solution pertaining to the protein system was drawn up into a syringe. The agarose was allowed to equilibrate to room temperature for approximately 20 min before 5 µL protein crystals were mixed throughout the agarose using a syringe coupler(Cheng, Hummel et al. 1998); at least 40 syringe-mixing exchanges were performed or until the crystals were visually homogenously distributed in the agarose medium (Figure 3.1).

3.2.3. DATA COLLECTION

Data were collected using the CXI instrument at the Linac Coherent Light Source at SLAC (Boutet and Williams 2010). A continuous stream of agarose with crystals embedded
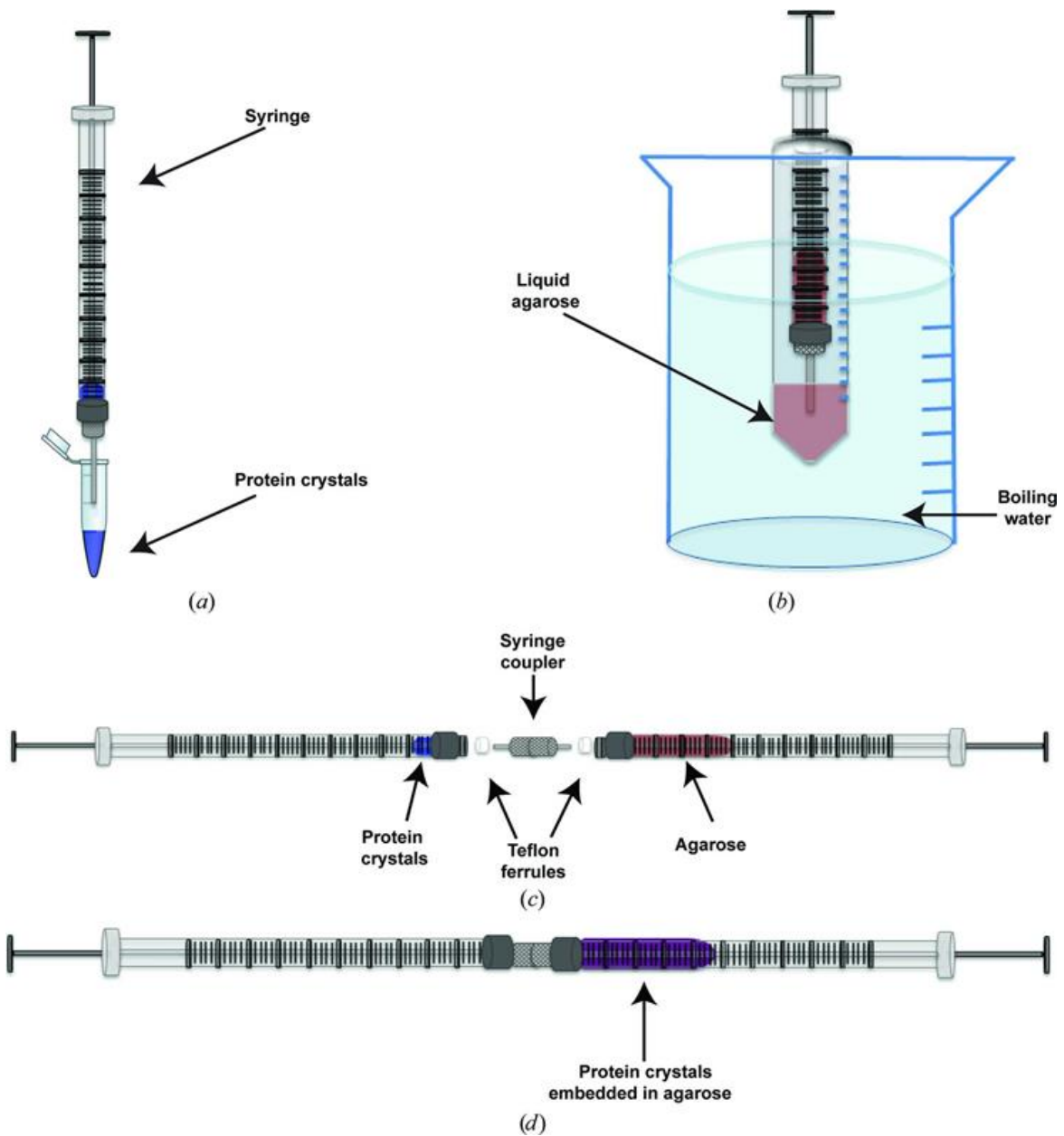
Figure 3.1 Diagram showing how crystals are embedded into the agarose medium. (a) A dense pellet of crystals is drawn up into a syringe, (b) the agarose solutions (contained in a 15 mL centrifuge tube) is submerged in boiling water until the agarose dissolves, the liquid agarose is drawn up into a warmed syringe and the agarose is allowed to gel and equilibrate to room temperature, (c) the protein crystals and agarose syringes are connected by a syringe coupler and (d) using the syringe coupler, the crystals are embedded throughout the agarose by moving the plungers back and forth.

64

was extruded from a 50 μm capillary into the X-ray interaction region using the LCP injector (Weierstall, James et al. 2014) at a flow rate of 160 nL/ min .

3.2.4. DATA PROCESSING

During 6 h of protein crystal screening experiments at LCLS, diffraction patterns were collected from different protein crystals (PC, PSI and PSII). PC was chosen as a model system and a complete data set was collected from PC crystals delivered in agarose medium in ~72 min. The 513,848 detector readouts were background-corrected and the hits were filtered out using Cheetah (Barty, Kirian et al. 2014), yielding 41,100 diffraction patterns that contained 25 or more Bragg spots (an average hit rate of 8%) see Figure 3.2. 14,143 patterns were indexed (i.e. an indexing yield of 34%) and integrated using CrystFEL (Kirian, White et al. 2011, White, Barty et al. 2013) with a hexagonal lattice type with unit-cell parameters a = b = 153.4, c = 39.6 Å (see Table 1). The merohedral space group of the crystals, P63, exhibited an indexing ambiguity which was resolved by ambigator, an implementation within CrystFEL of an algorithm related to that described by Brehm & Diederichs (Brehm and Diederichs 2014). We decided on a resolution cutoff at 2.5 Å based on the multiplicity and the CC* value (see Table 1) (Karplus and Diederichs 2012). The merged data set (truncated at 2.5 Å resolution) was phased by molecular replacement (MR) using phenix.phaser (McCoy 2007) with PDB entry 4gy3 as the search model (after removing waters and ligands). The MR model was first refined using a segmented rigid-body protocol in which each subunit was considered as a rigid entity using phenix.refine. A total of ten cycles of positional, individual B factor refinement, including two cycles of simulated-annealing refinement, were then performed. In this step, water molecules were added and refined using phenix.refine at 2.5 Å resolution. The refined structure resulted in an R_{work} of 18.7% and an R_{free} of 25.5% (see Tables 3.1 and 3.2). In order to demonstrate that agarose is a suitable delivery medium for SFX data collection from soluble proteins and various membrane proteins, we have also provided diffraction patterns from PSI and PSII (see Figures 3.3 and 3.4).

Table 3.1 Phycocyanin delivered in agarose data statistics. Values in parentheses are for the highest shell.

Wavelength (Å)	1.33
Space group	$P6_3$
Resolution (Å)	29.5–2.5 (2.55–2.50)
Unit-cell parameters (Å, °)	$a = b = 153.4$, $c = 39.6$, $\alpha = \beta = 90$, $\gamma = 120$
No. of crystal hits	41100
No. of indexed patterns	14143
Duration of data collection (min)	72
Unique reflections	18908
Reflections used in refinement	18871
$\langle I/\sigma(I)\rangle$	3.2 (0.83)
Multiplicity	250.67 (12.5)
CC*	0.971 (0.487)
R_{work}/R_{free} (%)	18.7 (32.7)/25.5 (35.5)
Completeness (%)	99.82
Average B factor (Å^2)	38.34

Table 3.2 Data quality statistics for phycocyanin delivered in agarose.

Resolution (Å)	#Reflections	#Measurement	Multiplicity	Completeness (%)	CC*	SNR* (CrystFEL)
11.04	1013	1154949	1140.1	100.00	0.989	7.90
5.99	980	636800	649.8	100.00	0.981	5.67
5.02	959	558792	582.7	100.00	0.983	6.00
4.48	950	517920	545.2	100.00	0.983	6.37
4.11	939	422140	449.6	100.00	0.978	5.87
3.85	951	322650	339.3	100.00	0.976	5.01
3.64	952	264625	278.0	100.00	0.969	4.36
3.47	931	211411	227.1	100.00	0.959	3.81
3.33	951	145805	153.3	100.00	0.956	2.88
3.20	940	100473	106.9	100.00	0.907	2.45
3.10	925	85798	92.8	100.00	0.876	2.11
3.01	970	77473	79.9	100.00	0.894	1.86
2.92	911	59827	65.7	100.00	0.866	1.55
2.85	933	48409	51.9	100.00	0.802	1.43
2.78	965	39337	40.8	100.00	0.802	1.26
2.72	898	27798	31.0	100.00	0.737	1.12
2.67	924	21450	23.2	100.00	0.603	0.99
2.61	942	17822	18.9	100.00	0.574	0.82
2.57	947	14732	15.6	100.00	0.640	0.80
2.52	927	11574	12.5	100.00	0.487	0.83
Overall	**18,908**	**473,9785**	**250.67**	**100.0**	**0.971**	**3.19**
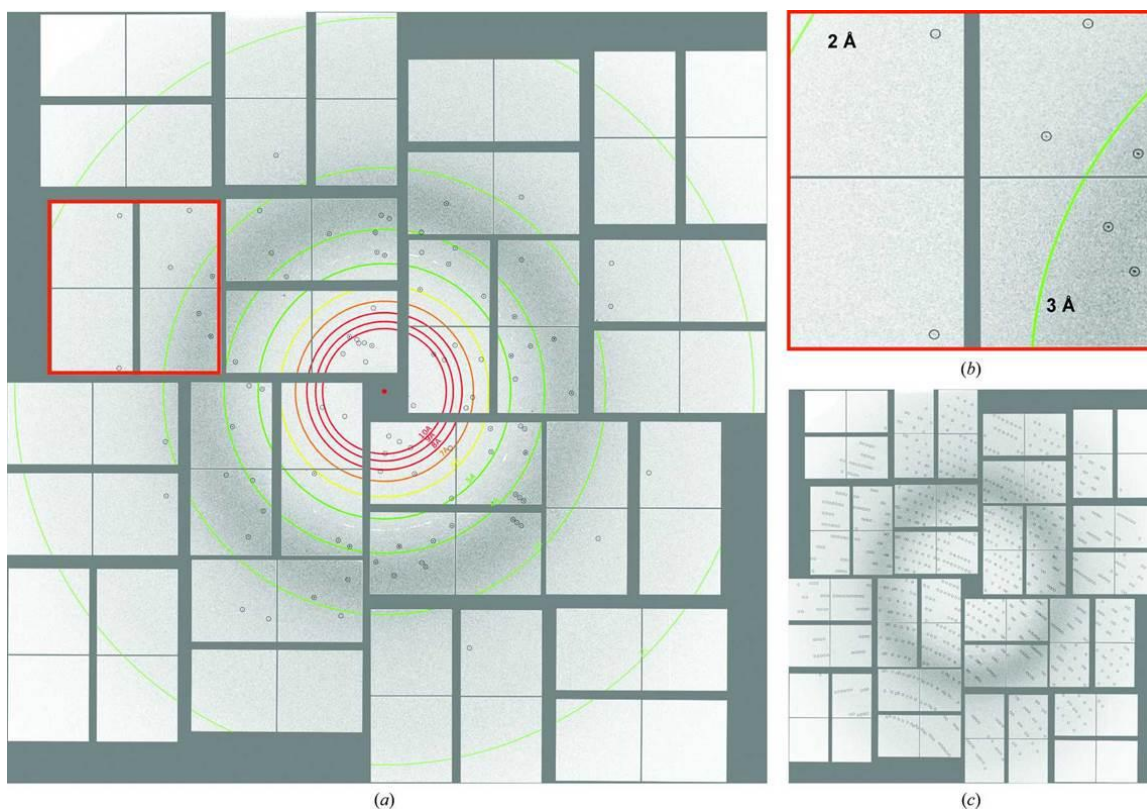
Figure 3.2 Single diffraction pattern of PC in agarose measured using the CXI at LCLS, with the red box magnified in (b) and predicted peak positions circled after indexing with CrystFEL (c).
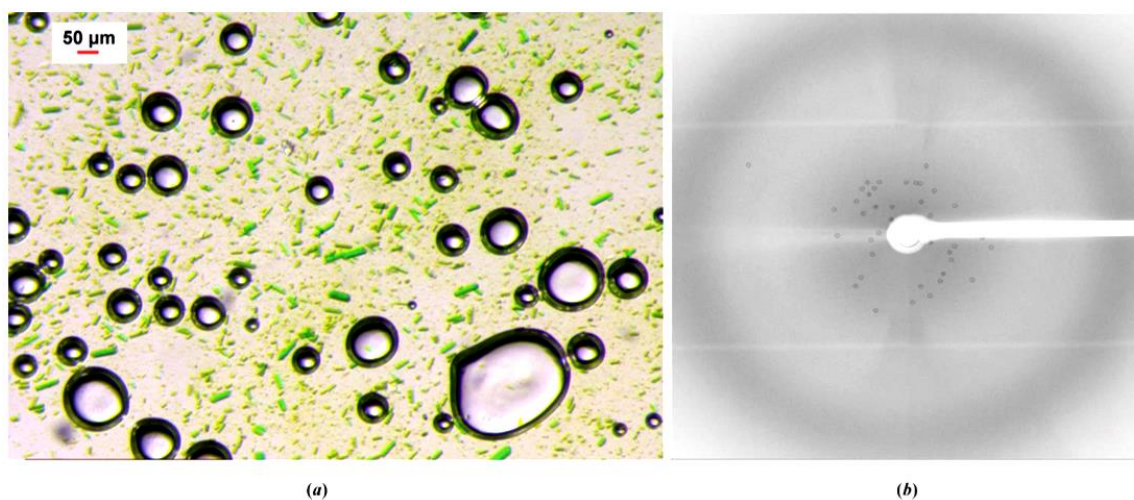
Figure 3.3 PSI embedded in agarose and delivered in a helium atmosphere. (a) Rod –like PSI crystals embedded in agarose, (b) diffraction pattern from PSI microcrystal in agarose.
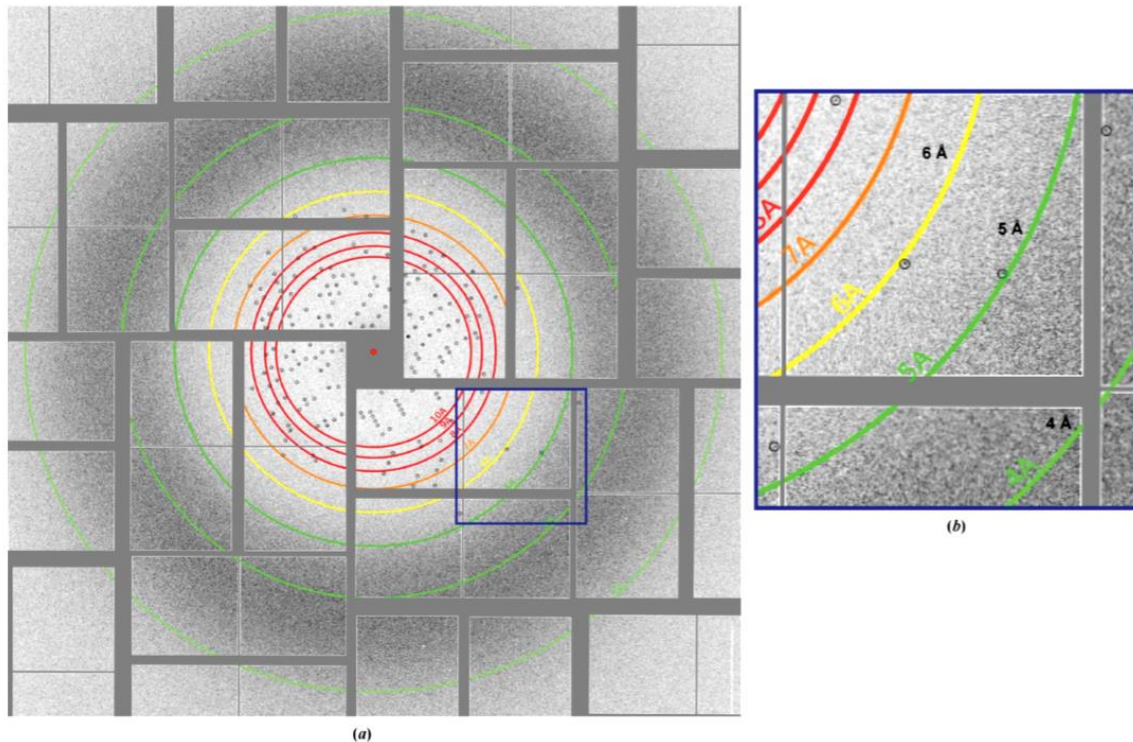
Figure 3.4 PSII embedded in agarose and delivered in a vacuum chamber. (a) Diffraction pattern from PSII in agarose, (b) magnified subset from (a).

3.2.5. RESULTS AND DISCUSSION

For a viscous medium to be suitable for SFX, three primary requirements must be met: the medium must maintain crystal integrity, must form a stable and continuous stream and the diffraction from the medium should produce minimal background scattering. Several viscous media were tested in order to investigate their potential as a general viscous, non-Newtonian, carrying medium, including tapioca corn starch, gelatin, silica hydrogel, polyacrylamide, polyvinyl alcohol and poly(ethylene oxide). None of these media established stable streams. Initial tests using agarose as a crystal delivery medium showed signs of dehydration in vacuum, leading to the formation of ice as detected by X-ray diffraction. To prevent freezing, we tested several potential cryoprotectants for crystal delivery in high vacuum. From those screened, we narrowed our selection to glycerol, which also increased the viscosity of the agarose stream, a welcome side effect that makes extrusion more reliable. Different concentrations of agarose and glycerol

were screened to optimize the extrusion conditions and 5.6% agarose dissolved in 30% glycerol was found to be the most suitable medium because it formed a stable, continuous stream and no ice-crystal diffraction artefacts were observed (Figure 3.5).

The next challenge was to explore the best way to embed the crystals into the agarose. We explored three ways to embed the crystals into the agarose medium: (i) the growth of crystals in agarose, (ii) simple manual mixing on a glass slide (as has been used for the oil-based grease method (Sugahara, Mizohata et al. 2015)) and (Maune, Han et al.) the use of a syringe setup (Figure 3.1), which was originally developed for the crystallization of proteins in LCP (Cheng, Hummel et al. 1998, Caffrey and Cherezov 2009). The growth of crystals in agarose has been described in the literature as a method to slow down crystal growth and to counteract effects such as sedimentation and convection that influence the crystallization process under gravity (Biertumpfel, Basquin et al. 2002). We first investigated the growth of PC crystals in agarose. Owing to the large size of PC, its diffusion constant is very low and crystal growth in agarose is very slow, leading to the formation of few nuclei. Furthermore, no nucleation occurred in agarose in the presence of 30% glycerol even at very high protein concentrations (>20 mg/mL). Although PC could not be crystallized directly in the gel owing to its large size and low diffusion constant, other proteins might be suitable for crystal formation inside the agarose gel as demonstrated previously (García-Ruiz, Novella et al. 2001, Lorber, Sauter et al. 2009).

While the growth of crystals of PC in agarose was very difficult, we succeeded in embedding pre-grown crystals into the agarose medium (Figures 3.1 and 3.6), which allowed a full SFX data set to be collected from PC crystals delivered in agarose. The mixing of pre-formed crystals is therefore suggested as the preferred method of crystal delivery in the agarose stream, as it does not depend on the size of the protein and allows pre-grown crystals to be delivered to the XFEL beam. However, simple mixing of crystals
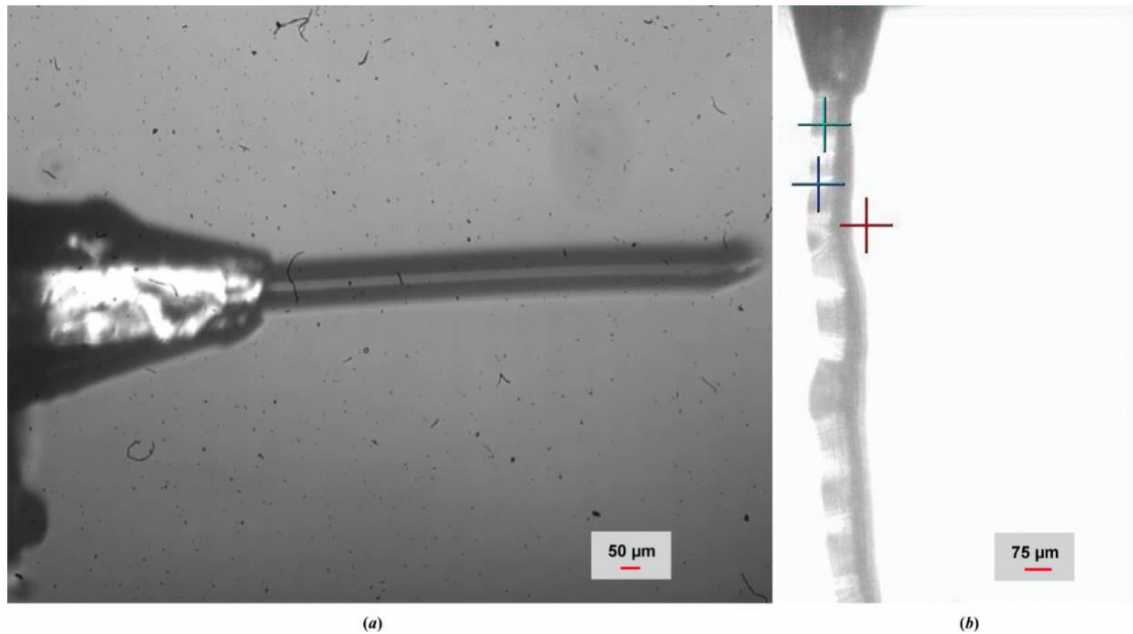
Figure 3.5 Agarose stream extrusion. (a) Agarose stream with no embedded crystals extruded in vacuum in a test chamber (b) agarose stream with embedded crystals extruded in a vacuum in the CXI chamber.

with agarose leads to an inhomogeneous distribution of crystals and further problems, including partial drying of crystals, the formation of crystals of salt or other precipitants and the loss of protein crystals during transfer to the injector crystal reservoir. We have therefore adapted the LCP syringe setup for embedding crystals into the agarose medium, as shown in Figure 3.1. In order to stabilize the crystals, the agarose solution was prepared in the crystallization buffer corresponding to each of the proteins. The agarose was dissolved by vortex mixing the mother liquor and glycerol (for sample delivery in vacuum) with the agarose powder in a 15 mL centrifuge tube. The tube was then submerged in a water bath of boiling water for approximately 30 min. A syringe was then warmed by drawing up boiling water from the water bath all the way through the syringe and quickly ejecting it 10–15 times. With the centrifuge tube submerged in boiling water, 20 µL agarose was drawn up into the heated syringe and allowed to cool to ambient temperature. A second syringe was filled with 5 mL of the highly concentrated PC crystal suspension (ideally 10^{11} crystals/mL) in the crystallization mother liquor (the same mother liquor as

70

used in the agarose preparation). The desired high crystal densities can be achieved by either sedimentation or low-speed centrifugation of the crystal suspensions prior to mixing with the agarose medium.

After the agarose had entered the gel phase in the syringe, the syringes containing agarose and the protein crystals were connected using a syringe coupler (Figure 3.1; Cheng et al., 1998). The crystals were then embedded into the agarose by alternate movement of the two plungers, whereby the solutions moved back and forth between the two syringes at least 40 times, leading to the embedding of the crystals in the agarose medium at a crystal density of 2 x 10^{10} crystals/mL (Figure 3.6). Owing to the dilution caused by mixing of the agarose medium with the crystal suspension,
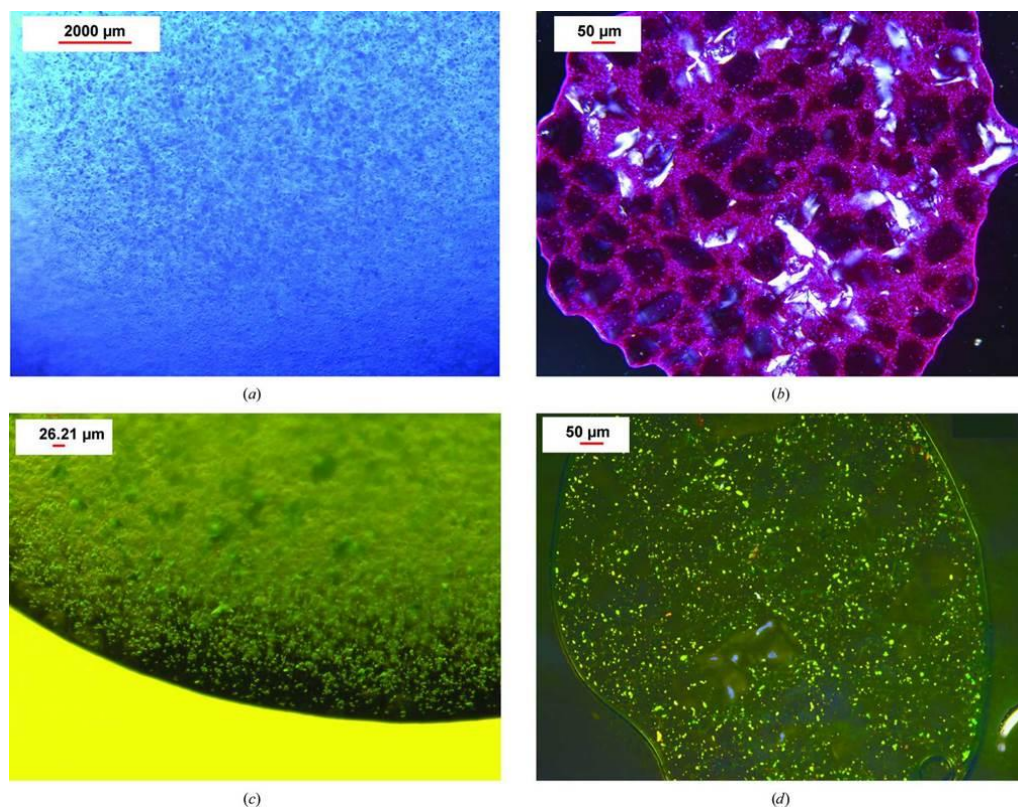
Figure 3.6 Protein crystals before and after mixing with agarose. (a) PC microcrystals, (b) PC crystals after mixing with agarose (birefrigent), (c) PSII microcrystals (birefrigent), (d) PSII crystals after mixing with agarose (birefrigent).

the medium becomes less viscous, and the initial percentage of agarose must be increased to compensate for the dilution. Thus, the initial agarose concentration was increased to 7% agarose in order to achieve a final concentration of 5.6% after mixing with the crystals. We used the same procedure of embedding crystals of soluble model proteins such as lysozyme and the large protein–cofactor complex PC, as well as one of the largest and most complex membrane protein complexes that have been crystallized so far: PSII (a dimer of 700 kDa containing 38 protein subunits and more than 100 cofactors). Pictures of the different crystals embedded in agarose are shown in Figures 3.3, 3.6, and 3.7. A large variety of different precipitants commonly used for crystallization are compatible with the agarose medium, including high salt concentrations as well as polyethylene glycols (PEGs). Examples include 1 M NaCl, 1.25 M ammonium sulfate, 0.2 M $CaCl_2$ and a large range of PEGs commonly used for crystallization (PEG 400– 8000 at a concentration of up to 30%). The stability of the agarose-based stream is a function of its specific viscoelastic and surface-tension properties; notable variations were observed over the range of protein crystal compositions tested. The most stable stream was achieved with protein crystals that contained high-molecular-weight PEGs (>2000) as the precipitant. Furthermore, agarose is also compatible with organic precipitants such as 2-methyl-2,4-pentanediol (MPD). Dissolving the agarose in different precipitants in some cases decreased the viscosity. In these cases, the agarose concentration was adjusted to 9%, which increased the viscosity and the ability to form a stable stream. An especially challenging case for crystal delivery in agarose was the large membrane protein complex.

PSI (a trimer of 1,080 kDa containing 36 protein subunits and more than 300 noncovalently bound cofactors), which crystallizes at low ionic strength without the addition of any salt or precipitant (Jordan, Fromme et al. 2001, Chapman, Fromme et al. 2011, Hunter and Fromme 2011) (the final crystallization buffer contained only 5 mM 2-(N-morpholino) ethanesulfonic acid (MES) pH 6.4 and 0.02% β-dodecylmaltoside (β-DDM) detergent). PSI crystals dissolve in the presence of glycerol or salt and do not tolerate the
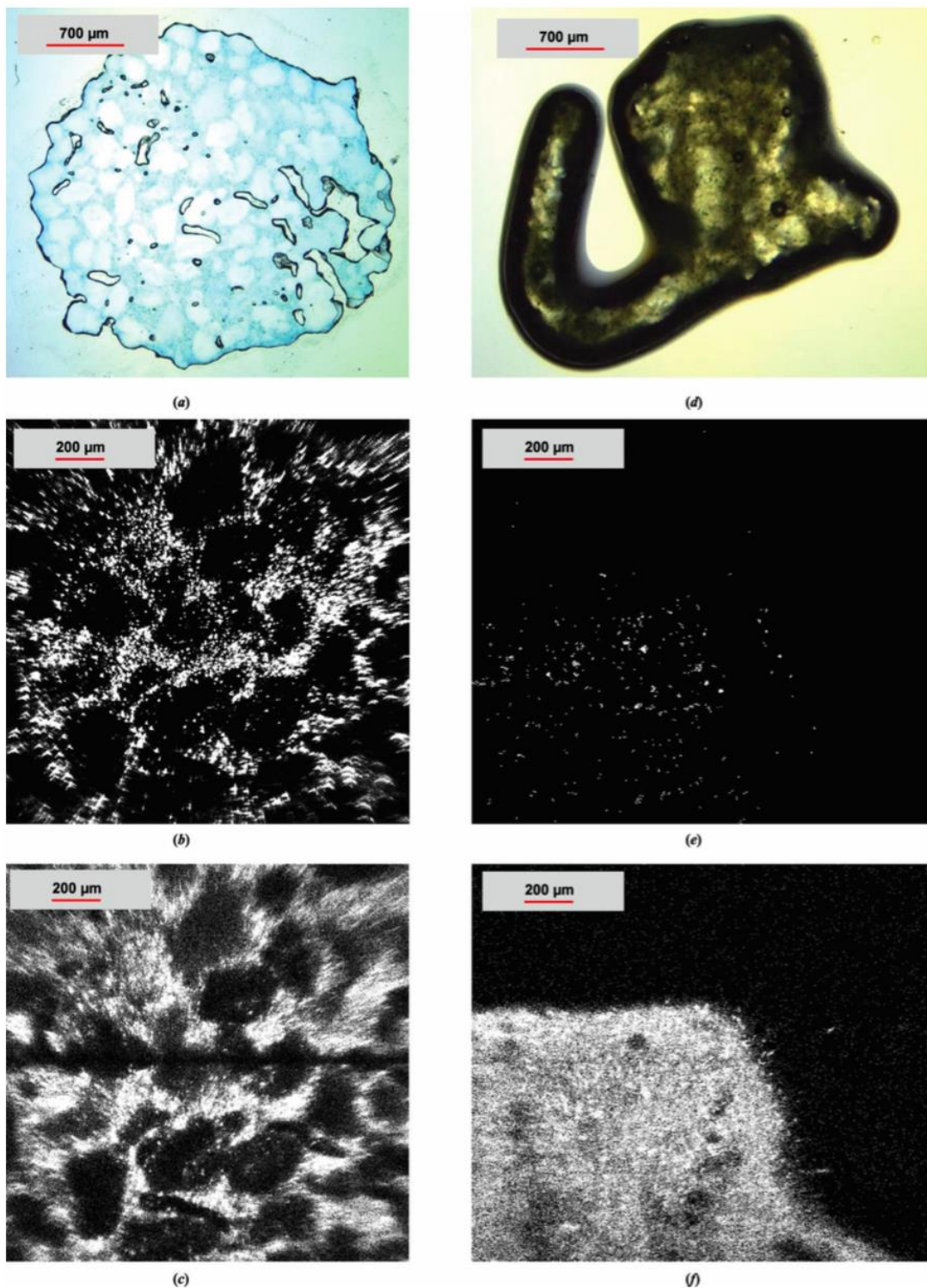
Figure 3.7 Characterization of PC and PSII embedded in agarose. (a) Brightfield of PC (b) second order non-linear imagine of chiral crystals of PC (c) ultraviolet two-photon excited fluorescence of PC microcrystals (d) brightfield of PSII (e) second order non-linear imaging of chiral crystals of PSII (f) ultraviolet two-photon excited fluorescence of PSII.

addition of any organic solvents or PEGs. To prevent the freezing of the PSI crystals in the agarose stream in high vacuum, we stabilized the PSI crystals by embedding them in agarose prepared with the PSI crystallization buffer and with 0.6 M sucrose. After optimization of the crystallization buffer, PSI crystals could be embedded into agarose and delivered to the XFEL beam in agarose with suitable crystal delivery stream stability using the crystallization buffer with sucrose described above in 9% agarose.

The agarose stream was tested using the Coherent X-ray Imaging (CXI) instrument at the Linac Coherent Light Source (LCLS) at the SLAC National Accelerator Laboratory in the vacuum-chamber setup (Boutet, Lomb et al. 2012) used for most of the SFX experiments published to date. Most of the SFX data were collected in the vacuum chamber, except for PSI, where the data shown in Figure 3.3 were collected in a new ambient-pressure setup with a helium environment. The advantage of using an ambient-pressure setup is that freezing by evaporative cooling is avoided. At ambient pressure cryoprotectant is not essential as dehydration occurs much more slowly than in vacuum.

The agarose stream relies on a high-velocity inert-gas (nitrogen) sheath to center and stabilize the emerging crystal jet extrusion (Weierstall, James et al. 2014) . This stability is required in order to reliably align the agarose stream with the XFEL beam axis. We observed a higher stability of the stream in vacuum compared with the ambient-pressure setup in the helium atmosphere. The lower stability of the atmospheric pressure is presumably owing to a turbulent boundary layer at the interface between the inert-gas sheath stream and the surrounding ambient-pressure inert gas. Furthermore, the background is higher in the He atmosphere compared with the vacuum setup. For these reasons, vacuum operation of the stream is preferred when freezing can be avoided by the addition of PEG, glycerol or other cryoprotectants. SFX data for PC and PSII were collected using the vacuum-chamber setup and SFX data for PSI and PSII were collected using the helium ambient-pressure setup. Figure 3.8 shows a comparison of the X-ray scattering from the agarose stream compared with the LCP stream. We calculated the average scattered

74

intensity from each medium delivered in a stream of the same width (50 µm) using detector-readout events that contained no crystal diffraction. We analyzed 13,902 frames from the agarose stream data and 14,592 frames from the LCP stream data. Frames that contained no scattering from the jets/streams (owing to the jet/stream temporarily fluctuating out of the path of the X-rays) were easily recognized on the basis of their very low photon counts (~10–20 detector units) and were excluded from the mean background calculation, leaving 9,147 and 8,326 frames with scattering from the LCP and agarose jets,
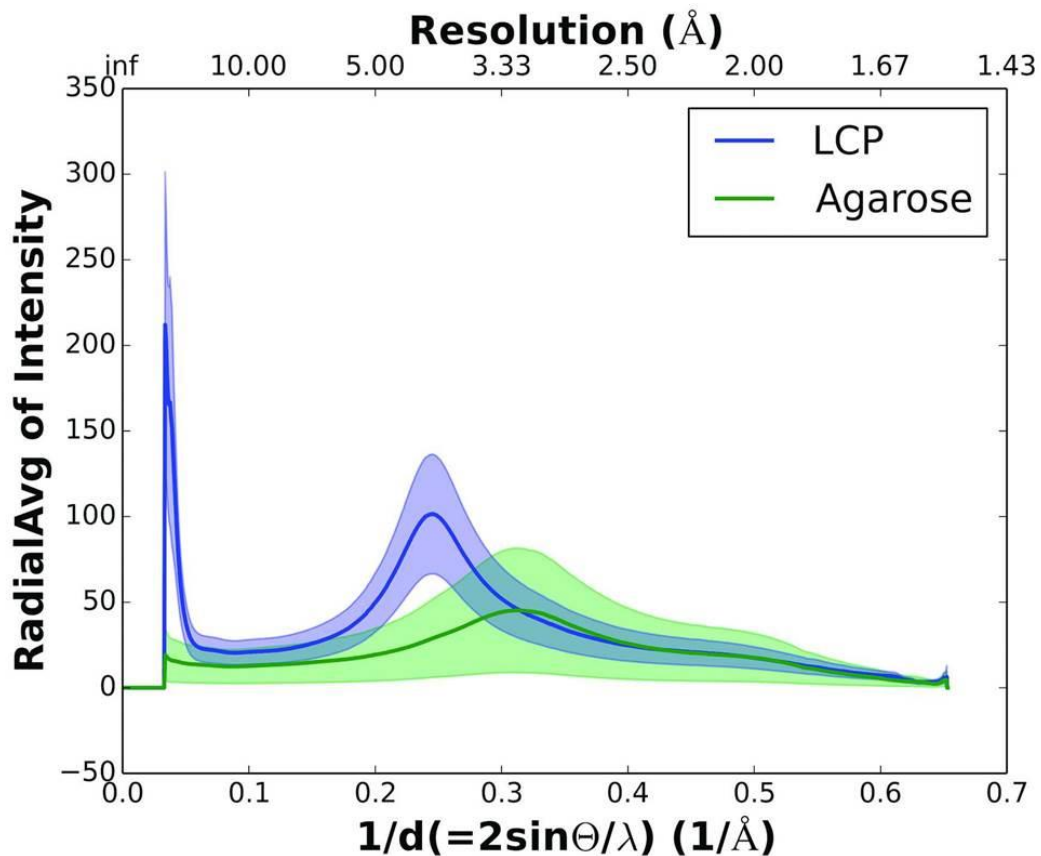
Figure 3.8 Diffuse background scattering comparison between agarose and LCP. 1/d (x axis) is plotted against the mean radial intensity over the total number of frames used from each medium (y axis). The blue line represents the mean radial intensity for LCP medium as a function of 1/d (or resolution in Å on the second x axis). The green line represents the mean radial intensity for agarose as a function of 1/d. The error or fluctuation in the radial intensity is quantified using the mean absolute deviation for both media, which is shown as a transparent region.

75

respectively. Thereby, bias from large jet/stream flow instabilities was avoided in the calculation of the mean radial intensities for each medium. To reduce the influence of shot-to-shot variations in the XFEL pulse intensities, each frame was scaled to the readings from the gas-ionization detector upstream of the vacuum chamber at the CXI. Finally, the mean radial intensities from the LCP and agarose jets were scaled to be equal at a resolution of 2 Å, where neither medium should produce a background signal. As shown in Figure 3.8, a broad peak corresponding to diffuse scattering from the lipid chains of LCP can be seen at 4.5 Å resolution. Diffuse scattering from agarose can be seen in the 3.3 Å region. The gray regions represent the mean absolute deviation around the mean. Overall, the background scattering from the agarose medium is roughly 2.3 times less than that from LCP in the diffuse-ring regions. Furthermore, LCP scatters strongly at very low resolution (>30 Å), while the low-angle scattering is very low in the agarose medium owing to the lack of long-range order and thus is ideal for large unit cells (Lawrence, Conrad et al. 2015). Indeed, LCP (Liu, Wacker et al. 2013, Weierstall, James et al. 2014), mineral oil-based grease (Sugahara, Mizohata et al. 2015) and petroleum jelly (Botha, Nass et al. 2015) all result in higher background scattering than agarose, especially at low resolution (below ~ 30 Å). Each of the media also produces diffuse scattering and/or Debye–Scherrer rings at 4–5 Å for LCP, 4–5 and 14 Å for mineral oil-based grease and 4.2 and 3.77 Å for petroleum jelly. The low background of agarose is not surprising considering that it is composed of 93% water and only 7% agarose, compared with 50% water and 50% lipids in LCP and 100% oil in grease or petroleum jelly.

The time available for data collection was limited to 4 h of protein crystal screening beamtime at LCLS. A full data set for PC crystals was collected using the vacuum setup at CXI (Figure 3.9) during this time as well as a brief test run on PSII crystals. In addition, data were collected from PSII and PSI during short test runs using the ambient-pressure setup (Figures 3 and 4). These complexes were chosen to demonstrate that agarose is an

excellent carrier medium that can be used for SFX data collection from even the largest protein complexes containing non-covalently bound cofactors (Figures 3.3 and 3.4). The statistics of the PC data set are shown in Table 1. In 72 min of data collection, we collected 41,100 crystal hits from PC, of which 14,143 could be indexed in a hexagonal lattice with unit-cell parameters a = b = 153.4, c = 39.6 Å. A high multiplicity is essential for the determination of accurate structure factors by Monte Carlo integration (Kirian, Wang et al. 2010) to average out the fluctuating parameters such as pulse intensity, partiality of reflections and crystal size distribution. The PC data set showed a high overall multiplicity of 250.6 and a multiplicity of 12.5 in the highest resolution shell (2.63– 2.5 Å). The structure was solved using molecular replacement and the structure was refined with final values of R_{work} = 18.7% and R_{free} = 25.2% (see Table 3.1). Figure 3.9 shows the electron density map for the loops and side chains from subunit (cyan) and subunit (Banerjee, Bartesaghi et al.), as well as a detailed view of phycocyanobilin, the chromophore of PC.

3.3. CONCLUSION

In comparison to the commonly used GDVN liquid jet, which consumes protein crystal suspension at 10–25 mL/min, the agarose delivery method presented here delivers protein crystals at a flow rate of only 160 nL/min, reducing net protein consumption by two orders of magnitude. We have shown that the agarose medium might be suitable as a general delivery system for SFX of both soluble and membrane protein crystals and that it is compatible with a wide range of crystallization conditions as well as temperatures. The agarose jet can be used both in vacuum and at ambient pressure; so far, the stream has displayed better stability in vacuum. The agarose medium features lower X-ray scattering background compared with LCP or other viscous crystal delivery media such as mineral oil-based grease and petroleum jelly, especially at low resolution. Thus, agarose is an ideal SFX crystal delivery medium for protein crystals with large unit cells and medium-to-low resolution limits. The agarose delivery system is a low-cost, readily available medium for sample delivery of crystals of soluble and membrane protein complexes and is compatible
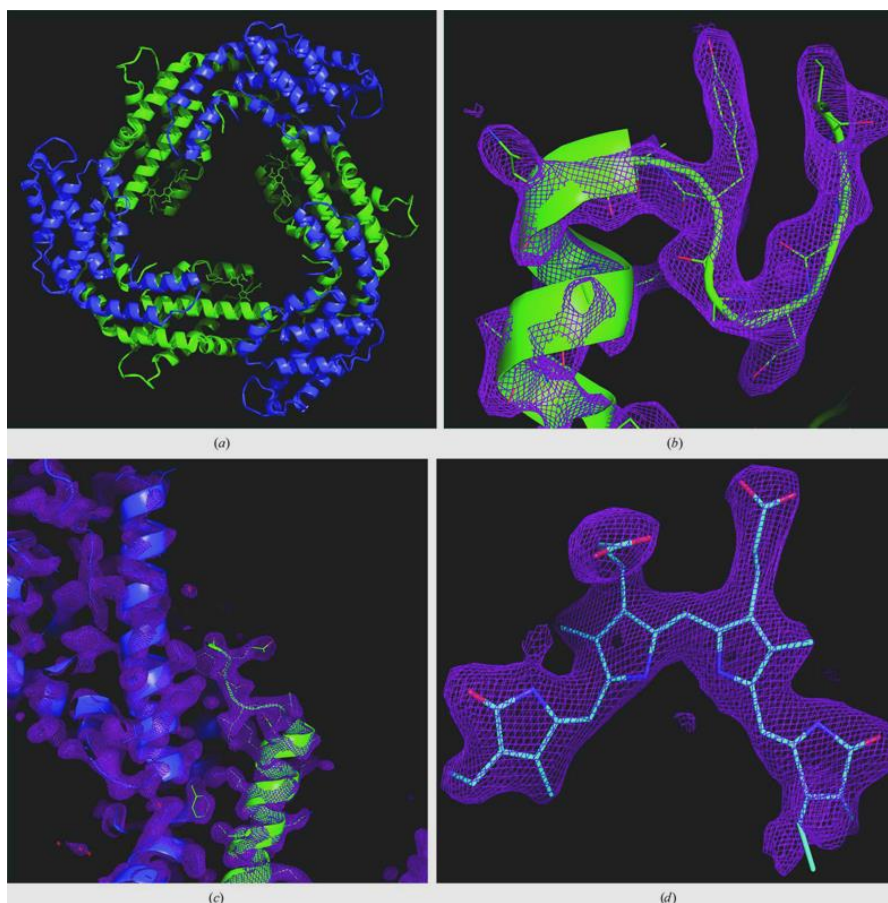
Figure 3.9 $2F_o - F_c$ electron-density maps of PC. (a) PC trimer composed of two subunits, α (blue) and β (Banerjee, Bartesaghi et al.), (b) an α-helix and loop from the α subunit contoured at 2.0σ, (c) α-helices from both subunits at 1.5σ and (d) the chromophore of PC at 1.5σ.

with most commonly used precipitants, including various PEGs as well as high-salt conditions. Here, we have demonstrated that crystals can be embedded into the agarose medium post-crystallization. Furthermore, low sample consumption extends the SFX method towards protein complexes that are difficult to express and isolate in large amounts. Thus, this technique will allow structures of scarce proteins and systems that are difficult to crystallize in large quantities to be investigated by serial femtosecond crystallography.

3.4. ACKNOWLEDGEMENTS

3.5. AGAROSE AS A GENERAL DELIVERY SYSTEM

Since the first proof of principle experiments, published in Conrad et al. 2015 agarose technique, developed in this thesis has applied to a wide variety of macromolecule crystal systems including ribose nucleic acids, whole viruses, insect cells containing *in vivo* grown crystals, and additional soluble and membrane proteins (Figure 3.10). Thus the agarose jetting system in this thesis has been quickly established as a general delivery system for a wide range of macromolecule crystals.

3.6. NEW DEVELOPMENTS OF THE AGAROSE DELIVERY METHOD

While the agarose jetting system has been accepted and is widely used now as a delivery system for soluble and membrane protein crystals for SFX data collection, some technical challenges remain which we have solved these challenges by further technique development. Depending on the mother liquor used to dissolve the agarose, large bubbles can be prevalent and cause the agarose stream to be discontinuous leading to variation in solvent background, decrease in hit rate, and to increase deposition of agarose material on the nozzle

that leads to freezing. Two methods were developed to remove the air bubbles resulting from vortexing and boiling of the agarose. The first method aims to degas the molten agarose using a vacuum pump. To do this, a custom aluminum block was made to fully surround a 50 mL centrifuge tube, the centrifuge tube was then connected to a vacuum pump by attaching a Millipore Steriflip filter unit (Figure 3.11). 5 mL of agarose is then prepared (as described in Conrad 2015). After the agarose melted and a solution is formed by heating the 50 mL centrifuge in the heat block, the solution was vortexed until homogenous. The vacuum was then turned on for 5 seconds. This short amount of time sufficiently removed large bubbles and greatly reduced the total number of bubbles. Although some bubbles remained, longer vacuum exposure times could not be used as they resulted in dehydration of the agarose and reduced the total volume. It

Francisella Tularenfis Schus4 Flpp3 *

In Vivo Grown µNS-GFP Crystals □

Bovine Cyctochrome C Oxidase ◊

Sindbis Virus ○

Adenine Riboswitch Aptamer Domain ∆

Adenosine-monophosphate activated protein kinase *
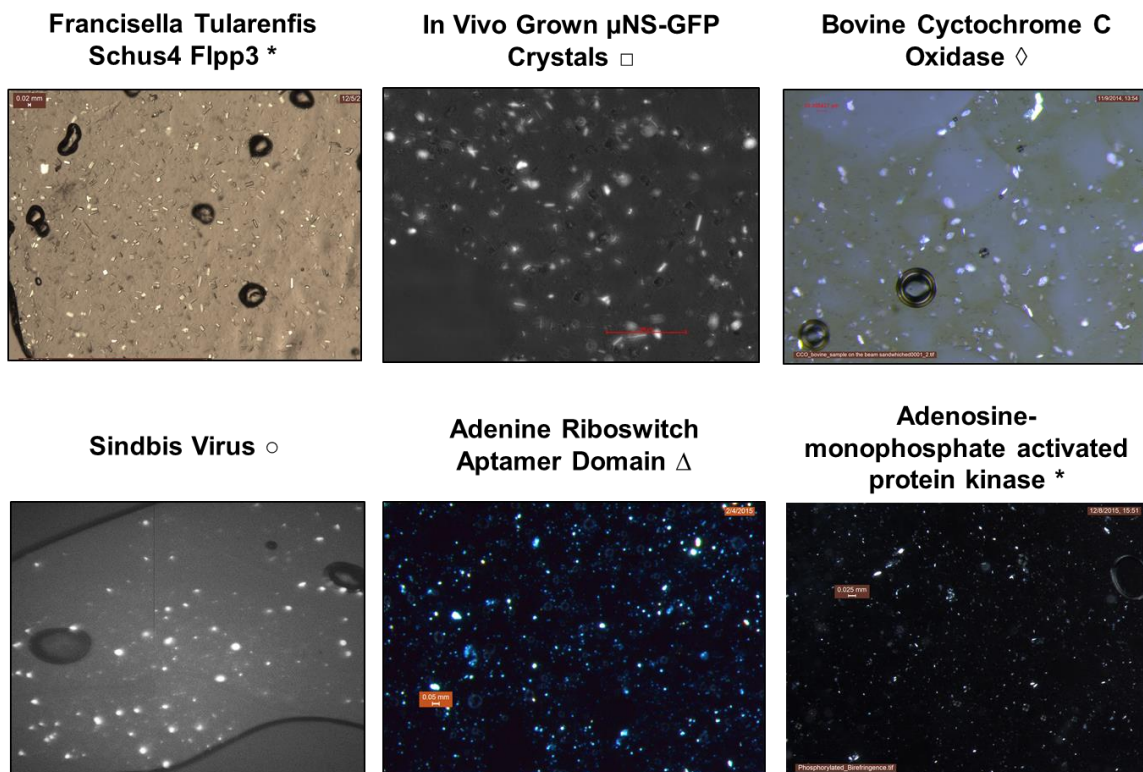
Figure 3.10 Additional crystal systems that have been mixed with agarose. * denotes soluble proteins, □ denotes insect cells with in vivo grown crystals, ◊ denotes membrane protein, ○ denotes virus crystals, and ∆ denotes ribose nucleic acid crystals.

is also important to note that stable agarose extrusions were difficult to reproduce. One 5 mL agarose batch would behave differently from another degassed batch. For some batches the extrusion was stable for hours at a time but other batches would constantly form buildup around the nozzle tip. The exact reasons why the results are inconsistent remain unknown. Thus, this degassing can be beneficial but other variables with degassing and extruding the degassed agarose need to be explored further. The second method is to centrifuge the molten agarose (1 mL volume) at 13.7k rpm for 2 minutes at 25°C. After centrifugation, the agarose solution gels but all visible bubbles are removed. Thus centrifugation worked surprisingly well at removing bubbles and did not result in agarose dehydration.

Figure 3.11 Agarose degassing system. 5 mL of agarose is dissolved by heating the solution at ~95°C in a 50 mL centrifuge tube with the standard cap attached, the falcon tube is removed several times for vortexing and placed back inside the heat block. The cap is then removed and a Millipore Steriflip unit is attached, an additional 50 mL centrifuge tube is attached to other side of the Steriflip (not shown) to create a seal and Tygon tubing is attached to both the Steriflip unit and the vacuum pump. The vacuum pump is then turned on for 5 seconds and then the agarose is harvested as described in (Conrad 2015).

3.7. ELECTROSPINNING INJECTION OF AGAROSE

As described earlier, agarose delivery should ideally be performed in vacuum, mainly because peripheral stream dehydration is necessary for a stable stream to form and thus allow for optimal SFX data collection. In atmosphere, the agarose just not form a stable jet and instead drips off the nozzle tip. This is most likely because some dehydration is necessary to form a jet. The ability to form a stable stream in atmosphere would allow the benefits of agarose to be extended to experiments performed in atmosphere at XFELs (such as the macromolecular femtosecond crystallography beamline at LCLS). It would also enable SMX data collection at synchrotrons. Prior, the high viscosity injector has been employed to extrude the agarose jet. This injector was originally developed for LCP which requires much higher pressures (30-100 psi) for this viscous medium to extrude to form when compared to the agarose (1-8 psi). Thus it is possible that other injection systems may better suit the different properties of the agarose jet. As an alternative injection method, an experiment was done where electrospinning was coupled with our media where crystals were embedded in agarose. Electrospinning (Sierra Laksmono et al. 2012), as described in chapter 2. Section 3.3, uses an applied electric current (not hydraulics or gas) to create a microjet (Figure 3.12). For this experiment, a 250 μL Hamilton gas-tight syringe was coupled to a 1 meter capillary via a green sleeve to which 10 kV was applied at the tip of the capillary (Figure 3.13). A Taylor cone was observed, which a typical characteristic of an electrospinning microjet (Yarin, Koombhongse et al. 2001).This injector test was done in a laboratory and thus no X-rays were available but diffraction of crystals embedded in agarose delivered by the electrospinning could easily be tested at a synchrotron in future.

The marriage of these two techniques allows for a continuous stream of agarose to be produced in air and vacuum (not shown) but also helps to prevent crystal settling and delays droplet formation, which are both common problems with the electrospray injection technique (Sierra Laksmono et al. 2012). It is important to note that high concentrations of agarose are not necessary (5.6-9% final concentration), instead a 3% final agarose concentration was found to be

optimal. Future experiments are needed to determine if the combination of electrospinning and agarose results in an increased background or may have detrimental effects on diffraction.
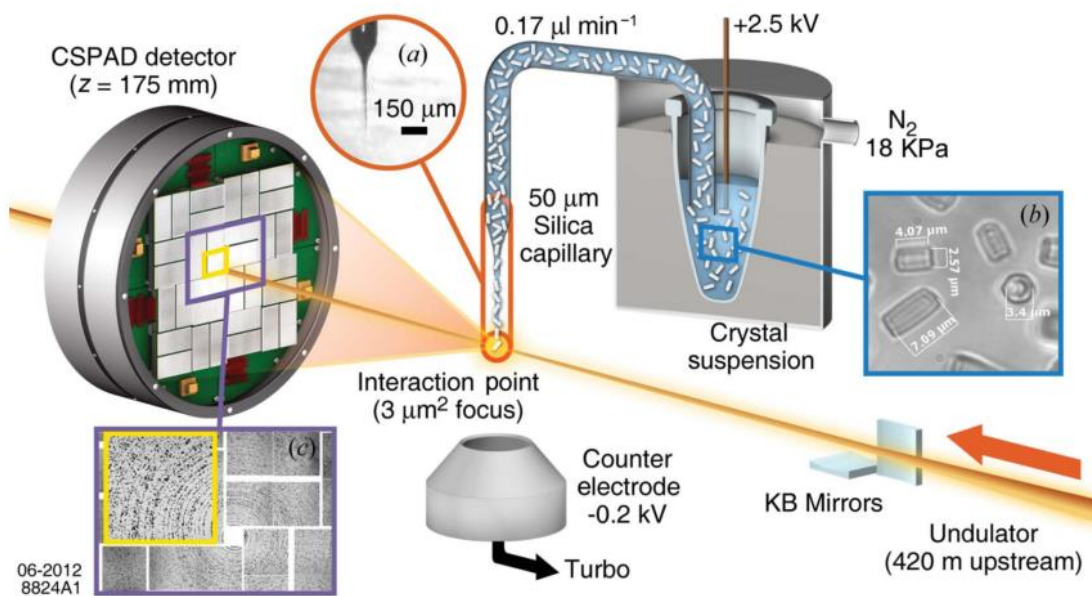
Figure 3.12 Electrospinning injector for SFX. This is a similar set as to what was used for the agarose elctrospinning experiment but the proof of principle experiment was done in lab and thus there were no X-rays. Additionally, instead of a capillary being placed in a 1.5 mL tube, a 250 μL gas tight Hamilton syringe was connected to a capillary via a green sleeve. Image reproduced with permission from (Sierra Laksmono et al. 2012).
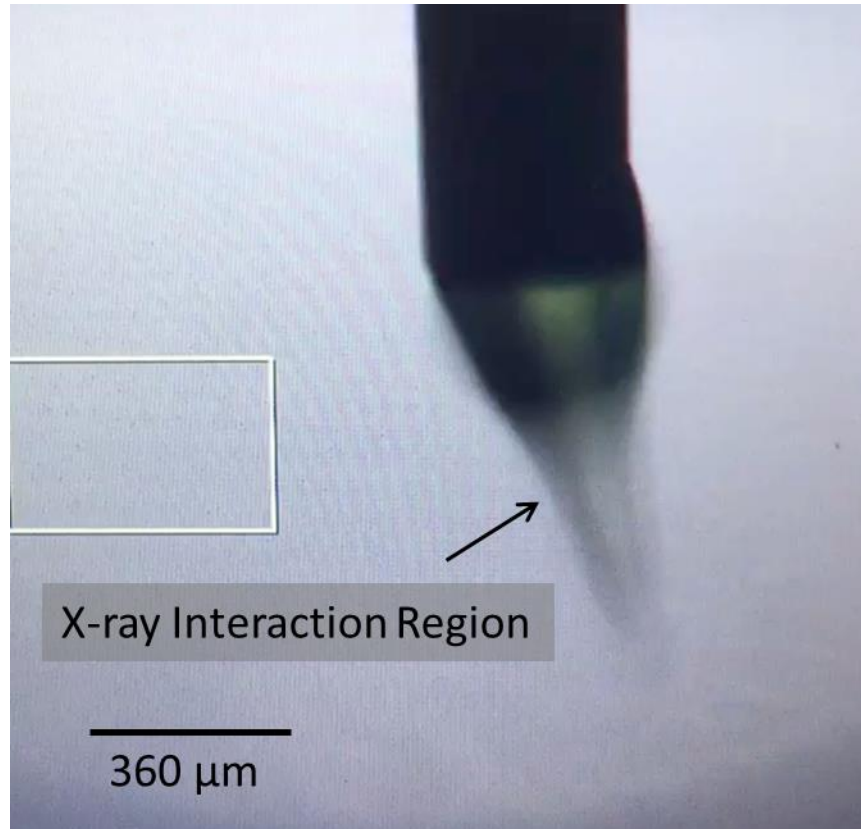
Figure 3.13 Electrospinning injection of agarose in air. 3% agarose embedded with PSI crystals shows a Taylor cone, a trait of materials being focused by the applied electric current. The PSI laden agarose was extruded through a capillary with an inner diameter of 250 µm and an outer diameter of 360 µm, 1 meter in length using an applied voltage of 10 kV.

CHAPTER 4

DECREASED SAMPLE VOLUME CONSUMPTION FOR SERIAL SYNCHROTRON CRYSTALLOGRAPHY USING HIGH MOLECULAR WEIGHT POLY(ETHYLENE OXIDE)

Chelsie E. Conrad[1,2], Jose Martin Garcia[1,2], Garret Nelson[1,3], Jesse Coe[1,2], Trent Engelman[3], Ganesh Subramaninan[1,3], Shatabdi Roy-Chowdhury[1,2], Dominik Oberthür[5], Kenneth Beyerlein[4], Joe Chen[1,3], Natasha Stander[1,3], Nadia A. Zatsepin[1,3], Thomas Grant[5], Marc Messershmidt[4], Anja Burkhardt[6], Pontus Fischer[6], Saravanan Panneerselvam[6], Olga Lorbeer[6], Craig Ogata[7], Robert Fischetti[7], Henry Chapman[5], Uwe Weierstall[1,3], John C.H. Spence[1,3], Petra Fromme[1,2]

Affiliations:
[1] Center for Applied Structural Discovery, the Biodesign Institute, Arizona State University. Tempe, AZ, USA, 85287-1604
[2] School of Molecular Sciences, Arizona State University, PO Box 871604, Tempe, AZ, USA 85287-1604
[3] Department of Physics, Arizona State University, PO Box 871604, Tempe, AZ, USA, 85287-1504
[4] Hauptman-Woodward Institute, State University of New York at Buffalo, 700 Ellicott Street, Buffalo, NY, USA,14203
[5] Center for Free-Electron Laser Science, Deutsches Elektronen-Synchrotron DESY, Notkestrasse 85, 22607 Hamburg, Germany
[6] PETRA III, Deutsches Elektronen-Synchrotron DESY, Notkestrasse 85, 22607 Hamburg, Germany
[7] Advanced Photon Source, Argonne National Laboratory, 9700 S. Cass Avenue, Argonne, IL, USA 60439

This is a manuscript will be combined with data collected using LCP as a crystal carrier, showing that both viscous media are amenable for serial millisecond crystallography at synchrotrons. Garrett Nelson originally proposed embedding crystals into high molecular weight poly(ethylene oxide) (PEO) as it had been successfully used as a carrier for an uncrystallized system. I characterized mixing, applied for the PETRA III beamtime, embedded PC in the PEO for the PETRA III beamtime, was involved in injection and sample preparation for the Advanced Photon Source beamtime which we collected data sets of phycocyanin and proteinase K, KDO8PS data. This chapter contains figures and portions of the manuscript being prepared for publication but only encompasses PEO. For this manuscript I participated in writing, figure making, and editing.

Experimental data collection at X-ray free electron lasers is limited for serial data collection but synchrotron sources are becoming viable options as a real alternative for serial millisecond crystallography (SMX) experiments. We have developed a viscous medium for decreasing sample consumption for SMX experiments for both soluble and potentially membrane proteins. Poly(ethylene oxide) molecular weight = 8,000,000 (PEO) was used to collected data sets of phycocyanin and proteinase K to a resolution of 3.0 Å and 2.65 Å, respectively. Additionally data was also collected on 3-deoxy-D-manno-2-octulosonate-8-phosphate-synthatse (KDO8PS). Preliminary data indicates that PEO may also be a suitable carrier for membrane proteins.

4.1. INTRODUCTION:

Serial crystallography (SX) experiments were originally developed out as a method to probe microcrystals with X-ray free electron lasers (XFEL) as each crystal is destroyed with every femtosecond XFEL X-ray pulse (Chapman, Fromme et al. 2011) . Although originally exclusively developed for XFEL data collection, SX data collection has been recently shown to be possible at synchrotron sources (Stellato, Oberthür et al. 2014, Nogly P 2015). Delivering crystals by SX provides the unique ability to probe very small crystals, sometimes better ordered crystals than larger crystals. These crystals that were previously unusable for X-ray structure determination as they are prone to radiation damage (Chapman, Fromme et al. 2011, Lyubimov, Murrary et al 2015, Stellato, Oberthür et al. 2014)). The serial method of data collection allows for small crystals to be measured at room temperature in their mother liquor without freezing artifacts (Chapman, Fromme et al. 2011). SX at synchrotron light sources, serial millisecond crystallography (SMX) allows for many of the same advantages of serial femtosecond crystallography without the disadvantage of very limited access to an XFEL sources.

XFEL experiments can produce diffraction from crystals as small as 200 nm in less than 50 fs (Hunter and Fromme 2011). The peak brilliance of an XFEL is orders of magnitude greater than 3rd generation synchrotron sources, thus synchrotrons require millisecond exposure times and micron sized crystals to produce quality diffraction (Stellato, Oberthür et al. 2014). Consequently, the work horse of XFEL SFX experiments, the gas dynamic virtual nozzle (GDVN) (DePonte, Weierstall et al. 2008), is not feasible for SMX experiments due to the speed at which the crystals are delivered (10-20 m s^{-1}). The millisecond exposure times also means the repetition rate is decreased (10 Hz compared to 60 (SACLA) or 120 Hz (LCLS)) and therefore the crystals are still prone to secondary radiation damage. One limitation of SX experiments in general is the large number of crystals needed to achieve a high redundancy of data (Fromme, Ishchenko et al. 2015). Thus, many proteins are currently unsuitable for this technique because they cannot be feasibly produced in large enough quantities.

To date, SMX data has been collected by flowing crystals through a capillary (Stellato, Oberthür et al. 2014), fixed target grids such as silicon and silicon nitride chips (Gati, Bourenkov et al. 2014, Murray, Lyubimov et al. 2015, Roedig, Vartiainen et al. 2015, Roedig, Duman et al. 2016), nylon loops (Gati, Bourenkov et al. 2014), and microfluidic devices (Heymann, Opthalage et al. 2014), extruding lipidic cubic phase (LCP) in which membrane proteins crystals were grown in (Nogly P 2015), or by mixing soluble proteins in grease (Botha, Nass et al. 2015). Delivering crystals through a capillary is undesirable as the X-rays heat the capillary over time which can destroy crystals upstream prior to interaction with X-rays. Fixed targets such a chips either have increased background (Murray, Lyubimov et al. 2015), cause the crystals to have a preferred orientation (Mueller, Marx et al. 2015), or require rastering (Gati, Bourenkov et al. 2014, Roedig, Duman et al. 2016). Where raster scanning entails manually searching for each small crystal. All of the chip methods require constant humidity on the chip or layers such nitride wafers to prevent drying which results in additional background (Roedig, Duman et al. 2016, Coquelle, Brewster et al. 2015). In contrast, slow moving streams of LCP or grease (0.5-1.44 mm s^{-1}, 0.1–0.3 mm s^{-1}, respectively) (Botha, Nass et al. 2015, Nogly P 2015) do not conduct heat to the same effect as the glass capillary. Furthermore data can be collected continuously without "hunting" for crystals and changing chips. However, LCP and grease have not been shown to be compatible with a wide range of proteins, notably membrane proteins crystallized *in surfo*. This is most likely due to the fact that mixing crystals with a detergent micelle into another detergent (LCP) results in the detergent being ripped from the protein as it embeds into the LCP, resulting in the crystals dissolving (Conrad, Basu 2015). Additionally, these media produce Debye-Sherrer rings which decrease signal to noise in characteristic radial regions, complicating analysis (Botha, Nass et al. 2015, Conrad, Basu et al. 2015, Sugahara, Mizohata et al. 2015).

Gel polymers of high molecular weight poly(ethylene oxide) (PEO) 8,000,000 as a viscous carrier medium have been explored to expand the available delivery techniques of SX for macromolecular crystals. Poly(ethylene glycol) (PEG) is a common precipitating agent used in protein crystallography. PEO has the same chemical composition as PEG but due to its high molecular weight it is referred to by a different name. Thus we hypothesized PEO to exhibit high

compatibility with a wide variety of protein crystal systems. Another benefit of the PEO system is low background as the main component of PEO gel is water (Conrad, Basu et al. 2015, Sugahara, Song et al. 2016). Phycocyanin (PC), The PC complex forms a disc-like trimer in which each monomer is composed of two subunits, α and β (Schirmer *et al.*, 1985). PC was chosen as a model system to explore the use of PEO jets for SMX as it has been used as a model system for SFX experiments (using LCP and the GDVN (Fromme, Ishchenko et al. 2015)). Proteinase K is an enzyme commercially available of 28.5 kDa that belongs to the serine proteases family, which has been used in numerous studies to identify disorder regions in intrinsically disordered proteins (IDPs) (Denning, Patel et al. 2003, Nyarko, Hare et al. 2004, Marin and Ott 2012, Martin-Garcia, Hansen et al. 2014). As an additionally system, 3-deoxy-D-manno-2-octulosonate-8-phosphate synthase (KDO8PS), an enzyme involved in the synthesis of the outer membrane in gram-negative bacteria (Levin and Racker 1959), was also mixed with PEO. Photosystem I, a large membrane protein, was also used to demonstrate the possibility of using PEO to deliver membrane proteins.

4.2. MATERIALS AND METHODS

4.2.1 PROTEIN CRYSTALLIZATION AND EMBEDMENT IN PEO MEDIUM

PC was isolated and crystallized as described in Fromme 2015 (Fromme, Ishchenko et al. 2015). PSI was purified and crystallized as described in Fromme & Witt 1998 (Fromme and Witt 1998) and Hunter & Fromme 2011 (Hunter and Fromme 2011) the final purification step for PSI was achieved by crystallization at low ionic strength. All of the crystals were gently centrifuged at 1,000xg for 5 minutes in order to pellet the crystals. The majority of the supernatant was then removed and the pellet was resuspended to form a concentrated suspension of crystals. Proteinase K (No. P2308, Sigma) was crystallized using batch method by mixing equal volumes of a protein solution at 40 mg·mL^{-1} in 20 mM MES pH 6.5 and a precipitant solution composed of 0.1 M MES pH 6.5, 0.5 M sodium nitrate, 0.1 M calcium chloride. Crystals between 5 and 10 μm in size appeared after 20 min incubation at 20 °C.

KDO8PS was overexpressed and treated as described in Ray P. 1980 (Ray 1980) with the following modifications. All buffers contained 2 mM 2-mercaptoethanol. The pellets were resuspended in a buffer containing 20 mM Tris pH 7.3, 300 mM potassium chloride, 1 SIGMAFAST protease inhibitor cocktail tablet (EDTA-free), and 10 mg/1 g cell pellet lyophilized lysozyme, from chicken egg white. After suspension, the cells were incubated in the lysis buffer for 30 minutes at room temperature and then incubated on ice for 20 minutes. The cells were broken using a sonicator with a microtip at 50% power, 10 second pulses for 6 cycles totaling 1 minute with a 30 second incubation on ice in between each cycle. In addition to the 2.2% protamine sulfate, 20 mM Tris pH 5, 300 mM potassium chloride, and 1 SIGMAFAST protease inhibitor cocktail tablet (EDTA-free). The supernatant was not adjusted to pH 5 and was not centrifuged an additional time prior to dialysis. The dialysis buffer was composed of 5 mM potassium phosphate pH 7.3, 75 mM potassium chloride pH and was changed once after 4 hours. The dialyzed enzyme preparation was then centrifuged at 7,000xg at 4 °C for 10 minutes to remove precipitated proteins. The supernatant was then filtered through a 0.22 µm filter and then applied to an anion exchange column (900 mm x 16 mm column packed with DEAE-Sepharose) equilibrated with 75 mM potassium chloride, 20 mM Tris pH 7.3, 2 mM 2-mercaptoethanol. The column was washed with 240 mL of the equilibration buffer and then potassium chloride was increased to 115 mM in a step gradient to elute the protein. Cubic KDO8PS 10-15 µm cubic microcrystals of KDO8PS were grown by free interface diffusion as described by Kupitz et al. (Kupitz, Grotjohann et al. 2014) by dropping 30 µLs of 16% poly(ethylene glycol) methyl ether (PEGME) 5,000 and into 30 µLs into 21 mg/mL KDO8PS. A 13% w/v PEO gel was prepared by inserting a weighed amount of poly(ethylene oxide) molecular weight = 8,000,000 (Sigma-Aldrich) into the back end of a 250 µL syringe (Hamilton part #7657-01) with a ferrule in place and parafilm covering the removable needle end. Then the crystal mother liquor (75 mM HEPES pH 7, 20 mM MgCl2, 17% PEG 3350 for PC, 10% poly(ethylene-glycol) methyl ether 5,000 for KDO8PS, 0.1 M MES pH 6.5, 0.5 M sodium nitrate, 0.1 M calcium chloride for proteinase K, and 5 mM MES pH 6.4, 0.02% ß-dodecylmaltoside) for PSI, was added
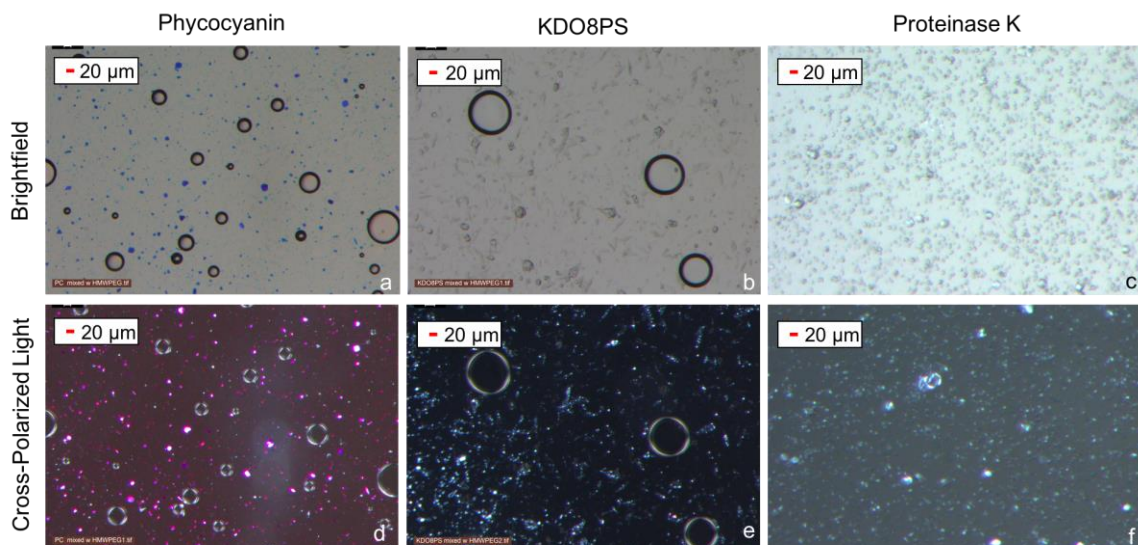
Figure 4.1 Protein crystals mixed with PEO a) PC brightfield b) KDO8PS brightfield c) Proteinase K brightfield d) PC polarized light e) KDO8PS polarized light f) Proteinase K polarized light.

to the back end of the syringe using a pipette. Then the plunger was inserted, the syringe was flipped upside down so that the plunger faced towards the ground and the plunger was moved up and down to remove air. Once the initial suspension was achieved, a 100 µL syringe (Hamilton part #7656-01) was connected to the 250 µL syringe via a syringe coupler (Cheng, Hummel et al. 1998) and the PEO solution was then homogenized by pushing the plungers of both syringes back and forth. A 4:1 volumetric ratio of the PEO gel and concentrated crystals were then mixed by oscillation of the crystals and gel through a syringe coupler (Cheng, Hummel et al. 1998) at a rate of approximately 0.5 oscillation/second (to avoid damage from mechanical heating) until homogeneity was achieved. Figure 4.1 shows each system after being mixed with the PEO with brightfield and under cross polarized light. Additionally, PC, proteinase K, and PSI after mixing were characterized by ultraviolet two-photon excited fluorescence and second-order nonlinear imaging (SONICC) (Kissick, Wanapun et al. 2011) (Figure 4.2). KDO8PS contains no tryptophan and thus does not show tryptophan fluorescence, additionally the high symmetry likely inhibits signal from SONICC.

4.2.2 DATA COLLECTION

In situ serial data collection was performed at the GM/CA 23-ID-D beamline at the 3rd generation synchrotron source, the Advanced Photon Source (APS), at the Argonne National Laboratory (Chicago, IL, USA). The GM/CA beamline is equipped with quad-mini-beam collimators that provide high intensity micron diameter beams between 5 and 20 microns with a scatter guard aperture (Fischetti, et al., 2009; Sanishvili et al., 2008). It also counts with sophisticated software
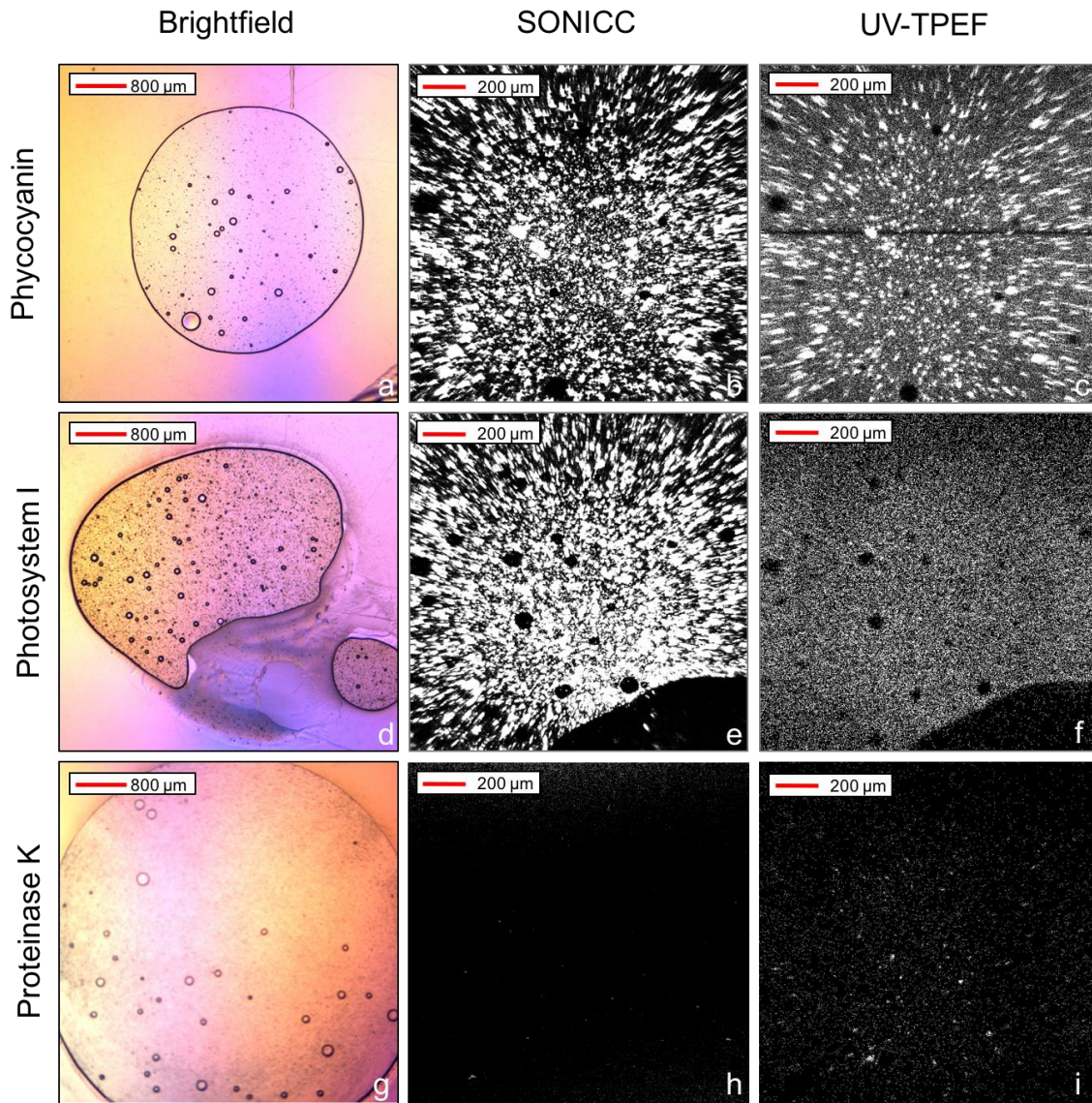
Figure 4.2 Characterization of crystals mixed with PEO a) PC brightfield b) PC SONICC c) PC ultraviolet two-photon excited fluorescence d) PSI brightfield e) PSI SONICC f) PSI ultraviolet two-photon excited fluorescence g) proteinase K brightfield h) proteinase K SONICC i) proteinase k two-photon excited fluorescence.

tools (JBluce-EPICS GUI) to allow users to fully exploit the rapid beam size change (Stepanov et al., 2011; Hilgart et al., 2011, Pothineni et al., 2014). A new optical layout been designed and will be shortly installed at the GM/CA beamline to be able to produce micro-focused beams as lower as 1 μm (Fischetti et al., 2013).

Micro-crystal/carrier suspensions were injected into the X-ray beam by using the LCP injector (Weierstall et. al., 2014) with a 50 μm inner diameter fused silica capillary (the so called nozzle). The injector was mounted on a fixed stage and placed perpendicular in the X-ray beam path. The crystal carrier stream was extruded out of the nozzle by a pressure that varied between 0.2 and 1 MPa depending on flow rate of the sample, which was also varied depending on sample composition and observed diffraction. A helium sheath was introduced at the point of extrusion to avoid curling up of the stream. An in line high resolution microscope was used to align the nozzle to the beam and to observe the jet. A catcher, consisting of a pipe connected to a sucking vacuum pump, was placed opposite to the jet to catch the extruded waste sample. A schematic of the experimental set-up used at the GM/CA 23-ID-D beamline is shown in Figure 4.3.

During our experiments the beam generated by the undulator was monochromated to 0.02 % bandwidth using a Si(111) monochromator and focused using K-B mirrors. The synchrotron operated at an energy of 12 keV (wavelength 1.03 Å) and the flux at the focus was 6.2 x 10^{11} photons·sec^{-1}. For data collection, the PILATUS3 6M detector was operated in a continuous shutter less mode while crystals were flowing. Sample to detector distance varied between 300 mm and 550 mm depending on sample diffraction. For each sample tens to hundreds of thousands of single shot diffraction patterns of randomly oriented micro-crystals were recorded at 10 Hz (100 ms exposure time) using a 10 μm (full width half maximum) beam size. In spite of, viscous flow rate was varied based on observed diffraction as above mentioned, most measurements were performed at an average flow rate of 100 nL·min^{-1}, corresponding to an average jet velocity of 850 microns·sec^{-1} in the 50 μm-diameter nozzle. Thus, we estimated that exposure time of a single micro-crystal across the 10 μm X-ray beam was about 85 ms.
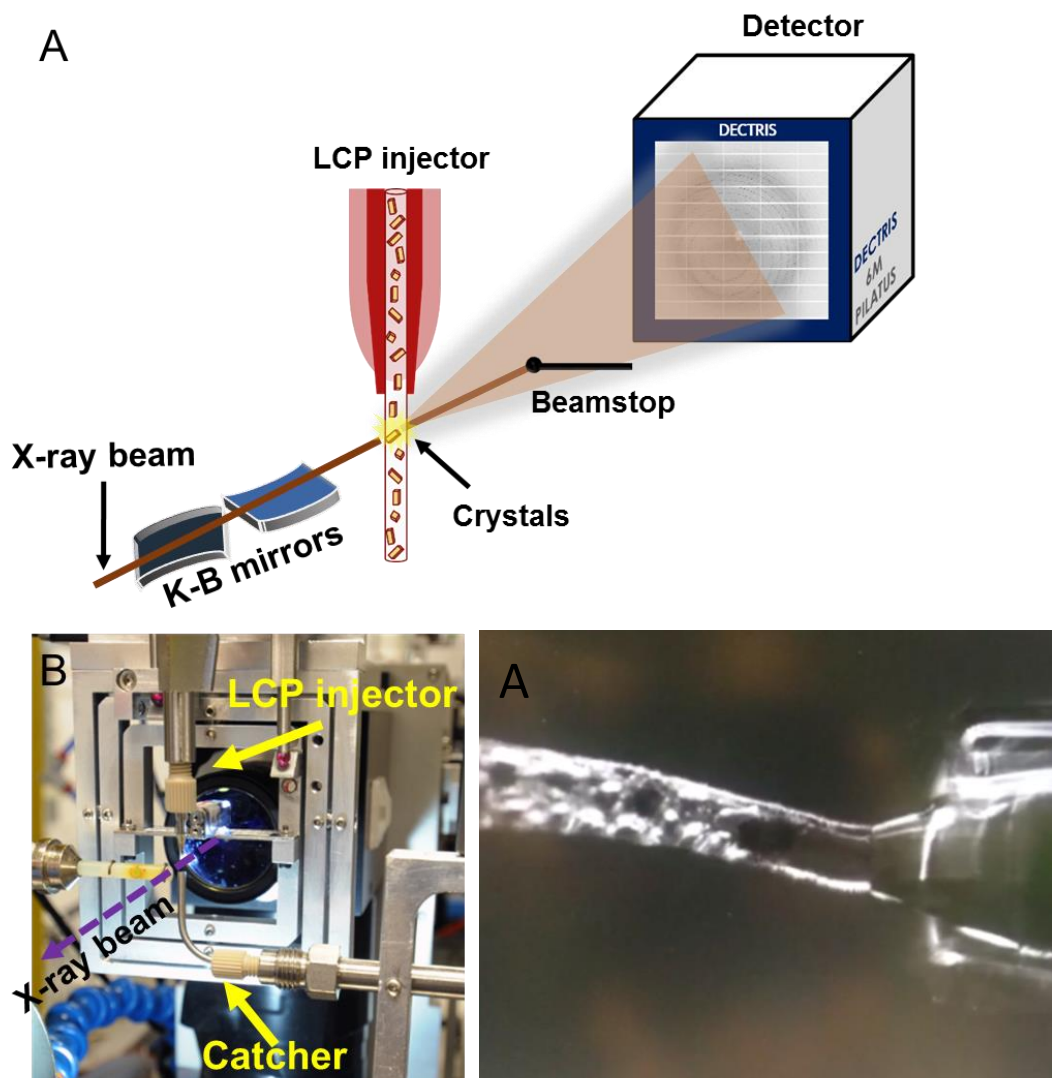
Figure 4.3 Experimental set-up at GM/CA 23-ID-D beamline. A) Schematic diagram of the set-up. B) LCP injector (Weierstall, James et al., 2014) mounted on fixed stage (not shown). Catcher is also shown. C) View of PEO stream embedded with PC extruding out of a 50 µm glass capillary nozzle.

4.2.3 DATA PROCESSING, MODEL BUILDING AND REFINEMENT

Data analysis in serial crystallography at XFELs as well as at synchrotrons is one of the major challenges of this approach. This is due to the serial nature from snapshot diffraction patterns of randomly oriented crystals with unknown partiality. In addition, the number of images collected during an experiment consists of both actual crystal hits and empty patterns resulting in

an enormous amount of patterns collected and, thus creating terabytes of data. In order to handle such amount of data we developed a Python-based hit finder at APS and an updated version of Cheetah (Barty et. al., 2014), which we named as Cheetah-cbf. This updated Cheetah's version is capable to read raw cbf images from PILATUS detector and convert them into a suitable format for data processing with CrystFEL (HDF5 format). Cheetah-cbf was also successfully installed on GM/CA 23-ID-D beamline and it is accessible to all APS users. For each experiment the peak finding thresholds were carefully tailored in order to maximize the number of crystal hits and the number of actual Bragg peaks in each diffraction pattern. Sorted diffraction patterns identified during the hit finding process were subjected to indexing and structure-factor integration by using the newest CrystFEL version 0.6.2 (White, Kirian et al. 2012, White, Barty et al. 2013, White, Mariani et al. 2016), which was carried out by the widely used algorithms such as MOSFLM (Powell, Johnson et al. 2013), DIRAX (Duisenberg, 1992), XDS (Kabsch. 2010), and a new algorithm known as ASDF built into CrystFEL itself. The new indexing option called "retry" which was implemented in all the above mentioned algorithms was used (White et. al., 2016) allowing to significantly increase the number of successfully indexed patterns. After each pattern was indexed, the intensities were merged and integrated using a Monte Carlo algorithm (Kirian et. al., 2010, 2011). Data collection statistics of PC, proteinase K, and KDO8PS are summarized in Table 4.1. The resolution cut-off criteria were based on signal to noise ratios, completeness and correlation coefficients CC* versus resolution (CC* ~ 0.5). The maximum radiation dose per crystal was estimated using RADDOSE-3D server (Zeldin, Gerstel et al. 2013), considering cuboid crystals of dimensions 5 x 5 x 10, a 10 μm beam size, a photon flux of 6.2×10^{11} photons·sec^{-1}, an energy of 12 keV, and an exposure time of 100 ms.

After integration with CrystFEL, the initial phases were obtained by molecular replacement with MOLREP (Vagin & Teplyakov, 1997) using known structures of the protein from the PDB (PBD entries were: 4ZIZ for PC (Fromme et al., 2015) and 5AVJ for proteinase K (Yazawa, Sugahara et al. 2016). Water molecules ad ligands were removed from reference structures for phasing step. Structures refinement was carried out through multiple iteration of REFMAC5

(Murshudov et. al., 2011) refining atomic coordinates and isotropic B factors. Manual inspection of the structures was carried out using COOT (Emsley & Cowtan, 2004), after each refinement step. Structure images were prepared with PyMOL (Schrödinger). All data refinement statistics of all structures solved in this study are summarize in Table 4.2. Electron density maps were calculated with MAPS tool in Phenix software suite (Adams et al., 2010). Validation of all solved structures was carried out with validation tools in Phenix software suite (Adams et al., 2010).

4.3. RESULTS

4.3.1. PHYCOCYANIN (PC)

Purification, micro-crystal formation and embedding in PEO gel of PC, a pigment-protein complex from the light harvesting phycobiliprotein family, were done as previously described in experimental procedures section. The PC micro-crystal suspension was injected at flow rates between 110 nL·min^{-1} and 300 nL·min^{-1} and 159809 images were collected which correspond to an effective measurement time of ~5 h (Table 4.1). This resulted in a PC sample consumption of about 60 µL. The structure of PC was determined to 3.1 Å resolution from 1,826 indexed patterns (indexing rate 23 %) (Table 4.1). The final collection and refinement statistics of the PC data set are shown in Table 4.1 and Table 4.2. Slightly smeared Bragg peaks were observed, which indicates that PC crystals were rotating azimuthally around the X-ray beam axis during the 100 ms exposure. The structure of PC was phased with molecular replacement using the SFX structure using a LCP injector as a search model (PDB 4ZIZ) (Fromme et al., 2015). Water molecules and the chromophores were removed from the model. The PC structure was refined to 3.1 Å resolution with final R_{work} and R_{free} values of 17.2 % and 20.4 %, respectively. The quality of the structure can be assessed from the 2mFo-DFc electron density maps of the three chromophores of PC as well as from the (Figure 4.4). To further evaluate the quality of our structure we compared our model to the two SFX structures recently described by using the LCP injector (PDB 4ZIZ) and the GDVN injector (PDB 4Q70) (Fromme et al., 2015). The three structures aligned very closely with each other with r.m.s.d. values for the Cα atoms of 0.1 Å and 0.7 Å for the LCP and GDVN structures,

respectively. Furthermore, we compared the PC structure with the previously solved structure at a synchrotron using a single cryo-cooled crystal (PDB 3L0F) (Fromme et al., 2015). Both structures superimposed very well with a r.m.s.d. value of 0.2 for all Cα atoms. A r.m.s.d. value of 0.5 Å indicates that small differences were, however, observed in the loop regions and in the solvent exposed regions. The average B factors of both chains of PC (45 Å for chain A, and 51 Å for chain B) showed no significant differences with the LCP structure (38 Å for chain A, and 45 Å for chain B). However, higher average B factors (~20 Å) were observed compare to those of the cryo-cooled and the GDVN structures.

Table 4.1 PEO SMX data collection statistics.

	Phycocyanin	KDO8PS	Proteinase K
	Values in parenthesis are for the highest resolution shell.		
Crystal size (μm)	20	10 - 15	10 - 15
Crystal-to-detector distance (mm)	300	550	400
Duration (h)	~5	~3	~3
Protein/carrier volume (μL)	60	10.1	13.0
Wavelength (Å)	1.03	1.03	1.03
Maximum Resolution (Å)	2.5	3.0	2.2
Resolution (Å)	50-3.1 (3.18-3.00)	60-(3.8)	50-2.65 (2.72-2.65)
Space group	H32	I23	$P4_32_12$
a b, c (Å)	186.4, 186.4, 60.3	118.6 ,118.6, 118.6	68.3, 68.3, 108.2
α,β, γ (°)	90, 90, 120	90, 90, 90	90, 90, 90
No. of collected images	159809	100282	97772
No. of hits/indexed patterns	7912/1826	1698/382	4497/817
I/δ(I)	7.6 (1.93)		4.6 (0.31)
Multiplicity	156.4 (4.8)	25.1 (9.0)	104.8 (40.6)
Completeness (%)	99.7	100	99.2
CC* (%)	0.986 (0.799)	0.932 (0.397)	0.954 (0.431
R_{split} (%)	14.2 (73.09)	37.3 (135.7)	22.4 (331.0)

4.3.2. PROTEINASE K (PK)

PK was purchased from Sigma and micro-crystals of a size between 10 and 15 μm were grown in mixed with PEO gel as above mentioned in section 4.2.1. Diffraction data of PK micro-crystals were collected at a constant flow rate of 79 nL·min^{-1} and an effective measurement time of

~3 h in which nearly 100000 images were recorded. This resulted in a PK sample consumption of less than 15 µL. A total of 4497 images diffracting to a maximum resolution of 2.2 Å were identified as hits (hit rate 4.2%), of which 817 were successfully indexed in a $P4_32_12$ space group (Table 4.1). The final quality collection and refinement statistics are given in Table 4.1 and Table 4.2. Figure S5 shows a diffraction pattern a single PK-PEO micro-crystal. As mentioned for PC, slightly smeared Bragg peaks were also observed, which indicates that PK crystals were rotating during the 100 ms exposure. Phasing was done with molecular replacement using the cryo-cooled structure at a synchrotron (PDB 5AVJ) as a search model (Yazawa et al., 2016). The final refinement gave a R_{work} and R_{free} of 22.4 % and 25.5 %, respectively. The PK structure was determined to 2.65 Å and, overall, our structure is very similar to the one solved using cryo-cooled crystals with a r.m.s.d. value of less than 0.1 Å for all Cα of the protein. The average B factor was 61 $Å^2$, as expected for a structure solved to 2.65 Å at room temperature. In our structure no water molecules were identified. The electron density around the calcium atoms can be used to assess the high quality of our PK structure (Figure4.4).

Table 4.2 PEO SMX data refinement statistics.

	Phycocyanin	Proteinase K
Total reflections	17002	29685
Number of reflections used in refinement	6280	5294
R_{work} / R_{free} (%)	17.2 / 20.5	22.4 / 25.5
No. of atoms	2626	2041
Protein	2499	2032
Water and others (ligands or ions)	127	9
Average B value ($Å^2$)	48.2	61.3
R.M.S. deviations from ideal values		
Bonds (Å)	0.011	0.008
Angles (°)	2.093	1.126
Ramachandran plot statistics† (%)		
Favored	98.8	97.1
Allowed	1.2	2.5
Disallowed	0	0.4
Rotamer outliers	2	0

†As calculated by *MOLPROBITY* (Chen et al., 2010).
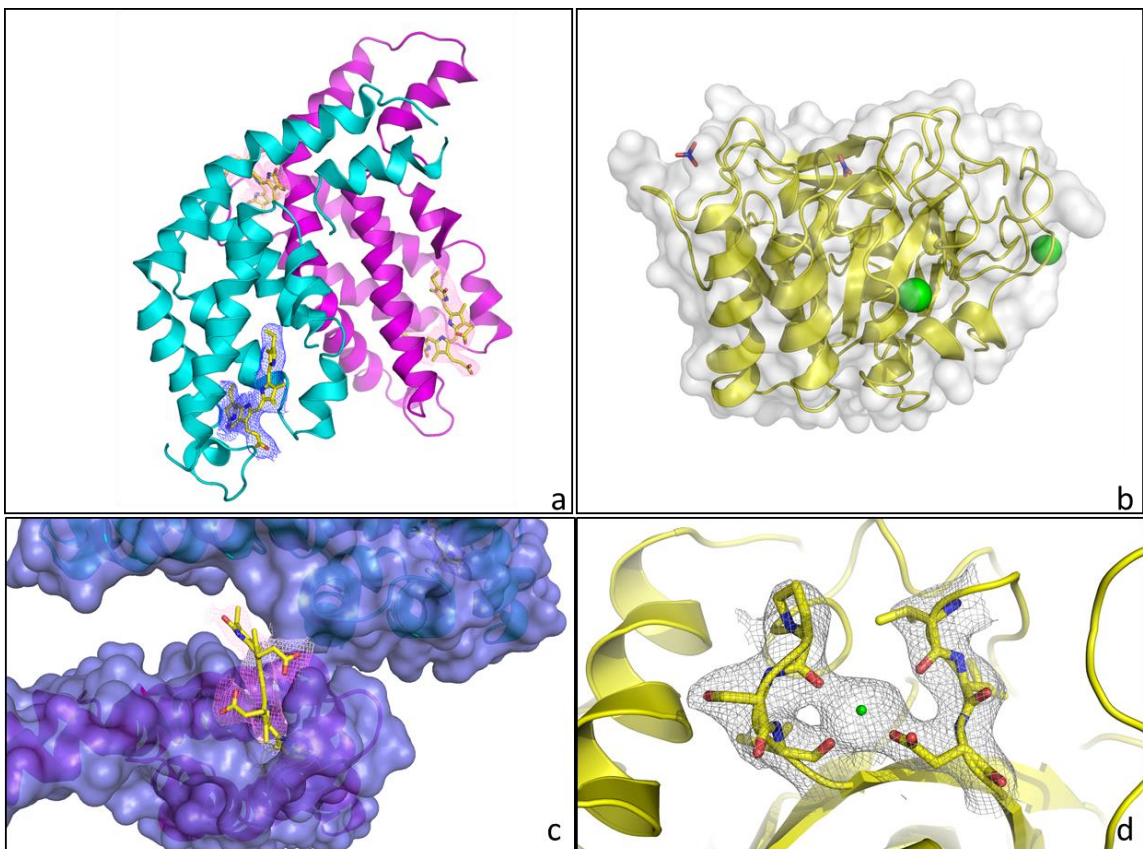
Figure 4.4 Cartoon models of protein structures solved using PEO as a viscous carrier. a) structure of PC monomer showing the α and β subunits with mesh surrounding the chromophores b) structure of proteinase K, green globes represent calcium molecules c) enlarged image of the PC chromophore d) electron density of the residues surrounding calcium 2 in proteinase K.

4.3.3 3-DEOXY-D-MANNO-2-OCTULSONATE-8-PHOSPHATE SYNTHASE (KDO8PS)

Cubic crystals of KDO8PS re-suspended in PEO gel were diffracted for about 3 h of beamtime collecting a total of 100282 images, of which 1698 were hits and of these 382 were successfully indexed in a space group I23 (Figure 4.5). Despite KDO8PS crystallizes in a high symmetry space group, poor data collection statistics as shown in Table 4.1, indicate that a higher number of patterns need to be indexed in order to solve its structure.

98
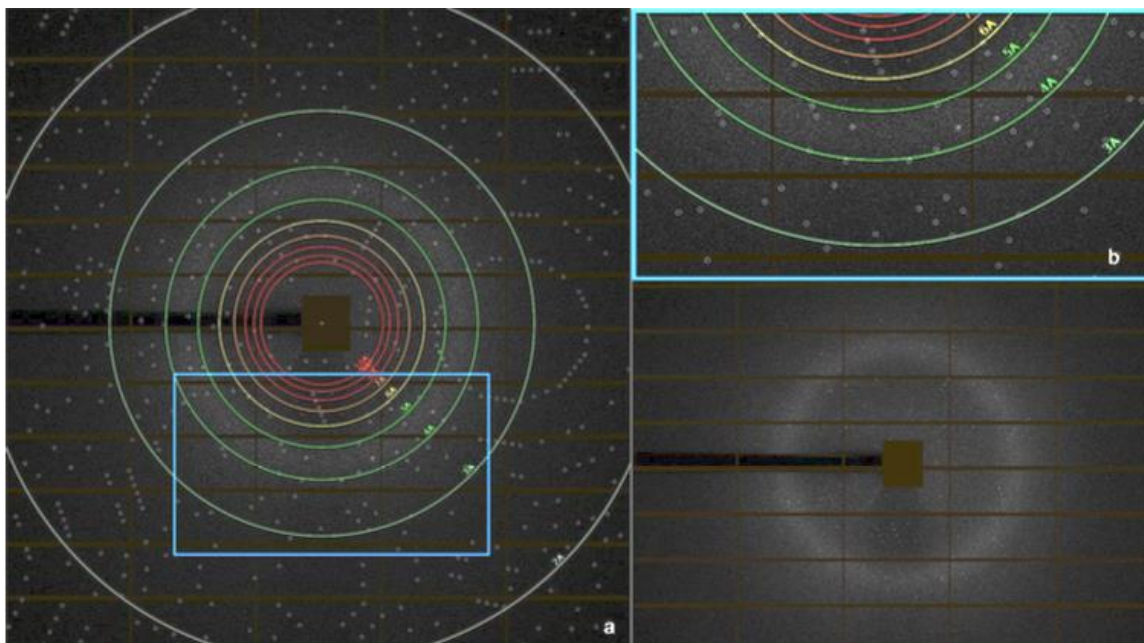
Figure 4.5 Diffraction of KDO8PS in PEO. a) Indexed diffraction pattern of KDO8PS b) zoomed in subset from a) c) unprocessed diffraction pattern, showing the low background from the PEO.

4.4 DISCUSSION AND CONCLUSION

Here we show the PEO is a viable delivery system for SMX experiments. PEO gels are highly stable in a wide range of temperatures so that crystal delivery based on PEO can be accomplished at the traditional crystallization temperatures from 4 °C to 30 °C. Unlike previously described for agarose-embedded crystals (Conrad, Basu et al., 2015), mixing of pre-formed crystals with the PEO gel is a very simple and straightforward procedure as described in experimental procedures section leading to a highly homogeneous crystal distribution. PEO gels, as any other PEG, are compatible with a wide variety of precipitants commonly used in protein crystallization. Furthermore, PEO gels have been also shown to be compatible with a wide variety of organic solvents which are commonly used as additives in many crystallization recipes (Choquesillo-Lazarte and Garcia-Ruiz, 2011). In all our experiments, PEO-embedded crystals established very stable streams and no signs of dehydration were observed. It is important to note

that the vacuum catcher was critical to form a continuous jet. Without the vacuum the PEO viscous stream often curls back.

Preliminary studies indicate that PEO have also the potential to serve as a viscous carrier for membrane proteins as PSI crystals appear undamaged after mixing. Diffraction was not tested as much larger crystals would be required due to the large unit cell. However, we do have preliminary data, ultraviolet two-photon excited fluorescence (Figure 4.2) , SONICC (Kissick, Wanapun et al. 2011) (Figure 4.2), polarized light (4.6), indicating that crystals of PSI, a large membrane protein complex, survive mixing with PEO. Currently the only viscous medium that has been shown to be compatible with membrane proteins grown in detergent micelles *in surfo* is agarose (Conrad, Basu et al. 2015). Agarose has been demonstrated to work in atmosphere however we indicated that the primary use of the viscous medium is for SFX experiments in vacuum. Therefore, we hypothesize that PEO would be a suitable medium to deliver membrane protein crystals grown via any method of choice (vapor diffusion, dialysis, hanging drop) for SX at ambient pressure both a synchrotrons and XFEL sources in the future.

It is important to note that radiation damage is currently inevitable when using synchrotron sources. For decades, cryo-cooling has been used to mitigate the effect of radiation damage, which is one of the primary factors limiting the quality of structural information that can be obtained from small protein crystals (Garman, 2010). The new the serial crystallography strategy in which X-ray diffraction snap-shots are collected from a stream of crystals where each crystal is only exposed once has demonstrated to reduce radiation damage even when measuring crystals at room temperature at synchrotron sources (Stellato, Oberthür et al. 2014, Nogly et al. 2015). Several radiation damage studies carried out on macromolecular crystals have revealed that the lifetime of the crystals can be increased with an increase of the beam intensity and the corresponding decrease in exposure time (Owen, Axford et al. 2012; (Warkentin, Badeau et al. 2011, Warkentin, Hopkins et al. 2013). These studies have also shown that the global radiation damage occurs on a timescale of the order of seconds and that even with a 100 ms exposure, radiation damage can be notably reduced by outrunning the secondary and tertiary damage

effects (Owen, Axford et al. 2012; Warkentin, Badeau et al. 2011). This is because the diffusion of radicals in the crystal takes time, so secondary radiation damage can be reduced by millisecond X-ray exposure. In our experiment, the LCP injector was operated to an average flow rate of 100 nL·min^{-1} providing a constant stream of fresh crystals, so that each crystal was exposed for about 85 ms. The total radiation dose each and every single crystal received was estimated to be 0.2 MGy, which remains lower than the "safe" dose limit reported by Garman and co-workers for room temperature measurements (Nave and Garman, 2005; Garman and McSweeney, 2007).

One of the largest limitations of synchrotron SMX data collection is that crystals need to be larger (>10 µm, depending on the unit cell size) (Stellato, Oberthür et al. 2014) than those used for SFX experiments (>200 nm) (Hunter and Fromme 2011). Larger crystals result in a lower hit rate and may have an increased mosaicity. Additionally, the need for longer exposure times decreases the repetition rate (currently FELs operate at 60 Hz at SACLA and 120 Hz at LCLS) in comparison to the 10 Hz in which data was collected at APS. However, because an XFEL produces a more monochromatic beam in comparison to a synchrotron, thus synchrotron radiation has a higher bandwidth resulting in larger "slices" through the sphere of reflections are recorded at a synchrotron which allows for less data to be collected for a complete data set. To enhance this affect, a higher bandwidth of a pink beam could be deployed to further decrease the number of diffraction patterns required (Stellato, Oberthür et al. 2014). Synchrotrons also have a very stable X-ray flux, so the pulse to pulse intensity fluctuation is significantly less than an XFEL. Furthermore, beamtime on a microfocus beamline is significantly easier to acquire than XFEL beamtime and planned upgrades at microfocus beamlines will allow for even smaller crystals to be probed.

In conclusion, PEO is easy to prepare, has low background, and is a versatile carrier for soluble proteins and protein complexes with great potential to be also suitable for membrane proteins. This sample delivery technique allows for semi-automated, serial data collection. Although this experiment was done at microfocus beamlines, there is no limitation why this couldn't be used an XFEL source as well which would be extremely useful for membrane proteins

and radiation sensitivity proteins. Additionally, recent work has shown that LCP is amenable for time-resolved crystallography via photoexcitation (Nogly 2016). PEO also may be amenable for time-resolved crystallography, especially for membrane proteins that do not crystallize in LCP.

Photosystem I
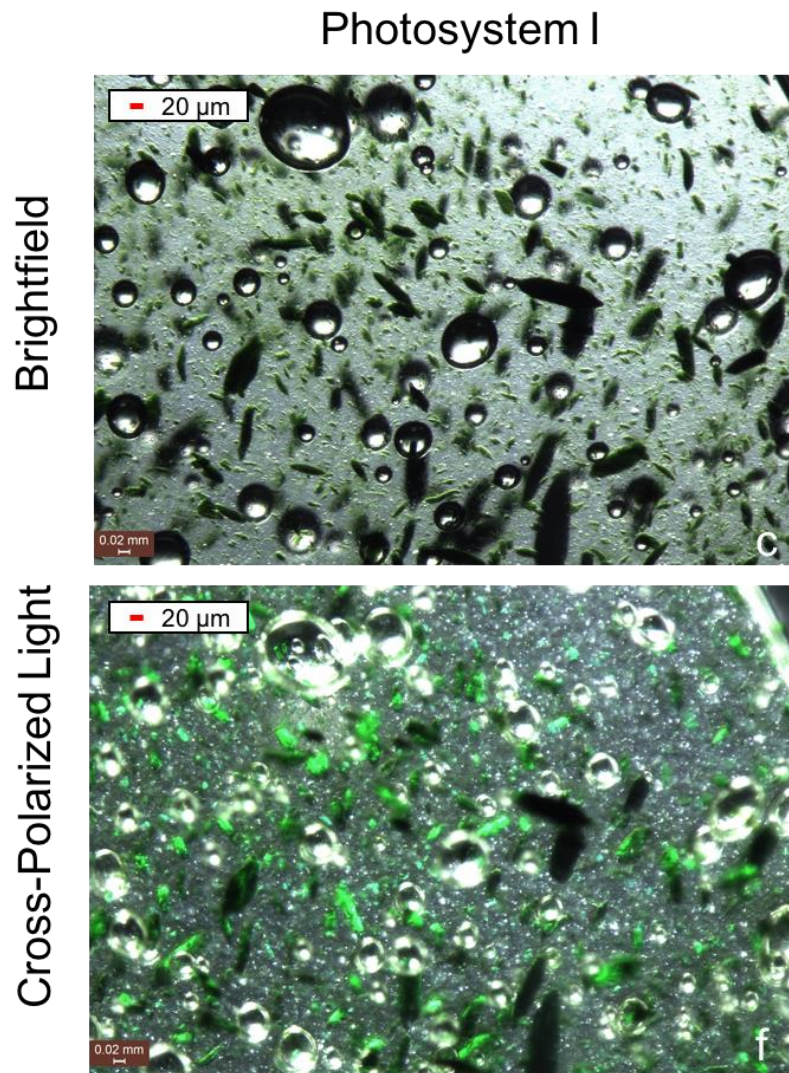
Figure 4.6 PSI mixed with PEO a) brightfield of PSI crystals mixed with PEO b) PSI crystals after mixing with PEO viewed by cross-polarized light.

4.5. ACKNOWLEDGEMENTS:

CHAPTER 5

SUBSTRATE DIFFUSION TRIGGERED TIME-RESOLVED SERIAL CRYSTALLOGRAPHY USING KDO8PS MICROCRYSTALS

Chelsie E. Conrad[1,2], Jesse Coe[1,2*], Austin Echelmeier[1,2], Gerrit Brehm [2,3], Raimund Fromme[1,2], James Zook[1,2], Felicia Craciunescu[2], Deborah Hansen[2], Alexander Schaffer[1,2], Michael Vaughn[1,2], Alexandra Ros[1,2], Petra Fromme[1,2]

[1]Center for Applied Structural Discovery, the Biodesign Institute, Arizona State University. Tempe, AZ, USA, 85287-1604
[2]School of Molecular Sciences, Arizona State University, PO Box 871604, Tempe, AZ, USA 85287-1604
[3] Institute for X-ray Physics, Georg-August –University Göttingen, Friedrich-Hund-Platz 1 37077 Göttingen
Germany

[*]These authors contributed equally

Presented here are preliminary results related to the "mix and inject" project where crystals are mixed with substrate prior to diffraction. With the help of my colleagues, a new purification protocol was designed, I was primarily focused growing crystals of various sizes for future time-resolved mixing experiments.

Most enzymatic turnovers occur on millisecond time scales, impeding visualization of the structural evolution along the reaction pathway using standard X-ray crystallography techniques. Rapid mixing of enzyme crystals with their substrate(s) followed by subsequent probing with ultrashort X-ray pulses allows snapshots of these enzymatic processes to be captured. As a model enzyme, 3-deoxy-D-manno-2-octulosonate-8-phosphate synthase (KDO8PS) has exhibited intermediate and product formation on a millisecond time scale as shown through time-resolved mass spectrometry. Macro- and micro- crystals of KDO8PS have been produced and characterized. In future, diffusive time-resolved serial crystallography, time points ranging from 7-400 ms along the reaction pathway could potentially be probed. Experiment designs to utilizing both microfocus synchrotron and X-ray free electron laser light sources are described.

5.1. INTRODUCTION

Time-resolved crystallography has shed valuable insight into the structural dynamics of enzymes in motion. However, many of these time-resolved crystallography experiments have been limited to the study of light triggered reactions in photoactive systems. While these enzymes are important, most proteins in Nature are not light-driven. The ability to study time-resolved crystallography of enzymes during catalysis would open an entirely new field of enzymology,

allowing substrate binding, intermediates, product binding, and kinetics all to be studied by structural biology.

Diffusion times of a substrate into a biomacromolecular crystal are governed by Fick's 2nd law of diffusion and, for crystal sizes typical for standard crystallography, this becomes prohibitive for the temporal regime (typically 1-100 ms) (Wolfenden and Snider 2001) often seen in enzymatic processes. Methods for observing intermediate structures such as mutagenesis to slow reaction kinetics or substrate modification, photoactivatable substrate caging (Stoddard, Cohen et al. 1998), and freeze trapping (Moffat and Henderson 1995) are possible but may introduce unnatural artifacts and are system specific, precluding generalization of biologically relevant, enzymatic intermediate structural discovery. So for many enzymes time-resolved diffusion mixing experiments are out of reach. However, with micro/nanocrystals, diffusion of substrate into the crystal is can be shorter than the enzymatic reaction (Schmidt 2013). Until recently these crystals were too small for structure determination and too prone to radiation damage. Today higher brilliance achieved at microfocus synchrotron beamlines and the advent of X-ray free electron lasers (XFELs) has allowed structural determination of increasingly smaller crystals to be possible. Additionally the serial crystallography (SX) data collection method mitigates radiation as only one diffraction pattern per crystal is collected, minimizing the limitation of radiation damage (Chapman, Fromme et al. 2011). In SX, samples are delivered at room temperature in their mother liquor (Chapman, Fromme et al. 2011) and thus the crystals are not frozen. For these reasons, short lived states such as intermediates could be captured by SX snapshot diffraction (Schmidt 2013). Where fast mixing of two liquids, such as those containing enzyme microcrystals and substrate(s), immediately before being exposed to an X-ray beam. Thus the ability to determine X-ray structures from microcrystals opens a new era in time-resolved structural biology as future studies may allow enzymatic reactions to be captured in high resolution without altering the enzyme.

3-deoxy-D-manno-2-octulosonate-8-phosphate synthase (KDO8PS)(Levin and Racker 1959) was developed for this study as a model system for time-resolved serial crystallography (TR-SX).

KDO8PS is an enzyme unique to Gram-negative bacteria and catalyzes the first step of the molecule, 3-deoxy-D-manno-octulsonic acid (KDO) that anchors the lipopolysaccharide to the outer cell membrane (Figure 5.1). The virulence and growth of gram-negative bacterium are dependent on lipopolysaccharide attachment, thus making KDO8PS a promising antibiotic target (Asojo, Friedman et al. 2001). Initializing the first step of KDO, KDO8PS catalyzes a net aldol condensation between arabinose-5-phosphate (A5P), phosphoenol pyruvate (PEP), and water (Figure 5.2). Two subgroups of KDO8PS exist, the metallo and nonmetallo enzyme which are evenly divided among the phylogenic tree (Birck and Woodard 2001). In the metallo enzyme three residues are conserved, a cysteine in which the thiolate coordinates the metal, a histidine, and a carboxylate from either aspartic or glutamic acid moieties. Non-metallo enzymes instead replace the cysteine with asparagine (Oliynyk, Briseno-Roa et al. 2004). Additionally, the metallo enzyme can be converted to a non-metallo enzyme by a cysteine to asparagine mutation and vice versa (Oliynyk, Briseno-Roa et al. 2004, Kona, Xu et al. 2007). During catalysis an unstable transient intermediate is formed. The structure of the enzyme bound intermediate has not been resolved for the wild-type enzyme but the presence of an intermediate has been identified by fast mixing coupled with electrospray ionization mass spectroscopy (ESI-MS)(Li, Sau et al. 2005). Because the intermediate can be observed on a millisecond timescale (Figure 5.2), KDO8PS is an ideal model protein for TR-SX experiments, involving conformational changes induced by mixing of small microcrystals with a substrate. Currently, no other structural biology technique has the ability to resolve short-lived (millisecond time resolution) intermediate structures without modifying either the substrate and/or the enzyme. Prior to the formation of product, 3-deoxy-D-manno-2-octulosonate-8-phosphate (KDO8P), the reaction progresses through a labile bisphosphate enzyme intermediate (Figure 5.3). The intermediate complex is the most attractive antibiotic target since inhibitors resembling the intermediate have been shown to be the most potent (Baasov and Kohen 1995, Liang, Lewis et al. 1998, Wang, Duewel et al. 2001).
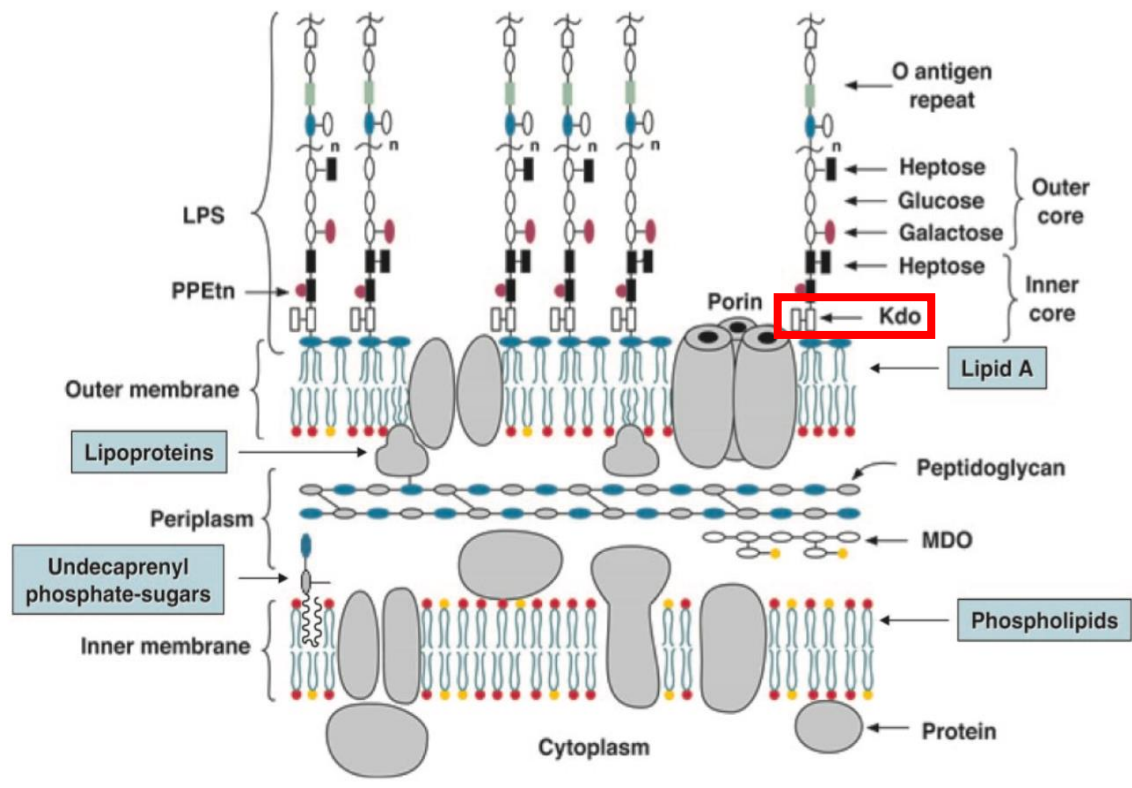
Figure 5.1 Diagram of the gram-negative bacteria envelope. KDO is an essential building block which anchors the lipopolysaccharide to the outer membrane. Figure from (Raetz and Whitfield 2002).

synthesized cyclic bisphosphate as an alternative substrate (Baasov and Kohen 1995, D'Souza, Benenson et al. 1997). The cyclic bisphosphate molecule proved to be a poor substrate as well as an inhibitor, supporting the hypothesis of a linear intermediate (Liang, Lewis et al. 1998). Nearly a decade later, the acyclic intermediate theory was supported by the structure of a metal dependent KDO8PS (*Aquifex aeolicus*) with the intermediate bound to the active site (Kona, Xu et al. 2007). However, the intermediate was only captured by studying a mutant enzyme, where three point mutations were introduced which prevented metal binding and drastically decreased the turnover rate of KDO8PS (0.47 ± 0.02 and 0.16 ± 0.01 s^{-1}/μM^{-1}, wild type and triple mutant, respectively) and decreased activity levels from 24%-46% of the wild type enzyme (Kona, Xu et
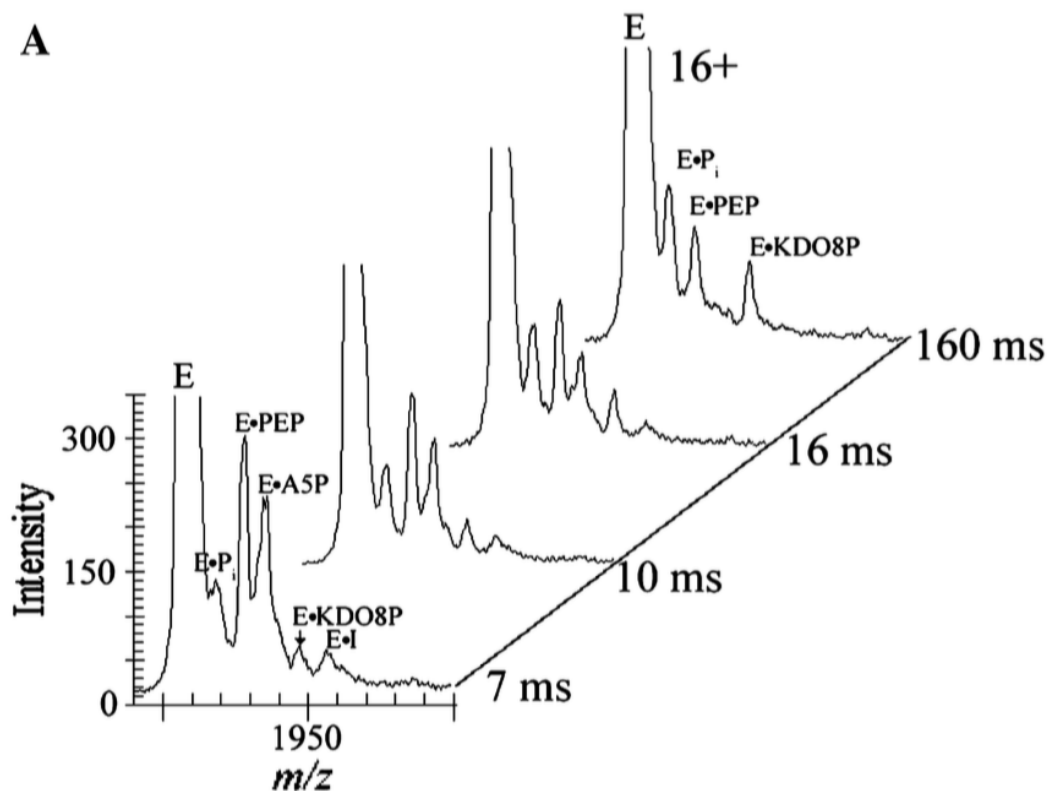
Figure 5.2 Time-resolved ESI-MS results. 80 µM of KDO8PS with PEP pre-bound was mixed, via a mixing tee junction with 60 µM A5P. Various time points were achieved by changing the flow rate while the ESI-MS quenched the reaction. E is the enzyme unbound, E·P$_i$ is enzyme plus inorganic phosphate, E·PEP is enzyme bound to PEP, E·A5P is enzyme bound to A5P, pathways are possible depending on whether the water molecule attacks prior to the bond E·KDO8P is the enzyme bound to the product, and E·I is the enzyme bound to the intermediate. The 7 and 10 ms time points revealed the enzyme bound to the intermediate while all the time points revealed a population of enzyme bound to the product. Figure reproduced with permission from (Li, Sau et al. 2005).

al. 2007). Additionally, the mechanism for intermediate formation is debated as two possible

pathways are possible depending on whether the water molecule attacks prior to the bond

formation between C3^{PEP} to C1^{A5P} or after (Figure 5.3)(Wang, Duewel et al. 2001). Two pathways

have been proposed for the formation of the bisphosphate intermediate, one in which a carbanion

is formed and the other where an oxocarbenium ion is formed. These pathways are labelled as

pathway I and II in Figure 5.3. Pathway I, has been proposed for the metallo enzyme based on

the fact that a water bound to a metal will have a significantly lower pK$_a$, thus one of the waters

coordinated to the metal will be deprotonated resulting in a hydroxide attacks PEP (Duewel and Woodard 2000, Kona, Xu et al. 2007). The non-metallo KDO8PS is hypothesized to proceed through pathway II based on the crystal structure of PEP bound to the non-metallo *E. coli* KDO8PS. In this model, the PEP carboxylate holds a strong negative charge is not surrounded by any residues to stabilize the charge. Because this strong negative charge is not stabilized, the nucleophilicty of the surrounding double bond is increased. This increased nuceophilicity supports the idea of nucleophilic attack on A5P may lead to the formation of an oxocarbenium intermediate (Asojo, Friedman et al. 2001). Additionally, the positive charge on C2 of PEP is stabilized by the negative charge on the carboxylate (Asojo, Friedman et al. 2001). Quantum mechanical/molecular mechanical simulations agree with this hypothesis(Tao, Schlegel et al. 2010). However, electron densities of PEP and A5P bound to a metallo KDO8PS that was converted to a nonmetallo enzyme show only one of the two water molecules is visible. It speculated that other water molecule might be the hydroxide that attacks PEP in pathway 1, indicating that both the metallo and nonmetallo enzyme might proceed through pathway 1 (Kona, Xu et al. 2007).

5.2. MATERIALS AND METHODS

5.2.1. CLONING, EXPRESSION, AND PREPARATION OF CELL FREE EXTRACT

The wild-type KDO8PS gene was purchased from GenScript and was cloned into a pET-23d vector (Figure. 5.4). The protein was overexpressed in Lemo21 (DE3) *E. coli* cells under the control of a T7 promoter. LB media containing ampicillin and chloramphenicol was inoculated with the culture and vigorously shaken at 37 °C until an A_{600} = 0.6-0.8 was reached and then 0.2 mM isopropyl-1-thio-ß-D-galactopyranoside was added (Figure 5.5). After 4 hours of incubation at 37 °C the cells were harvested by centrifugation at 8,000 rcf for 10 minutes at 4 °C and then frozen at -80 °C. The frozen pellet was then treated as described in Ray P. 1980 (Ray 1980) with the
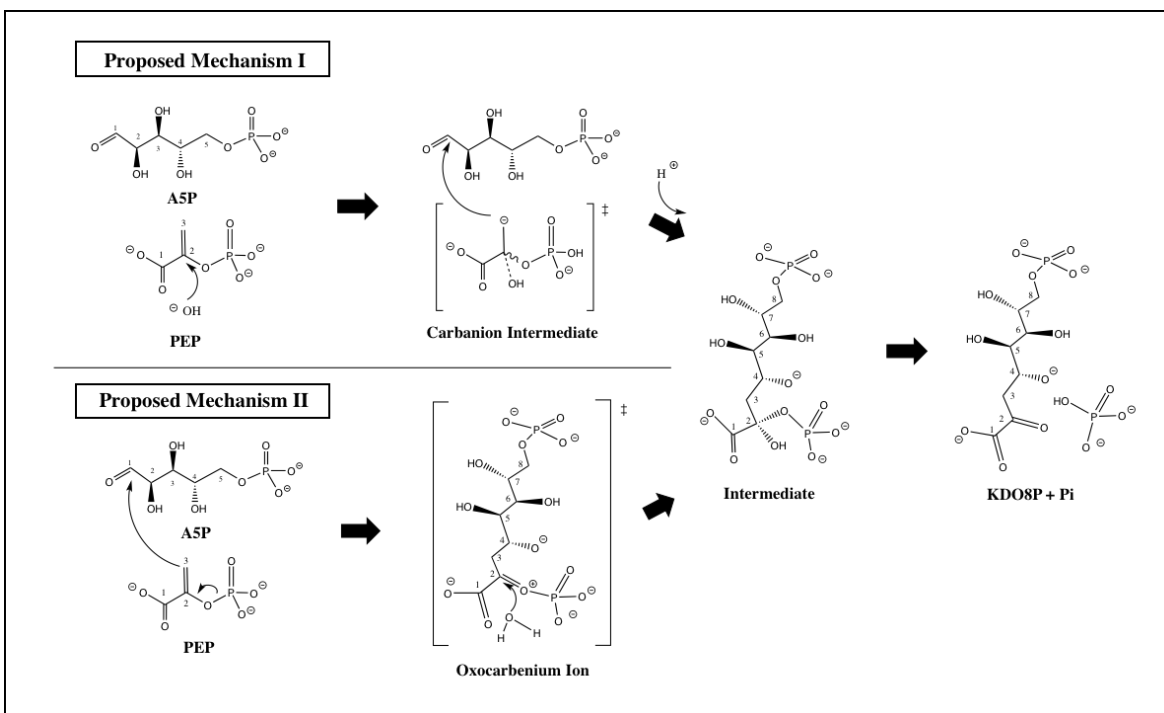
Figure 5.3 Proposed mechanisms for KDO8PS. Mechanism I produces a carbanion intermediate where mechanism II produces an oxocarbenium intermediate. Both mechanisms produce the same linear intermediate.

following modifications. Briefly, the cell pellet was re-suspended in a buffer containing 20 mM Tris pH 7.3, 300 mM potassium chloride, 1 SIGMAFAST protease inhibitor cocktail tablet (EDTA-free) (Sigma), and 10 mg/1 g cell pellet lyophilized lysozyme. After suspension, the cells were incubated in the lysis buffer for 30 minutes at room temperature followed by incubation on ice for 20 minutes. The cells were then broken using a sonicator with a microtip at 50 % power, 10 second pulses for 6 cycles totaling 1 minute with a 30 second incubation on ice in between each cycle. The cells were then centrifuged at 24000 g for 30 minutes. A protamine sulfate precipitation was then done on the supernatant. For this step a 2.2% protamine sulfate, 20 mM Tris pH 5, 300 mM potassium chloride, and 1 SIGMAFAST protease inhibitor cocktail tablet (EDTA-free) solution was added to achieve a final concentration of 0.26%. The precipitation was carried out for 15 minutes on ice and then the solution was centrifuged for 30 minutes at 48000 g. The supernatant was then dialyzed against 5 mM potassium phosphate pH 7.3, 75 mM potassium chloride. One

buffer exchange was carried out after 4 h. The dialyzed enzyme preparation was then centrifuged at 7,000 g at 4 °C for 10 minutes to remove precipitated proteins. The supernatant was then filtered through a 0.22 μm filter and then loaded onto an anion exchange column (900 mm x 16 mm column packed with DEAE-Sepharose) previously equilibrated with 75 mM potassium chloride, 20 mM Tris pH 7.3. The column was washed with 240 mL of the equilibration buffer and then potassium chloride was increased to 115 mM in a step gradient to elute the protein. All buffers used during purification contained 2 mM 2-mercaptoethanol.
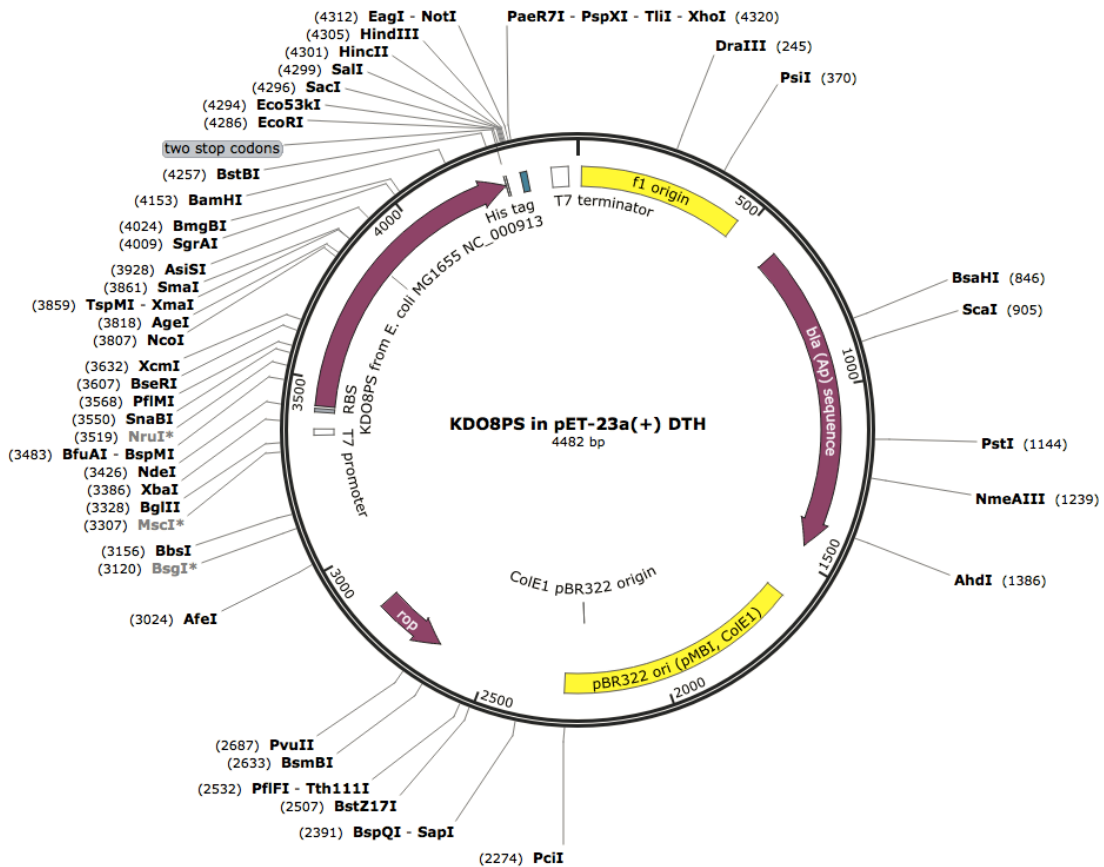
Figure 5.4 pET vector map with the KDO8PS gene under control of a T7 promoter. The plasmid contains two selection markers, ampicillin and chloramphenicol and has an option for a C-terminal histidine tag.
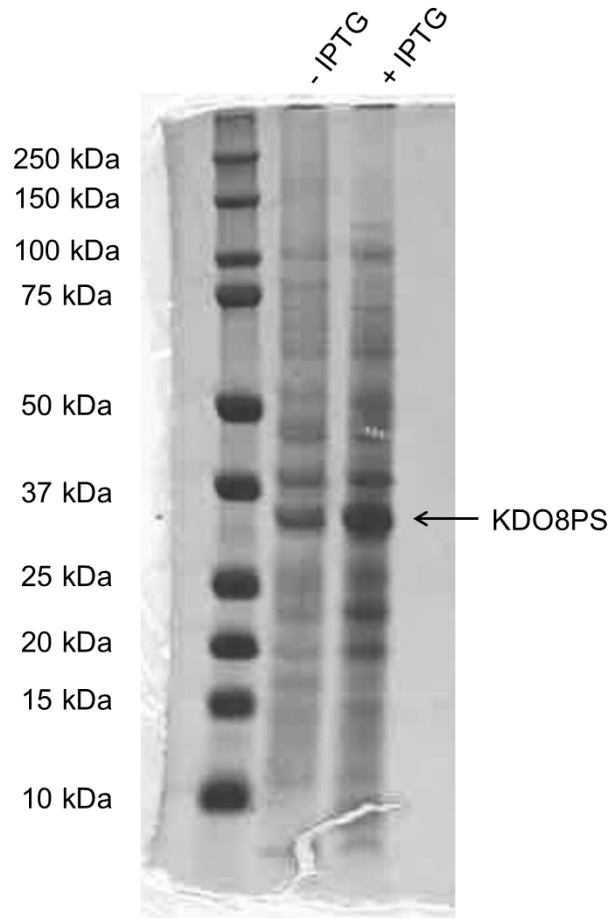
Figure 5.5 Soluble Protein Extract from Non-Induced and Induced *E. coli* Cells.

5.2.2. ANION EXCHANGE CHROMATOGRAPHY

The dialyzed enzyme preparation was then centrifuged at 7,000xg at 4°C for 10 minutes to remove precipitated proteins (SDS PAGE confirmed that the precipitate was not KDO8PS see Figure 5.8). The supernatant was then filtered through a 0.22 μm filter and then applied to an anion exchange column (900 mm x16 mm column packed with DEAE-Sepharose) equilibrated with 75 mM potassium chloride, 20 mM Tris pH 7.3, 2 mM 2-mercaptoethanol. The column was washed with 240 mL of the equilibration buffer and then potassium chloride concentration was increased from 75 mM to 115 mM in one step to elute the protein (Figure 5.6). Elution profile of the chromatography runs were monitored by

absorption at 215 nm as KDO8PS contains no tryptophans and only 4 tyrosines thus absorbance at 280 nm is low (see Figure 5.6). The protein elution fractions were further analyzed by sodium dodecyl sulfate polyacrylamide gel electrophoresis (SDS-PAGE) (Figure 5.7), and the thiobarbituric acid assay. The fractions containing KDO8PS were then pooled and concentrated using Centricon-30 ultrafiltration (Millipore).

Microcrystallization was used as a final purification step where protein for all assays and crystallization was derived from microcrystals that were dissolved by the addition of buffer containing no precipitant and then concentrated to the desired concentration (Figure 5.8). Protein concentration was determined by using the extinction coefficient of 15,219 $M^{-1} cm^{-1}$ at 280 nm (Li, Sau et al. 2005). Tris(2-carboxyethyl)phosphine (TCEP) was explored as a long term reducing agent and was added and DLS was used to characterize the distribution of monomers. The protein with TCEP was monodisperse while the protein without TCEP was polydisperse (Figure 5.9). However, protein that contained TCEP would not crystallize and thus only DTT was added during purification. Attempts to scale protein purification for SX experiments resulted in an elutant contaminated with many other proteins (Figure 5.10).
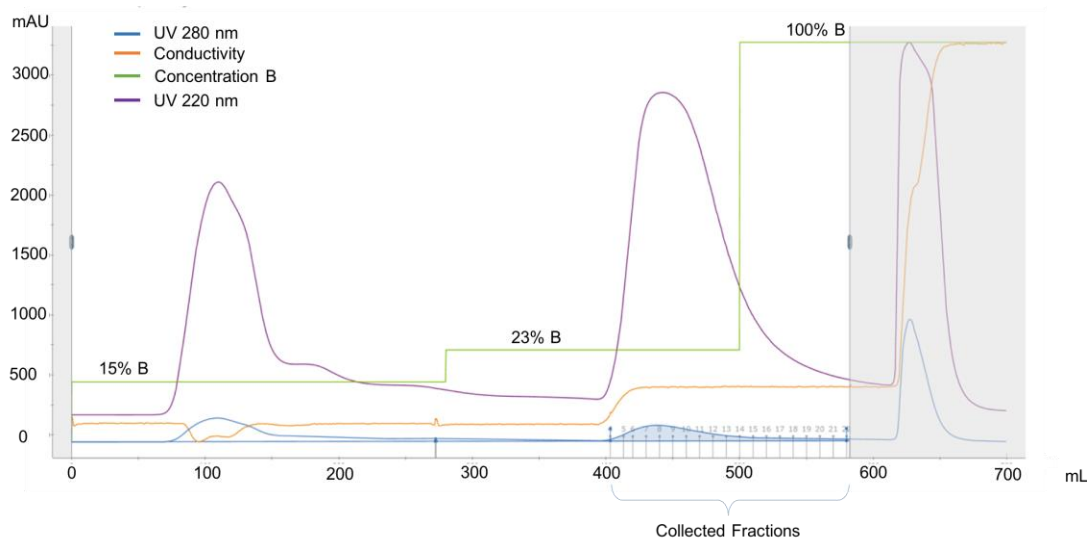
Figure 5.6 Chromatogram of anion exchange chromatography. KDO8PS was eluted at 115 mM KCl and monitored by absorbance at 220 nm.

113
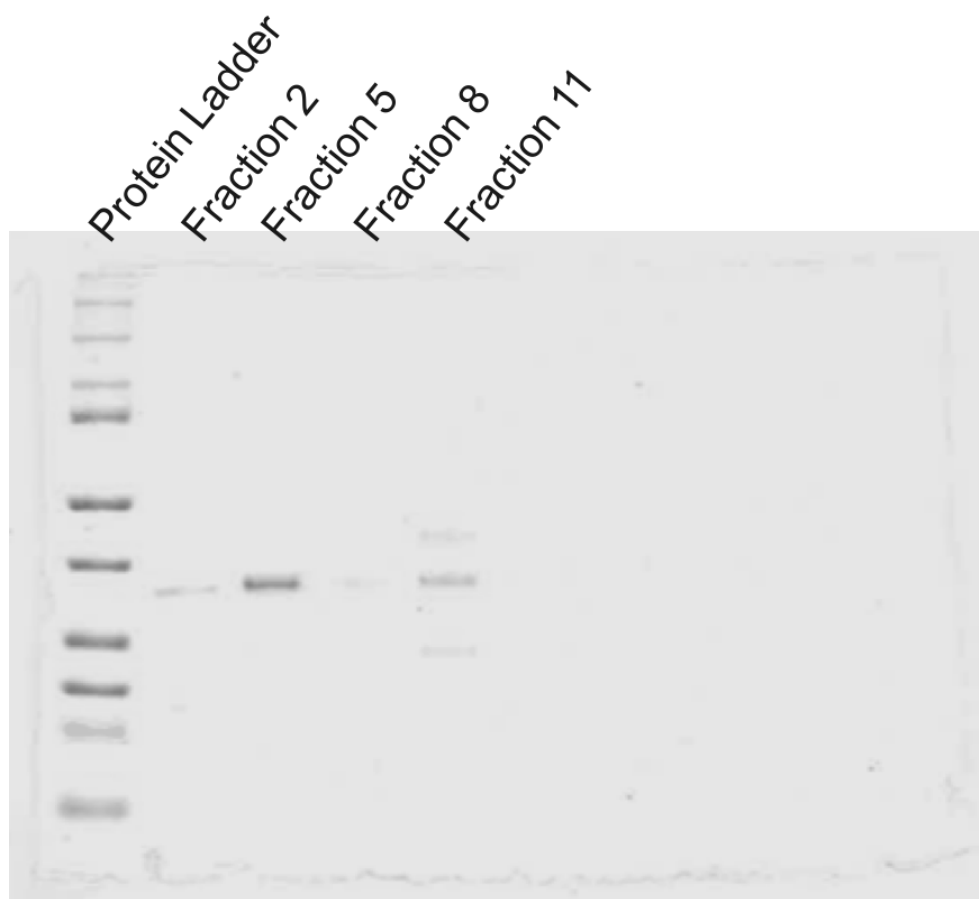
Figure 5.7 SDS-PAGE of fractions from anion exchange chromatography. Stained with coomassie blue.
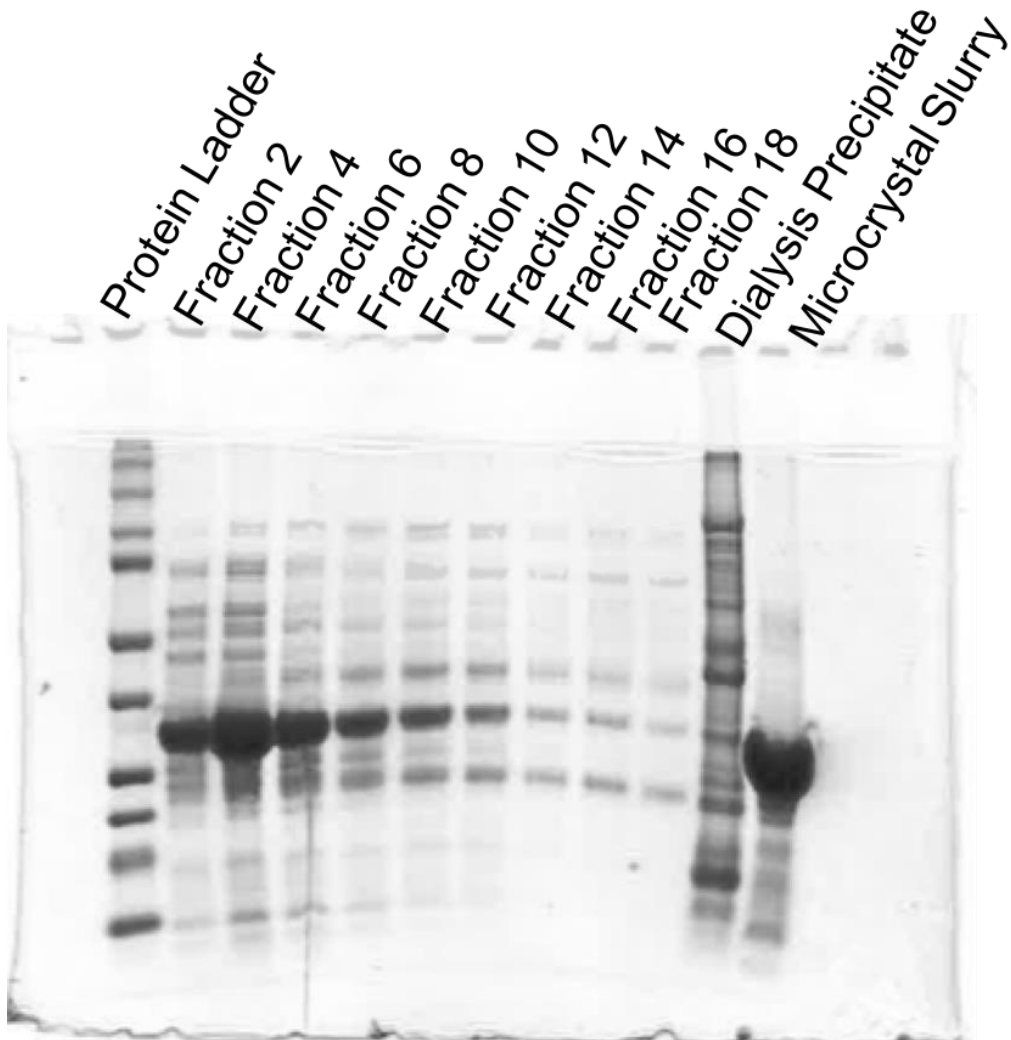
Figure 5.8 SDS-PAGE of fractions from a scaled anion exchange purification, dialysis precipitate, and microcrystals. Attempts to scale purification resulted in large contamination. Crystallization was from these combined fractions was unsuccessful. Thus, scaling up most will require another purification step. 1 µL of crystals grown from a smaller purification was loaded on lane. Some impurities remain as the crystals were not washed prior to loading to ensure they did not dissolve.
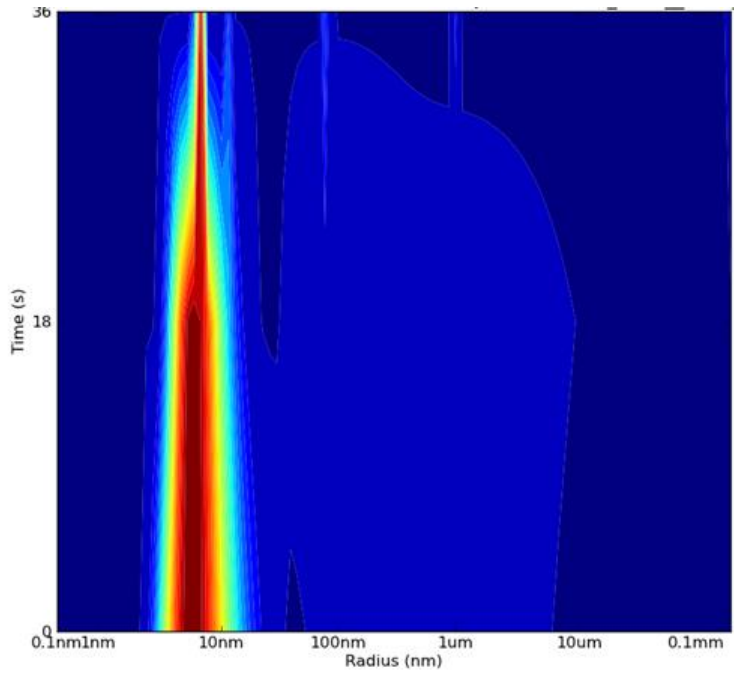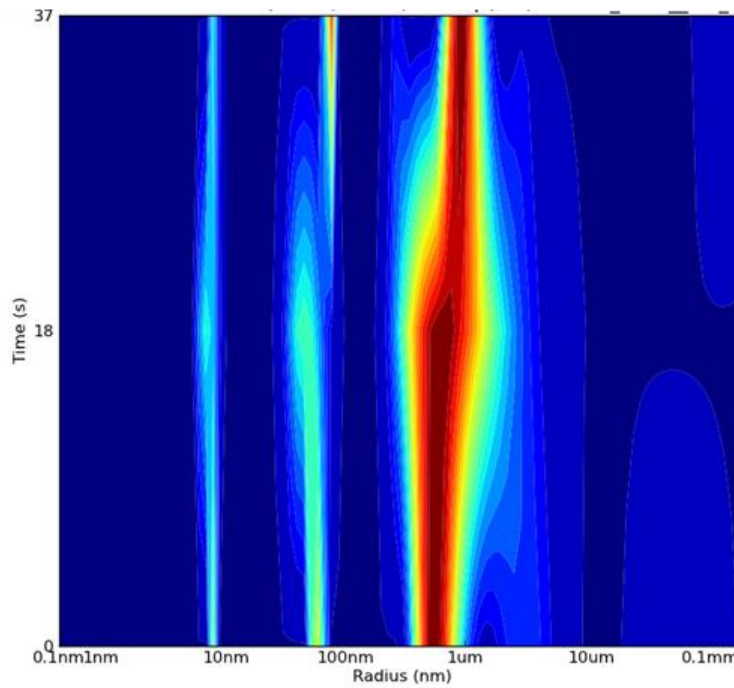
Figure 5.9 DLS heat map of purified protein with (a) and without (b) the addition of TCEP as a long term reducing agent.

5.2.3. MACROCRYSTALLIZATION OF KDO8PS

Macrocrystals approximately 0.1 mm that were grown via vapor diffusion (Figure 5.9) via the Phoenix robot in a 96 well plate. Drops were prepared by mixing 4 µL of KDO8PS (~20 mg/mL) with 2 µL of reservoir solution. The reservoir solution of the most promising condition was composed of 0.428 M 2-(*N*-morpholino)ethanesulfonate (MOPS) pH 6.1 and 2.72% PEG 400. The crystals were grown at room temperature over a time period of approximately one month. Prior to freezing, the looped crystal were dipped in the reservoir solution to which 30% glycerol was added as cryoprotectant. Data was collected at the Advanced Photon Source. Indexing was perfumed with MOSFLM and the phase was determined using molecular replacement using protein data bank entry 1X8F. The structure of KDO8PS was solved to a resolution of 2.0 Å, the data statistics are shown in table 5.1. The $(\beta/\alpha)_8$ monomer of KDO8PS is shown in Figure 5.10. The crystals were purified with only one chromatography step with the last purification step being a recrystallization. The majority of the literature uses up to four chromatography purifications, from native *E. coli* cell pellet but a one-step purification step has been employed for NMR studies (Dotson, Dua et al 1995). This lack of additional steps resulted in a higher resolution (2.0 Å) than any other structure deposited in the protein data bank. We hypothesize that small impurities may aid in increased resolution.
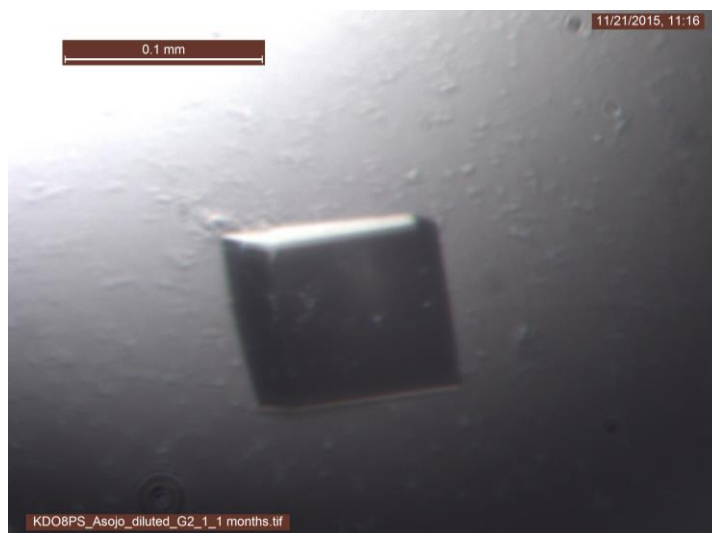
Figure 5.10 Macrocrystal grown via vapor diffusion.
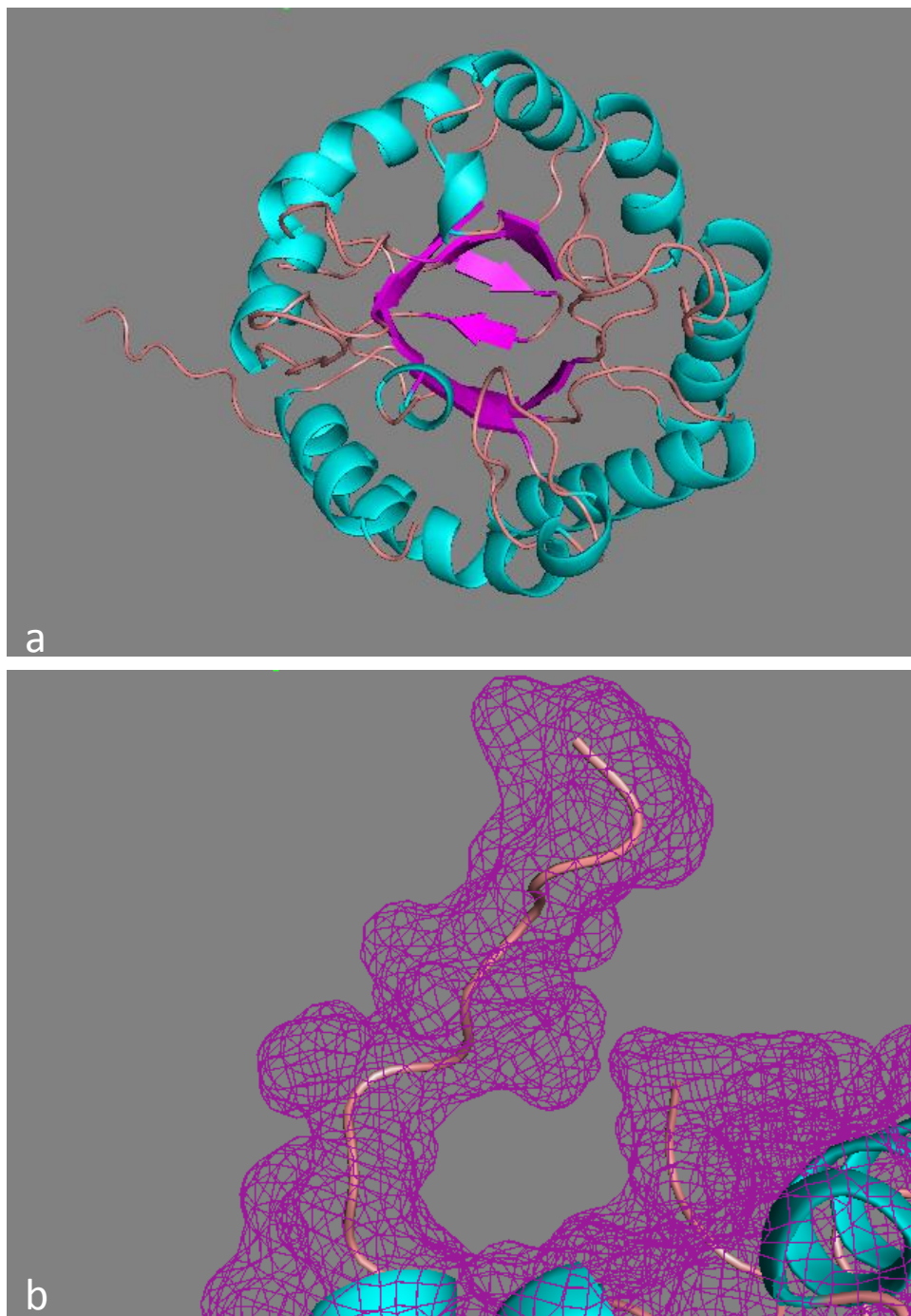
Figure 5.11 Structure of KDO8PS monomer. a) View looking down the "uneven funnel" active site of the $(\beta/\alpha)_8$ barrel of KDO8PS, where PEP binds at the bottom of the funnel and A5P binds near the entrance of the funnel. b) electron density of N terminus.

Table 5.1
Data quality statistics of KDO8PS dataset.

Values in parenthesis are for the highest resolution shell.

Wavelength (Å)	0.97
Maximum Resolution (Å)	2.0
Resolution (Å)	41.57 - 2.0 (2.072- 2.0)
Space group	I 2 3
a b, c (Å)	117.579, 117.579, 117.579
α,β, γ (°)	90, 90, 90
Total reflections	84767 (3873)
Unique reflections	18214 (1695)
I/δ(I)	17.7 (1.77)
Multiplicity	4.7 (2.3)
Completeness (%)	99.7
CC*(%)	1 (0.792)
R_{merge}	0.04278 (0.5097)
Maximum Resolution (Å)	2.0
Resolution (Å)	41.57 - 2.0 (2.072- 2.0)
Space group	I 2 3
a b, c (Å)	117.579, 117.579, 117.579
α,β, γ (°)	90, 90, 90
Total reflections	84767 (3873)
Unique reflections	18214 (1695)
I/δ(I)	17.7 (1.77)
Multiplicity	4.7 (2.3)
Completeness (%)	99.7
CC*(%)	1 (0.792)
R_{merge}	0.04278 (0.5097)
R_{free}	0.2918 (0.3932)
R_{work}	0.2654 (0.4165)
Wilson B-factor	40.26

5.2.3. MICROCRYSTALLIZATION OF KDO8PS

Figure 5.12 shows 3-10 µm cubic microcrystals of KDO8PS were grown by the method of free interface diffusion described by Kupitz et al. (Kupitz, Grotjohann et al. 2014) by dropping 30 µLs of 20% poly(ethylene glycol) methyl ether (PEGME) 5,000 were dropped into 30 µLs into 21 mg/mL KDO8PS. The crystals were incubated at room temperature for one and a half hours, then the supernatant was removed and the pellet was collected. The microcrystals were then prefiltered with a 20 µm stainless steel filter and delivered to the XFEL beam using a 50 µm inner diameter gas dynamic virtual nozzle. The microcrystals were characterized by optical microscopy and differential interference contrast microscopy. 3-10 µm KDO8PS microcrystals showed

diffraction at Linac Coherent Light Source using the Coherent X-ray Imaging instrument (Figure 5.13). Data were collected for 5 minutes at 9.57 keV, 100% transmission, at an X-ray pulse energy of 1.43 mJ, a detector distance of 186 mm.

To determine if substrate soaking and/or binding impacted the diffraction of microcrystals, the microcrystals were soaked with one or both substrates and then powder diffraction was measured. After mixing with 2.5 mM A5P or 2.5 mM PEP or both (substrate was dissolved in 10% PEGME 5k), the microcrystals were pipetted into a Mitogen sleeve and centrifuged for 1 minute. Powder diffraction was taken at time intervals of ten minutes, 3 hours, and 24 hours and no difference in powder diffraction was seen between any of the soaked samples when compared to the control (Figure 5.14). This experiment indicated that PEP could be soaked prior to the time-resolved mixing and that the crystals do not dissolve in the presence of both substrates.

For SMX studies, slightly larger crystals 20-25 µm crystals (Figure 5.15) can be grown using the batch method where an equal volume of 21 mg/mL KDO8PS was pipette mixed with ¼ total volume aliquots of PEGME 5,000. For example, 100 µL of protein was mixed with 25 uLs of 20% PEGME 5000 until completely homogenous for a total of four times. Although there is not a full data set of KDO8PS microcrystals (due to limited beamtime), data from poly(ethylene oxide) embedded with KDO8PS crystals (see section 4.2 and 4.3) show that the crystals have the expected unit cell dimensions (5.16).

5.2.4 ENZYME ACTIVITY ASSAY

Enzyme activity was verified by using the thiobarbituric acid assay which detects the formation of deoxy sugars such as KDO8P as described in Duewel and Woodard 2000 (Duewel and Woodard 2000). Briefly, ~0.15 mg/mL KDO8PS, 10 mM PEP, 10 mM A5P, 50 mM Tris pH 7.3 at 37°C for 5 mins at 37°C allowing the product, KDO8P to be produced by KDO8PS. The reaction is then quenched with an equal volume of *cold* 10% wt/vol trichloroacetic acid by precipitating the protein. The reaction is then centrifuged at 10,000xg for 2 mins to pellet the
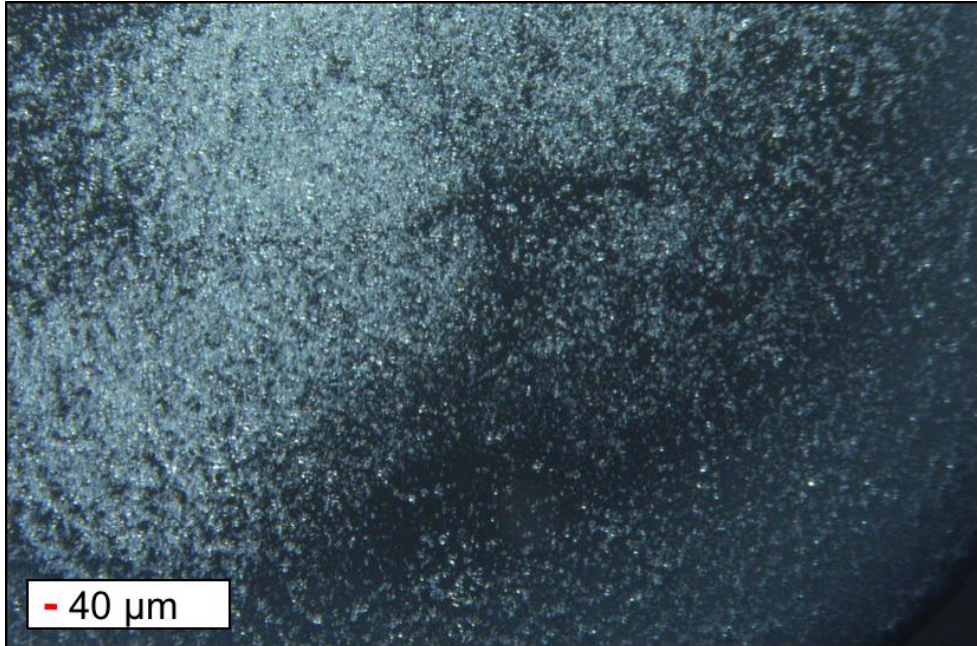
(a)
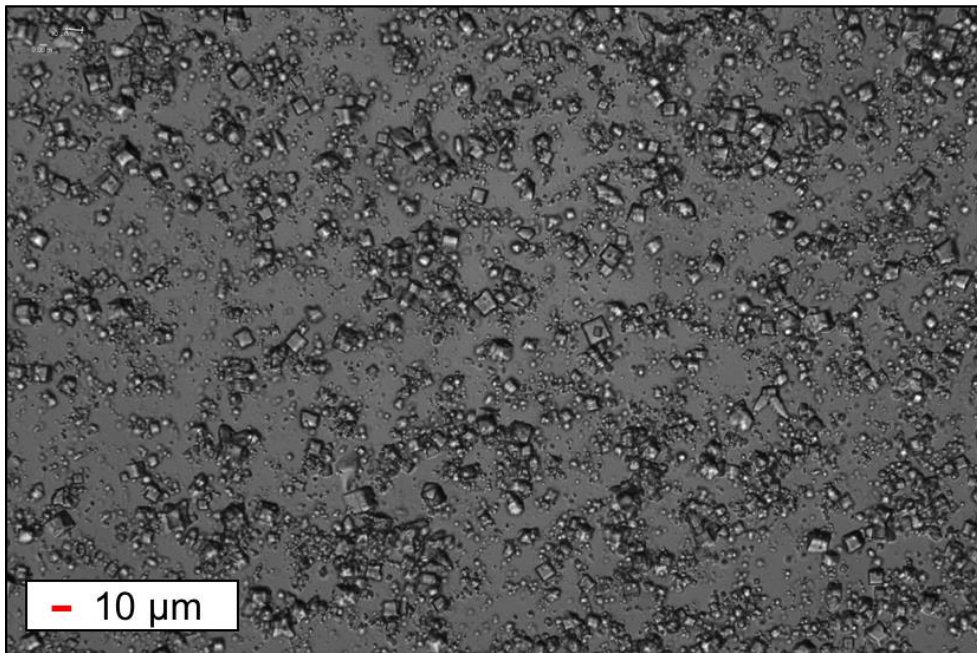
(b)

Figure 5.12 *KDO8PS Microcrystals a) crystals observed under polarized light b) crystals observed by a differential interference contrast microscope.*
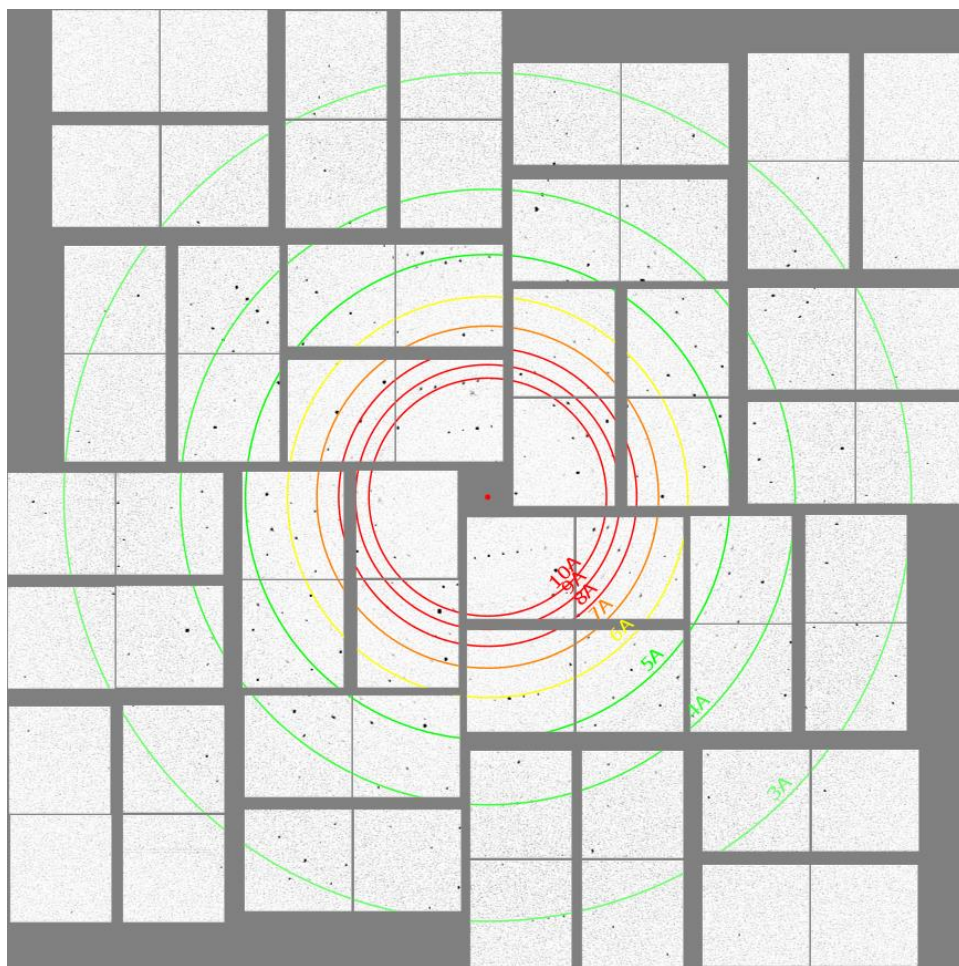
Figure 5.13 Diffraction of KDO8PS microcrystals at the coherent X-ray imaging instrument at the Linac Coherent Light Source.

precipitated protein. 50 µLs of the supernatant is then added to a glass vial. 100 µLs of 25 mM sodium periodate (NaIO$_4$) in H$_2$SO$_4$ (0.125 N) is then mixed with the reaction mixture and incubated for 10 minutes at room temperature. The periodate reaction results in oxidation of the alcohols of KDO8P causing the ring to open and split into two molecules, one of the two molecules most likely is malondialdehyde (MDA), the actual mechanism remains unknown. The excess oxidant is reduced by the addition of 200 µLs of NaAsO$_2$ 2% w/v in 0.5 M HCl, incubated until the yellow color disappears. Then 2 mLs of thiobarbituric acid solution 0.36% w/v, pH 9 is added and the solution is heated to 100 °C for 10 minutes to produce a pinkish/red color. The chromophore that results after heating most likely occurs from one MDA reacting with two
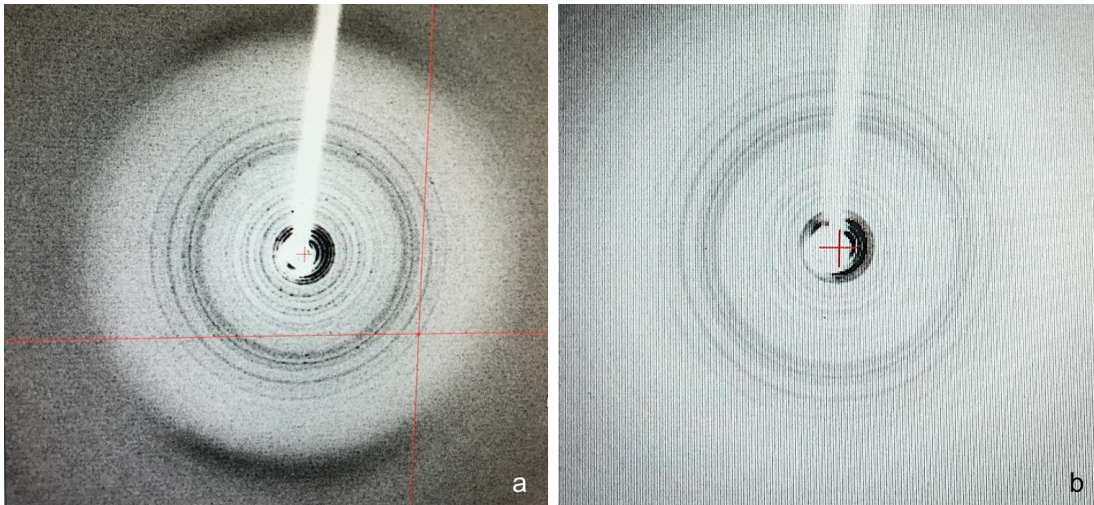
Figure 5.14 Substrate Soaking Powder Diffraction Experiment. a) microcrystals unexposed to both A5P and PEP. b) microcrystals soaked with both A5P and PEP for 23 hours. Both diffracted to 7.5 Å.
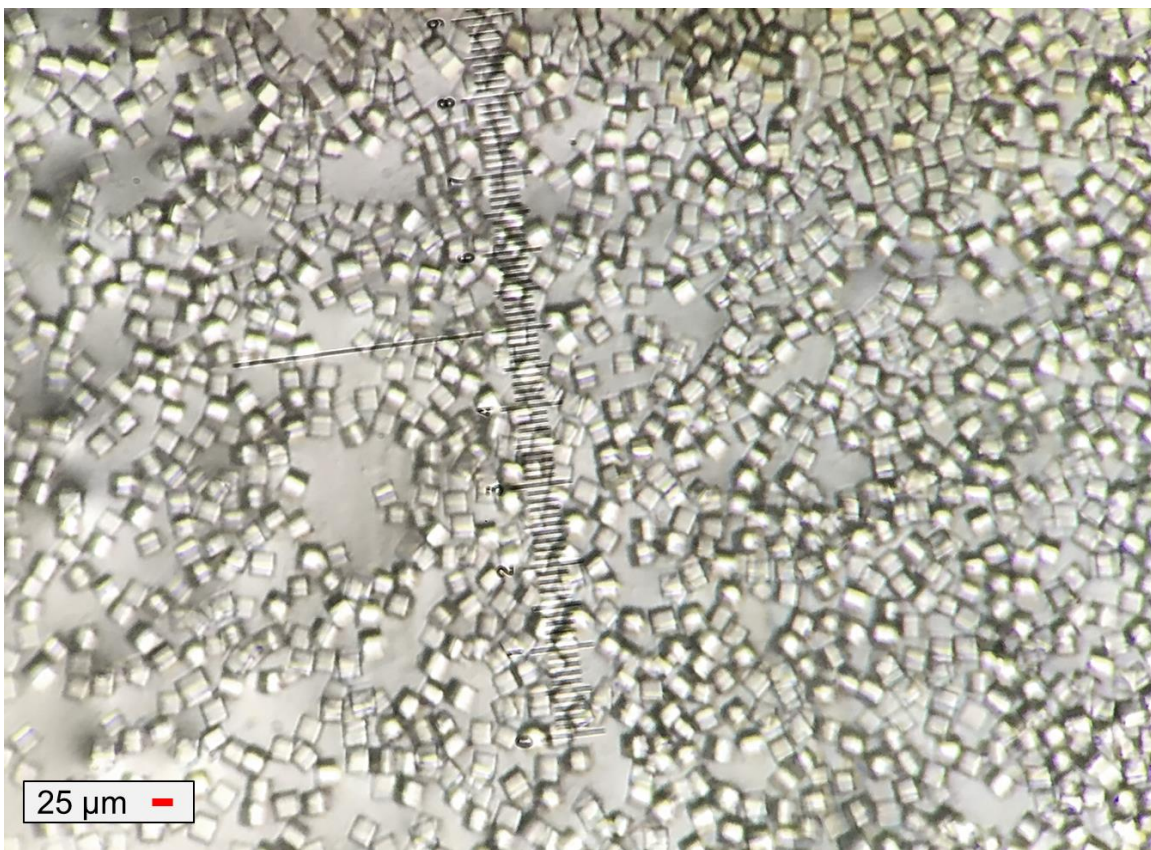
Figure 5.15 KDO8PS microcrystals for synchrotron studies
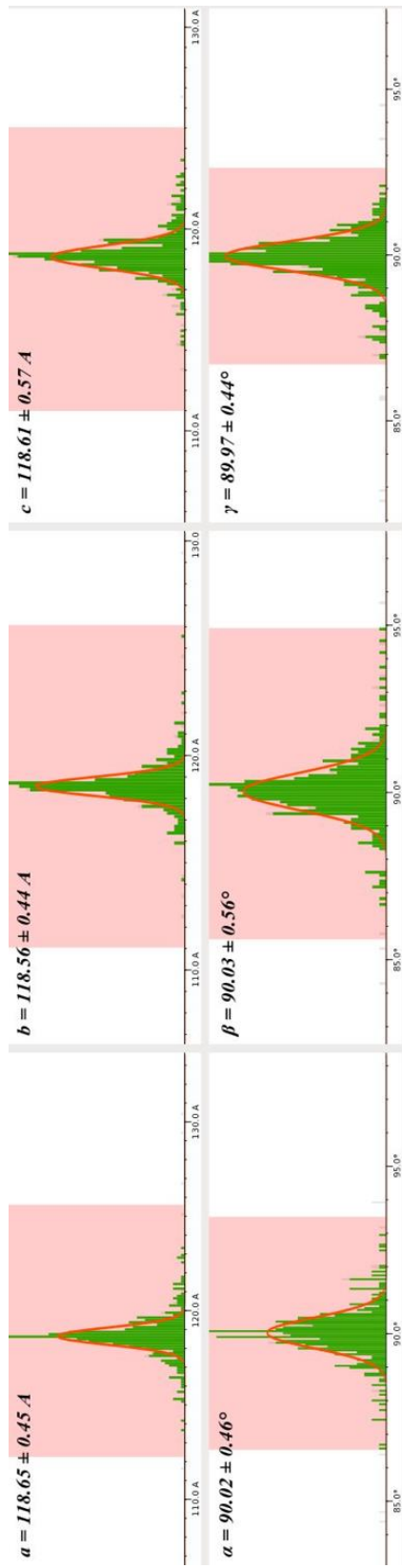
Figure 5.16 Unit cell distribution of KDO8PS delivered in PEO at Advanced Photon Source. The unit cell is presumed to be I23.

124

thiobarbituric acid molecules via a condensation reaction. After cooling the absorbance at 549 nm (ε =1.03 x $10^5 M^{-1}$ cm^{-1}) is measured. ~1 mg of deoxyribose is used a positive control, as this assays detects deoxy sugars, to indicate that the periodate and thiobarbituric acid are reactive. Enzyme activity from protein that had been crystallized was checked to ensure that crystallization did not affect enzyme activity by dissolving KDO8PS crystals and then executing the assay as described (Figure 5.15).

KDO8P Production vs Time
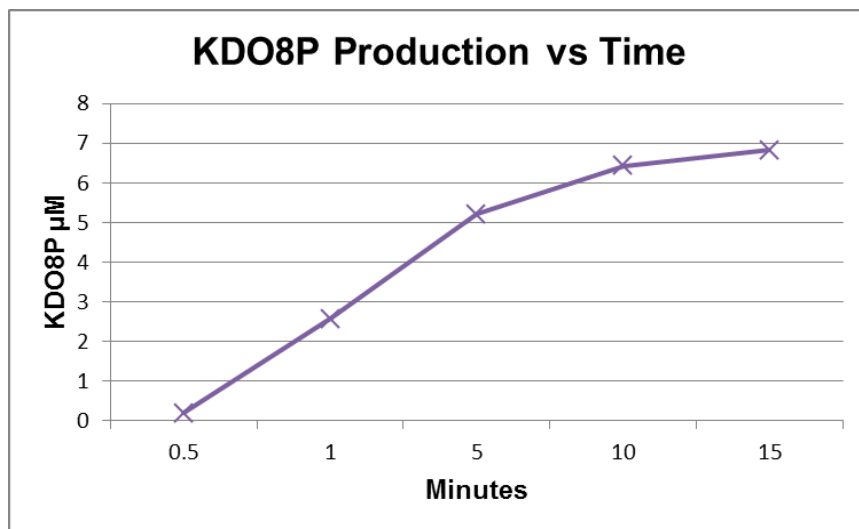
Figure 5.17 KDO8P Production over time. 1 µL of KDO8PS crystals were subjected to the activity assay described in section 5.2.4.

5.3. OUTLOOK

Structural dynamics of most enzymes by X-ray crystallography was unattainable due to diffusion times being much slower than the enzymatic process itself. The renaissance of serial crystallography has allowed much smaller crystals to be probed by X-ray crystallography. These small crystals have much smaller diffusion times, thus opening up the possibility of time-resolved crystallography by diffusion of a substrate into the microcrystal. As a model system for these time-resolved experiments, KDO8PS has been explored. For these experiments, KDO8PS microcrystals have been characterized via powder diffraction and enzyme activity assays. As

XFEL beamtime is limited, two different strategies for time-resolved KDO8PS diffusion mixing experiments are possible.

Lysozyme crystals down 4x6 μm^2 at microfocus beamlines have resulted in high resolution diffraction (2.1 Å) (Stellato, Oberthür et al. 2014) but this is a function of specific experimental and sample parameters (e.g. unit cell size, beam focus, brilliance). Typically, minimal crystal sizes in microfocus experiments are at least 10 µm and require "snapshot" exposures in excess of 10 ms for reliable signal to noise. This limits the time resolution possible to the hundreds of millisecond regime due to both the diffusion time of substrate into crystals of this size, sample delivery, and the exposure time. Unlike synchrotron light sources, XFEL pulses are so brilliant that nanocrystals (≤ 200 nm) with ≤50 fs pulse length produce diffraction and thus much faster temporal resolution is possible with diffusion becoming the limiting step (Hunter and Fromme 2011) (Schmidt 2013). In order to accommodate the difference in experimental and instrumental parameters, two different experimental setups could be used at each respective light source and subsequent time points. To achieve sufficient exposure times at the microfocus beamline a tape drive could be employed in which the crystal slurry is delivered by "writing" the crystals onto Kapton tape that moves at a programmed speed through the X-ray interaction region. The crystal slurry could be delivered onto the tape by a capillary coupled to a microfluidic chip that provided short mixing times. See Figures 5.18 for simulations of microfluidic mixing and Figure 5.19 for a depiction of the tape drive coupled with a microfluidic chip. For faster time points, similar to the GDVN (DePonte, Weierstall et al. 2008, Wang, Weierstall et al. 2014) to form a 2- µm stream of crystals at the interaction region (Figure 5.20). Using a microfluidic nozzle, less than 10 ms time points can be achieved as mixing occurs very close to the X-ray interaction region. This experiment would require an XFEL as the crystals would need to be below approximately 5x5x5 μm^3 in order to minimize diffusion times. Currently, only an electron density can be used to determine if time-resolved diffusion mixing has resulted in a change in the enzyme. Therefore, without prior kinetic information, probing for changes such an intermediate or product bound can be equated to throwing darts in the dark. Finding an interesting time point is 20 especially difficult with the lack of XFEL experimental time. KDO8PS thus is an ideal model

for these experiments as previous time-resolved solution mixing provides information about the

expected populations over time (Figure 5.2). With this prior knowledge, KDO8PS serves as an

ideal model for proof of principle experiments and may help to better understand diffusion times
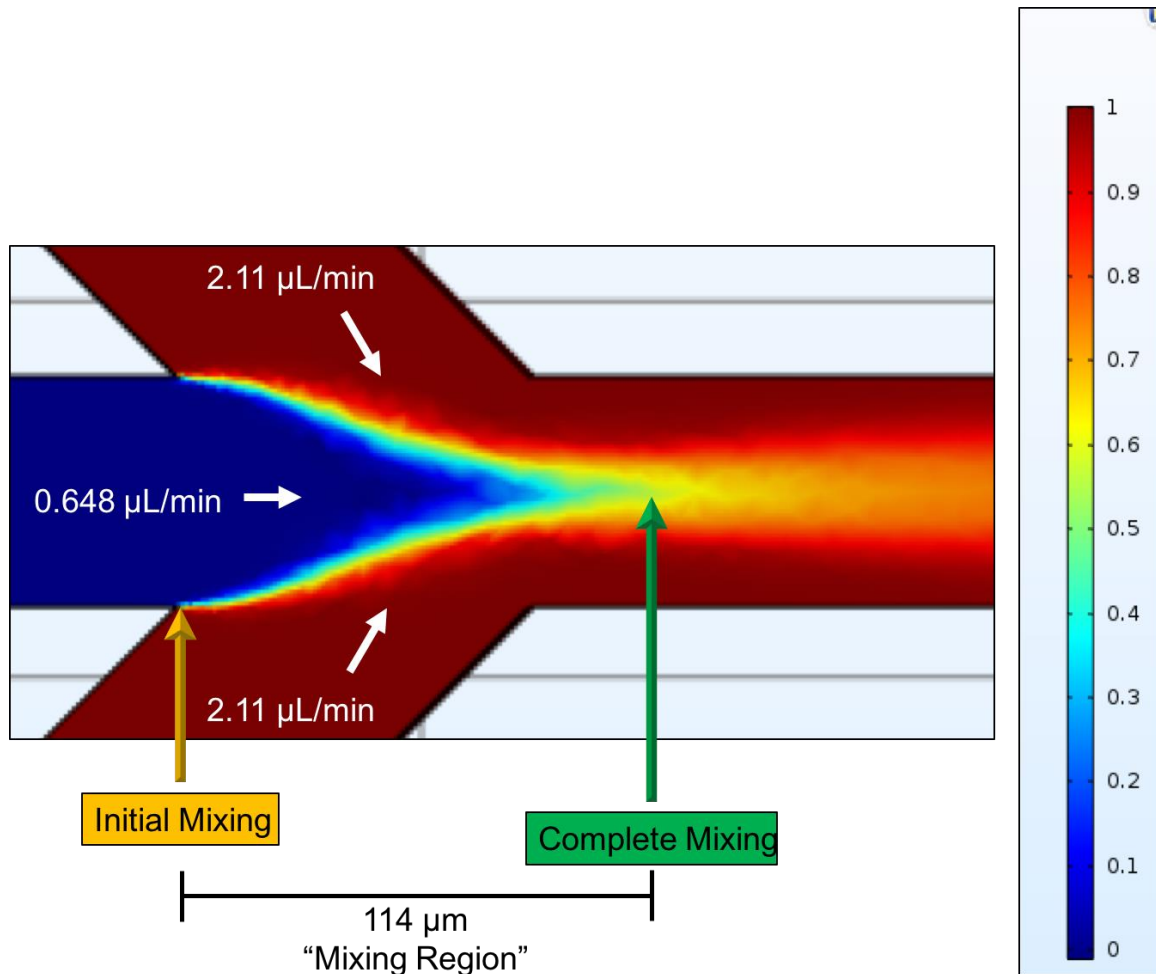
Figure 5.18 Finite element analysis of mixing times with hydrodynamic focusing in microfluidic channels employing a convection diffusion model for synchrotron studies. The substrate enters from the two side channels, depicted in blue while the crystals, shown in red, enter from the center channel. At a flow velocity of 0.007 m/s in the focusing cone, the distance from the substrate (side inlets) meeting the crystal suspension (center inlet) is 114 μm (in a microfluidic chip with channels 60 μm high), thus mixing time is ~16 ms. The heat scale depicts normalized concentration where 1 is only substrate solution, thus at 0.5 mixing is complete. A similar design with increased flow rates would produce faster mixing times for XFEL experiments. Simulation courtesy of Austin Echelmeier.
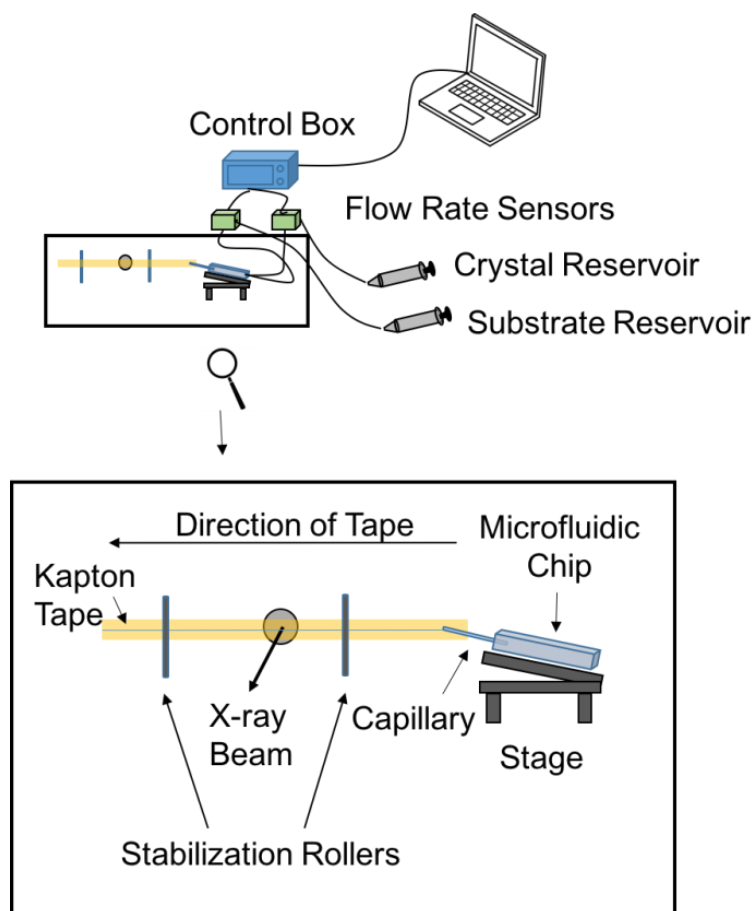
Figure 5.19 Tape drive setup for time-resolved diffusion mixing experiments at a synchrotron. Substrate and crystals could be mixed in a microfluidic chip coupled with a capillary as an outlet. The capillary could then be positioned as to "write" the mixed solution onto the tape which then moves across the X-ray interaction region, slow enough to achieve 10 ms exposure times. The total time after mixing until exposure time is estimated to be 357 ms which is the shortest time possible with the tape drive delivery.

into microcrystals. Moreover, short time points (tens of milliseconds) employing a microfluidic nozzle may allow for KDO8PS bound to the intermediate to be resolved, shedding light onto the mechanism which may aid in developing new antibiotics for gram-negative bacteria.
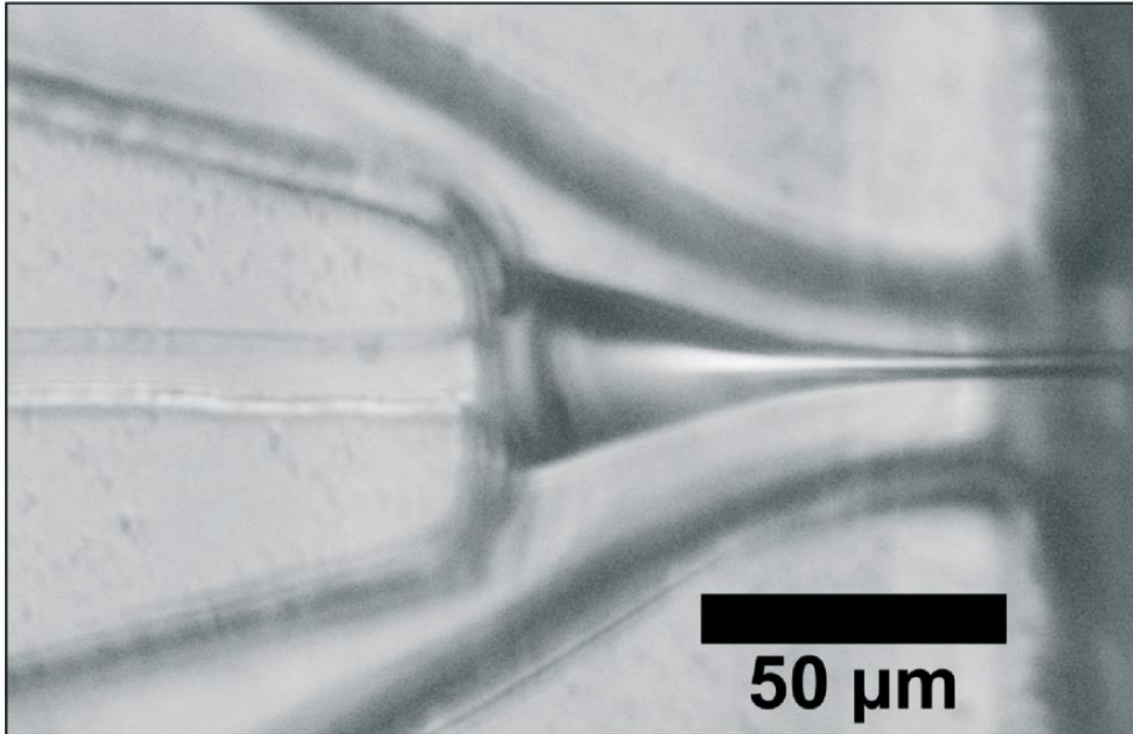
Figure 5.19 Nozzle coupled to a microfluidic chip. Light microscopic image of one microfluidic nozzle during operation. The liquid in the central channel is focused with pressured air which enables stable liquid jets with small diameters at low sample flow rates while it runs essentially with no clogging due to this air sheath. Image reprinted and caption modified with permission from (Trebbin, Kruger et al. 2014).

CHAPTER 6

CONCLUSION AND OUTLOOK

6.1 *CONCLUSION*

Serial femtosecond crystallography has been shown to solve some of the major limitations of X-ray crystallography: radiation damage and growing large crystals. This technique will most likely never replace traditional crystallography especially as beamtime is very limited, but it has proven to be a valuable tool to study radiation sensitive proteins, systems that only produce nano/microcrystals and opens a new era in structural biology as it allows structural biologists to study dynamics of reactions in Biology. Particularly impactful is the ability to study enzyme dynamics at room temperature. To date time-resolved serial femtosecond crystallography has probed states in the kok cycle which uses light driven reactions to split water (Kupitz, 2014), the photocycle of photoactive protein (Tenboer, 2014), the photocycle of bacteriorhodpsin (Nogly, 2016), and photolysis of the Fe-CO bond (Barends, 2015). With this new tool of time-resolved serial femtosecond crystallography, structural biologists can now make "molecular movies" where each time point is a still frame, when many of these still frames are played together, a movie of the enzyme in motion is observed.

6.2 RESULTS SUMMARY

6.2.1. VISCOUS SAMPLE DELIVERY

One of the largest limitations of serial femtosecond crystallography remains the high sample consumption. Agarose has proven to be a viable option for a wide variety of macromolecular crystals systems, particularly for membrane proteins which can be especially difficult to produce in large volumes. Agarose has been shown to work in vacuum and in atmosphere, proving that it is amenable for expanding experimental setups. Additional work such as degassing and using an electrospinning delivery method have been explored to further the uses and efficiency of this technique. Agarose has shown to be a viable carrier for soluble

proteins and preliminary data shows it may also be amenable for membrane proteins. To date, the agarose jet has formed the basis to achieve the first X-ray diffraction results for a large virus system (Lawrence, Conrad et al. 2015) and formed the basis for the discovery of the dynamics of ribonucleic acids (Stagno, Liu et al. 2016). It can be applied to membrane proteins (Conrad, Basu et al. 2015), multi-protein complexes (Conrad, Basu et al. 2015), and soluble proteins (Conrad, Basu et al. 2015) as well as viruses (Lawrence, Conrad et al. 2015). Poly(ethylene oxide) has been shown to be a useful tool for serial millisecond crystallography experiments and preliminary results also show that it may be suitable for serial femtosecond crystallography experiments in vacuum and ambient conditions experiments and that it may also be highly suitable for membrane protein delivery. In the future, both media may also be shown to be amenable for time-resolved serial crystallography experiments, widening their applications further. Both the agarose and poly(ethylene oxide) delivery systems have been critical new technologies for serial femtosecond and serial millisecond crystallography and both decreased sample consumption, allowing for structure discovery of difficult to express, purify, and crystallize macromolecular systems.

6.2.2. KDO8PS AS A MODEL FOR TIME-RESOLVED DIFFUSION MIXING EXPERIMENTS

While light triggered enzymatic reactions are important, the majority of enzymes are not light triggered. Constraints such as long diffusion times, radiation damage, and lack of enzymatic knowledge have limited time-resolved diffusion mixing experiments. With microcrystals, long diffusion times are no longer the limiting factor. Consequently, time-resolved serial femtosecond crystallography has allowed the first opportunity to study enzymatic reaction dynamics in crystals in real time by triggering the reaction by rapid mixing. This technique has the potential to revolutionize structural enzymology, and the first step has been the publication of the dynamics of ribonucleic acids by time-resolved serial femtosecond crystallography in Nature, November 2016.

Previous time-resolved electrospray ionization mass spectrometry experiments, where 3-deoxy-D-manno-2-octulosonate-8-phosphate synthase (KDO8PS) was mixed with one of its

substrates (A5P), have shown intermediate and product populations can be observed on a millisecond timescale. Presently, experimental determination of diffusion of substrate into a microcrystal is difficult. The only way to currently determine if a change has occurred is from the electron density. So without prior knowledge of the kinetics in the crystals, many time points must be probed to determine the progression of the reaction. Because time-resolved electrospray ionization mass spectrometry experiments have already been carried out on KDO8PS, time points to probe have already been determined. Thus KDO8PS is an ideal model for the development of time-resolved serial femtosecond crystallography of enzymatic reactions. To obtain KDO8PS bound to the product on a 100s of ms time scale, mixing via a microfluidic chip followed by tape drive delivery was proposed. Furthermore, a snapshot of tens of ms time scale, using a microfluidic nozzle and an XFEL may allow for the intermediate to be captured. Well diffracting KDO8PS microcrystals have been made for these future time-resolved diffusion mixing experiments which are scheduled for December 7th, 2016 at the Linac Coherent Light Source. In this experiment, crystals will be soaked in phosphoenolpyruvate prior and arabinose 5 phosphate will be mixed with the microcrystals prior to diffraction using a 3D printed mixer coupled to a 3D printed nozzle. By engineering a mixer attached to a nozzle, mixing occurs immediately prior to sample injection to the X-ray interaction region, allowing tens of milliseconds after mixing to be probed. The cubic shape of these crystals is ideal as diffusion of substrate into the crystal should be equal on all sides. Additionally, the resolution of the unbound crystals is high enough that equal resolution after mixing would show substrate, intermediate, and product bound.

6.3 SUMMARY OF EXPERIMENTS

Serial crystallography experiments require large international collaborations to be successful as many different types of expertise are necessary to perform these challenging experiments. For example, a typical serial crystallography experiment requires protein purification and characterization, microcrystallization, sample loading, sample injection, and data collection. From the many serial crystallography experiments that I have been involved in, I have learned

microcrystallization techniques which have been applied to many systems (TMEM205, mKate, rhodopsin, photoactive yellow protein, photosystem II, KDO8PS, and adenine riboswitch). I have also been involved in crystal characterization via second order non-linear imaging of chiral crystals, tryptophan fluorescence, and dynamic light scattering and sample injection via both the gas dynamic virtual nozzle and lipidic cubic phase injector. Because these experiments require so many different expertise and because the field is so young, I have collaborated with many groups due to my serial femtosecond crystallography experience. These groups collaborated with me for my expertise in microcrystallization, crystal characterization, large scale sample preparation, as well as sample loading and sample injection. In some of these collaborations I have participated in on-site crystal characterization and data collection, while for others I have also been involved in finding or optimizing microcrystallization conditions, characterizing microcrystals, planning the experiment, as well as on-site data collection. Additionally, many of these collaborations were initiated by the agarose jet techniques that I developed. Its low sample consumption and low background have been critical for some projects which could not produce a large enough quantity for serial crystallography experiments. Below I summarize the publications to which I have made important contributions that have resulted from these serial crystallography collaborations or are related to method development for serial crystallography.

6.3.1. TIME-RESOLVED SERIAL CRYSTALLOGRAPHY OF A LIGHT-DRIVEN PROTON PUMP USING A LIPIDIC CUBIC PHASE INJECTOR

P. Nogly, V. Panneels, G. Nelson, C. Gati, T. Kimura, C. Milne, D. Milathianaki, M. Kubo, W. Wu, **C.E. Conrad**, J. Coe, R. Bean, Y. Zhao, P. Båth, R. Dods, R. Harimoorthy, K. Beyerlein, J. Rheinberger, D. James, D. DePonte, C. Li, L. Sala, G. Williams, M. Hunter, J.E. Koglin, P. Berntsen, E. Nango, S. Iwata, H. Chapman, P. Fromme, M. Frank, R. Abela, S.Boutet, A. Barty, T. White, U. Weierstall, J. Spence, R. Neutze, G. Schertler, J. Standfuss, Time-resolved serial crystallography of a light-driven proton pump using a lipidic cubic phase injector, Nature Communications **7**:12314 *(*2016).

Abstract: Serial femtosecond crystallography (SFX) using X-ray free-electron laser sources is an emerging method with considerable potential for time-resolved pump-probe experiments. Here we present a lipidic cubic phase SFX structure of the light-driven proton pump bacteriorhodopsin (bR) to 2.3 Å resolution and a method to investigate protein dynamics with modest sample requirement. Time-resolved SFX (TR-SFX) with a pump-probe delay of 1 ms yields difference Fourier maps compatible with the dark to M state transition of bR. Importantly, the method is very sample efficient and

reduces sample consumption to about 1 mg per collected time point. Accumulation of M intermediate within the crystal lattice is confirmed by time-resolved visible absorption spectroscopy. This study provides an important step towards characterizing the complete photocycle dynamics of retinal proteins and demonstrates the feasibility of a sample efficient viscous medium jet for TR-SFX.

This experiment was the first to show that time-resolved SFX studies could also be executed at XFELs by viscous sample delivery, not just the GDVN. As a model system for this time-resolved study, bacteriorhodpsin was chosen as the photocycle is well studied and the crystals can be grown in LCP. To prove that time-resolved studies are possible, bacteriorhodopsin crystals grown in LCP were delivered to the XFEL beam via the LCP injector, prior to extrusion, the crystals were pumped with a femtosecond laser. Dark state data collected from cryo cooled crystals and data from serial synchrotron crystallography agrees with the data (Figure 6.1). In addition, the bacteriorhodopsin intermediate state, M was resolved at the 1 ms time point which matches previous measurements using Raman, absorption, infrared spectroscopy. These results indicate that the LCP medium does not affect photoactivation. Thus, this proves that pump probe experiments can be done in LCP which opens a new avenue for studying other light activated proteins that can only be grown in LCP. Moreover, this paper demonstrates that time-resolved studies no longer require large sample volumes. It is important to note that to avoid exciting a crystal upstream that these viscous jet must be run at a higher velocity (4.22 μm/ms) so more sample is consumed than non time-resolved viscous jet experiments (3.6 mm/s). But because the sample is already diluted by the carrier medium, the total sample volumes are reduced at least ten fold or more. Additionally, this paper indicates that agarose, PEO, and other viscous crystal carriers in the future may be amenable for time-resolved experiments.
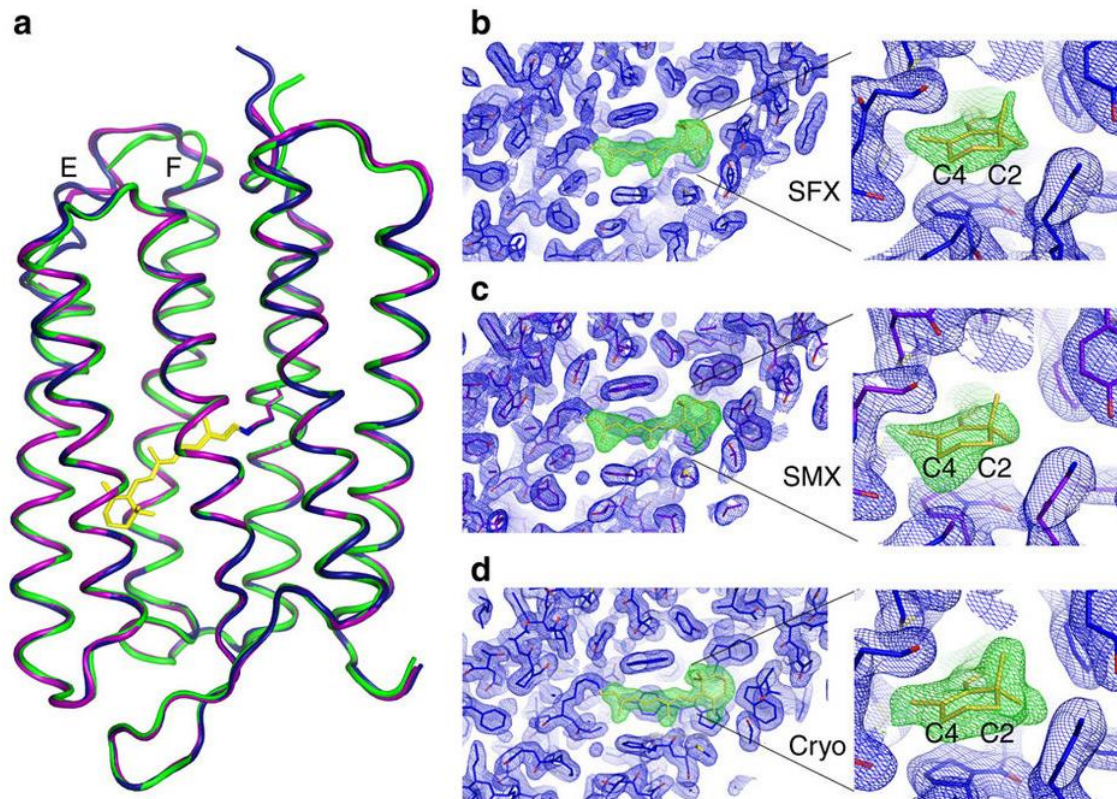
Figure 6.1 Comparison of bR dark-state structures. Overall structures determined by SFX (purple), SMX (blue) and conventional cryo-crystallography (Banerjee, Bartesaghi et al.). (a) Overall structures are highly similar with only minor deviations in loop regions and the termini. (b–d) Comparison of electron density maps in the retinal-binding pocket (SFX (b), SMX (c) and Cryo (d)). The electron density maps (blue, $2F_o−F_c$, 1 σ) are well defined in all three cases and strong positive density is observed when retinal (yellow sticks; left panel) is omitted during refinement (green, $F_o−F_c$, 2.5 σ). Flexible regions of the retinal β-ionone ring (insets), which are not part of the retinal conjugated double bond system, can be clearly identified in the two room temperature structures. Figure and caption used with permission from (Nogly, Panneels et al. 2016).

6.3.2. TIME-RESOLVED SERIAL CRYSTALLOGRAPHY CAPTURES HIGH-RESOLUTION INTERMEDIATES OF PHOTOACTIVE YELLOW PROTEIN

J. Tenboer, S. Basu, N. Zatsepin, K. Pande, D. Milathianaki, M. Frank, M. Hunter, S. Boutet, G.J. Williams, J.E. Koglin, D. Oberthuer, M. Heymann, C. Kupitz, **C. Conrad**, J. Coe, S. Roy-Chowdhury, U. Weierstall, D. James, D. Wang, T. Grant, A. Barty, O. Yefanov, J. Scales, Cornelius Gati, C. Seuring, V. Srajer, R. Henning, P. Schwander, R. Fromme, A. Ourmazd, Keith Moffat, J.J. Van Thor, J.C.H. Spence, P. Fromme, Henry N Chapman, and M. Schmidt, Time-Resolved Serial Crystallography Captures High-Resolution Intermediates of Photoactive Yellow Protein, *Science* **346** (6214) [2014].

Abstract: Serial femtosecond crystallography using ultrashort pulses from x-ray free electron lasers (XFELs) enables studies of the light-triggered dynamics of biomolecules. We used microcrystals of photoactive yellow protein (a bacterial blue light photoreceptor) as a model system and obtained high-resolution, time-resolved difference electron density maps of excellent quality with strong features; these allowed the determination of structures of reaction intermediates to a resolution of 1.6 angstroms. Our results open the way to the study of reversible and nonreversible biological reactions on time scales as short as femtoseconds under conditions that maximize the extent of reaction initiation throughout the crystal.

This publication was the first to present a high resolution structure produced by TR-SFX. Prior to this study, Laue crystallography was the most widely used method for TR crystallography experiments. Synchrotrons offer constant beam energy, photon flux, bandwidth, and data is collected on a small number of crystals. In comparison, XFELs collect data on a new crystal per shot, the microcrystals probed are not homogenous, the beam has shot to shot variation on peak energy and spectral content, and only partial reflections are recorded. Because such a small difference needs to be detected in time resolved data collection, it is imperative that fluctuations be minimized. In SFX these fluctuations are minimized by the fact that SFX requires merging of thousands of diffraction patterns. This experiment proved that although there are many factors that vary between each diffraction pattern, high resolution TR data could still be collected at an XFEL. TR-SFX offers several advantages over Laue crystallography, time resolution can be pushed to the femtosecond regime, microcrystals can be probed, mosaicity is less of a concern, smaller crystals allow for greater reaction initiation, limited radiation damage, room temperature measurements, and the ability to study irreversible reactions. As a model system, photoactive yellow protein (PYP) was studied as it has been used as a model for Laue experiments. For these experiments, two 20 Hz nanosecond lasers were used which allowed for every third diffraction pattern to be from an illuminated crystal. Six intermediates of PYP were probed via different time delays, each matched difference electron density maps from previous Laue experiments. One of the largest advantages to TR-SFX vs. Laue is the small crystal size which allows for the laser to completely penetrate the crystals, permitting uniform illumination in most cases. This allowed for a reaction initiation of 40% compared to 10-15% typically

achieved from synchrotron experiments. Thus, this experiment showed that the TR-SFX is possible and that TR-SFX has significant benefits over Laue crystallography.

6.3.3. MACROMOLECULAR DIFFRACTIVE IMAGING USING IMPERFECT CRYSTALS

K. Ayyer, O.M. Yefanov, D. Oberthür, S. Roy-Chowdhury, L. Galli, V. Mariani, S. Basu, J. Coe, **C.E. Conrad**, R. Fromme, A. Schaffer, K. Dörner, D. James, C. Kupitz, M. Metz, G. Nelson, P.L. Xavier, K.R. Beyerlein. M. Schmidt, I. Sarrou, J.C.H. Spence, U. Weierstall, T. A. White, J.-H. Yang, Y. Zhao, M. Liang, A. Aquila, M.S. Hunter, J.S. Robinson, J.E. Koglin, S. Boutet, P. Fromme, A. Barty, H.N. Chapman, Macromolecular diffractive imaging using imperfect crystals, *Nature* **530**, 7589 (2016).

Abstract: The three-dimensional structures of macromolecules and their complexes are mainly elucidated by X-ray protein crystallography. A major limitation of this method is access to high-quality crystals, which is necessary to ensure X-ray diffraction extends to sufficiently large scattering angles and hence yields information of sufficiently high resolution with which to solve the crystal structure. The observation that crystals with reduced unit-cell volumes and tighter macromolecular packing often produce higher-resolution Bragg peaks suggests that crystallographic resolution for some macromolecules may be limited not by their heterogeneity, but by a deviation of strict positional ordering of the crystalline lattice. Such displacements of molecules from the ideal lattice give rise to a continuous diffraction pattern that is equal to the incoherent sum of diffraction from rigid individual molecular complexes aligned along several discrete crystallographic orientations and that, consequently, contains more information than Bragg peaks alone. Although such continuous diffraction patterns have long been observed—and are of interest as a source of information about the dynamics of proteins—they have not been used for structure determination. Here we show for crystals of the integral membrane protein complex photosystem II that lattice disorder increases the information content and the resolution of the diffraction pattern well beyond the 4.5-ångström limit of measurable Bragg peaks, which allows us to phase the pattern directly. Using the molecular envelope conventionally determined at 4.5 ångströms as a constraint, we obtain a static image of the photosystem II dimer at a resolution of 3.5 ångströms. This result shows that continuous diffraction can be used to overcome what have long been supposed to be the resolution limits of macromolecular crystallography, using a method that exploits commonly encountered imperfect crystals and enables model-free phasing.

Additional X-ray scattering from imperfect crystals has been observed for many decades and was seen as unwanted background from poorly ordered crystals. As small translational misalignment in the crystal lattice leads to decreased Bragg diffraction, however, with decreasing Bragg diffraction comes increased scattering from these individually misaligned molecules, Figure 6.2. This scattering from individual molecules produces continuous diffraction. Thus because information from "single molecules" is being exploited, the phase problem no longer exists. In this

paper, imperfect PSII crystals were studied. The Bragg diffraction was limited to 4.5 Å but the continuous diffraction extended well past the water ring. Using the continuous diffraction resolution of the PSII structural model was extended to 3.5 Å and the phase was determined. To do this, the Bragg diffraction was used separately to create a low resolution envelope of a single PSII dimer. Iterative phasing of just the continuous diffraction data was then executed, where each iteration was restrained by the support obtained by the diffraction. After convergence was achieved, the Fourier amplitudes and phases were combined across all resolutions generating
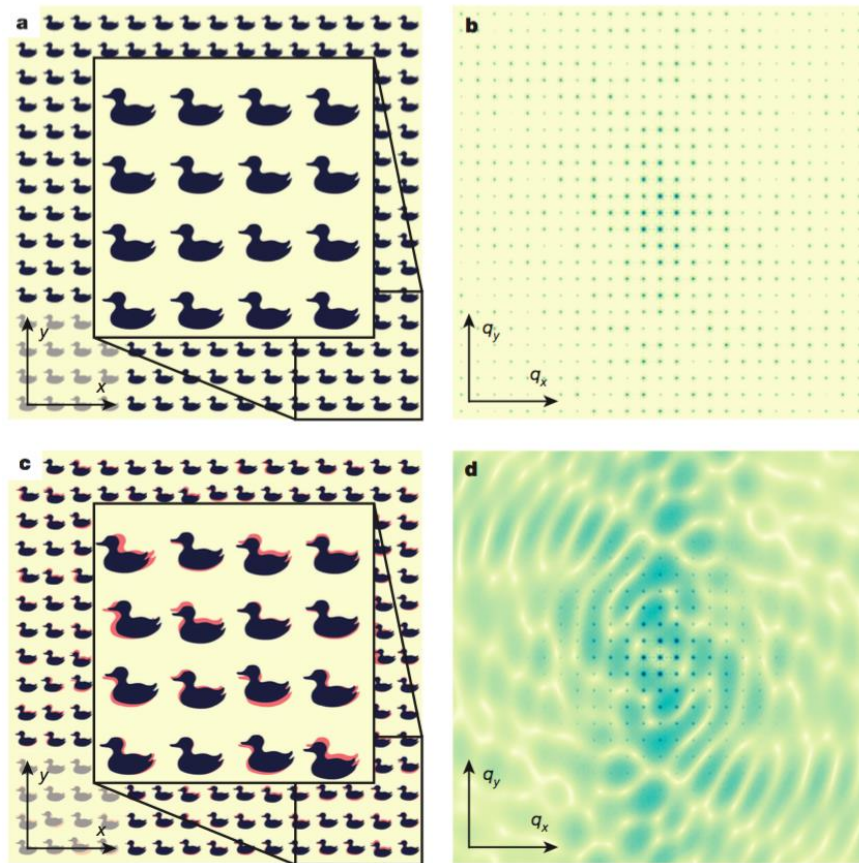
Figure 6.2 Lattice disorder reveals the continuous molecular transform. a, b, Diffraction from an arrangement of objects in a perfect lattice (a) results in regularly spaced Bragg peaks (b) as a result of constructive interference. c, d, Translational disorder of the objects at a length scale σ (c) disrupts Bragg interference beyond a reciprocal-lattice resolution length of $d = 1/q = 2\pi\sigma$ (d). The loss of correlation gives rise to the incoherent sum of the Fraunhofer diffraction patterns of individual objects, which increases with q in balance with the diminishing Bragg intensities. Here, σ was chosen to be 4% of the lattice spacing, leading to reduction of Bragg peaks at the fourth order. Figure and caption reproduced with permission from (Ayyer, Yefanov et al. 2016).

a 3.5 Å electron density. This study was done with only 2,848 diffraction patters so it is possible the resolution could be pushed even further. Although new, this paper made a significant impact in the field of crystallography, showing a new method to obtain structural information as well as phasing. In the future, this technique may push the resolution of other imperfect crystals using either SFX or traditional crystallography.

6.3.4. SERIAL FEMTOSECOND X-RAY DIFFRACTION OF ENVELOPED VIRUS MICROCRYSTALS, STRUCTURAL DYNAMICS

R.M. Lawrence, **C.E. Conrad**, N.A. Zatsepin, T.D. Grant, H. Liu, D. James, G. Nelson, G. Subramanian, A. Aquila, M.S. Hunter, M. Liang, S. Boutet, J. Coe, J.C.H. Spence, U. Weierstall, W. Liu, P. Fromme, V. Cherezov, and B.G. Hogue, Serial Femtosecond X-Ray Diffraction of Enveloped Virus Microcrystals, *Structural Dynamics* **2** (4), [2015].

Abstract: Serial femtosecond crystallography (SFX) using X-ray free-electron lasers has produced high-resolution, room temperature, time-resolved protein structures. We report preliminary SFX of Sindbis virus, an enveloped icosahedral RNA virus with ~700 Å diameter. Microcrystals delivered in viscous agarose medium diffracted to ~40 Å resolution. Small-angle diffuse X-ray scattering overlaid Bragg peaks and analysis suggests this results from molecular transforms of individual particles. Viral proteins undergo structural changes during entry and infection, which could, in principle, be studied with SFX. This is an important step toward determining room temperature structures from virus microcrystals that may enable time-resolved studies of enveloped viruses.

This was the first publication that used the agarose delivery method for structure determination after the agarose method was proven viable. Previously, these sindbis virus crystals were delivered via the GDVN but no diffraction was collected. Then these crystals were delivered both by LCP and agarose but only to low resolution. The Debye-Sherrer rings characteristic of LCP severely impacted the data collection and thus agarose was chosen as the primary delivery method. Due to the large size of these crystals (20-50 μm) the GDVN may have damaged the crystals during the delivery process; however, the agarose method does not require the crystals to be pre-filtered or focused into a smaller diameter which may have preserved the crystals. Interestingly, the crystals produced small angle X-ray angle scattering (SAXS) and Bragg diffraction. The factors that contribute to the SAXS remain uncertain but it is clear that the

SAXS signal is not from free virus particles as non-hits did not show SAXS signal. Further studies are needed to determine how this SAXS data can be used for structural information.

6.3.5. CRYSTAL STRUCTURE OF RHODOPSIN BOUND TO ARRESTIN BY FEMTOSECOND X-RAY LASER

Y. Kang, X.E. Zhou, X. Gao, Y. He, W. Liu, A. Ishchenko, A. Barty, T.A. White, O. Yefanov, G.W. Han, Q. Xu, P.W. de Waal, J. Ke, M.H.E. Tan, C. Zhang, A. Moeller, G.M. West, B.D. Pascal, N. van Eps, L.N. Caro, S.A. Vishnivetskiy, R.J. Lee, K.M. Suino-Powell, X. Gu, K. Pal, J. Ma, X. Zhi, S. Boutet, G.J. Williams, M. Messerschmidt, C. Gati, N.A. Zatsepin, D. Wang, D. James, S. Basu, **C.E. Conrad**, J. Coe, H. Liu, S. Lisova, C. Kupitz, I. Grotjohann, R. Fromme, Y. Jiang, M. Tan, H. Yang, J. Li, M. Wang, Z. Zheng, D. Li, N. Howe, Y. Zhao, J. Standfuss, K. Diederichs, Y. Dong, C.S. Potter, B. Carragher, M. Caffrey, H. Jiang, H.N. Chapman, J.C.H. Spence, P. Fromme, U. Weierstall, O.P. Ernst, V. Katritch, V.V. Gurevich, P.R. Griffin, W.L. Hubbell, R.C. Stevens, V. Cherezov, K. Melcher, and H.E. Xu, Crystal Structure of Rhodopsin Bound to Arrestin by Femtosecond X-Ray Laser, *Nature* **523** (7562), 561–567, [2015].

Abstract: G-protein-coupled receptors (GPCRs) signal primarily through G proteins or arrestins. Arrestin binding to GPCRs blocks G protein interaction and redirects signaling to numerous G-protein-independent pathways. Here we report the crystal structure of a constitutively active form of human rhodopsin bound to a pre-activated form of the mouse visual arrestin, determined by serial femtosecond X-ray laser crystallography. Together with extensive biochemical and mutagenesis data, the structure reveals an overall architecture of the rhodopsin-arrestin assembly in which rhodopsin uses distinct structural elements, including transmembrane helix 7 and helix 8, to recruit arrestin. Correspondingly, arrestin adopts the pre-activated conformation, with a ~20° rotation between the amino and carboxyl domains, which opens up a cleft in arrestin to accommodate a short helix formed by the second intracellular loop of rhodopsin. This structure provides a basis for understanding GPCR-mediated arrestin-biased signaling and demonstrates the power of X-ray lasers for advancing the frontiers of structural biology.

One of the most frequently accessed Nature publications, this paper made a large contribution to the field of G-protein coupled receptors (GPCR) as it showed arrestin bound to a GPCR. GPCRs are a large family of signal transducing membrane proteins characterized by having 7 transmembrane helices. This family of proteins are responsible for vision, smell, taste, among many other cellular communications. It has been estimated that 50% of all modern pharmaceuticals target GPCRs (Tautermann 2014). This extremely important class of proteins are regulated by heterotrimeric guanine-nucleotide-binding proteins (G proteins), GPCR kinases (GRKs) and arrestins. Only one structure of a GPCR bound to a G protein existed until this

publication which showed for the first time a GPCR bound to an arrestin. GPCRs are notorious for being difficult to crystallize as exhibited by the fact that as of 2015 only 33 unique GPCR structures had been solved out of the 800 known GPCRs. In order to grow crystals of the rhodopsin-arrestin complex, two point mutations were made so no light activation and phosphorylation was required for arrestin binding. Additionally, T4 lysozyme and a 15 residue linker were fused to rhodopsin to increase surface area and crystal contacts. Further validation of the complex's structure was done by double electron–electron resonance, hydrogen-deuterium exchange mass spectrometry, site specific disulfide cross linking studies, and cell-based rhodopsin–arrestin interaction assays, all were in agreeance with the SFX model. Surprisingly, arrestin binds rhodopsin in an asymmetric fashion, where the C domain embeds or touches the membrane, Figure 6.3. This now explains previous studies which showed that mutation of these residues affected arresting binding. This model also provides insight into arrestin recruiting, where upon recruitment arrestin rotates 20° and C-loop (CL) to accommodate the intracellular 2 helix of rhodopsin (fully activated state). The activated receptor also opens the cytoplasmic side of the transmembrane bundle to adopt the finger loop (FL) of arrestin. In this model, the tip of arrestin's C-domain contacts the membrane (red asterisk) between the N and C domains which opens a cleft for rhodopsins intracellular loop 2 (Figure 6.3). Future structures of other arrestin bound GPCRs will provide more information about arrestin binding such as if this a common binding motif or if this rotation only applies to rhodopsin.
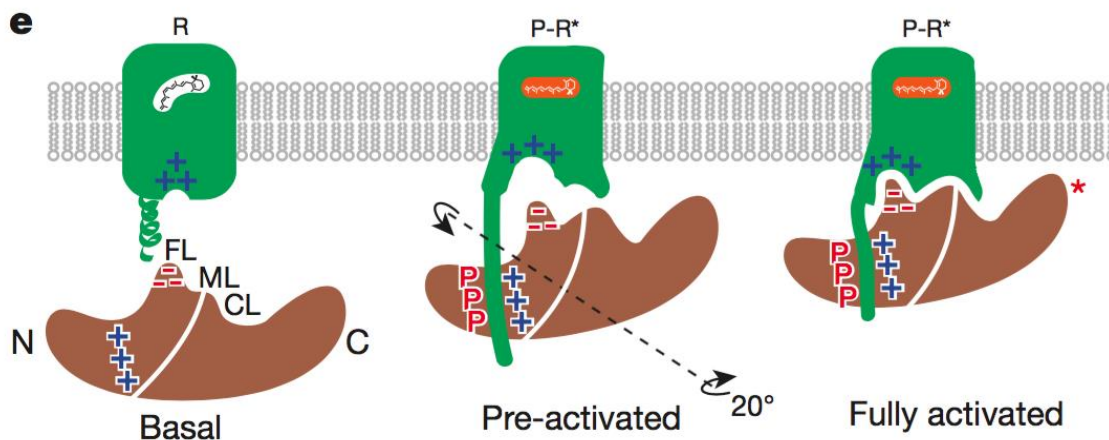
Figure 6.3 Structural basis of arrestin-biased signaling and arrestin recruitment. A cartoon model of arrestin recruitment by a phosphorylated and active rhodopsin. In the dark state, the receptor is inactive (R-state) and arrestin is in the closed state (basal state). Receptor activation and phosphorylation (P-R* state) allow the phosphorylated C-terminal tail of rhodopsin to bind to the N-domain of arrestin (pre-activated state), thus displacing the arrestin C-terminal tail. This displacement destabilizes the polar core of arrestin, which allows a 20° rotation between the arrestin N- and C-domains, leading to the opening of the middle loop (Henderson, Baldwin et al.). Figure and caption used with permission from (Kang, Zhou et al. 2015).

6.3.6. STRUCTURE OF THE ANGIOTENSIN RECEPTOR REVEALED BY SERIAL FEMTOSECOND CRYSTALLOGRAPHY

H. Zhang, H. Unal, C. Gati, G.W. Han, W. Liu, N.A. Zatsepin, D. James, D. Wang, G. Nelson, U. Weierstall, M.R. Sawaya, Q. Xu, M. Messerschmidt, G.J. Williams, S. Boutet, O.M. Yefanov, T.A. White, C. Wang, A. Ishchenko, K.C. Tirupula, R. Desnoyer, J. Coe, **C.E. Conrad**, P. Fromme, R.C. Stevens, V. Katritch, S.S. Karnik, and V. Cherezov, Structure of the Angiotensin Receptor Revealed by Serial Femtosecond Crystallography, *Cell* **161** (4) [2015].

Abstract: Angiotensin II type 1 receptor (AT_1R) is a G protein-coupled receptor that serves as a primary regulator for blood pressure maintenance. Although several anti-hypertensive drugs have been developed as AT_1R blockers (ARBs), the structural basis for AT_1R ligand-binding and regulation has remained elusive, mostly due to the difficulties of growing high-quality crystals for structure determination using synchrotron radiation. By applying the recently developed method of serial femtosecond crystallography at an X-ray free-electron laser, we successfully determined the room-temperature crystal structure of the human AT_1R in complex with its selective antagonist ZD7155 at 2.9-Å resolution. The AT_1R-ZD7155 complex structure revealed key structural features of AT_1R and critical interactions for ZD7155 binding. Docking simulations of the clinically used ARBs into the AT_1R structure further elucidated both the common and distinct binding modes for these anti-hypertensive drugs. Our results thereby provide fundamental insights into AT_1R structure-function relationship and structure-based drug design.

As described previously, GPCRs are extremely important family of proteins but they remain evasive to structural determination methods. AT_1R has been associated with heart failure and cardiac hypertrophy yet is critical for normal cardiovascular homeostasis (Ma, Kam et al. 2010) AT_1R blockers (ARBs) are routinely used to treat cardiovascular diseases such as heart failure, hypertension, arrhythmia, and cardiac hypertrophy. To date, the mechanism of ARB binding remains unknown and without structural knowledge of AT_1R it is difficult to find new therapeutic leads. In this study, the structure of ZD7155, an experimental anti-hypertensive compound complexed with AT_1R was determined. In order to produce crystals, three modifications to AT_1R were necessary. A thermostabilized apocytochrome $b_{562}RIL$ was fused to the N terminus, 11 residues were removed to shorten the flexible N-terminal region, and 40 residues were truncated from the C terminus. To ensure that truncations and fusion did not hinder ligand binding and signaling, a calcium mobilization assay was employed. Attempts to crystallize AT_1R only resulted in microcrystals, at a synchrotron the crystals diffracted to only 4 Å under cryogenic conditions. Thus, to improve resolution, avoiding harvesting the crystals, and collect data at room temperature, SFX was employed and a 2.9 Å data set was collected. From the structure and site directed mutagenesis, Trp84 was found to form extensive π-π interactions with the ligand while residues Arg167, Tyr35, were found to form key hydrogen bonds with the ligand. Additionally, the structure enabled docking studies of anti-hypertensive ARBs to AT_1R to be further investigated. This study attributed low binding affinities of some pharmaceutical compounds to AT_1R to be related to a lack of interactions in the binding pocket. Therefore, the results from this experiment extend past understanding the binding of ZD7155 to AT_1R and may aid in developing compounds with greater affinity and specificity to AT_1R.

6.3.7. MICROFLUIDIC SORTING OF PROTEIN NANOCRYSTALS BY SIZE FOR X-RAY FREE-ELECTRON LASER DIFFRACTION

B.G. Abdallah, N.A. Zatsepin, S. Roy-Chowdhury, J. Coe, **C.E. Conrad**, K. Dörner, R.G. Sierra, H.P. Stevenson, F. Camacho-Alanis, T.D. Grant, G. Nelson, D. James, G. Calero, R.M. Wachter, J.C.H. Spence, U. Weierstall, P. Fromme, and A. Ros, Microfluidic Sorting of Protein Nanocrystals by Size for X-Ray Free-Electron Laser Diffraction, *Structural Dynamics* **2** (4) [2015].

Abstract: The advent and application of the X-ray free-electron laser (XFEL) has uncovered the structures of proteins that could not previously be solved using traditional crystallography. While this new technology is powerful, optimization of the process is still needed to improve data quality and analysis efficiency. One area is sample heterogeneity, where variations in crystal size (among other factors) lead to the requirement of large data sets (and thus 10-100 mg of protein) for determining accurate structure factors. To decrease sample dispersity, we developed a high-throughput microfluidic sorter operating on the principle of dielectrophoresis, whereby polydisperse particles can be transported into various fluid streams for size fractionation. Using this microsorter, we isolated several milliliters of photosystem I nanocrystal fractions ranging from 200 to 600 nm in size as characterized by dynamic light scattering, nanoparticle tracking, and electron microscopy. Sorted nanocrystals were delivered in a liquid jet via the gas dynamic virtual nozzle into the path of the XFEL at the Linac Coherent Light Source. We obtained diffraction to ~4 Å resolution, indicating that the small crystals were not damaged by the sorting process. We also observed the shape transforms of photosystem I nanocrystals, demonstrating that our device can optimize data collection for the shape transform-based phasing method. Using simulations, we show that narrow crystal size distributions can significantly improve merged data quality in serial crystallography. From this proof-of-concept work, we expect that the automated size-sorting of protein crystals will become an important step for sample production by reducing the amount of protein needed for a high quality final structure and the development of novel phasing methods that exploit inter-Bragg reflection intensities or use variations in beam intensity for radiation damage-induced phasing. This method will also permit an analysis of the dependence of crystal quality on crystal size.

Growing a uniform size distribution of microcrystals in a large volume can be difficult. However, uniform crystals are highly desirable for SFX experiments because diffraction patterns from many different crystals must be merged together in order to obtain a high multiplicity. A large size distribution of crystals can result in a distribution of intensities which may in turn result in scaling issues. Additionally, large crystals can require beam attenuation that decreases the intensities of smaller crystals and can also result in injector clogging. Crystal uniformity is especially critical for time-resolved experiments (both pump probe and diffusion mixing) where reaction homogeneity is a fundamental parameter. Currently, the only tool to control maximum crystal size it to filter crystals, which has been linked to

damaging crystals (Demirci, Sierra et al. 2013), additionally these filters are limited to 2, 5, 10 and 20 µm.

This paper presents a new method to sort crystals via dielectrophoresis in which PSI crystals 200-600 nm were sorted from crystals ranging from 0.1-10 µm. The sorted crystals were characterized by dynamic light scattering, Nanosight, SONICC, TEM, and X-ray diffraction which showed that the sorting process did not harm the crystals. Remarkably, the X-ray diffraction of these nanocrystals showed shape transforms, which have the potential to be used as new phasing method. From these shape transforms, the number of unit cells can be determined as the number of fringes between the Bragg peaks, corresponds to the number of unit cells (n-1) (Sayre 1952). Phasing from these shape transforms is currently being explored. However, the fringes are limited to a countable number of unit cells. Thus, sorting via deielectorphoresis is a straightforward method to produce crystals in the nanometer size regime. Additionally, sorting has the potential to improve SFX data collection by controlling size homogeneity.

6.3.8. SERIAL TIME-RESOLVED CRYSTALLOGRAPHY OF PHOTOSYSTEM II USING A FEMTOSECOND X-RAY LASER

C. Kupitz, S. Basu, I. Grotjohann, R. Fromme, N.A. Zatsepin, K.N. Rendek, M.S. Hunter, R.L. Shoeman, T.A. White, D. Wang, D. James, J.-H. Yang, D.E. Cobb, B. Reeder, R.G. Sierra, H. Liu, A. Barty, A.L. Aquila, D. Deponte, R.A. Kirian, S. Bari, J.J. Bergkamp, K.R. Beyerlein, M.J. Bogan, C. Caleman, T.-C. Chao, **C.E. Conrad**, K.M. Davis, H. Fleckenstein, L. Galli, S.P. Hau-Riege, S. Kassemeyer, H. Laksmono, M. Liang, L. Lomb, S. Marchesini, A.V. Martin, M. Messerschmidt, D. Milathianaki, K. Nass, A. Ros, S. Roy-Chowdhury, K. Schmidt, M. Seibert, J. Steinbrener, F. Stellato, L. Yan, C. Yoon, T.A. Moore, A.L. Moore, Y. Pushkar, G.J. Williams, S. Boutet, R.B. Doak, U. Weierstall, M. Frank, H.N. Chapman, J.C.H. Spence, and P. Fromme, Serial Time-Resolved Crystallography of Photosystem II Using a Femtosecond X-Ray Laser, *Nature* **513** (7517) [2014].

Abstract: Photosynthesis, a process catalyzed by plants, algae and cyanobacteria converts sunlight to energy thus sustaining all higher life on Earth. Two large membrane protein complexes, photosystem I and II (PSI and PSII), act in series to catalyze the light-driven reactions in photosynthesis. PSII catalysis the light-driven water splitting process, which maintains the Earth's oxygenic atmosphere. In this process, the oxygen-evolving complex (Barends, Foucar et al.) of PSII cycles through five states, S0 to S4, in which four electrons are sequentially extracted from the OEC in four light-driven charge-separation events. Here we describe time resolved experiments on PSII

nano/microcrystals from Thermosynechococcus elongatus performed with the recently developed technique of serial femtosecond crystallography. Structures have been determined from PSII in the dark S1 state and after double laser excitation (putative S3 state) at 5 and 5.5 Å resolution, respectively. The results provide evidence that PSII undergoes significant conformational changes at the electron acceptor side and at the Mn4CaO5 core of the OEC. These include an elongation of the metal cluster, accompanied by changes in the protein environment, which could allow for binding of the second substrate water molecule between the more distant protruding Mn (referred to as the 'dangler' Mn) and the Mn3CaOx cubane in the S2 to S3 transition, as predicted by spectroscopic and computational studies. This work shows the great potential for time-resolved serial femtosecond crystallography for investigation of catalytic processes in biomolecules.

This paper was the first publication of TR-SFX where changes in the protein were detected (Kern et al. 2014 had published TR-SFX experiments and saw no change). This ground breaking experiment showed that XFELs can provide structural information of transient intermediate states. In this experiment, the crystals were pumped with two flashes of light prior to being probed by the XFEL beam. The laser flashes were staggered to capture alternating light and dark data as a constant experimental control. The "probe" step occurred during the transition from S2 to S3 in the Kok, thus capturing the transition between these two states. Although the data is low resolution, an increase in the distance between the cubane and the dangler Mn is observed and the cubane appears to become distorted (Figure 6.4ab).

In contrast to the previous publications, I was not yet involved in the data collection as this came before I started my PhD. During the review process, one reviewer requested the occupancy of the Q_B quinone binding site to be determined and I performed the experiment to determine this. To estimate the plastoquinone (PQ) content after each PEG 2000 precipitation step, chlorophyll (chl) content of the protein was measured and was adjusted to 0.31 mM Chl. The protein was then subjected to a pigment extraction according to the protocol from (Patzlaff and Barry 1996) and the quinone content of nanocrystals was determined by HPLC chromatography. Prior to crystallization, the Q_B content was estimated to be 91.8% . While PSII crystals used for the LCLS experiments correspond to sample number 3, i.e. PSII was 3 times

crystallized, which has an overall PQ content of 81.1%., which leads to an estimation of a quinone content of 73.4% after 3 crystallization steps of photosystem II (PSII), as it was used for data collection at LCLS.
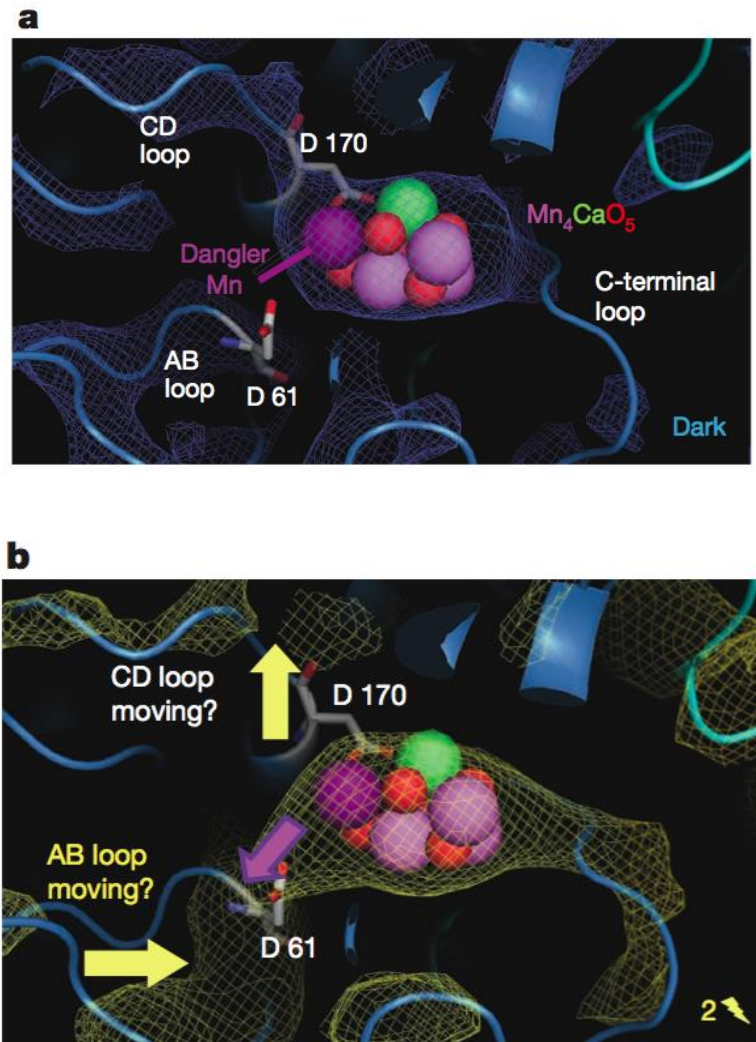
Figure 6.4 The OEC simulated annealed omit maps. a, b, At 1.5 s for dark and double-flash states of the Mn_4CaO_5 cluster of PSII for the dark S_1-state (blue) (a) and double-flash, putative S_3 state (b) with the 1.9 A° structural model (3ARC) from (Umena, Kawakami et al. 2011) Mn in the distorted Mn_3O_XCa cubane (Mn-1 to Mn-3) (light-pink), dangler manganese (Mn-4) (violet), calcium (Banerjee, Bartesaghi et al.) and oxygen (red). Figure and caption reprinted with permission from (Kupitz, Basu et al. 2014).

6.3.9. MICROCRYSTALLIZATION TECHNIQUES FOR SERIAL FEMTOSECOND CRYSTALLOGRAPHY USING PHOTOSYSTEM II FROM THERMOSYNECHOCOCCUS ELONGATUS AS A MODEL SYSTEM

Abstract: Serial femtosecond crystallography (SFX) is a new emerging method, where X-ray diffraction data are collected from a fully hydrated stream of nano- or microcrystals of biomolecules in their mother liquor using high-energy, X-ray free-electron lasers. The success of SFX experiments strongly depends on the ability to grow large amounts of well-ordered nano/microcrystals of homogeneous size distribution. While methods to grow large single crystals have been extensively explored in the past, method developments to grow nano/microcrystals in sufficient amounts for SFX experiments are still in their infancy. Here, we describe and compare three methods (batch, free interface diffusion (FID) and FID centrifugation) for growth of nano/microcrystals for time-resolved SFX experiments using the large membrane protein complex photosystem II as a model system.

Prior to the birth of SFX, nano/microcrystals were undesired. Thus, techniques to grow these small crystals has remained largely unexplored. Furthermore, the large volume of crystals need for SFX was an additional challenge. Microcrystallization via free interface diffusion (FID) was designed specifically for SFX experiments (described in Section 2.2.1). In this publication, PSII crystallization via FID, FID with centrifugation (FIDC) and batch are compared. The FID method has been successfully used for many other systems other than PSII, these include PC, KDO8PS, lysozyme, adenine riboswitch aptamer domain, and PYP. In the case of PSII, FID produces smaller crystals with a much narrower size distribution in comparison to batch crystallization. An adaptation of the FID method, is FIDC (also described in Section 2.2.1) where the FID is centrifuged to induce rapid crystallization in as little as 30 minutes. Because, crystallization occurs so rapidly, smaller crystals are produced. This paper allows provides important discussion that only applies to microcrystallization such as transport and quenching which is not discussed elsewhere in the literature, thus helping those that are unfamiliar with microcrystallization and serial crystallography.

G. Fenalti, N.A. Zatsepin, C. Betti, P. Giguere, G.W. Han, A. Ishchenko, W. Liu, K. Guillemyn, H. Zhang, D. James, D. Wang, U. Weierstall, J.C.H. Spence, S. Boutet, M. Messerschmidt, G.J. Williams, C. Gati, O.M. Yefanov, T.A. White, D. Oberthuer, M. Metz, C.H. Yoon, A. Barty, H.N. Chapman, S. Basu, J. Coe, **C.E. Conrad**, R. Fromme, P. Fromme, D. Tourwé, P.W. Schiller, B.L. Roth, S. Ballet, V. Katritch, R.C. Stevens, and V. Cherezov, Structural Basis for Bifunctional Peptide Recognition at Human δ-Opioid Receptor, *Nature Structural & Molecular Biology* **22** (Brooks, Brooks et al.) [2015].

Abstract: Bifunctional μ- and δ-opioid receptor (OR) ligands are potential therapeutic alternatives, with diminished side effects, to alkaloid opiate analgesics. We solved the structure of human δ-OR bound to the bifunctional δ-OR antagonist and μ-OR agonist tetrapeptide H-Dmt-Tic-Phe-Phe-NH2 (DIPP-NH2) by serial femtosecond crystallography, revealing a cis-peptide bond between H-Dmt and Tic. The observed receptor-peptide interactions are critical for understanding of the pharmacological profiles of opioid peptides and for development of improved analgesics.

This publication revealed the structure of the δ-opioid receptor (OR) bound to a bifunctional peptide containing antagonist (blocks signaling function) and agonist (activates signaling) characteristics. Opioids are commonly used to treat moderate to severe pain but chronic usage can result in tolerance and dependence. Dual administration of naltrindole, an δ-opioid receptor antagonist, with an agonist has been found to prevent tolerance and dependence. Thus a peptide with bifunctionallity would have significant therapeutic promise. In order to aid in crystallization, apocytochrome b_{562}RIL (BRIL) was fused to the N-terminus of OR. OR bound with DIPP-NH$_2$, a peptide exhibiting mixed bifunctional agonist and antagonist properties, diffracted to 3.2 Å at a synchrotron while diffraction to 2.8 Å was collected at an XFEL. Compared to other δ-OR structures, the δ-OR orthosteric site is expanded in the XFEL agonist-OR structure. Additionally DIPP-NH$_2$ shows binding overlap of another agonist, naltrindole, while the dmt residue of DIPP-NH$_2$ approximately overlaps with known agonist binding but with a 30° rotation. However, the key residue attributed to the bifunctionality were found to be from the Tic resiude of DIPP-NH$_2$ after mutagenesis of two non-conserved residues resulted in a two order of magnitude decrease in affinity of two OR ligands. Thus, the structure of OR bound to DIPP-NH$_2$ insight explains why this ligand has bifunctional agonist and antagonist properties. From this structure, key residues for peptide binding have been identified. With this knowledge new pharmaceutical opioid therapies

containing bifunctional properties to be developed. This publication provides evidence as to the importance of being able to deliver microcrystals to an XFEL beam.

6.3.11. FEMTOSECOND STRUCTURAL DYNAMICS DRIVES THE TRANS/CIS ISOMERIZATION IN PHOTOACTIVE YELLOW PROTEIN

K. Pande, C. D. M. Hutchinson, G. Groenhof, A. Aquila, J. S. Robinson, J. Tenboer, S. Basu, S. Boutet, D.P. DePonte, M. Liang, T.A. White, N.A. Zatsepin, O.M. Yefanov, D. Oberthuer, D. Morozov, D. Oberthuer, C. Gati, G. Subramanian, D.R. James, Y. Zhao, J. Koralek, J. Brayshaw, C. Kupitz, **C.E. Conrad**, S. Roy-Chowdhury, J. D. Coe, M. Metz, X. P. Lourdu, T. D. Grant, J. E. Koglin, G. Ketawala, R. Fromme, V. Šrajer, R. Henning, J.C.H. Spence, A. Ourmazd, P. Schwander, U. Weierstall, M. Frank, P. Fromme, A. Barty, H.N. Chapman, K. Moffat, J.J. Van Thor, and M. Schmidt, Femtosecond Structural Dynamics Drives the Trans/Cis Isomerization in Photoactive Yellow Protein, *Science*, **352** (6286), 2016.

Abstract: A variety of organisms have evolved mechanisms to detect and respond to light, in which the response is mediated by protein structural changes after photon absorption. The initial step is often the photoisomerization of a conjugated chromophore. Isomerization occurs on ultrafast time scales and is substantially influenced by the chromophore environment. Here we identify structural changes associated with the earliest steps in the trans-to-cis isomerization of the chromophore in photoactive yellow protein. Femtosecond hard x-ray pulses emitted by the Linac Coherent Light Source were used to conduct time-resolved serial femtosecond crystallography on photoactive yellow protein microcrystals over a time range from 100 femtoseconds to 3 picoseconds to determine the structural dynamics of the photoisomerization reaction.

As a follow up to the previous PYP experiments that served as a proof of principle for TR-SFX, this experiment showed the photoisomerization of the PYP chromophore. The photoisomeriazation of a conjugated chromophore was estimated to occur on a fs to ps time regime which is below the reach of Laue crystallography. With the advent of XFELs, X-ray pulses in the tens of fs became possible allowing ultra-fast dynamics to be studied for the first time. Because the exact time regime for photoisomerization is currently unknown, delay times of 300 and 600 fs were explored. In comparison to the nanosecond laser which allowed for a 40% photoactivation, the femtosecond laser only allowed for 10% photoactivation. While only 30% of these photoactivated PYP molecules entered the photocycle. Times above and below 300 and 600 fs were studied by exploiting the timing jitter between the 140 fs X-ray pulse and the 140 Hz femtosecond laser. A timing tool was used to "stamp" the time point of each diffraction pattern and then the diffraction patterns were binned according to their time stamp. A total of 8 bins were

created, each with 40,000 diffraction patterns, ranging from 100-1000 fs. Electron density maps from time points below 500 fs were all similar while time points above 700 fs were also similar but were different from sub 500 fs time points. Thus, a change was expected between these two time points. Diffraction patterns in these time points were rebinned into 16 narrower time bins. Further analysis revealed that the photoisomerization occurred at 550 fs with a lifetime of approximately 180 fs. During this transition, the electron densities revealed substantial rotation about the double bond. Additionally, movement in the single bonds surrounding the double bonds is seen to minimize the swept volume after photoionization. Thus, each of the 8 original bins represents a still snapshot of each time points, played together, a "molecular movie" of the photoiosmerization of PYP can be seen.

6.3.12 STRUCTURES OF RIBOSWITCH RNA REACTION STATES BY MIX-AND-INJECT XFEL SERIAL CRYSTALLOGRAPHY

J.R. Stagno, Y. R. Bhandari, Y. Liu, **C.E. Conrad**, S. Panja, M. Swain, L. Fan, G. Nelson, C. Li, D.R. Wendel, T.A. White, A. Barty, M. O. Wiedorn, D. Oberthuer, J. Knoska, R.A. Tuckey, P. Yu, M. Dyba, S. Tarasov, U. Weierstall, , N.A. Zatsepin, T.D. Grant, C.D. Schwieters, J. Zhang, A. Ferré-D'Amaré, P. Fromme, D.E. Draper, K. Tan, X. Zuo, X. Ji, J.C.H. Spence, S. A. Woodson, & Y.-X. Wang, Structures of Riboswitch RNA Reaction States By Mix-And-Inject XFEL Serial Crystallography Nature *in press* [2016].

Abstract: Riboswitches are RNA structural elements generally located in the 3′untranslated region (3′UTR) of mRNA. In the genetic regulation, ligand binding to the aptamer domain of a riboswitch triggers a signal to the downstream expression platform. A complete understanding of the structural basis for this mechanism requires the ability to study structural changes over time. Here we apply femtosecond X-ray free electron laser (XFEL) pulses to obtain structural measurements from crystals so small that diffusion of a ligand can be timed to initiate a reaction prior to diffraction. We demonstrate this approach by determining four structures of the adenine riboswitch aptamer domain during the course of a reaction involving two apo, one ligand-bound intermediate, and the final bound states. These structures support a reaction mechanism model with at least four states and illustrate the structural basis for signal transmission. The two apo conformers differ significantly in the three-way junction and the P1 switch helix relative to the ligand bound conformation. Our time-resolved crystallographic measurements with a 10-second delay captured the structure of an intermediate with changes in the binding pocket that accommodate the ligand. With a >10-minute delay, the RNA molecules were fully converted to the bound state, in which the substantial conformational changes resulted in conversion of the space group. Such drastic changes in crystallo highlight the important opportunities that micro/nanocrystals may offer in these and similar time-resolved diffraction studies. These results all together demonstrate the potential of "mix-and-inject" time-resolved serial crystallography to study biochemically important interactions between

biomacromolecules and ligands, including those involving large conformational changes.

Just accepted, this publication is the first to demonstrate the ability of SFX to perform time-resolved mixing or "mix-and-inject" experiments. Two time points were captured, a 10 s delay employed by a Tee junction to mix crystals with ligand and a >10 min delay where the crystals were mixed with ligand in the reservoir. In addition, an apo structure was determined by delivering the crystals with agarose without ligand present. The >10 min time point showed a change in the unit cell from $P2_1$ to $P2_12_12$ suggesting "sufficiently ordered" conformational changes occurring in the crystal where all apo molecules were converted to bound. The ten s delay had the same unit cell as the apo, but an additional yet distinct apo conformation was observed, apo2, where the apo2 conformation is believed to be the ligand competent conformation. Prior to this experiment, the ligand unbound binding pocket was thought to be disordered, but structures of both apo confirmations show this not be true. These two confirmations show that upon ligand binding, the base pairs in the binding pocket are rewired in order to accommodate the ligand. Additionally, an intermediate bound state was also resolved. Stopped flow mixing experiments agree with two apo states and one intermediate hypothesis as the data indicated a four-state kinetic model. From these stopped flowed experiments, the maximum population of intermediate bound occurred on a ms to s timescale. But the fact that the intermediate is still bound after 10 s indicates that intermediate formation and/or release is delayed due to constrained motion in the tight crystals packing.

This paper has proven that time-resolved mixing experiments are now possible. Thus this new technique has opened the door to study non-photoactiaved enzymes on biologically relevant timescales via mixing. With the use of mixing injectors and microfluidic nozzles, time points can be extended down to as low as hundreds of µs. Not only did this experiment show TR diffusion mixing, it also presented the first RNA structure solved by an XFEL.

6.4 OUTLOOK: A BRIGHT FUTURE FOR XFELS

With the advent of several new hard XFEL facilities, more beamtime will allow more systems to be studied and further technique development (Figure 6.5). The high repletion rate, 2,700 Hz of the European XFEL will also dramatically decrease the beamtime needed to collect a data set in turn it will significantly decrease sample consumption. Although these facilities will not require viscous sample delivery, it will still conserve sample at the lower repetition rate facilities (LCLS, SwissFEL, SACLA PAL-XFEL, and the Shanghai XFEL). In the future, these high repetition rate hard XFEL facilities may be devoted to time resolved studies while the lower repletion rate facilities will be used for method development, protein screening, LCP, and fixed target setups. The field of serial data collection has even extended to synchrotrons, where serial data collection has allowed microcrystals to be probed without an XFEL (Stellato, Oberthür et al. 2014, Nogly, Panneels et al. 2016). Thus increasing capabilities of microfocus beamlines, will also decrease the demand for XFEL beamtime and microcrystallography will become more routine.

Currently SFX experiments still require large teams as a wide range of specialties are needed but with further technique development this field will become more approachable for new SFX users. In the future, self-seeded XFEL beams may provide less shot to shot variation while increasing spectral flux. Data collection will become more routine and will be supported more by the facility and less by the users. New detectors will provide lower noise, higher dynamic range, and faster readout speeds. Robotics may be developed to setup large scale production of microcrystals such as large scale batch. Or, sample consumption might be decreased significantly allowing for collecting vapor diffusion drops to be feasible. Additionally, experimental setups, such as fixed target approaches, may become automated even allowing for "off site" data collection. Data processing may become more user friendly such as a GUI opposed to current line based commands. Moreover, work is currently being done to phase PSI using shape transforms. If this method is proven valid, it would allow for diffraction patterns to be collected on a front detector and shape transforms to be collected simultaneously on a back detector. Thus allowing synchronized data collection and phasing without any modifications to the

macromolecular system or the crystals. However, the most exciting glimpse into the future, is that

XFELs may allow for single particle structural determination, removing the need for crystallization

all together.
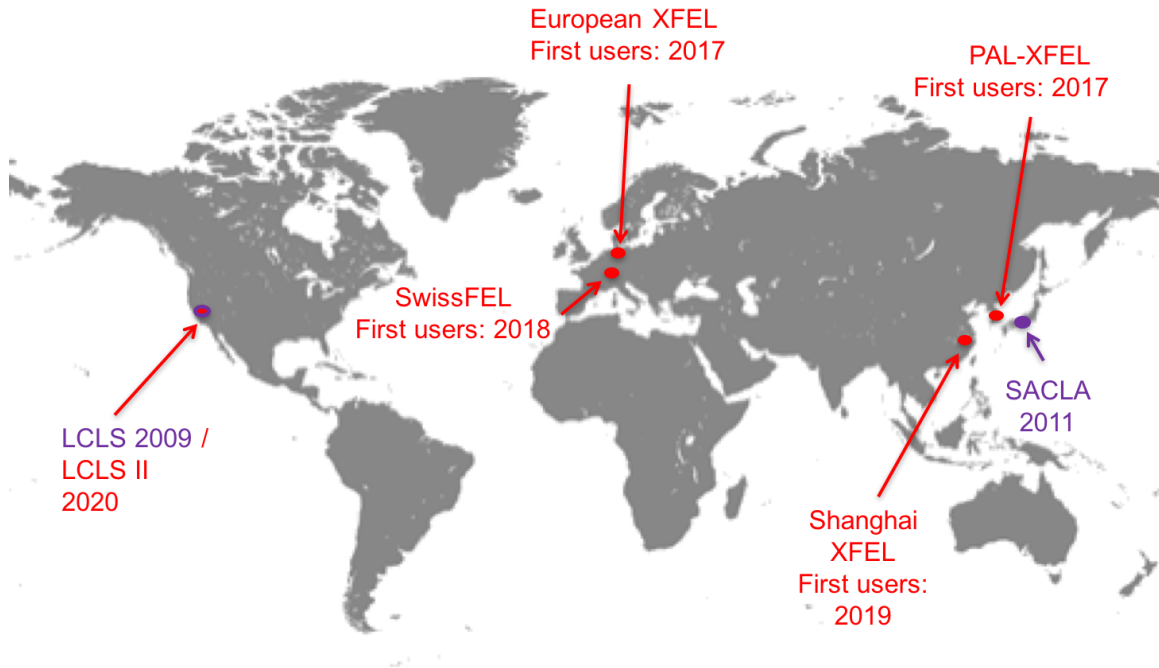
Figure 6.5 Existing and future hard XFEL facilities. Current facilities are denoted in purple while future XFELs are denoted in red.

REFERENCES

Abdallah, B. G., S. Roy-Chowdhury, J. Coe, P. Fromme and A. Ros (2015). "High throughput protein nanocrystal fractionation in a microfluidic sorter." Anal Chem **87**(8): 4159-4167.

Ackermann, W. a., G. Asova, V. Ayvazyan, A. Azima, N. Baboi, J. Bähr, V. Balandin, B. Beutner, A. Brandt and A. Bolzmann (2007). "Operation of a free-electron laser from the extreme ultraviolet to the water window." Nature photonics **1**(6): 336-342.

Adams, P. D., P. V. Afonine, G. Bunkóczi, V. B. Chen, I. W. Davis, N. Echols, J. J. Headd, L.-W. Hung, G. J. Kapral, R. W. Grosse-Kunstleve, A. J. McCoy, N. W. Moriarty, R. Oeffner, R. J. Read, D. C. Richardson, J. S. Richardson, T. C. Terwilliger and P. H. Zwart (2010). "PHENIX: a comprehensive Python-based system for macromolecular structure solution." Acta Crystallographica Section D: Biological Crystallography **66**(Pt 2): 213-221.

Allahgholi, A., J. Becker, L. Bianco, A. Delfs, R. Dinapoli, P. Goettlicher, H. Graafsma, D. Greiffenberg, H. Hirsemann and S. Jack (2015). "AGIPD, a high dynamic range fast detector for the European XFEL." Journal of Instrumentation **10**(01): C01023.

Altarelli, M. (2010). "From 3rd-to 4th-generation light sources: Free-electron lasers in the X-ray range." Crystallography Reports **55**(7): 1145-1151.

Altarelli M, M. A. (2014). "Structural biology at the European X-ray free-electron laser facility." Philosophical Transactions of the Royal Society B: Biological Sciences. **369**.

Aquila, A., M. S. Hunter, R. B. Doak, R. A. Kirian, P. Fromme, T. A. White, J. Andreasson, D. Arnlund, S. Bajt and T. R. Barends (2012). "Time-resolved protein nanocrystallography using an X-ray free-electron laser." Optics express **20**(3): 2706-2716.

Arnlund, D., L. C. Johansson, C. Wickstrand, A. Barty, G. J. Williams, E. Malmerberg, J. Davidsson, D. Milathianaki, D. P. DePonte and R. L. Shoeman (2014). "Visualizing a protein quake with time-resolved X-ray scattering at a free-electron laser." Nature methods **11**(9): 923-926.

Arnott, S., A. Fulmer, W. E. Scott, I. C. Dea, R. Moorhouse and D. A. Rees (1974). "The agarose double helix and its function in agarose gel structure." J Mol Biol **90**(2): 269-284.

Asojo, O., J. Friedman, N. Adir, V. Belakhov, Y. Shoham and T. Baasov (2001). "Crystal structures of KDOP synthase in its binary complexes with the substrate phosphoenolpyruvate and with a mechanism-based inhibitor." Biochemistry **40**(21): 6326-6334.

Axford, D., R. L. Owen, J. Aishima, J. Foadi, A. W. Morgan, J. I. Robinson, J. E. Nettleship, R. J. Owens, I. Moraes, E. E. Fry, J. M. Grimes, K. Harlos, A. Kotecha, J. Ren, G. Sutton, T. S. Walter, D. I. Stuart and G. Evans (2012). "In situ macromolecular crystallography using microbeams." Acta Crystallographica Section D **68**(5): 592-600.

Ayvazyan, V., N. Baboi, J. Bähr, V. Balandin, B. Beutner, A. Brandt, I. Bohnet, A. Bolzmann, R. Brinkmann, O.I. Brovko, J.P. Carneiro, S. Casalbuoni, M. Castellano, P. Castro, L. Catani, E. Chiadroni, S. Choroba, A. Cianchi, H. Delsim-Hashemi, G. Di Pirro, M. Dohlus, S. Düsterer, H.T. Edwards, B. Faatz, A.A. Fateev, J. Feldhaus, K. Flöttmann, J. Frisch, L. Fröhlich, T. Garvey, U. Gensch, N. Golubeva, H.-J. Grabosch, B. Grigoryan, O. Grimm, U. Hahn, J.H. Han, M. v. Hartrott, K. Honkavaara, M. Hüning, R. Ischebeck, E. Jaeschke, M. Jablonka, R. Kammering, V. Katalev, B. Keitel S. Khodyachykh, Y. Kim, V. Kocharyan, M. Körfer, M. Kollewe, D. Kostin, D. Krämer, M.

Krassilnikov, G. Kube, L. Lilje, T. Limberg, D. Lipka, F. Löhl, M. Luong, C. Magne, J. Menzel, P. Michelato, V. Miltchev, M. Minty, W.D. Möller, L. Monaco, W. Müller, M. Nagl, O. Napoly, P. Nicolosi, D. Nölle, T. Nuñez, A. Oppelt, C. Pagani, R. Paparella, B. Petersen, B. Petrosyan, J. Pflüger, P. Piot, E. Plönjes, L. Poletto, D. Proch, D. Pugachov, K. Rehlich, D. Richter, S. Riemann, M. Ross, J. Rossbach, M. Sachwitz, E.L.Saldin, W. Sandner, H. Schlarb, B. Schmidt, M. Schmitz, P. Schmüser, J.R. Schneider, E.A. Schneidmiller, H.-J. Schreiber, S. Schreiber, A.V. Shabunov, D. Sertore, S. Setzer, S. Simrock, E. Sombrowski, L. Staykov, B. Steffen, F. Stephan, F. Stulle, K.P. Sytchev, H. Thom, K. Tiedtke, M. Tischer, R. Treusch, D. Trines, I. Tsakov, A. Vardanyan, R. Wanzenberg, T. Weiland, H. Weise, M. Wendt, I. Will, A. Winter, K. Wittenburg, M.V. Yurkov, I. Zagorodnov, P. Zambolin, K. Zapfe (2006). "First operation of a Free-Electron Laser generating GW power radiation at 32 nm wavelength." Eur.Phys.J.D **37**: p.297

Ayyer, K., O. M. Yefanov, D. Oberthur, S. Roy-Chowdhury, L. Galli, V. Mariani, S. Basu, J. Coe, C. E. Conrad, R. Fromme, A. Schaffer, K. Dorner, D. James, C. Kupitz, M. Metz, G. Nelson, P. L. Xavier, K. R. Beyerlein, M. Schmidt, I. Sarrou, J. C. Spence, U. Weierstall, T. A. White, J. H. Yang, Y. Zhao, M. Liang, A. Aquila, M. S. Hunter, J. S. Robinson, J. E. Koglin, S. Boutet, P. Fromme, A. Barty and H. N. Chapman (2016). "Macromolecular diffractive imaging using imperfect crystals." Nature **530**(7589): 202-206.

Baasov, T. and A. Kohen (1995). "Synthesis, Inhibition, and Acid-Catalyzed Hydrolysis Studies of Model Compounds of the Proposed Intermediate in the Kdo8P-Synthase-Catalyzed Reaction." Journal of the American Chemical Society **117**(23): 6165-6174.

Balbirnie, M., R. Grothe and D. S. Eisenberg (2001). "An amyloid-forming peptide from the yeast prion Sup35 reveals a dehydrated β-sheet structure for amyloid." Proceedings of the National Academy of Sciences **98**(5): 2375-2380.

Barends, T. R., L. Foucar, S. Botha, R. B. Doak, R. L. Shoeman, K. Nass, J. E. Koglin, G. J. Williams, S. Boutet, M. Messerschmidt and I. Schlichting (2014). "De novo protein crystal structure determination from X-ray free-electron laser data." Nature **505**(7482): 244-247.

Barends, T. R., L. Foucar, R. L. Shoeman, S. Bari, S. W. Epp, R. Hartmann, G. Hauser, M. Huth, C. Kieser, L. Lomb, K. Motomura, K. Nagaya, C. Schmidt, R. Strecker, D. Anielski, R. Boll, B. Erk, H. Fukuzawa, E. Hartmann, T. Hatsui, P. Holl, Y. Inubushi, T. Ishikawa, S. Kassemeyer, C. Kaiser, F. Koeck, N. Kunishima, M. Kurka, D. Rolles, B. Rudek, A. Rudenko, T. Sato, C. D. Schroeter, H. Soltau, L. Strueder, T. Tanaka, T. Togashi, K. Tono, J. Ullrich, S. Yase, S. I. Wada, M. Yao, M. Yabashi, K. Ueda and I. Schlichting (2013). "Anomalous signal from S atoms in protein crystallographic data from an X-ray free-electron laser." Acta Crystallogr D Biol Crystallogr **69**(Pt 5): 838-842.

Barty, A., C. Caleman, A. Aquila, N. Timneanu, L. Lomb, T. A. White, J. Andreasson, D. Arnlund, S. Bajt, T. R. Barends, M. Barthelmess, M. J. Bogan, C. Bostedt, J. D. Bozek, R. Coffee, N. Coppola, J. Davidsson, D. P. Deponte, R. B. Doak, T. Ekeberg, V. Elser, S. W. Epp, B. Erk, H. Fleckenstein, L. Foucar, P. Fromme, H. Graafsma, L. Gumprecht, J. Hajdu, C. Y. Hampton, R. Hartmann, A. Hartmann, G. Hauser, H. Hirsemann, P. Holl, M. S. Hunter, L. Johansson, S. Kassemeyer, N. Kimmel, R. A. Kirian, M. Liang, F. R. Maia, E. Malmerberg, S. Marchesini, A. V. Martin, K. Nass, R. Neutze, C. Reich, D. Rolles, B. Rudek, A. Rudenko, H. Scott, I. Schlichting, J. Schulz, M. M. Seibert, R. L. Shoeman, R. G. Sierra, H. Soltau, J. C. Spence, F. Stellato, S. Stern, L. Struder, J. Ullrich, X. Wang, G. Weidenspointner, U. Weierstall, C. B. Wunderer and H. N. Chapman (2012). "Self-terminating diffraction gates femtosecond X-ray nanocrystallography measurements." Nat Photonics **6**: 35-40.

Barty, A., R. A. Kirian, F. R. Maia, M. Hantke, C. H. Yoon, T. A. White and H. Chapman (2014). "Cheetah: software for high-throughput reduction and analysis of serial femtosecond X-ray diffraction data." J Appl Crystallogr **47**(Pt 3): 1118-1131.

Berne, B. and R. Pecora (2000). <u>Dynamic Light Scattering: With Applications to Chemistry, Biology, and Physics</u>. Mineola, Dover Publications.

Biertumpfel, C., J. Basquin, D. Suck and C. Sauter (2002). "Crystallization of biological macromolecules using agarose gel." <u>Acta Crystallographica Section D</u> **58**(10 Part 1): 1657-1659.

Birck, M. R. and R. W. Woodard (2001). "Aquifex aeolicus 3-deoxy-D-manno-2-octulosonic acid 8-phosphate synthase: a new class of KDO 8-P synthase?" <u>J Mol Evol</u> **52**(2): 205-214.

Bolduc, J. M., D. H. Dyer, W. G. Scott, P. Singer, R. M. Sweet, D. Koshland and B. L. Stoddard (1995). "Mutagenesis and Laue structures of enzyme intermediates: isocitrate dehydrogenase." <u>Science</u> **268**(5215): 1312-1318.

Botha, S., K. Nass, T. R. M. Barends, W. Kabsch, B. Latz, F. Dworkowski, L. Foucar, E. Panepucci, M. Wang, R. L. Shoeman, I. Schlichting and R. B. Doak (2015). "Room-temperature serial crystallography at synchrotron X-ray sources using slowly flowing free-standing high-viscosity microstreams." <u>Acta Crystallographica Section D</u> **71**(2): 387-397.

Boutet, S., L. Lomb, G. J. Williams, T. R. Barends, A. Aquila, R. B. Doak, U. Weierstall, D. P. DePonte, J. Steinbrener, R. L. Shoeman, M. Messerschmidt, A. Barty, T. A. White, S. Kassemeyer, R. A. Kirian, M. M. Seibert, P. A. Montanez, C. Kenney, R. Herbst, P. Hart, J. Pines, G. Haller, S. M. Gruner, H. T. Philipp, M. W. Tate, M. Hromalik, L. J. Koerner, N. van Bakel, J. Morse, W. Ghonsalves, D. Arnlund, M. J. Bogan, C. Caleman, R. Fromme, C. Y. Hampton, M. S. Hunter, L. C. Johansson, G. Katona, C. Kupitz, M. Liang, A. V. Martin, K. Nass, L. Redecke, F. Stellato, N. Timneanu, D. Wang, N. A. Zatsepin, D. Schafer, J. Defever, R. Neutze, P. Fromme, J. C. Spence, H. N. Chapman and I. Schlichting (2012). "High-resolution protein structure determination by serial femtosecond crystallography." <u>Science</u> **337**(6092): 362-364.

Boutet, S. and G. J. Williams (2010). "The Coherent X-ray Imaging (CXI) instrument at the Linac Coherent Light Source (LCLS)." <u>New Journal of Physics</u> **12**(3).

Bragg, W. H. and W. L. Bragg (1913). "The Reflection of X-rays by Crystals." <u>Proceedings of the Royal Society of London. Series A</u> **88**(605): 428-438.

Brehm, W. and K. Diederichs (2014). "Breaking the indexing ambiguity in serial crystallography." <u>Acta Crystallographica Section D</u> **70**(1): 101-109.

Brooks, B. R., C. L. Brooks, 3rd, A. D. Mackerell, Jr., L. Nilsson, R. J. Petrella, B. Roux, Y. Won, G. Archontis, C. Bartels, S. Boresch, A. Caflisch, L. Caves, Q. Cui, A. R. Dinner, M. Feig, S. Fischer, J. Gao, M. Hodoscek, W. Im, K. Kuczera, T. Lazaridis, J. Ma, V. Ovchinnikov, E. Paci, R. W. Pastor, C. B. Post, J. Z. Pu, M. Schaefer, B. Tidor, R. M. Venable, H. L. Woodcock, X. Wu, W. Yang, D. M. York and M. Karplus (2009). "CHARMM: the biomolecular simulation program." <u>J Comput Chem</u> **30**(10): 1545-1614.

Bublitz, M., K. Nass, N. D. Drachmann, A. J. Markvardsen, M. J. Gutmann, T. R. Barends, D. Mattle, R. L. Shoeman, R. B. Doak and S. Boutet (2015). "Structural studies of P-type ATPase–ligand complexes using an X-ray free-electron laser." <u>IUCrJ</u> **2**(4): 409-420.

Burmeister, W. P. (2000). "Structural changes in a cryo-cooled protein crystal owing to radiation damage." <u>Acta Crystallogr D Biol Crystallogr</u> **56**(Pt 3): 328-341.

C. Pellegrini, J. S. (2003). "X-ray free-electron lasersdprinciples, properties and applications." <u>Nuclear Instrum. Methods Phys. Res. Sect. A Accel. Spectrom. Detect. Assoc. Equip.</u>(500): 33-40.

Caffrey, M. (2015). "A comprehensive review of the lipid cubic phase or in meso method for crystallizing membrane and soluble proteins and complexes." Acta Crystallogr F Struct Biol Commun **71**(Pt 1): 3-18.

Caffrey, M. and V. Cherezov (2009). "Crystallizing membrane proteins using lipidic mesophases." Nat Protoc **4**(5): 706-731.

Carr, B. and A. Malloy (2006). NanoParticle Tracking Analysis–The NANOSIGHT system.

Carugo, O. and K. D. Carugo (2005). "When X-rays modify the protein structure: radiation damage at work." Trends in Biochemical Sciences **30**(4): 213-219.

Chapman, H. N., A. Barty, S. Marchesini, A. Noy, S. P. Hau-Riege, C. Cui, M. R. Howells, R. Rosen, H. He, J. C. Spence, U. Weierstall, T. Beetz, C. Jacobsen and D. Shapiro (2006). "High-resolution ab initio three-dimensional x-ray diffraction microscopy." J Opt Soc Am A Opt Image Sci Vis **23**(5): 1179-1200.

Chapman, H. N., P. Fromme, A. Barty, T. A. White, R. A. Kirian, A. Aquila, M. S. Hunter, J. Schulz, D. P. DePonte, U. Weierstall, R. B. Doak, F. R. Maia, A. V. Martin, I. Schlichting, L. Lomb, N. Coppola, R. L. Shoeman, S. W. Epp, R. Hartmann, D. Rolles, A. Rudenko, L. Foucar, N. Kimmel, G. Weidenspointner, P. Holl, M. Liang, M. Barthelmess, C. Caleman, S. Boutet, M. J. Bogan, J. Krzywinski, C. Bostedt, S. Bajt, L. Gumprecht, B. Rudek, B. Erk, C. Schmidt, A. Homke, C. Reich, D. Pietschner, L. Struder, G. Hauser, H. Gorke, J. Ullrich, S. Herrmann, G. Schaller, F. Schopper, H. Soltau, K. U. Kuhnel, M. Messerschmidt, J. D. Bozek, S. P. Hau-Riege, M. Frank, C. Y. Hampton, R. G. Sierra, D. Starodub, G. J. Williams, J. Hajdu, N. Timneanu, M. M. Seibert, J. Andreasson, A. Rocker, O. Jonsson, M. Svenda, S. Stern, K. Nass, R. Andritschke, C. D. Schroter, F. Krasniqi, M. Bott, K. E. Schmidt, X. Wang, I. Grotjohann, J. M. Holton, T. R. Barends, R. Neutze, S. Marchesini, R. Fromme, S. Schorb, D. Rupp, M. Adolph, T. Gorkhover, I. Andersson, H. Hirsemann, G. Potdevin, H. Graafsma, B. Nilsson and J. C. Spence (2011). "Femtosecond X-ray protein nanocrystallography." Nature **470**(7332): 73-77.

Chen, A. U. and O. A. Basaran (2002). "A new method for significantly reducing drop radius without reducing nozzle radius in drop-on-demand drop production." Physics of Fluids **14**(1): L1-L4.

Cheng, A., B. Hummel, H. Qiu and M. Caffrey (1998). "A simple mechanical mixer for small viscous lipid-containing samples." Chemistry and Physics of Lipids **95**(1): 11-21.

Cherezov, V. (2011). "Lipidic cubic phase technologies for membrane protein structural studies." Curr Opin Struct Biol **21**(4): 559-566.

Choquesillo-Lazarte, D. and J. M. Garcia-Ruiz (2011). "Poly(ethylene) oxide for small-molecule crystal growth in gelled organic solvents." Journal of Applied Crystallography **44**(1): 172-176.

Claudio Pellegrini, S. R. (2004). "The Development of X-Ray Free-Electron Lasers." Ieee journal of selected topics in quantum electronics **10**(6): 1393-1404.

Cohen, A. E., S. M. Soltis, A. Gonzalez, L. Aguila, R. Alonso-Mori, C. O. Barnes, E. L. Baxter, W. Brehmer, A. S. Brewster, A. T. Brunger, G. Calero, J. F. Chang, M. Chollet, P. Ehrensberger, T. L. Eriksson, Y. Feng, J. Hattne, B. Hedman, M. Hollenbeck, J. M. Holton, S. Keable, B. K. Kobilka, E. G. Kovaleva, A. C. Kruse, H. T. Lemke, G. Lin, A. Y. Lyubimov, A. Manglik, Mathews, II, S. E. McPhillips, S. Nelson, J. W. Peters, N. K. Sauter, C. A. Smith, J. Song, H. P. Stevenson, Y. Tsai, M. Uervirojnangkoorn, V. Vinetsky, S. Wakatsuki, W. I. Weis, O. A. Zadvornyy, O. B.

Zeldin, D. Zhu and K. O. Hodgson (2014). "Goniometer-based femtosecond crystallography with X-ray free electron lasers." Proc Natl Acad Sci U S A **111**(48): 17122-17127.

Conrad, C. E., S. Basu, D. James, D. Wang, A. Schaffer, S. Roy-Chowdhury, N. A. Zatsepin, A. Aquila, J. Coe, C. Gati, M. S. Hunter, J. E. Koglin, C. Kupitz, G. Nelson, G. Subramanian, T. A. White, Y. Zhao, J. Zook, S. Boutet, V. Cherezov, J. C. Spence, R. Fromme, U. Weierstall and P. Fromme (2015). "A novel inert crystal delivery medium for serial femtosecond crystallography." IUCrJ **2**(Pt 4): 421-430.

Coquelle, N., A. S. Brewster, U. Kapp, A. Shilova, B. Weinhausen, M. Burghammer and J. P. Colletier (2015). "Raster-scanning serial protein crystallography using micro- and nano-focused synchrotron beams." Acta Crystallogr D Biol Crystallogr **71**(Pt 5): 1184-1196.

Cusack, S., H. Belrhali, A. Bram, M. Burghammer, A. Perrakis and C. Riekel (1998). "Small is beautiful: protein micro-crystallography." Nat Struct Mol Biol **5**: 634-637.

D'Souza, F. W., Y. Benenson and T. Baasov (1997). "Catalytic mechanism of KDO8P synthase: synthesis and evaluation of a putative reaction intermediate." Bioorganic & Medicinal Chemistry Letters **7**(19): 2457-2462.

Dattoli, G. R., A. (1984). "Experimental and Theoretical Aspects of Free-Electron Lasers, Laser Handbook." Vol. 4, edited by M. L. Stich and M. S. Bass. Amsterdam: North Holland.

Demirci, H., R. G. Sierra, H. Laksmono, R. L. Shoeman, S. Botha, T. R. M. Barends, K. Nass, I. Schlichting, R. B. Doak, C. Gati, G. J. Williams, S. Boutet, M. Messerschmidt, G. Jogl, A. E. Dahlberg, S. T. Gregory and M. J. Bogan (2013). "Serial femtosecond X-ray diffraction of 30S ribosomal subunit microcrystals in liquid suspension at ambient temperature using an X-ray free-electron laser." Acta Crystallographica Section F **69**(9): 1066-1069.

Denes, P. and B. Schmitt (2014). "Pixel detectors for diffraction-limited storage rings." J Synchrotron Radiat **21**(Pt 5): 1006-1010.

Denning, D. P., S. S. Patel, V. Uversky, A. L. Fink and M. Rexach (2003). "Disorder in the nuclear pore complex: the FG repeat regions of nucleoporins are natively unfolded." Proc Natl Acad Sci U S A **100**(5): 2450-2455.

DePonte, D. P., U. Weierstall, K. Schmidt, J. Warner, D. Starodub, J. C. H. Spence and R. B. Doak (2008). "Gas dynamic virtual nozzle for generation of microscopic droplet streams." Journal of Physics D: Applied Physics **41**(19): 195505.

Diaz-Quintana, A., W. Leibl, H. Bottin and P. Sétif (1998). "Electron transfer in photosystem I reaction centers follows a linear pathway in which iron-sulfur cluster FB is the immediate electron donor to soluble ferredoxin." Biochemistry **37**(10): 3429-3439.

Diusenberg, A. J. M. (1992). "Indexing in single-crystal diffractometry with an obstinate list of reflections." J. Appl. Cryst. **25**: 92-96.

Doering, D., Y. D. Chuang, N. Andresen, K. Chow, D. Contarato, C. Cummings, E. Domning, J. Joseph, J. S. Pepper, B. Smith, G. Zizka, C. Ford, W. S. Lee, M. Weaver, L. Patthey, J. Weizeorick, Z. Hussain and P. Denes (2011). "Development of a compact fast CCD camera and resonant soft x-ray scattering endstation for time-resolved pump-probe experiments." Rev Sci Instrum **82**(7): 073303.

Dotson, G. D., R. K. Dua, J. C. Clemens, E. W. Wooten and R. W. Woodard (1995). "Overproduction and one-step purification of Escherichia coli 3-deoxy-D-manno-octulosonic acid 8-phosphate synthase and oxygen transfer studies during catalysis using isotopic-shifted heteronuclear NMR." J Biol Chem **270**(23): 13698-13705.

Doye, J. P. K. and W. C. K. Poon (2006). "Protein crystallization in vivo." Current Opinion in Colloid & Interface Science **11**(1): 40-46.

Drenth, J. Principles of Protein X-ray Crystallography. Springer Science+Business Media, LLC, New York, 3rd edition (2007).

Duewel, H. S. and R. W. Woodard (2000). "A metal bridge between two enzyme families. 3-deoxy-D-manno-octulosonate-8-phosphate synthase from Aquifex aeolicus requires a divalent metal for activity." J Biol Chem **275**(30): 22824-22831.

Duisenberg, A. (1992). "Indexing in single-crystal diffractometry with an obstinate list of reflections." Journal of Applied Crystallography **25**(2): 92-96.

Emma, P. A., R.; Arthur, J.; Bionta, R.; Bostedt, C.; Bozek, J.; Brachmann, A.; Bucksbaum, P.; Coffee, R.; Decker, F.-J.; Ding, Y.; Dowell, D.; Edstrom, S.; Fisher, A.; Frisch, J.; Gilevich, S.; Hastings, J.; Hays, G.; Hering, Ph.; Huang, Z.; Iverson, R.; Loos, H.; Messerschmidt, M.; Miahnahri, A.; Moeller, S.; Nuhn, H.-D.; Pile, G.; Ratner, D.; Rzepiela, J.; Schultz, D.; Smith, T.; Stefan, P.; Tompkins, H.; Turner, J.; Welch, J.; White, W.; Wu, J.; Yocky, G.; Galayda, J. (2010). "First lasing and operation of an ångstrom-wavelength free-electron laser." Nature Photon **4**: 641-647.

Emsley, P. and K. Cowtan (2004). "Coot: model-building tools for molecular graphics." Acta Crystallogr D Biol Crystallogr **60**(Pt 12 Pt 1): 2126-2132.

Feld, G. K., M. Heymann, W. H. Benner, T. Pardini, C.-J. Tsai, S. Boutet, M. A. Coleman, M. S. Hunter, X. Li, M. Messerschmidt, A. Opathalage, B. Pedrini, G. J. Williams, B. A. Krantz, S. Fraden, S. Hau-Riege, J. E. Evans, B. W. Segelke and M. Frank (2015). "Low-Z polymer sample supports for fixed-target serial femtosecond X-ray crystallography." Journal of Applied Crystallography **48**(4): 1072-1079.

Fenalti, G., N. A. Zatsepin, C. Betti, P. Giguere, G. W. Han, A. Ishchenko, W. Liu, K. Guillemyn, H. Zhang, D. James, D. Wang, U. Weierstall, J. C. Spence, S. Boutet, M. Messerschmidt, G. J. Williams, C. Gati, O. M. Yefanov, T. A. White, D. Oberthuer, M. Metz, C. H. Yoon, A. Barty, H. N. Chapman, S. Basu, J. Coe, C. E. Conrad, R. Fromme, P. Fromme, D. Tourwe, P. W. Schiller, B. L. Roth, S. Ballet, V. Katritch, R. C. Stevens and V. Cherezov (2015). "Structural basis for bifunctional peptide recognition at human delta-opioid receptor." Nat Struct Mol Biol **22**(3): 265-268.

Filipe, V., A. Hawe and W. Jiskoot (2010). "Critical evaluation of Nanoparticle Tracking Analysis (NTA) by NanoSight for the measurement of nanoparticles and protein aggregates." Pharmaceutical research **27**(5): 796-810.

Foucar, L., Barty, A., Coppola, N., Hartmann, R., Holl, P., Hoppe, U., et al. (2012). "CASS—CFEL-ASG software suite." Computer Physics Communications **183**(10): 2207-2213.

Friedrich, W., P. Knipping and M. v. Laue (1912). Interferenz-Erscheinungen bei Röntgenstrahlen, von W. Friedrich, P. Knipping und M. Lane. München, Verlag der Königlich-Bayerischen Akademie der Wissenschaften.

Fromme, P., H. Bottin, N. Krauss and P. Setif (2002). "Crystallization and electron paramagnetic resonance characterization of the complex of photosystem I with its natural electron acceptor ferredoxin." Biophys J **83**(4): 1760-1773.

Fromme, P. and H. T. Witt (1998). "Improved isolation and crystallization of photosystem I for structural analysis." Biochimica et Biophysica Acta (BBA) - Bioenergetics **1365**(1–2): 175-184.

Fromme, R., A. Ishchenko, M. Metz, S. R. Chowdhury, S. Basu, S. Boutet, P. Fromme, T. A. White, A. Barty and J. C. Spence (2015). "Serial femtosecond crystallography of soluble proteins in lipidic cubic phase." IUCrJ **2**(5): 545-551.

Gallat, F.-X., N. Matsugaki, N. P. Coussens, K. J. Yagi, M. Boudes, T. Higashi, D. Tsuji, Y. Tatano, M. Suzuki, E. Mizohata, K. Tono, Y. Joti, T. Kameshima, J. Park, C. Song, T. Hatsui, M. Yabashi, E. Nango, K. Itoh, F. Coulibaly, S. Tobe, S. Ramaswamy, B. Stay, S. Iwata and L. M. G. Chavas (2014). "In vivo crystallography at X-ray free-electron lasers: the next generation of structural biology?" Philosophical Transactions of the Royal Society of London B: Biological Sciences **369**(1647).

Galli, L., S. K. Son, T. A. White, R. Santra, H. N. Chapman and M. H. Nanao (2015). "Towards RIP using free-electron laser SFX data." J Synchrotron Radiat **22**(Pt 2): 249-255.

García-Ruiz, J. M., M. L. Novella, R. Moreno and J. A. Gavira (2001). "Agarose as crystallization media for proteins: I: Transport processes." Journal of Crystal Growth **232**(1–4): 165-172.

Garman, E. F. (2010). "Radiation damage in macromolecular crystallography: what is it and why should we care?" Acta Crystallographica Section D: Biological Crystallography **66**(Pt 4): 339-351.

Garman, E. F. and S. M. McSweeney (2007). "Progress in research into radiation damage in cryo-cooled macromolecular crystals." J Synchrotron Radiat **14**(Pt 1): 1-3.

Garman, E. F. and R. L. Owen (2006). "Cryocooling and radiation damage in macromolecular crystallography." Acta Crystallographica Section D **62**(1): 32-47.

Gati, C., G. Bourenkov, M. Klinge, D. Rehders, F. Stellato, D. Oberthur, O. Yefanov, B. P. Sommer, S. Mogk, M. Duszenko, C. Betzel, T. R. Schneider, H. N. Chapman and L. Redecke (2014). "Serial crystallography on in vivo grown microcrystals using synchrotron radiation." IUCrJ **1**(Pt 2): 87-94.

Genick, U. K., G. E. Borgstahl, K. Ng, Z. Ren, C. Pradervand, P. M. Burke, V. Šrajer, T.-Y. Teng, W. Schildkamp and D. E. McRee (1997). "Structure of a protein photocycle intermediate by millisecond time-resolved crystallography." Science **275**(5305): 1471-1475.

Ginn, H. M., M. Messerschmidt, X. Ji, H. Zhang, D. Axford, R. J. Gildea, G. Winter, A. S. Brewster, J. Hattne and A. Wagner (2015). "Structure of CPV17 polyhedrin determined by the improved analysis of serial femtosecond crystallographic data." Nature communications **6**.

Hajdu, J. and L. N. Johnson (1990). "Progress with Laue diffraction studies on protein and virus crystals." Biochemistry **29**(7): 1669-1678.

Hart P., S. B. G. C. M. D. B. D. D. F. G. H. R. H. S. H. C. K. N. K. (2012). "The CSPAD megapixel x-ray camera at LCLS " Proc. SPIE 8504, X-Ray Free-Electron Lasers: Beam Diagnostics, Beamline Instrumentation, and Applications: 85040C.

Hattne, J., N. Echols, R. Tran, J. Kern, R. J. Gildea, A. S. Brewster, R. Alonso-Mori, C. Glockner, J. Hellmich, H. Laksmono, R. G. Sierra, B. Lassalle-Kaiser, A. Lampe, G. Han, S. Gul, D. DiFiore, D. Milathianaki, A. R. Fry, A. Miahnahri, W. E. White, D. W. Schafer, M. M. Seibert, J. E. Koglin, D. Sokaras, T. C. Weng, J. Sellberg, M. J. Latimer, P. Glatzel, P. H. Zwart, R. W. Grosse-Kunstleve, M. J. Bogan, M. Messerschmidt, G. J. Williams, S. Boutet, J. Messinger, A. Zouni, J. Yano, U. Bergmann, V. K. Yachandra, P. D. Adams and N. K. Sauter (2014). "Accurate macromolecular structures using minimal measurements from X-ray free-electron lasers." <u>Nat Methods</u> **11**(5): 545-548.

Hau-Riege, S. P., R. A. London and A. Szoke (2004). "Dynamics of biological molecules irradiated by short x-ray pulses." <u>Phys Rev E Stat Nonlin Soft Matter Phys</u> **69**(5 Pt 1): 051906.

Helliwell, J. R. (1984). "Synchrotron X-radiation protein crystallography: instrumentation, methods and applications." <u>Reports on Progress in Physics</u> **47**(11): 1403.

Helliwell, J. R., Y. P. Nieh, J. Habash, P. F. Faulder, J. Raftery, M. Cianci, M. Wulff and A. Hädener (2003). "Time-resolved and static-ensemble structural chemistry of hydroxymethylbilane synthase." <u>Faraday discussions</u> **122**: 131-144.

Hellmich, J., M. Bommer, A. Burkhardt, M. Ibrahim, J. Kern, A. Meents, F. Müh, H. Dobbek and A. Zouni (2014). "Native-like Photosystem II Superstructure at 2.44 Å Resolution through Detergent Extraction from the Protein Crystal." <u>Structure</u> **22**(11): 1607-1615.

Hendrickson, W. A. (2014). "Anomalous diffraction in crystallographic phase evaluation." <u>Q Rev Biophys</u> **47**(1): 49-93.

Heymann, M., A. Opthalage, J. L. Wierman, S. Akella, D. M. Szebenyi, S. M. Gruner and S. Fraden (2014). "Room-temperature serial crystallography using a kinetically optimized microfluidic device for protein crystallization and on-chip X-ray diffraction." <u>IUCrJ</u> **1**(Pt 5): 349-360.

Hirata, K., K. Shinzawa-Itoh, N. Yano, S. Takemura, K. Kato, M. Hatanaka, K. Muramoto, T. Kawahara, T. Tsukihara and E. Yamashita (2014). "Determination of damage-free crystal structure of an X-ray-sensitive protein using an XFEL." <u>Nature Methods</u> **11**(7): 734-736.

Hofbauer, W., A. Zouni, R. Bittl, J. Kern, P. Orth, F. Lendzian, P. Fromme, H. T. Witt and W. Lubitz (2001). "Photosystem II single crystals studied by EPR spectroscopy at 94 GHz: the tyrosine radical Y(D)(*)." <u>Proc Natl Acad Sci U S A</u> **98**(12): 6623-6628.

Holton, J. M. (2009). "A beginner's guide to radiation damage." <u>J Synchrotron Radiat</u> **16**(Pt 2): 133-142.

Hopkins, A. L. and C. R. Groom (2002). "The druggable genome." <u>Nat Rev Drug Discov</u> **1**(9): 727-730.

Howells, M. R., T. Beetz, H. N. Chapman, C. Cui, J. M. Holton, C. J. Jacobsen, J. Kirz, E. Lima, S. Marchesini, H. Miao, D. Sayre, D. A. Shapiro, J. C. Spence and D. Starodub (2009). "An assessment of the resolution limitation due to radiation-damage in x-ray diffraction microscopy." <u>J Electron Spectros Relat Phenomena</u> **170**(1-3): 4-12.

Hunter, M. S. and P. Fromme (2011). "Toward structure determination using membrane-protein nanocrystals and microcrystals." <u>Methods</u> **55**(4): 387-404.

Hunter, M. S., B. Segelke, M. Messerschmidt, G. J. Williams, N. A. Zatsepin, A. Barty, W. H. Benner, D. B. Carlson, M. Coleman and A. Graf (2014). "Fixed-target protein serial microcrystallography with an x-ray free electron laser." Scientific reports **4**.

Ibrahim, M., R. Chatterjee, J. Hellmich, R. Tran, M. Bommer, V. K. Yachandra, J. Yano, J. Kern and A. Zouni (2015). "Improvements in serial femtosecond crystallography of photosystem II by optimizing crystal uniformity using microseeding procedures." Structural Dynamics **2**(4): 041705.

Johansson, L. C., D. Arnlund, G. Katona, T. A. White, A. Barty, D. P. DePonte, R. L. Shoeman, C. Wickstrand, A. Sharma, G. J. Williams, A. Aquila, M. J. Bogan, C. Caleman, J. Davidsson, R. B. Doak, M. Frank, R. Fromme, L. Galli, I. Grotjohann, M. S. Hunter, S. Kassemeyer, R. A. Kirian, C. Kupitz, M. Liang, L. Lomb, E. Malmerberg, A. V. Martin, M. Messerschmidt, K. Nass, L. Redecke, M. M. Seibert, J. Sjohamn, J. Steinbrener, F. Stellato, D. Wang, W. Y. Wahlgren, U. Weierstall, S. Westenhoff, N. A. Zatsepin, S. Boutet, J. C. Spence, I. Schlichting, H. N. Chapman, P. Fromme and R. Neutze (2013). "Structure of a photosynthetic reaction centre determined by serial femtosecond crystallography." Nat Commun **4**: 2911.

Johansson, L. C., D. Arnlund, T. A. White, G. Katona, D. P. Deponte, U. Weierstall, R. B. Doak, R. L. Shoeman, L. Lomb, E. Malmerberg, J. Davidsson, K. Nass, M. Liang, J. Andreasson, A. Aquila, S. Bajt, M. Barthelmess, A. Barty, M. J. Bogan, C. Bostedt, J. D. Bozek, C. Caleman, R. Coffee, N. Coppola, T. Ekeberg, S. W. Epp, B. Erk, H. Fleckenstein, L. Foucar, H. Graafsma, L. Gumprecht, J. Hajdu, C. Y. Hampton, R. Hartmann, A. Hartmann, G. Hauser, H. Hirsemann, P. Holl, M. S. Hunter, S. Kassemeyer, N. Kimmel, R. A. Kirian, F. R. Maia, S. Marchesini, A. V. Martin, C. Reich, D. Rolles, B. Rudek, A. Rudenko, I. Schlichting, J. Schulz, M. M. Seibert, R. G. Sierra, H. Soltau, D. Starodub, F. Stellato, S. Stern, L. Struder, N. Timneanu, J. Ullrich, W. Y. Wahlgren, X. Wang, G. Weidenspointner, C. Wunderer, P. Fromme, H. N. Chapman, J. C. Spence and R. Neutze (2012). "Lipidic phase membrane protein serial femtosecond crystallography." Nat Methods **9**(3): 263-265.

Jordan, P., P. Fromme, H. T. Witt, O. Klukas, W. Saenger and N. Krauss (2001). "Three-dimensional structure of cyanobacterial photosystem I at 2.5 A resolution." Nature **411**(6840): 909-917.

Kabsch, W. (2010). "Xds." Acta Crystallogr D Biol Crystallogr **66**(Pt 2): 125-132.

Kang, Y., X. E. Zhou, X. Gao, Y. He, W. Liu, A. Ishchenko, A. Barty, T. A. White, O. Yefanov and G. W. Han (2015). "Crystal structure of rhodopsin bound to arrestin by femtosecond X-ray laser." Nature **523**(7562): 561-567.

Kang, Y., X. E. Zhou, X. Gao, Y. He, W. Liu, A. Ishchenko, A. Barty, T. A. White, O. Yefanov, G. W. Han, Q. Xu, P. W. de Waal, J. Ke, M. H. Tan, C. Zhang, A. Moeller, G. M. West, B. D. Pascal, N. Van Eps, L. N. Caro, S. A. Vishnivetskiy, R. J. Lee, K. M. Suino-Powell, X. Gu, K. Pal, J. Ma, X. Zhi, S. Boutet, G. J. Williams, M. Messerschmidt, C. Gati, N. A. Zatsepin, D. Wang, D. James, S. Basu, S. Roy-Chowdhury, C. E. Conrad, J. Coe, H. Liu, S. Lisova, C. Kupitz, I. Grotjohann, R. Fromme, Y. Jiang, M. Tan, H. Yang, J. Li, M. Wang, Z. Zheng, D. Li, N. Howe, Y. Zhao, J. Standfuss, K. Diederichs, Y. Dong, C. S. Potter, B. Carragher, M. Caffrey, H. Jiang, H. N. Chapman, J. C. Spence, P. Fromme, U. Weierstall, O. P. Ernst, V. Katritch, V. V. Gurevich, P. R. Griffin, W. L. Hubbell, R. C. Stevens, V. Cherezov, K. Melcher and H. E. Xu (2015). "Crystal structure of rhodopsin bound to arrestin by femtosecond X-ray laser." Nature **523**(7562): 561-567.

Karplus, P. A. and K. Diederichs (2012). "Linking crystallographic model and data quality." Science (New York, N.Y.) **336**(6084): 1030-1033.

Katona, G., U. Andréasson, E. M. Landau, L.-E. Andréasson and R. Neutze (2003). "Lipidic Cubic Phase Crystal Structure of the Photosynthetic Reaction Centre from Rhodobacter sphaeroides at 2.35 Å Resolution." Journal of Molecular Biology **331**(3): 681-692.

Keedy, D. A., L. R. Kenner, M. Warkentin, R. A. Woldeyes, J. B. Hopkins, M. C. Thompson, A. S. Brewster, A. H. Van Benschoten, E. L. Baxter, M. Uervirojnangkoorn, S. E. McPhillips, J. Song, R. Alonso-Mori, J. M. Holton, W. I. Weis, A. T. Brunger, S. M. Soltis, H. Lemke, A. Gonzalez, N. K. Sauter, A. E. Cohen, H. van den Bedem, R. E. Thorne and J. S. Fraser (2015). "Mapping the conformational landscape of a dynamic enzyme by multitemperature and XFEL crystallography." eLife **4**: e07574.

Kendrew, J. C., G. Bodo, H. M. Dintzis, R. G. Parrish, H. Wyckoff and D. C. Phillips (1958). "A Three-Dimensional Model of the Myoglobin Molecule Obtained by X-Ray Analysis." Nature **181**(4610): 662-666.

Kern, J., R. Alonso-Mori, J. Hellmich, R. Tran, J. Hattne, H. Laksmono, C. Glöckner, N. Echols, R. G. Sierra, J. Sellberg, B. Lassalle-Kaiser, R. J. Gildea, P. Glatzel, R. W. Grosse-Kunstleve, M. J. Latimer, T. A. McQueen, D. DiFiore, A. R. Fry, M. Messerschmidt, A. Miahnahri, D. W. Schafer, M. M. Seibert, D. Sokaras, T.-C. Weng, P. H. Zwart, W. E. White, P. D. Adams, M. J. Bogan, S. Boutet, G. J. Williams, J. Messinger, N. K. Sauter, A. Zouni, U. Bergmann, J. Yano and V. K. Yachandra (2012). "Room temperature femtosecond X-ray diffraction of photosystem II microcrystals." Proceedings of the National Academy of Sciences of the United States of America **109**(25): 9721-9726.

Kern, J., R. Alonso-Mori, R. Tran, J. Hattne, R. J. Gildea, N. Echols, C. Glöckner, J. Hellmich, H. Laksmono and R. G. Sierra (2013). "Simultaneous femtosecond X-ray spectroscopy and diffraction of photosystem II at room temperature." Science **340**(6131): 491-495.

Kirian, R. A., R. J. Bean, K. R. Beyerlein, O. M. Yefanov, T. A. White, A. Barty and H. N. Chapman (2014). "Phasing coherently illuminated nanocrystals bounded by partial unit cells." Philos Trans R Soc Lond B Biol Sci **369**(1647): 20130331.

Kirian, R. A., X. Wang, U. Weierstall, K. E. Schmidt, J. C. Spence, M. Hunter, P. Fromme, T. White, H. N. Chapman and J. Holton (2010). "Femtosecond protein nanocrystallography—data analysis methods." Optics express **18**(6): 5713-5723.

Kirian, R. A., T. A. White, J. M. Holton, H. N. Chapman, P. Fromme, A. Barty, L. Lomb, A. Aquila, F. R. Maia, A. V. Martin, R. Fromme, X. Wang, M. S. Hunter, K. E. Schmidt and J. C. Spence (2011). "Structure-factor analysis of femtosecond microdiffraction patterns from protein nanocrystals." Acta Crystallogr A **67**(Pt 2): 131-140.

Kissick, D. J., D. Wanapun and G. J. Simpson (2011). "Second-order nonlinear optical imaging of chiral crystals." Annu Rev Anal Chem (Palo Alto Calif) **4**: 419-437.

Koerner, L. J., Philipp, H. T., Hromalik, M. S., Tate, M. W. & Gruner, S. M. (2009). "X-ray tests of a Pixel Array Detector for coherent x-ray imaging at the Linac Coherent Light Source " JINST **4**: P03001–P03001.

Kona, F., X. Xu, P. Martin, P. Kuzmic and D. L. Gatti (2007). "Structural and Mechanistic Changes along an Engineered Path from Metallo to Nonmetallo 3-Deoxy-d-manno-octulosonate 8-Phosphate Synthases." Biochemistry **46**(15): 4532-4544.

Koopmann, R., K. Cupelli, L. Redecke, K. Nass, D. P. Deponte, T. A. White, F. Stellato, D. Rehders, M. Liang, J. Andreasson, A. Aquila, S. Bajt, M. Barthelmess, A. Barty, M. J. Bogan, C.

Bostedt, S. Boutet, J. D. Bozek, C. Caleman, N. Coppola, J. Davidsson, R. B. Doak, T. Ekeberg, S. W. Epp, B. Erk, H. Fleckenstein, L. Foucar, H. Graafsma, L. Gumprecht, J. Hajdu, C. Y. Hampton, A. Hartmann, R. Hartmann, G. Hauser, H. Hirsemann, P. Holl, M. S. Hunter, S. Kassemeyer, R. A. Kirian, L. Lomb, F. R. Maia, N. Kimmel, A. V. Martin, M. Messerschmidt, C. Reich, D. Rolles, B. Rudek, A. Rudenko, I. Schlichting, J. Schulz, M. M. Seibert, R. L. Shoeman, R. G. Sierra, H. Soltau, S. Stern, L. Struder, N. Timneanu, J. Ullrich, X. Wang, G. Weidenspointner, U. Weierstall, G. J. Williams, C. B. Wunderer, P. Fromme, J. C. Spence, T. Stehle, H. N. Chapman, C. Betzel and M. Duszenko (2012). "In vivo protein crystallization opens new routes in structural biology." Nat Methods **9**(3): 259-262.

Kourkoutis, L. F., J. M. Plitzko and W. Baumeister (2012). "Electron Microscopy of Biological Materials at the Nanometer Scale." Annual Review of Materials Research **42**(1): 33-58.

Kupitz, C., S. Basu, I. Grotjohann, R. Fromme, N. A. Zatsepin, K. N. Rendek, M. S. Hunter, R. L. Shoeman, T. A. White, D. Wang, D. James, J. H. Yang, D. E. Cobb, B. Reeder, R. G. Sierra, H. Liu, A. Barty, A. L. Aquila, D. Deponte, R. A. Kirian, S. Bari, J. J. Bergkamp, K. R. Beyerlein, M. J. Bogan, C. Caleman, T. C. Chao, C. E. Conrad, K. M. Davis, H. Fleckenstein, L. Galli, S. P. Hau-Riege, S. Kassemeyer, H. Laksmono, M. Liang, L. Lomb, S. Marchesini, A. V. Martin, M. Messerschmidt, D. Milathianaki, K. Nass, A. Ros, S. Roy-Chowdhury, K. Schmidt, M. Seibert, J. Steinbrener, F. Stellato, L. Yan, C. Yoon, T. A. Moore, A. L. Moore, Y. Pushkar, G. J. Williams, S. Boutet, R. B. Doak, U. Weierstall, M. Frank, H. N. Chapman, J. C. Spence and P. Fromme (2014). "Serial time-resolved crystallography of photosystem II using a femtosecond X-ray laser." Nature **513**(7517): 261-265.

Kupitz, C., I. Grotjohann, C. E. Conrad, S. Roy-Chowdhury, R. Fromme and P. Fromme (2014). "Microcrystallization techniques for serial femtosecond crystallography using photosystem II from Thermosynechococcus elongatus as a model system." Philosophical Transactions of the Royal Society B: Biological Sciences **369**(1647): 20130316.

Landau, E. M. and J. P. Rosenbusch (1996). "Lipidic cubic phases: a novel concept for the crystallization of membrane proteins." Proc Natl Acad Sci U S A **93**(25): 14532-14535.

Lawrence, R. M., C. E. Conrad, N. A. Zatsepin, T. D. Grant, H. Liu, D. James, G. Nelson, G. Subramanian, A. Aquila and M. S. Hunter (2015). "Serial femtosecond X-ray diffraction of enveloped virus microcrystals." Structural Dynamics **2**(4): 041720.

Lee, H. H., I. Cherni, H. Yu, R. Fromme, J. D. Doran, I. Grotjohann, M. Mittman, S. Basu, A. Deb, K. Dorner, A. Aquila, A. Barty, S. Boutet, H. N. Chapman, R. B. Doak, M. S. Hunter, D. James, R. A. Kirian, C. Kupitz, R. M. Lawrence, H. Liu, K. Nass, I. Schlichting, K. E. Schmidt, M. M. Seibert, R. L. Shoeman, J. C. Spence, F. Stellato, U. Weierstall, G. J. Williams, C. Yoon, D. Wang, N. A. Zatsepin, B. G. Hogue, N. Matoba, P. Fromme and T. S. Mor (2014). "Expression, purification and crystallization of CTB-MPR, a candidate mucosal vaccine component against HIV-1." IUCrJ **1**(Pt 5): 305-317.

Levin, D. H. and E. Racker (1959). "Condensation of arabinose 5-phosphate and phosphorylenol pyruvate by 2-keto-3-deoxy-8-phosphooctonic acid synthetase." J Biol Chem **234**: 2532-2539.

Li, D., P. J. Stansfeld, M. S. Sansom, A. Keogh, L. Vogeley, N. Howe, J. A. Lyons, D. Aragao, P. Fromme, R. Fromme, S. Basu, I. Grotjohann, C. Kupitz, K. Rendek, U. Weierstall, N. A. Zatsepin, V. Cherezov, W. Liu, S. Bandaru, N. J. English, C. Gati, A. Barty, O. Yefanov, H. N. Chapman, K. Diederichs, M. Messerschmidt, S. Boutet, G. J. Williams, M. Marvin Seibert and M. Caffrey (2015). "Ternary structure reveals mechanism of a membrane diacylglycerol kinase." Nat Commun **6**: 10140.

Li, Z., A. K. Sau, C. M. Furdui and K. S. Anderson (2005). "Probing the role of tightly bound phosphoenolpyruvate in Escherichia coli 3-deoxy-d-manno-octulosonate 8-phosphate synthase catalysis using quantitative time-resolved electrospray ionization mass spectrometry in the millisecond time range." Anal Biochem **343**(1): 35-47.

Liang, P.-H., J. Lewis, K. S. Anderson, A. Kohen, F. W. D'Souza, Y. Benenson and T. Baasov (1998). "Catalytic Mechanism of Kdo8P Synthase: Transient Kinetic Studies and Evaluation of a Putative Reaction Intermediate." Biochemistry **37**(46): 16390-16399.

Liao, J., H. Li, W. Zeng, D. B. Sauer, R. Belmares and Y. Jiang (2012). "Structural Insight into the Ion-Exchange Mechanism of the Sodium/Calcium Exchanger." Science **335**(6069): 686-690.

Liu, H., B. K. Poon, D. K. Saldin, J. C. Spence and P. H. Zwart (2013). "Three-dimensional single-particle imaging using angular correlations from X-ray laser data." Acta Crystallogr A **69**(Pt 4): 365-373.

Liu, W., A. Ishchenko and V. Cherezov (2014). "Preparation of microcrystals in lipidic cubic phase for serial femtosecond crystallography." Nat Protoc **9**(9): 2123-2134.

Liu, W., D. Wacker, C. Gati, G. W. Han, D. James, D. Wang, G. Nelson, U. Weierstall, V. Katritch, A. Barty, N. A. Zatsepin, D. Li, M. Messerschmidt, S. Boutet, G. J. Williams, J. E. Koglin, M. M. Seibert, C. Wang, S. T. Shah, S. Basu, R. Fromme, C. Kupitz, K. N. Rendek, I. Grotjohann, P. Fromme, R. A. Kirian, K. R. Beyerlein, T. A. White, H. N. Chapman, M. Caffrey, J. C. Spence, R. C. Stevens and V. Cherezov (2013). "Serial femtosecond crystallography of G protein-coupled receptors." Science **342**(6165): 1521-1524.

Liu, W., D. Wacker, C. Wang, E. Abola and V. Cherezov (2014). "Femtosecond crystallography of membrane proteins in the lipidic cubic phase." Philos Trans R Soc Lond B Biol Sci **369**(1647): 20130314.

Lomb, L., T. R. Barends, S. Kassemeyer, A. Aquila, S. W. Epp, B. Erk, L. Foucar, R. Hartmann, B. Rudek, D. Rolles, A. Rudenko, R. L. Shoeman, J. Andreasson, S. Bajt, M. Barthelmess, A. Barty, M. J. Bogan, C. Bostedt, J. D. Bozek, C. Caleman, R. Coffee, N. Coppola, D. P. Deponte, R. B. Doak, T. Ekeberg, H. Fleckenstein, P. Fromme, M. Gebhardt, H. Graafsma, L. Gumprecht, C. Y. Hampton, A. Hartmann, G. Hauser, H. Hirsemann, P. Holl, J. M. Holton, M. S. Hunter, W. Kabsch, N. Kimmel, R. A. Kirian, M. Liang, F. R. Maia, A. Meinhart, S. Marchesini, A. V. Martin, K. Nass, C. Reich, J. Schulz, M. M. Seibert, R. Sierra, H. Soltau, J. C. Spence, J. Steinbrener, F. Stellato, S. Stern, N. Timneanu, X. Wang, G. Weidenspointner, U. Weierstall, T. A. White, C. Wunderer, H. N. Chapman, J. Ullrich, L. Struder and I. Schlichting (2011). "Radiation damage in protein serial femtosecond crystallography using an x-ray free-electron laser." Phys Rev B Condens Matter Mater Phys **84**(21): 214111.

Lorber, B., C. Sauter, A. Théobald-Dietrich, A. Moreno, P. Schellenberger, M.-C. Robert, B. Capelle, S. Sanglier, N. Potier and R. Giegé (2009). "Crystal growth of proteins, nucleic acids, and viruses in gels." Progress in Biophysics and Molecular Biology **101**(1–3): 13-25.

Lyubimov, A. Y., T. D. Murray, A. Koehl, I. E. Araci, M. Uervirojnangkoorn, O. B. Zeldin, A. E. Cohen, S. M. Soltis, E. L. Baxter, A. S. Brewster, N. K. Sauter, A. T. Brunger and J. M. Berger (2015). "Capture and X-ray diffraction studies of protein microcrystals in a microfluidic trap array." Acta Crystallogr D Biol Crystallogr **71**(Pt 4): 928-940.

Ma, T. K., K. K. Kam, B. P. Yan and Y. Y. Lam (2010). "Renin-angiotensin-aldosterone system blockade for cardiovascular diseases: current status." Br J Pharmacol **160**(6): 1273-1292.

Madey, J. (1971). "Stimulated emission of bremsstrahlung in a periodic magnetic field." J. Appl. Phys **42**: 1906-1913.

Mariani, V., A. Morgan, C. H. Yoon, T. J. Lane, T. A. White, C. O'Grady, M. Kuhn, S. Aplin, J. Koglin, A. Barty and H. N. Chapman (2016). "OnDA: online data analysis and feedback for serial X-ray imagingThis article will form part of a virtual special issue of the journal on free-electron laser software." Journal of Applied Crystallography **49**(3): 1073-1080.

Marin, M. and T. Ott (2012). "Phosphorylation of intrinsically disordered regions in remorin proteins." Front Plant Sci **3**: 86.

Martin-Garcia, J. M., D. T. Hansen, J. Zook, A. V. Loskutov, M. D. Robida, F. M. Craciunescu, K. F. Sykes, R. M. Wachter, P. Fromme and J. P. Allen (2014). "Purification and Biophysical Characterization of the CapA Membrane Protein FTT0807 from Francisella tularensis." Biochemistry **53**(12): 1958-1970.

Maune, H. T., S. P. Han, R. D. Barish, M. Bockrath, W. A. Iii, P. W. Rothemund and E. Winfree (2010). "Self-assembly of carbon nanotubes into two-dimensional geometries using DNA origami templates." Nat Nanotechnol **5**(1): 61-66.

McCoy, A. J. (2007). "Solving structures of protein complexes by molecular replacement with Phaser." Acta Crystallographica Section D: Biological Crystallography **63**(Pt 1): 32-41.

McNeil, B. W. J. and N. R. Thompson (2010). "X-ray free-electron lasers." Nat Photon **4**(12): 814-821.

McPherson, A. (1999). Crystallization of biological macromolecules, Cold Spring Harbor Laboratory Press.

McPherson, A. and B. Cudney (2014). "Optimization of crystallization conditions for biological macromolecules." Structural Biology and Crystallization Communications **70**(11): 1445-1467.

Miao, J., H. N. Chapman, J. Kirz, D. Sayre and K. O. Hodgson (2004). "Taking X-ray diffraction to the limit: macromolecular structures from femtosecond X-ray pulses and diffraction microscopy of cells with synchrotron radiation." Annu Rev Biophys Biomol Struct **33**: 157-176.

Mizianty, M. J., X. Fan, J. Yan, E. Chalmers, C. Woloschuk, A. Joachimiak and L. Kurgan (2014). "Covering complete proteomes with X-ray structures: a current snapshot." Acta Crystallogr D Biol Crystallogr **70**(Pt 11): 2781-2793.

Moffat, K. (2001). "Time-resolved biochemical crystallography: a mechanistic perspective." Chemical reviews **101**(6): 1569-1582.

Moffat, K. and R. Henderson (1995). "Freeze trapping of reaction intermediates." Curr Opin Struct Biol **5**(5): 656-663.

Mueller, C., A. Marx, S. W. Epp, Y. Zhong, A. Kuo, A. R. Balo, J. Soman, F. Schotte, H. T. Lemke, R. L. Owen, E. F. Pai, A. R. Pearson, J. S. Olson, P. A. Anfinrud, O. P. Ernst and R. J. Dwayne Miller (2015). "Fixed target matrix for femtosecond time-resolved and in situ serial micro-crystallography." Structural Dynamics **2**(5): 054302.

Murshudov, G. N., P. Skubak, A. A. Lebedev, N. S. Pannu, R. A. Steiner, R. A. Nicholls, M. D. Winn, F. Long and A. A. Vagin (2011). "REFMAC5 for the refinement of macromolecular crystal structures." Acta Crystallographica Section D **67**(4): 355-367.

Murray, T. D., A. Y. Lyubimov, C. M. Ogata, H. Vo, M. Uervirojnangkoorn, A. T. Brunger and J. M. Berger (2015). "A high-transparency, micro-patternable chip for X-ray diffraction analysis of microcrystals under native growth conditions." Acta Crystallogr D Biol Crystallogr **71**(Pt 10): 1987-1997.

Nave, C. and E. F. Garman (2005). "Towards an understanding of radiation damage in cryocooled macromolecular crystals." Journal of Synchrotron Radiation **12**(3): 257-260.

Neutze, R., R. Wouts, D. van der Spoel, E. Weckert and J. Hajdu (2000). "Potential for biomolecular imaging with femtosecond X-ray pulses." Nature **406**(6797): 752-757.

Newman, J. A., N. M. Scarborough, N. R. Pogranichniy, R. K. Shrestha, R. G. Closser, C. Das and G. J. Simpson (2015). "Intercalating dyes for enhanced contrast in second-harmonic generation imaging of protein crystals." Acta Crystallogr D Biol Crystallogr **71**(Pt 7): 1471-1477.

Nogly P, J. D., Wang D, et al (2015). " Lipidic cubic phase serial millisecond crystallography using synchrotron radiation." IUCrJ **2**: 168-176.

Nogly, P., V. Panneels, G. Nelson, C. Gati, T. Kimura, C. Milne, D. Milathianaki, M. Kubo, W. Wu, C. Conrad, J. Coe, R. Bean, Y. Zhao, P. Bath, R. Dods, R. Harimoorthy, K. R. Beyerlein, J. Rheinberger, D. James, D. DePonte, C. Li, L. Sala, G. J. Williams, M. S. Hunter, J. E. Koglin, P. Berntsen, E. Nango, S. Iwata, H. N. Chapman, P. Fromme, M. Frank, R. Abela, S. Boutet, A. Barty, T. A. White, U. Weierstall, J. Spence, R. Neutze, G. Schertler and J. Standfuss (2016). "Lipidic cubic phase injector is a viable crystal delivery system for time-resolved serial crystallography." Nat Commun **7**: 12314.

Nyarko, A., M. Hare, T. S. Hays and E. Barbar (2004). "The Intermediate Chain of Cytoplasmic Dynein Is Partially Disordered and Gains Structure upon Binding to Light-Chain LC8." Biochemistry **43**(49): 15595-15603.

Oliynyk, Z., L. Briseno-Roa, T. Janowitz, P. Sondergeld and A. R. Fersht (2004). "Designing a metal-binding site in the scaffold of Escherichia coli KDO8PS." Protein Eng Des Sel **17**(4): 383-390.

Owen, R. L., E. Rudino-Pinera and E. F. Garman (2006). "Experimental determination of the radiation dose limit for cryocooled protein crystals." Proc Natl Acad Sci U S A **103**(13): 4912-4917.

Owen, R. L., D. Axford, J. E. Nettleship, R. J. Owens, J. I. Robinson, A. W. Morgan, A. S. Dore, G. Lebon, C. G. Tate, E. E. Fry, J. Ren, D. I. Stuart and G. Evans (2012). "Outrunning free radicals in room-temperature macromolecular crystallography." Acta Crystallogr D Biol Crystallogr **68**(Pt 7): 810-818.

Pande, K., C. D. M. Hutchinson, G. Groenhof, A. Aquila, J. S. Robinson, J. Tenboer, S. Basu, S. Boutet, D. Deponte, M. Liang, T. White, N. Zatsepin, O. Yefanov, D. Morozov, D. Oberthuer, C. Gati, G. Subramanian, D. James, Y. Zhao, J. Koralek, J. Brayshaw, C. Kupitz, C. Conrad, S. Roy-Chowdhury, J. Coe, M. Metz, X. Paulraj Lourdu, T. Grant, J. Koglin, G. Ketawala, R. Fromme, V. Srajer, R. Henning, J. Spence, A. Ourmazd, P. Schwander, U. Weierstall, M. Frank, P. Fromme, A. Barty, H. Chapman, K. Moffat, J. J. Van Thor and M. Schmidt (2015). "Femtosecond Structural Dynamics Drives the Trans/Cis Isomerization in Photoactive Yellow Protein." in submission.

Pedrini, B., C. J. Tsai, G. Capitani, C. Padeste, M. S. Hunter, N. A. Zatsepin, A. Barty, W. H. Benner, S. Boutet, G. K. Feld, S. P. Hau-Riege, R. A. Kirian, C. Kupitz, M. Messerschmitt, J. I. Ogren, T. Pardini, B. Segelke, G. J. Williams, J. C. Spence, R. Abela, M. Coleman, J. E. Evans, G. F. Schertler, M. Frank and X. D. Li (2014). "7 A resolution in protein two-dimensional-crystal X-ray diffraction at Linac Coherent Light Source." <u>Philos Trans R Soc Lond B Biol Sci</u> **369**(1647): 20130500.

Pellegrini, C. (2012). "The history of X-ray free-electron lasers." <u>The European Physical Journal H</u> **37**(5): 659-708.

Perutz, M. (1956). "Isomorphous replacement and phase determination in non-centrosymmetric space groups." <u>Acta Crystallographica</u> **9**(11): 867-873.

Philipp H. T., M. H., Mark Tate, Lucas Koerner, Sol M. Gruner (2011). "Pixel array detector for x-ray free electron laser experiments." <u>Nucl. Instr. Meth. Phys Res. A</u> **649**(67).

Philipp, H. T., Koerner, L. J., Hromalik, M. S., Tate, M. W. & Gruner, S. M. (2010). "Femtosecond radiation experiment detector for x-ray free-electron laser (XFEL) coherent x-ray imaging." <u>IEEE Trans. Nucl. Sci.</u> **57**: 3795-3799.

Patzlaff, J. S. and B. A. Barry (1996). "Pigment Quantitation and Analysis by HPLC Reverse Phase Chromatography: A Characterization of Antenna Size in Oxygen-Evolving Photosystem II Preparations from Cyanobacteria and Plants." <u>Biochemistry</u> **35**(24): 7802-7811.

Powell, H. R. (1999). "The Rossmann Fourier autoindexing algorithm in MOSFLM." <u>Acta Crystallogr D Biol Crystallogr</u> **55**(Pt 10): 1690-1695.

Powell, H. R., O. Johnson and A. G. Leslie (2013). "Autoindexing diffraction images with iMosflm." <u>Acta Crystallogr D Biol Crystallogr</u> **69**(Pt 7): 1195-1203.

Prince, R. C. and H. S. Kheshgi (2005). "The photobiological production of hydrogen: potential efficiency and effectiveness as a renewable fuel." <u>Crit Rev Microbiol</u> **31**(1): 19-31.

Proteau, A., R. Shi and M. Cygler (2010). "Application of dynamic light scattering in protein crystallization." <u>Curr Protoc Protein Sci</u> **Chapter 17**: Unit 17.10.

Raetz, C. R. and C. Whitfield (2002). "Lipopolysaccharide endotoxins." <u>Annu Rev Biochem</u> **71**: 635-700.

Ravelli, R. B. and S. M. McSweeney (2000). "The 'fingerprint' that X-rays can leave on structures." <u>Structure</u> **8**(3): 315-328.

Ray, P. H. (1980). "Purification and characterization of 3-deoxy-D-manno-octulosonate 8-phosphate synthetase from Escherichia coli." <u>J Bacteriol</u> **141**(2): 635-644.

Redecke, L., K. Nass, D. P. DePonte, T. A. White, D. Rehders, A. Barty, F. Stellato, M. Liang, T. R. Barends, S. Boutet, G. J. Williams, M. Messerschmidt, M. M. Seibert, A. Aquila, D. Arnlund, S. Bajt, T. Barth, M. J. Bogan, C. Caleman, T. C. Chao, R. B. Doak, H. Fleckenstein, M. Frank, R. Fromme, L. Galli, I. Grotjohann, M. S. Hunter, L. C. Johansson, S. Kassemeyer, G. Katona, R. A. Kirian, R. Koopmann, C. Kupitz, L. Lomb, A. V. Martin, S. Mogk, R. Neutze, R. L. Shoeman, J. Steinbrener, N. Timneanu, D. Wang, U. Weierstall, N. A. Zatsepin, J. C. Spence, P. Fromme, I. Schlichting, M. Duszenko, C. Betzel and H. N. Chapman (2013). "Natively inhibited Trypanosoma brucei cathepsin B structure determined by using an X-ray laser." <u>Science</u> **339**(6116): 227-230.

Roedig, P., R. Duman, J. Sanchez-Weatherby, I. Vartiainen, A. Burkhardt, M. Warmer, C. David, A. Wagner and A. Meents (2016). "Room-temperature macromolecular crystallography using a micro-patterned silicon chip with minimal background scattering." J Appl Crystallogr **49**(Pt 3): 968-975.

Roedig, P., I. Vartiainen, R. Duman, S. Panneerselvam, N. Stube, O. Lorbeer, M. Warmer, G. Sutton, D. I. Stuart, E. Weckert, C. David, A. Wagner and A. Meents (2015). "A micro-patterned silicon chip as sample holder for macromolecular crystallography experiments with minimal background scattering." Sci Rep **5**: 10451.

Roessler, C. G., A. Kuczewski, R. Stearns, R. Ellson, J. Olechno, A. M. Orville, M. Allaire, A. S. Soares and A. Heroux (2013). "Acoustic methods for high-throughput protein crystal mounting at next-generation macromolecular crystallographic beamlines." J Synchrotron Radiat **20**(Pt 5): 805-808.

Rossmann, M. G. and D. M. Blow (1962). "The detection of sub-units within the crystallographic asymmetric unit." Acta Crystallographica **15**(1): 24-31.

Rossmann, M. G. and C. G. van Beek (1999). "Data processing." Acta Crystallogr D Biol Crystallogr **55**(Pt 10): 1631-1640.

Rupp, B. Biomolecular Crystallography. Garland Science, New York (2010).

Saldin, E., Schneidmiller, E. & Yurkov, M. (2000). "The Physics of the Free Electron Laser." Berlin: Springer.

Sang-Kil Son, H. N. C. a. R. S. (2013). "Determination of multiwavelength anomalous diffraction coefficients at high X-ray intensity." JOURNAL OF PHYSICS B: ATOMIC, MOLECULAR AND OPTICAL PHYSICS **46**: 164015 (164018pp).

Saridakis, E. and N. E. Chayen (2003). "Systematic Improvement of Protein Crystals by Determining the Supersolubility." Biophys. J. **84**(2): 1218-1222.

Sauter, N. K., R. W. Grosse-Kunstleve and P. D. Adams (2004). "Robust indexing for automatic data collection." J Appl Crystallogr **37**(Pt 3): 399-409.

Sawaya, M. R., D. Cascio, M. Gingery, J. Rodriguez, L. Goldschmidt, J. P. Colletier, M. M. Messerschmidt, S. Boutet, J. E. Koglin, G. J. Williams, A. S. Brewster, K. Nass, J. Hattne, S. Botha, R. B. Doak, R. L. Shoeman, D. P. DePonte, H. W. Park, B. A. Federici, N. K. Sauter, I. Schlichting and D. S. Eisenberg (2014). "Protein crystal structure obtained at 2.9 A resolution from injecting bacterial cells into an X-ray free-electron laser beam." Proc Natl Acad Sci U S A **111**(35): 12769-12774.

Sayre, D. (1952). "Some implications of a theorem due to Shannon." Acta Crystallographica **5**(6): 843.

Sayre, D. (1952). "The squaring method: a new method for phase determination." Acta Crystallographica **5**(1): 60-65.

Scapin, G. (2013). "Molecular replacement then and now." Acta Crystallographica Section D **69**(11): 2266-2275.

Schirmer, T., W. Bode, R. Huber, W. Sidler and H. Zuber (1985). "X-ray crystallographic structure of the light-harvesting biliprotein C-phycocyanin from the thermophilic cyanobacterium Mastigocladus laminosus and its resemblance to globin structures." J Mol Biol **184**(2): 257-277.

Schlichting, I. (2015). "Serial femtosecond crystallography: the first five years." IUCrJ **2**(2): 0-0.

Schlichting, I. and J. Miao (2012). "Emerging opportunities in structural biology with X-ray free-electron lasers." Curr Opin Struct Biol **22**(5): 613-626.

Schlichting, I., G. Rapp, J. John, A. Wittinghofer, E. F. Pai and R. S. Goody (1989). "Biochemical and crystallographic characterization of a complex of c-Ha-ras p21 and caged GTP with flash photolysis." Proceedings of the National Academy of Sciences **86**(20): 7687-7690.

Schmidt, M. (2013). "Mix and inject: reaction initiation by diffusion for time-resolved macromolecular crystallography." Advances in Condensed Matter Physics **2013**.

Schmidt, M., V. Srajer, R. Henning, H. Ihee, N. Purwar, J. Tenboer and S. Tripathi (2013). "Protein energy landscapes determined by five-dimensional crystallography." Acta Crystallographica Section D: Biological Crystallography **69**(12): 2534-2542.

Schotte, F., H. S. Cho, V. R. Kaila, H. Kamikubo, N. Dashdorj, E. R. Henry, T. J. Graber, R. Henning, M. Wulff and G. Hummer (2012). "Watching a signaling protein function in real time via 100-ps time-resolved Laue crystallography." Proceedings of the National Academy of Sciences **109**(47): 19256-19261.

Schubert, R., A. Meyer, K. Dierks, S. Kapis, R. Reimer, H. Einspahr, M. Perbandt and C. Betzel (2015). "Reliably distinguishing protein nanocrystals from amorphous precipitate by means of depolarized dynamic light scattering." Journal of Applied Crystallography **48**(5): 1476-1484.

Setif, P. Q. and H. Bottin (1995). "Laser flash absorption spectroscopy study of ferredoxin reduction by photosystem I: spectral and kinetic evidence for the existence of several photosystem I-ferredoxin complexes." Biochemistry **34**(28): 9059-9070.

Sierra, R. G., H. Laksmono, J. Kern, R. Tran, J. Hattne, R. Alonso-Mori, B. Lassalle-Kaiser, C. Glockner, J. Hellmich, D. W. Schafer, N. Echols, R. J. Gildea, R. W. Grosse-Kunstleve, J. Sellberg, T. A. McQueen, A. R. Fry, M. M. Messerschmidt, A. Miahnahri, M. M. Seibert, C. Y. Hampton, D. Starodub, N. D. Loh, D. Sokaras, T. C. Weng, P. H. Zwart, P. Glatzel, D. Milathianaki, W. E. White, P. D. Adams, G. J. Williams, S. Boutet, A. Zouni, J. Messinger, N. K. Sauter, U. Bergmann, J. Yano, V. K. Yachandra and M. J. Bogan (2012). "Nanoflow electrospinning serial femtosecond crystallography." Acta Crystallogr D Biol Crystallogr **68**(Pt 11): 1584-1587.

Smith, J. L., R. F. Fischetti and M. Yamamoto (2012). "Micro-crystallography comes of age." Current opinion in structural biology **22**(5): 602-612.

Soares, A. S., M. A. Engel, R. Stearns, S. Datwani, J. Olechno, R. Ellson, J. M. Skinner, M. Allaire and A. M. Orville (2011). "Acoustically mounted microcrystals yield high-resolution X-ray structures." Biochemistry **50**(21): 4399-4401.

Son, S. K., H. N. Chapman and R. Santra (2011). "Multiwavelength anomalous diffraction at high x-ray intensity." Phys Rev Lett **107**(21): 218102.

Spence, J. C., R. A. Kirian, X. Wang, U. Weierstall, K. E. Schmidt, T. White, A. Barty, H. N. Chapman, S. Marchesini and J. Holton (2011). "Phasing of coherent femtosecond X-ray diffraction from size-varying nanocrystals." Opt Express **19**(4): 2866-2873.

Spence, J. C., U. Weierstall and H. N. Chapman (2012). "X-ray lasers for structural and dynamic biology." Rep Prog Phys **75**(10): 102601.

Steitz, T. A., T. J. Richmond, D. Wise and D. Engelman (1974). "The lac repressor protein: molecular shape, subunit structure, and proposed model for operator interaction based on structural studies of microcrystals." Proceedings of the National Academy of Sciences **71**(3): 593-597.

Stellato, F., D. Oberthür, M. Liang, R. Bean, C. Gati, O. Yefanov, A. Barty, A. Burkhardt, P. Fischer, L. Galli, R. A. Kirian, J. Meyer, S. Panneerselvam, C. H. Yoon, F. Chervinskii, E. Speller, T. A. White, C. Betzel, A. Meents and H. N. Chapman (2014). "Room-temperature macromolecular serial crystallography using synchrotron radiation." IUCrJ **1**(Pt 4): 204-212.

Stevenson, H., D. DePonte, A. Makhov, J. F. Conway, O. Zeldin, S. Boutet, G. Calero and A. Cohen (2014). "Transmission electron microscopy as a tool for nanocrystal characterization pre- and post-injector." Philosophical Transactions of the Royal Society B: Biological Sciences **369**(1647): 20130322.

Stevenson, H. P., A. M. Makhov, M. Calero, A. L. Edwards, O. B. Zeldin, Mathews, II, G. Lin, C. O. Barnes, H. Santamaria, T. M. Ross, S. M. Soltis, C. Khosla, V. Nagarajan, J. F. Conway, A. E. Cohen and G. Calero (2014). "Use of transmission electron microscopy to identify nanocrystals of challenging protein targets." Proc Natl Acad Sci U S A **111**(23): 8470-8475.

Stoddard, B. L., B. E. Cohen, M. Brubaker, A. D. Mesecar and D. E. Koshland (1998). "Millisecond Laue structures of an enzyme-product complex using photocaged substrate analogs." Nat Struct Mol Biol **5**(10): 891-897.

Stoddard, B. L. and G. K. Farber (1995). "Direct measurement of reactivity in the protein crystal by steady-state kinetic studies." Structure **3**(10): 991-996.

Strüder, L. E., S. W.; Rolles, D.; Hartmann, R.; Holl, P.; Lutz, G.; Soltau, H.; Eckart, R.; Reich, C.; Heinzinger, K. et al (2010). " Large−format, high−speed, X−ray pnCCDs combined with electron and ion imaging spectrometers in a multipurpose chamber for experiments at 4th generation light sources." Nucl. Instrum. Methods Phys. Res. A **614**: 483-496.

Suga, M., F. Akita, K. Hirata, G. Ueno, H. Murakami, Y. Nakajima, T. Shimizu, K. Yamashita, M. Yamamoto, H. Ago and J.-R. Shen (2015). "Native structure of photosystem II at 1.95 A resolution viewed by femtosecond X-ray pulses." Nature **517**(7532): 99-103.

Sugahara, M., E. Mizohata, E. Nango, M. Suzuki, T. Tanaka, T. Masuda, R. Tanaka, T. Shimamura, Y. Tanaka, C. Suno, K. Ihara, D. Pan, K. Kakinouchi, S. Sugiyama, M. Murata, T. Inoue, K. Tono, C. Song, J. Park, T. Kameshima, T. Hatsui, Y. Joti, M. Yabashi and S. Iwata (2015). "Grease matrix as a versatile carrier of proteins for serial crystallography." Nat Meth **12**(1): 61-63.

Sugahara, M., C. Song, M. Suzuki, T. Masuda, S. Inoue, T. Nakane, F. Yumoto, E. Nango, R. Tanaka, K. Tono, Y. Joti, T. Kameshima, T. Hatsui, M. Yabashi, O. Nureki, K. Numata and S. Iwata (2016). "Oil-free hyaluronic acid matrix for serial femtosecond crystallography." Scientific Reports **6**: 24484.

Tao, P., H. B. Schlegel and D. L. Gatti (2010). "Common basis for the mechanism of metallo and non-metallo KDO8P synthases." J Inorg Biochem **104**(12): 1267-1275.

Tautermann, C. S. (2014). "GPCR structures in drug design, emerging opportunities with new structures." Bioorg Med Chem Lett **24**(17): 4073-4079.

Taylor, G. L. (2010). "Introduction to phasing." Acta Crystallogr D Biol Crystallogr **66**(Pt 4): 325-338.

Tenboer, J., S. Basu, N. Zatsepin, K. Pande, D. Milathianaki, M. Frank, M. Hunter, S. Boutet, G. J. Williams and J. E. Koglin (2014). "Time-resolved serial crystallography captures high-resolution intermediates of photoactive yellow protein." Science **346**(6214): 1242-1246.

Trebbin, M., K. Kruger, D. DePonte, S. V. Roth, H. N. Chapman and S. Forster (2014). "Microfluidic liquid jet system with compatibility for atmospheric and high-vacuum conditions." Lab Chip **14**(10): 1733-1745.

Umena, Y., K. Kawakami, J. R. Shen and N. Kamiya (2011). "Crystal structure of oxygen-evolving photosystem II at a resolution of 1.9 A." Nature **473**(7345): 55-60.

Ursby, T., M. Weik, E. Fioravanti, M. Delarue, M. Goeldner and D. Bourgeois (2002). "Cryophotolysis of caged compounds: a technique for trapping intermediate states in protein crystals." Acta Crystallographica Section D: Biological Crystallography **58**(4): 607-614.

Vagin, A. and A. Teplyakov (1997). "MOLREP: an Automated Program for Molecular Replacement." Journal of Applied Crystallography **30**(6): 1022-1025.

Von, R. (2007). "Multipattern Rietveld refinement of protein powder data: an approach to higher resolution." Journal of Applied Crystallography **40**(1): 133-143.

W. T. Astbury, R. L. (1934). "X-Ray Photographs of Crystalline Pepsin." Nature **133**(795).

Wampler, R. D., D. J. Kissick, C. J. Dehen, E. J. Gualtieri, J. L. Grey, H. F. Wang, D. H. Thompson, J. X. Cheng and G. J. Simpson (2008). "Selective detection of protein crystals by second harmonic microscopy." J Am Chem Soc **130**(43): 14076-14077.

Wang, D., U. Weierstall, L. Pollack and J. Spence (2014). "Double-focusing mixing jet for XFEL study of chemical kinetics." Journal of Synchrotron Radiation **21**(Pt 6): 1364-1366.

Wang, J., H. S. Duewel, R. W. Woodard and D. L. Gatti (2001). "Structures of Aquifex aeolicus KDO8P synthase in complex with R5P and PEP, and with a bisubstrate inhibitor: role of active site water in catalysis." Biochemistry **40**(51): 15676-15683.

Warkentin, M., R. Badeau, J. Hopkins and R. E. Thorne (2011). "Dark progression reveals slow timescales for radiation damage between T = 180 and 240 K." Acta Crystallogr D Biol Crystallogr **67**(Pt 9): 792-803.

Warkentin, M., J. B. Hopkins, R. Badeau, A. M. Mulichak, L. J. Keefe and R. E. Thorne (2013). "Global radiation damage: temperature dependence, time dependence and how to outrun it." Journal of Synchrotron Radiation **20**(Pt 1): 7-13.

Watson, J. D. and F. H. C. Crick (1953). "Molecular Structure of Nucleic Acids: A Structure for Deoxyribose Nucleic Acid." Nature **171**(4356): 737-738.

Weierstall, U. (2014). "Liquid sample delivery techniques for serial femtosecond crystallography." Philos Trans R Soc Lond B Biol Sci **369**(1647): 20130337.

Weierstall, U., D. James, C. Wang, T. A. White, D. Wang, W. Liu, J. C. Spence, R. Bruce Doak, G. Nelson, P. Fromme, R. Fromme, I. Grotjohann, C. Kupitz, N. A. Zatsepin, H. Liu, S. Basu, D. Wacker, G. W. Han, V. Katritch, S. Boutet, M. Messerschmidt, G. J. Williams, J. E. Koglin, M. Marvin Seibert, M. Klinker, C. Gati, R. L. Shoeman, A. Barty, H. N. Chapman, R. A. Kirian, K. R. Beyerlein, R. C. Stevens, D. Li, S. T. Shah, N. Howe, M. Caffrey and V. Cherezov (2014). "Lipidic cubic phase injector facilitates membrane protein serial femtosecond crystallography." Nat Commun **5**: 3309.

Weierstall, U., J. C. Spence and R. B. Doak (2012). "Injector for scattering measurements on fully solvated biospecies." Rev Sci Instrum **83**(3): 035108.

Wen, J. G. (2014). Transmission Electron Microscopy. Practical Materials Characterization. M. Sardela. New York, Springer-Verlag New York**:** 189-229.

White, T. A., A. Barty, F. Stellato, J. M. Holton, R. A. Kirian, N. A. Zatsepin and H. N. Chapman (2013). "Crystallographic data processing for free-electron laser sources." Acta Crystallogr D Biol Crystallogr **69**(Pt 7): 1231-1240.

White, T. A., A. Barty, F. Stellato, J. M. Holton, R. A. Kirian, N. A. Zatsepin and H. N. Chapman (2013). "Crystallographic data processing for free-electron laser sources." Acta Crystallographica Section D **69**(7): 1231-1240.

White, T. A., R. A. Kirian, A. V. Martin, A. Aquila, K. Nass, A. Barty and H. N. Chapman (2012). "CrystFEL: a software suite for snapshot serial crystallography." Journal of Applied Crystallography **45**(2): 335-341.
White, T. A., V. Mariani, W. Brehm, O. Yefanov, A. Barty, K. R. Beyerlein, F. Chervinskii, L. Galli, C. Gati, T. Nakane, A. Tolstikova, K. Yamashita, C. H. Yoon, K. Diederichs and H. N. Chapman (2016). "Recent developments in CrystFELThis article will form part of a virtual special issue of the journal on free-electron laser software." Journal of Applied Crystallography **49**(2): 680-689.

Williams, G. P. (1982). "A general review of synchrotron radiation, its uses and special technologies." Vacuum **32**(6): 333-345.

Wolfenden, R. and M. J. Snider (2001). "The depth of chemical time and the power of enzymes as catalysts." Acc Chem Res **34**(12): 938-945.

Woolfson, M. An introduction to X-ray crystallography. Cambridge University Press, Cambridge, 2nd edition (1997).

Wu, W., P. Nogly, J. Rheinberger, L. M. Kick, C. Gati, G. Nelson, X. Deupi, J. Standfuss, G. Schertler and V. Panneels (2015). "Batch crystallization of rhodopsin for structural dynamics using an X-ray free-electron laser." Acta Crystallogr F Struct Biol Commun **71**(Pt 7): 856-860.

Yamashita, K., D. Pan, T. Okuda, M. Sugahara, A. Kodan, T. Yamaguchi, T. Murai, K. Gomi, N. Kajiyama and E. Mizohata (2015). "An isomorphous replacement method for efficient de novo phasing for serial femtosecond crystallography." Scientific reports **5**.

Yano, J., J. Kern, K.-D. Irrgang, M. J. Latimer, U. Bergmann, P. Glatzel, Y. Pushkar, J. Biesiadka, B. Loll, K. Sauer, J. Messinger, A. Zouni and V. K. Yachandra (2005). "X-ray damage to the Mn4Ca complex in single crystals of photosystem II: A case study for metalloprotein crystallography." Proceedings of the National Academy of Sciences of the United States of America **102**(34): 12047-12052.

Yarin, A. L., S. Koombhongse and D. H. Reneker (2001). "Taylor cone and jetting from liquid droplets in electrospinning of nanofibers." <u>Journal of Applied Physics</u> **90**(9): 4836-4846.

Yazawa, K., M. Sugahara, K. Yutani, M. Takehira and K. Numata (2016). "Derivatization of Proteinase K with Heavy Atoms Enhances Its Thermal Stability." <u>ACS Catalysis</u> **6**(5): 3036-3046.

Zeldin, O. B., M. Gerstel and E. F. Garman (2013). "RADDOSE-3D: time- and space-resolved modelling of dose in macromolecular crystallography." <u>Journal of Applied Crystallography</u> **46**(4): 1225-1230.

Zhang, H., H. Unal, C. Gati, G. W. Han, W. Liu, N. A. Zatsepin, D. James, D. Wang, G. Nelson, U. Weierstall, M. R. Sawaya, Q. Xu, M. Messerschmidt, G. J. Williams, S. Boutet, O. M. Yefanov, T. A. White, C. Wang, A. Ishchenko, K. C. Tirupula, R. Desnoyer, J. Coe, C. E. Conrad, P. Fromme, R. C. Stevens, V. Katritch, S. S. Karnik and V. Cherezov (2015). "Structure of the Angiotensin receptor revealed by serial femtosecond crystallography." <u>Cell</u> **161**(4): 833-844.

Zink, F. E. (1997). "X-ray tubes." <u>Radiographics</u> **17**(5): 1259-1268.

Zhou, Q., Y. Lai, T. Bacaj, M. Zhao, A. Y. Lyubimov, M. Uervirojnangkoorn, O. B. Zeldin, A. S. Brewster, N. K. Sauter, A. E. Cohen, S. M. Soltis, R. Alonso-Mori, M. Chollet, H. T. Lemke, R. A. Pfuetzner, U. B. Choi, W. I. Weis, J. Diao, T. C. Sudhof and A. T. Brunger (2015). "Architecture of the synaptotagmin-SNARE machinery for neuronal exocytosis." <u>Nature</u> **525**(7567): 62-67.

Zuo, J. M. and J. L. Rouviere (2015). "Solving difficult structures with electron diffraction." <u>IUCrJ</u> **2**(Pt 1): 7-8.

APPENDIX A

PERMISSIONS

Chapter 1:

Reprinted by permission from Synchrotron Soleil: schéma de principe Copyright © Chaix & Morel et associés, used with permission. Obtained from https://commons.wikimedia.org/wiki/File:Sch%C3%A9ma_de_principe_du_synchrotron.jpg on 10/24/2016.

Chapter 2:

Text, Figures 2.1-2, 2.5, 2.7, 2.9, and Tables 2.1-2 reprinted from Garcia J.M., Conrad, C.E., Coe, J., Fromme P. (2016). "Serial femtosecond crystallography: a revolution in structural biology" Archives of Biochemistry and Biophysics 602(2016):32-47 with permission from Elsevier.

Figure 2.3 reprinted from Axford D. et al. (2012). "In situ macromolecular crystallography using microbeams." Acta. Cryst. D. 68(5):592-600 with permission from IUCr.

Figure 2.4 reprinted from Neutze, R., R. Wouts, D. van der Spoel, E. Weckert and J. Hajdu (2000). "Potential for biomolecular imaging with femtosecond X-ray pulses." Nature **406**(6797): 752-757 with permisison from Nature Publishing Group.

Figure 2.6 reprinted from Caffrey, M. (2015). "A comprehensive review of the lipid cubic phase or in meso method for crystallizing membrane and soluble proteins and complexes." Acta Crystallogr F Struct Biol Commun **71**(Pt 1): 3-18 with permission from IUCr.

Figure 2.8 reprinted from Weierstall, U., D. James, C. Wang, T. A. White, D. Wang, W. Liu, J. C. Spence, R. Bruce Doak, G. Nelson, P. Fromme, R. Fromme, I. Grotjohann, C. Kupitz, N. A. Zatsepin, H. Liu, S. Basu, D. Wacker, G. W. Han, V. Katritch, S. Boutet, M. Messerschmidt, G. J. Williams, J. E. Koglin, M. Marvin Seibert, M. Klinker, C. Gati, R. L. Shoeman, A. Barty, H. N. Chapman, R. A. Kirian, K. R. Beyerlein, R. C. Stevens, D. Li, S. T. Shah, N. Howe, M. Caffrey and V. Cherezov (2014). "Lipidic cubic phase injector facilitates membrane protein serial femtosecond crystallography." Nat Commun **5**: 3309 with permission from Nature Publishing Group.

Chapter 3:

Text from 3.1-3.4, Figures 3.1-3.9, and Tables 3.1-2 from Conrad, C. E., S. Basu, D. James, D. Wang, A. Schaffer, S. Roy-Chowdhury, N. A. Zatsepin, A. Aquila, J. Coe, C. Gati, M. S. Hunter, J. E. Koglin, C. Kupitz, G. Nelson, G. Subramanian, T. A. White, Y. Zhao, J. Zook, S. Boutet, V. Cherezov, J. C. Spence, R. Fromme, U. Weierstall and P. Fromme (2015). "A novel inert crystal delivery medium for serial femtosecond crystallography." IUCrJ **2**(Pt 4): 421-430 with permission from IUCr.

Figure 3.12 from Sierra, R. G., H. Laksmono, J. Kern, R. Tran, J. Hattne, R. Alonso-Mori, B. Lassalle-Kaiser, C. Glockner, J. Hellmich, D. W. Schafer, N. Echols, R. J. Gildea, R. W. Grosse-Kunstleve, J. Sellberg, T. A. McQueen, A. R. Fry, M. M. Messerschmidt, A. Miahnahri, M. M. Seibert, C. Y. Hampton, D. Starodub, N. D. Loh, D. Sokaras, T. C. Weng, P. H. Zwart, P. Glatzel, D. Milathianaki, W. E. White, P. D. Adams, G. J. Williams, S. Boutet, A. Zouni, J. Messinger, N. K. Sauter, U. Bergmann, J. Yano, V. K. Yachandra and M. J. Bogan (2012). "Nanoflow electrospinning serial femtosecond crystallography." Acta Crystallogr D Biol Crystallogr **68**(Pt 11): 1584-1587 with permission from IUCr.

Chapter 5:

Figure 5.1 from Raetz, C. R. and C. Whitfield (2002). "Lipopolysaccharide endotoxins." <u>Annu Rev Biochem</u> **71**: 635-700 with permission from Annual Reviews.

Figure 5.2 from Li, Z., A. K. Sau, C. M. Furdui and K. S. Anderson (2005). "Probing the role of tightly bound phosphoenolpyruvate in Escherichia coli 3-deoxy-d-manno-octulosonate 8-phosphate synthase catalysis using quantitative time-resolved electrospray ionization mass spectrometry in the millisecond time range." <u>Anal Biochem</u> **343**(1): 35-47 with permission from Elsevier.

Figure 5.15 from Trebbin, M., K. Kruger, D. DePonte, S. V. Roth, H. N. Chapman and S. Forster (2014). "Microfluidic liquid jet system with compatibility for atmospheric and high-vacuum conditions." <u>Lab Chip</u> **14**(10): 1733-1745 with permission from Royal Society of Chemistry.

Chapter 6:

Figure 6.1 from Nogly, P., V. Panneels, G. Nelson, C. Gati, T. Kimura, C. Milne, D. Milathianaki, M. Kubo, W. Wu, C. Conrad, J. Coe, R. Bean, Y. Zhao, P. Bath, R. Dods, R. Harimoorthy, K. R. Beyerlein, J. Rheinberger, D. James, D. DePonte, C. Li, L. Sala, G. J. Williams, M. S. Hunter, J. E. Koglin, P. Berntsen, E. Nango, S. Iwata, H. N. Chapman, P. Fromme, M. Frank, R. Abela, S. Boutet, A. Barty, T. A. White, U. Weierstall, J. Spence, R. Neutze, G. Schertler and J. Standfuss (2016). "Lipidic cubic phase injector is a viable crystal delivery system for time-resolved serial crystallography." <u>Nat Commun</u> **7**: 12314 with permission from Nature Publishing Group.

Figure 6.2 from Ayyer, K., O. M. Yefanov, D. Oberthur, S. Roy-Chowdhury, L. Galli, V. Mariani, S. Basu, J. Coe, C. E. Conrad, R. Fromme, A. Schaffer, K. Dorner, D. James, C. Kupitz, M. Metz, G. Nelson, P. L. Xavier, K. R. Beyerlein, M. Schmidt, I. Sarrou, J. C. Spence, U. Weierstall, T. A. White, J. H. Yang, Y. Zhao, M. Liang, A. Aquila, M. S. Hunter, J. S. Robinson, J. E. Koglin, S. Boutet, P. Fromme, A. Barty and H. N. Chapman (2016). "Macromolecular diffractive imaging using imperfect crystals." <u>Nature</u> **530**(7589): 202-206 with permission from Nature Publishing Group.

Figure 6.3 from Kang, Y., X. E. Zhou, X. Gao, Y. He, W. Liu, A. Ishchenko, A. Barty, T. A. White, O. Yefanov, G. W. Han, Q. Xu, P. W. de Waal, J. Ke, M. H. Tan, C. Zhang, A. Moeller, G. M. West, B. D. Pascal, N. Van Eps, L. N. Caro, S. A. Vishnivetskiy, R. J. Lee, K. M. Suino-Powell, X. Gu, K. Pal, J. Ma, X. Zhi, S. Boutet, G. J. Williams, M. Messerschmidt, C. Gati, N. A. Zatsepin, D. Wang, D. James, S. Basu, S. Roy-Chowdhury, C. E. Conrad, J. Coe, H. Liu, S. Lisova, C. Kupitz, I. Grotjohann, R. Fromme, Y. Jiang, M. Tan, H. Yang, J. Li, M. Wang, Z. Zheng, D. Li, N. Howe, Y. Zhao, J. Standfuss, K. Diederichs, Y. Dong, C. S. Potter, B. Carragher, M. Caffrey, H. Jiang, H. N. Chapman, J. C. Spence, P. Fromme, U. Weierstall, O. P. Ernst, V. Katritch, V. V. Gurevich, P. R. Griffin, W. L. Hubbell, R. C. Stevens, V. Cherezov, K. Melcher and H. E. Xu (2015). "Crystal structure of rhodopsin bound to arrestin by femtosecond X-ray laser." <u>Nature</u> **523**(7562): 561-567 with permission from Nature Publishing Group.

Figure 6.4 from Kupitz, C., S. Basu, I. Grotjohann, R. Fromme, N. A. Zatsepin, K. N. Rendek, M. S. Hunter, R. L. Shoeman, T. A. White, D. Wang, D. James, J. H. Yang, D. E. Cobb, B. Reeder, R. G. Sierra, H. Liu, A. Barty, A. L. Aquila, D. Deponte, R. A. Kirian, S. Bari, J. J. Bergkamp, K. R. Beyerlein, M. J. Bogan, C. Caleman, T. C. Chao, C. E. Conrad, K. M. Davis, H. Fleckenstein, L. Galli, S. P. Hau-Riege, S. Kassemeyer, H. Laksmono, M. Liang, L. Lomb, S. Marchesini, A. V. Martin, M. Messerschmidt, D. Milathianaki, K. Nass, A. Ros, S. Roy-Chowdhury, K. Schmidt, M. Seibert, J. Steinbrener, F. Stellato, L. Yan, C. Yoon, T. A. Moore, A. L. Moore, Y. Pushkar, G. J. Williams, S. Boutet, R. B. Doak, U. Weierstall, M. Frank, H. N. Chapman, J. C. Spence and P.

Fromme (2014). "Serial time-resolved crystallography of photosystem II using a femtosecond X-ray laser." <u>Nature</u> **513**(7517): 261-265 with permission from Nature Publishing Group.